UNIVERSIDADE DE SANTIAGO DE COMPOSTELA
INSTITUTO DE CERÁMICA DE GALICIA

AN EFFICIENT APPROACH TO THE SYNTHESIS OF A CALCIUM PHOSPHATE BONE-CEMENT AND ITS REINFORCEMENT BY HYDROXYAPATITE CRYSTALS OF VARIOUS PARTICLE MORPHOLOGIES

Mª Inés Sánchez Neira
Tesis de Doctorado
Santiago de Compostela, 2008

UNIVERSIDADE DE SANTIAGO DE COMPOSTELA

INSTITUTO DE CERÁMICA DE GALICIA

AN EFFICIENT APPROACH TO THE SYNTHESIS OF A CALCIUM PHOSPHATE BONE-CEMENT AND ITS REINFORCEMENT BY HYDROXYAPATITE CRYSTALS OF VARIOUS PARTICLE MORPHOLOGIES

Memoria presentada por D[a]. María Inés Sánchez Neira

para optar al grado de Doctor por la

Universidad de Santiago de Compostela.

Junio 2008

ACKNOWLEGMENTS

En primer lugar, quiero agradecer al Prof. Francisco Guitián Rivera la oportunidad de trabajar bajo su supervisión en el Instituto de Cerámica de Galicia. Gracias por los consejos, comentarios y apoyo que me han guiado a lo largo de estos años.

I would like to thank Prof. Masahiro Yoshimura for his kindly acceptance of my stay in his research group at the Tokyo Institute of Technology (Materials and Structures department, Japan). His knowledge about hydrothermal technique and his will to share it made this work possible.

Thank you to Prof. Peter Fratzl and Dr. Himadri S. Gupta for their gently agreement for my research stay at the Biomaterials department of the Max Planck Institute of Colloids and Interfaces (Potsdam, Germany). Their understanding of bone and the share of their knowledge improve much this research and open a new *biomimetic* world for me.

Thank you to Prof. Gustav Van Tendeloo and Dr. Oleg I. Lebedev from the Electron Microscopy for Materials Science (University of Antwerp, Belgium) for their help with transmission electron microscopy studies.

Gracias a Mar, Jose, Eva, Gabriel, María y Déborah por los buenos ratos compartidos dentro y fuera del Instituto. ¡Uno siempre necesita oxigenarse!. Gracias por vuestra amistad. Gracias también a Pablo por su ayuda con el porosímetro y a Alfredo y Jaime por sus enseñanzas sobre los aparatos del Instituto. Gracias a Mercedes por ser como es. En general, gracias a todos los compañeros, a los que todavía están en el Instituto y a los que ya no.

Thank you also to the members of Yoshimura-sensei's lab. Thanks to Gusan, Yury and Machan for the "Creative company". For the share of bin-birru and long funny crazy nihon-jin nights. Machida!. Thank you to Watanabe-san, Suda, Naota, Oga-chan, Kudo, Wagata, Yuzaburo, Sakamoto-san, Ruwan-san, Li-san, Ishigaki (Sacho!), Nakagawa and Subramani to make me feel like at home so far from home. Thank you to Matsushita-sensei for his kindest and to Yoshioka-san for her amazing efficiency. You all made my stay in Japan an incredible experience that I will never forget. The lab life (dinners, parties, travels,…) was just perfect. Thanks for make from me "Ine-chan". Arigato gozaimasu.

Thanks also to Sugata, Bidisa, Neli, Plamen and Vitor for the home parties, the discussions about Nihon, Nihon-jins and "the meaning of life". Spopa!.Ummm…

Gracias a María, Enrique e Irene por el toque español en Japón.

Thanks too to the members of the Biomaterials department at Potsdam. Thank you to Christoph, Claudia and Anna for the share lunches and coffees. Thanks to Maxim for the discussions on the train and at the office. Thanks to Jan and Antje for their friendly kindness. Thanks to Annemarie for her amazing preparation of my samples and to Petra for show me what I need to know about the nanoindentor. Gracias a Josefina por su argentino soplo de aire fresco. ¡Está tan bien poder olvidarse del inglés de vez en cuando!. ¡Y por las discusiones sobre mecánica!.

Thanks to Kirill, Julia, Peter, Tom, Almudena, Rosa and Carine for make Berliner life more funny and party-full.

Gracias a Iria, Carba, Raquel, Juan, Jorge y Paco por vuestra amistad continuada a lo largo de los años, ¡estemos donde estemos cada uno!.

Gracias a mi familia por su apoyo constante y cariño. Спасибо Коленькам за то, что приняли меня в семью.

Самое главное, большое спасибо моему любимому Юре. Спасибо за его помощь с диссертацией и за все хорошее. Спасибо за то, что связал свою жизнь со мной. Без тебя ничего этого бы не было. Я тебя люблю.

This work was partially supported by the Spanish Ministry of Education and Science with a Formación de Personal Investigador fellowship (project MAT2002-03857) and the European Union with a Marie Curie Early Stage Training fellowship on Biomimetic Systems (MEST-CT-2004-504465).

ありがとう, dankeschön, Спасибо. MUCHAS GRACIAS A TODOS

TABLE OF CONTENTS

ACRONYMES

3D – Three-dimensional;

ACP – Amorphous calcium phosphate $Ca_xH_y(PO_4)_z{\cdot}nH_2O$ (n = 3-4.5; 15-20% H_2O);

AFM – Atomic force microscopy;

BCP – Biphasic calcium phosphate;

BET – Brunauer-Emmett-Teller method;

BJH – Barrett-Joyner-Halenda method;

CDHA – Calcium deficient hydroxyapatite $Ca_{10-x}(HPO_4)_x(PO_4)_{6-x}(OH)_{2-x}$ ($0 < x < 1$);

ClAp – Chlorapatite $Ca_{10}(PO_4)_3Cl_2$;

CPC – Calcium phosphate bone-cement or calcium phosphate cement;

CS – Compressive strength;

CT – Cohesion time;

DCPA – Dicalcium phosphate anhydrous $CaHPO_4$;

DCPD – Dicalcium phosphate dihydrate $CaHPO_4{\cdot}2H_2O$;

DLS – Dynamic light scattering technique;

$\boldsymbol{E_s}$ – Elastic or Young's modulus;

ED – Electron diffraction;

EDX – Energy-dispersive X-ray spectroscopy;

FAp – Fluorapatite $Ca_{10}(PO_4)_6F_2$;

FE-ESEM – Field-emission environmental scanning electron microscopy;

FT – Fourier transform;

FHA – Fluorhydroxyapatite $Ca_{10}(PO_4)_6(OH)_{2-x}F_x$ ($0 < x < 2$);

FWHM – Full width at half maximum;

$\boldsymbol{H}$ – Hardness;

HA – Hydroxyapatite $Ca_{10}(PO_4)_6(OH)_2$;

HDPE – High-density polyethylene;

HFA – Hydroxyfluorapatite $Ca_{10}(PO_4)_6(OH)_{2-x}F_x$ ($0 < x < 2$);

HRTEM – High resolution transmission electron microscopy;

IR – Diffuse reflectance infrared Fourier-transform spectroscopy;

IUPAC – International union of pure and applied chemistry;

JCPDS – Joint committee of powder diffraction standards;

MCPA – Monocalcium phosphate anhydrous $Ca(H_2PO_4)_2$;

MCPM – Monocalcium phosphate monohydrate $Ca(H_2PO_4)_2{\cdot}H_2O$;

NI – Nano-indentation;

OCP – Octacalcium phosphate $Ca_8(HPO_4)_2(PO_4)_4 \cdot 5H_2O$;

PMMA – Polymethylmethacrylate;

PSD – Particle size distributions;

PTFE – Polytetrafluoroethylene;

SBF – Acellular simulated body fluid;

SEM – Scanning electron microscopy;

S/L ratio – Solid to liquid ratio (g/mL);

ST – Final setting time;

TCP – Tricalcium phosphate $Ca_3(PO_4)_2$;

TEM – Transmission electron microscopy;

TGA/DTA – Thermo-gravimetric and differential thermal analyses;

TTCP – Tetracalcium phosphate $Ca_4(PO_4)_2O$;

XRD – Powder X-ray diffraction;

RESUMEN

Motivación

Los huesos humanos fracturados tienen la capacidad de autorrepararse a través de un proceso natural. Sin embargo, existen muchas situaciones en las que las fracturas no cicatrizan de forma apropiada o espontánea. Es por ello que, hoy en día, la reparación y sustitución de huesos mediante el uso de implantes fabricados con diversos materiales artificiales son prácticas médicas corrientes. Estos materiales artificiales empleados para reemplazar una parte o una función del cuerpo humano de un modo seguro, fiable, económico y psicológicamente aceptable, reciben el nombre de biomateriales.

En este contexto los cementos de fosfato cálcico (CPCs) presentan unas propiedades excelentes, tanto biológicas como fisiológicas, para ser empleados en la reparación o sustitución de elementos óseos. Los CPCs son altamente bioactivos, biocompatibles y osteoconductivos, es decir, son resaborbidos por el suero fisiológico del cuerpo humano, permitiendo así su progresiva sustitución por hueso nuevo, recién formado.

De forma general, los CPCs se obtienen mediante la mezcla de uno o varios ortofosfatos de calcio, que actúan como precursores, en un medio acuoso. Dependiendo de la cantidad de fase líquida empleada, se obtiene una especie de masilla, fácilmente moldeable, o un líquido inyectable. Ambos productos son capaces de fraguar *in vivo*. Es por esto que los CPCs se presentan como unos biomateriales altamente prometedores en su uso para aplicaciones clínicas, como puede ser el relleno de cavidades óseas.

Además, en la mayoría de los CPC se obtiene hidroxiapatito deficiente en calcio como producto de la reacción de fraguado. Dicho hidroxiapatito (HA) es química y estructuralmente muy similar al apatito biológico, el principal componente inorgánico de los huesos, lo que confiere a los CPC unas características excelentes desde un punto de vista biológico y fisiológico para su uso en implantes óseos.

En general, la rápida conversión de los precursores de los CPCs al producto final HA no sólo conlleva un aumento de las propiedades fisiológicas adecuadas, sino también de las propiedades mecánicas. Sin embargo, hay que tener en cuenta que durante un proceso quirúrgico el CPC debe fraguar lo suficientemente lento como para permitir la implantación quirúrgica, y lo bastante rápido como para minimizar la duración de la operación. En consecuencia, desde un punto de vista fundamental y de aplicación, es importante diseñar CPCs que presenten tiempos de fraguado entre 10 y 30 minutos, así como una rápida conversión al producto final, preferiblemente, HA.

Debido a que los CPCs presentan una resistencia a la fractura menor que los huesos (~0.6-1.5 MPa/m^2 frente a 2-12 MPa/m^2), sus aplicaciones clínicas están, en la actualidad, limitadas a áreas dónde los huesos no soportan carga, por ejemplo, reparaciones craneofaciales o periodontales. Uno de los métodos más empleados para mejorar las propiedades mecánicas de los CPCs es la adición de fibras que actúen como fase de refuerzo. Por ejemplo, las cerámicas de HA han sido reforzadas con éxito mediante el empleo de fibras de SiC, carbón, Si_3N_4, Al_2O_3 o ZrO_2. Sin embargo, dichos materiales son, en el mejor de los casos, bioinertes, es decir, no interaccionan con el tejido óseo circundante, y su empleo conlleva una disminución de la bioactividad de los correspondientes composites cerámicos.

En contraste con estas fibras bioinertes, si se emplean partículas de HA como fase de refuerzo, éstas no sólo actúan como tal, sino que también mejoran la bioactividad de los composites finales, siendo ésta la gran ventaja de las fibras de HA empleadas como refuerzo de biomateriales cerámicos o de CPCs.

Cuando se quiere reforzar un material, es de vital importancia tener en cuenta la morfología de las partículas empleadas como fase de refuerzo. Así, en composites isotrópicos, las inclusiones con forma de lámina son las más efectivas, seguidas de las fibras, siendo la morfología menos efectiva la esférica. Por tanto, es importante desarrollar una ruta sintética efectiva que nos permita obtener cristales puros de HA sin defectos y con una morfología definida y controlable.

Así, con unos materiales de partida adecuados, es posible obtener nuevos biocomposites (composites empleados como biomateriales) para su empleo en sustitución y reparación ósea. Estos composites están compuestos por un CPC con una rápida conversión a HA y un tiempo de fraguado adecuado como matriz, y cristales de HA con diferentes morfologías como fase de refuerzo. Dichos materiales tienen la ventaja de que todos sus componentes son biocompatibles, bioactivos y osteoconductivos. Es decir, son aceptados por los tejidos circundantes y son capaces de establecer uniones con ellos, proporcionando un soporte en el que el nuevo hueso puede formarse.

Además de la morfología, el tamaño y la fracción volumétrica ocupada por el refuerzo de HA son factores clave en las propiedades mecánicas finales de estos biocomposites, y por lo tanto, necesitan ser optimizadas.

Objetivos

Tal y como se ha mencionado, los cementos de fosfato cálcico son uno de los materiales con mayor potencial para su empleo en reparación y/o sustitución ósea. Uno de los principales objetivos de este trabajo es preparar un cemento de fosfato cálcico bioactivo, que fragüe entre 10 y 30 minutos y con una rápida conversión al producto final, HA.

El segundo objetivo es el desarrollo de una ruta hidrotermal fácil y económica que nos permita obtener partículas de HA para su empleo como fase de refuerzo. Variando las condiciones de síntesis, es posible sintetizar monocristales de HA sin defectos y con distintas morfologías.

El CPC preparado, así como los cristales de HA sintetizados, deben de ser adecuadamente caracterizados con el objetivo de determinar su estructura, composición y propiedades físico-químicas.

Una vez logrados los componentes adecuados, se estudiará el refuerzo del CPC empleando los cristales de HA como inclusiones, obteniendo así una nueva familia de biocomposites con unas propiedades mecánicas mejoradas con respecto al CPC puro. Para ello, se estudiará la influencia de la morfología, tamaño y fracción volumétrica de los cristales de HA empleados como refuerzo en las propiedades mecánicas del biocomposite final. Por último, se optimizarán estos factores con el fin de obtener nuevos y funcionales biomateriales con unas propiedades mecánicas, biológicas y fisiológicas mejoradas con respecto al CPC puro.

Estrategias

–. Cemento de fosfato cálcico:

Se empleó fosfato dicálcio dihidratado (DCPD) y fosfato tetracálcico (TTCP) como precursores en la obtención del CPC, ya que dichos compuestos reaccionan para dar hidroxiapatito como producto final.

La estrategia empleada para acelerar la reacción de fraguado del cemento y su conversión a HA fue la disminución del tamaño de partícula de los precursores mediante molienda. El empleo de una fase líquida saturada con iones fosfatos es otro de los métodos empleados para activar la reacción de los precursores de los CPCs. Sin embargo, esta técnica presenta varias limitaciones, por ejemplo, la incorporación de iones extraños en la estructura cristalina del HA final. Así mismo, existe un exceso de iones reactivos que no participan en la reacción en el medio, y los bajos o altos valores iniciales de pH que ello conlleva suelen facilitar la formación de especies intermedias. Estos efectos pueden crear problemas de

biocompatibilidad o disminuir la velocidad de reacción del CPC. Por el contrario, el empleo de DCPD y TTCP finamente molidos asegura una rápida disolución de los precursores, lo que implica una mayor velocidad de la reacción de fraguado del CPC.

–. Cristales de hidroxiapatito (HA):

El método hidrotermal fue la ruta seleccionada para sintetizar cristales de HA ($Ca_{10}(PO_4)_6(OH)_2$) debido a su exitosa aplicación para la síntesis de la fase deseada bajo condiciones de reacción suaves y mediante un solo paso. Así mismo, la técnica hidrotermal permite la obtención de monocristales sin defectos, altamente cristalinos, con un tamaño de partícula relativamente controlable y con diversas características morfológicas.

Así, se sintetizaron monoscristales de HA con varias morfologías mediante un tratamiento hidrotermal, empleando nitrato de calcio tetrahidratado e hidrogenofosfato de diamonio como reactivos. Adicionalmente, se utilizó urea como agente de precipitación homogénea. La urea se descompone uniformemente entre 80° y 95°C, liberando $NH_{3(aq)}$ al medio de reacción, lo que a su vez, aumenta el pH del sistema hasta alcanzar valores en los cuales HA no es soluble, y por lo tanto, precipita. La urea es muy soluble en agua, y la cinética de su descomposición térmica depende de la temperatura y del tiempo que se caliente la mezcla. Por lo tanto, mediante la variación juiciosa de las condiciones del tratamiento hidrotermal, fue posible controlar el pH del medio de reacción y, en consecuencia, sintetizar monocristales de HA con diversas morfologías.

–. Biocomposites:

Se obtuvieron nuevos biocomposites mediante la combinación del CPC obtenido (matriz) y cristales de HA con diversas morfologías (fase de refuerzo bioactiva). La idea principal es que la presencia de una inclusión mecánicamente más fuerte que la matriz puede prevenir la propagación de fisuras y mejorar las propiedades mecánicas de dichos biocomposites frente al CPC puro. Ambas situaciones son de extrema importancia en el desarrollo de nuevos biomateriales para reparación de huesos que soportan carga.

La influencia de la morfología, tamaño y fracción volumétrica de las inclusiones de HA en las propiedades mecánicas finales de los correspondientes biocomposites fue estudiada y optimizada para obtener un biomaterial funcional.

Resultados y discusión

- ***Obtención y caracterización de los cementos de fosfato cálcico***

Para la obtención de los cementos de fosfato cálcico se eligió la reacción de disolución-precipitación entre fosfato dicálcico (DCPD, básico) y fosfato tetracálcico (TTCP, ácido) para preparar CPCs con HA $Ca_{10}(PO_4)_6(OH)_2$ como producto final. . El trabajar con un menor tamaño de partícula de los precursores conlleva un incremento en su solubilidad, lo que a su vez, implica un aumento de la velocidad de reacción de formación del CPC. Por ello, se realizó la síntesis de los CPCs mediante varias etapas.

La etapa inicial supuso la síntesis de DCPD y TTCP puros (muestras **D-raw** y **T-raw** respectivamente). A continuación, estos precursores fueron molidos mediante un molino de bolas con el fin de disminuir su tamaño de partícula. Se emplearon tres tamaños de bolas distintos con el fin de obtener distintos tamaños de partícula. Mediante combinación de los distintos precursores obtenidos tras la molienda, se obtuvieron nueve CPC, cuyas propiedades y características fueron estudiadas y comparadas con el fin de seleccionar el CPC óptimo con el que preparar los biocomposites.

El producto **D-raw** se obtuvo mediante una reacción de precipitación, mientras que **T-raw** fue sintetizado mediante una reacción a alta temperatura (1500°C). El análisis de las muestras **D-raw** y **T-raw** mediante microscopía electrónica de barrido (SEM) y dispersión de luz dinámica (DLS) muestra que ambos están compuestos por cristales y agregados de cristales de varias micras (~6 y ~7 μm respectivamente), lo que probablemente implique una velocidad de disolución baja en el caso de ambas muestras.

Con la idea de mejorar la reactividad y solubilidad de los precursores, **D-raw** y **T-raw** fueron molidos empleando tres tamaños de bolas distintos (3.6, 4.8 y 9.6 mm). La pureza de las muestras tras la molienda fue comprobada mediante difracción de rayos X (XRD). El estudio de las muestras obtenidas mediante SEM y DLS confirma que la molienda de **D-raw** y **T-raw** reduce de modo efectivo el tamaño de partícula y los agregados de los compuestos de partida. La distribución del tamaño de partícula indica que el tamaño de las bolas empleadas en la molienda influye en el tamaño de partícula obtenido: las bolas más pequeñas proporcionan muestras más finas y con una menor distribución de tamaño de partícula (PSD). Así, DCPD y TTCP se obtienen con un tamaño medio de partícula de 3.66 y 2.96 μm, 1.69 y 1.52 μm o 1.13 y 1.33 μm según las bolas empleadas sean de 9.6, 4.8 o 3.6 mm respectivamente.

Los tres DCPD y los tres TTCP obtenidos tras la molienda fueron combinados entre si y se obtuvieron nueve CPCs. En contraste con los datos publicados hasta la fecha para un CPC formado por DCPD y TTCP, el análisis mediante XRD muestra que, tras 24 horas de reacción, todos los CPC obtenidos consisten únicamente en HA puro. Muchos grupos han investigado la preparación de CPC empleando DCPD y TTCP como precursores, sin embargo, en la mayoría de los casos, tras 24 horas, la mezcla de reacción todavía contiene TTCP sin reaccionar, lo cual puede generar problemas de biocompatibilidad, ya que el TTCP se hidroliza en agua, generando iones OH^- que hacen aumentar el pH del medio a valores muy básicos, tóxicos para las células óseas:

$$Ca_4(PO_4)_2O_{(s)} + H_2O_{(aq)} \xrightarrow{H_2O} 4Ca^{2+}_{(aq)} + 2PO_4^{3-}{}_{(aq)} + 2OH^-_{(aq)}$$

Se cree que el TTCP remanente está relacionado con un mayor tamaño de partícula de este compuesto comparado con DCPD (~10 veces mayor) y con la formación de una capa de HA en la superficie de los reactantes que actúa como barrera y dificulta su disolución. Hasta la fecha, solo fue posible obtener un CPC basado en DCPD y TTCP que se convierte totalmente en HA tras 24 horas empleando una fase liquida saturada con iones fosfato. Sin embargo, dicho CPC presenta un alto valor de pH durante aproximadamente siete días, lo que provocaría daños celulares en el tejido circundante al emplearlo *in vivo*.

La determinación del tiempo de fraguado y los estudios de porcentaje de conversión a HA realizados para los nueve CPC preparados, indican que es el cemento **C-D36/T48** formado por DCPD y TTCP con un tamaño medio de partícula de 1.13 y 1.52 μm respectivamente el que presenta un menor tiempo de fraguado (~22 minutos) y una mayor conversión a HA tras tres horas de reacción (~33%). Es importante destacar que este tiempo de fraguado cumple los requisitos médicos para CPCs y que se obtiene usando sólo agua como fase liquida, es decir, sin emplear aceleradores de reacción que pueden presentar potenciales problemas de biocompatibilidad.

Los resultados obtenidos mediante el estudio de la evolución de la reacción empleando XRD, indican que **C-D36/T48** se transforma totalmente a HA tras sólo seis horas de reacción, lo cual es una clara ventaja comparado con cementos similares que tras 24 horas todavía no han reaccionado totalmente. Cuanto más rápido se produzca la reacción de fraguado del cemento, antes alcanzará éste sus propiedades mecánicas finales. El estudio de la evolución de la reacción de fraguado también muestra que ésta sigue un proceso de nucleación-crecimiento de cristales.

El análisis mediante espectroscopía de dispersión de rayos X (EDX) confirma que el cemento **C-D36/T48** es deficiente en calcio, ya que obtenemos una relación Ca/P ~1.49, cuando el valor del HA estequiométrico es 1.67. El análisis mediante espectroscopía de infrarrojo (IR), Raman y análisis elemental muestra la existencia de aniones HPO_4^{2-} y CO_3^{2-} sustituyendo parcialmente grupos PO_4^{3-} en la estructura cristalina del HA. La espectroscopia de IR muestra también la incorporación de moléculas de agua en la estructura del cemento **C-D36/T48**.

Según estos resultados, la fórmula del cemento puede representarse como $Ca_{10-x-y}(HPO_4)_x(CO_3)_y(PO_4)_{6-x-y}(OH)_{2-x-y}(H_2O)_z$.

Es importante señalar que el HA biológico presente en los huesos y dientes de los vertebrados, es deficiente en calcio y además, contiene ~3-5 % en peso de grupos carbonato. Por lo tanto, la obtención de un CPC como el **C-D36/T48** con grupos HPO_4^{2-} (presentes en la HA deficiente en calcio) y CO_3^{2-} en su estructura no representa ningún problema desde un punto de vista biocompatible.

Por otro lado, la determinación del área de superficie y de la porosidad indica que el **C-D36/T48** posee un alta área superficial (~169 m^2/g) y una porosidad de aproximadamente el 35% producida por mesoporos desordenados.

Estudios detallados mediante microscopía de transmisión electrónica (TEM) del cemento **C-D36/T48** tras 24 horas de reacción señalan que la muestra esta compuesta únicamente por HA, sin presencia de otras fases como impurezas. TEM confirma además que el CPC está formado por nanoláminas (10-15 nm) fuertemente entrelazadas entre si. Dicho entrelazamiento es el responsable de la solidez del CPC tras la reacción de fraguado. Estos nanocristales crecen según la dirección del eje *c*.

Estudios *in vitro* muestran la potencial capacidad de **C-D36/T48** para formar un enlace químico con el tejido óseo circundante. Es decir, el test *in vitro* confirma la bioactividad de **C-D36/T48**.

La resistencia a la compresión de este cemento fue establecida como 25 ± 3 MPa, un valor que entra en el rango de valores previamente establecidos para cementos basados en DCPD y TTCP (20-170 MPa). El módulo elástico (relacionado con las propiedades elásticas) y la dureza (relacionada con las propiedades plásticas) fueron determinados mediante nanoindentación. Los valores hallados (23.1 ± 2.6 y 0.73 ± 0.2 GPa respectivamente) son ligeramente superiores a los calculados para el hueso humano trabecular (15.0-19.4 GPa) y están en el rango de los hallados para el hueso cortical (20.0-25.8 GPa). La dureza de

C-D36/T48 sigue la misma tendencia, y es ligeramente superior a la del hueso trabecular (0.52-0.62 GPa) y está dentro de los valores del hueso cortical (0.62-0.74 GPa). Estos resultados muestran una gran similitud mecánica (elástica y plástica) entre **C-D36/T48** y los huesos, presentando el cemento preparado una gran compatibilidad biomecánica con los tejidos óseos. Dicha compatibilidad es de gran importancia en los biomateriales.

- ***Síntesis de monocristrales de hidroxiapatito con distintas morfologías***

La técnica hidrotermal es ampliamente empleada hoy en día en la síntesis de cristales de HA. En la mayor parte de los casos, los cristales obtenidos presentan una morfología fibrosa (whiskers, fibras, agujas, etc.) o de lámina. Adicionalmente, también existen trabajos en los que las partículas sintetizadas tienen forma de prisma hexagonal, elíptica o de lazo. A pesar de estas diferencias morfológicas, los cristales obtenidos crecen según el eje *c*, la tendencia natural del HA.

En este trabajo, los cristales de HA fueron sintetizados empleando $Ca(NO_3)_2{\cdot}4H_2O$ y $(NH_4)_2HPO_4$ como reactivos y urea como agente de precipitación. La urea se descompone entre 80° y 95°C liberando NH_3 al medio de reacción, elevando el pH del medio hasta valores a los cuales el HA es la fase menos soluble. La descomposición de la urea es dependiente de la temperatura, por lo cual es posible controlar su velocidad de descomposición aplicando distintos ciclos de temperatura durante el tratamiento hidrotermal ($T_{máx.}$ = 90°C). Todos los productos obtenidos son HA puro (XRD y Raman), ligeramente no estequiométrico (EDX, Ca/P ~1.75). Los análisis mediante IR muestra la parcial sustitución de iones OH^- y PO_4^{3-} por grupos CO_3^{2-} (~ 0.75% en peso según análisis elemental) en la estructura cristalina de los productos. La existencia de grupos HPO_4^{2-}, indicativos de una deficiencia en calcio del HA obtenido, no fue observada mediante IR, Raman o análisis termogravimétrico y diferencial (TGA/DTA), en concordancia con los resultados obtenidos mediante EDX.

Los estudios realizados mediante SEM muestran que las partículas sintetizadas presentan distinta morfología en función del ciclo de temperatura empleado durante el tratamiento hidrotermal y de la concentración de reactivos empleada.

Así, si la síntesis se realiza a una temperatura constante de 90°C, la urea se descompone de modo intensivo, proporcionando una importante supersaturación del medio de reacción y, consecuentemente, deberían formarse un gran número de núcleos de cristalización. Sin embargo, en nuestro caso las partículas obtenidas muestran forma de lámina (muestra **PT**), probablemente debido a un crecimiento epitaxial de los cristales de HA sobre cristales de

fosfato octacálcico $Ca_8H_2(PO_4)_6 \cdot 5H_2O$, precursor de los cristales de HA. Por tanto, se supone que la morfología de lámina de la muestra **PT** se debe a un predominio de efectos cinéticos sobre los efectos termodinámicos de la reacción.

Si el ciclo de temperatura empleado no se mantiene constante a 90°C sino que presenta varias etapas en las que se disminuye la temperatura a 70°C (por debajo del rango de descomposición de la urea), los cristales sintetizados presentan morfología de prisma hexagonal (muestra **HX**). Este resultado indica que con estas condiciones de reacción, los efectos termodinámicos son predominantes.

Si la descomposición de la urea se realiza lentamente, las partículas sintetizadas presentan forma de aguja (muestra **ND**). Dicha morfología concuerda con un predominio de los efectos termodinámicos sobre los cinéticos, ya que se forman un gran número de núcleos de cristalización que al crecer, producen cristales de gran tamaño y pequeña sección.

Con un ciclo de temperatura que implica no solo la interrupción de la descomposición de la urea sino que además mantiene dicha interrupción durante una hora, es imposible obtener HA puro si el resto de las condiciones de reacción se mantienen constantes. Sin embargo, si disminuimos la concentración de calcio y fósforo de 0.167 y 0.1 M respectivamente (muestras **PT**, **HX** y **ND**) a 0.083 y 0.05 M los cristales obtenidos presentan, mayoritariamente, forma de laminas finas (muestra **FP**). También se observa la presencia de partículas casi rectangulares. En general, el tamaño de partícula de esta muestra es mucho menor que el de los productos anteriores. Empleando esta misma concentración de calcio y fósforo (0.083 y 0.05 M respectivamente) pero utilizando cualquiera de los otros ciclos de temperatura mencionados, se obtienen partículas con el mismo tipo de morfología. Estos resultados indican que, para esta concentración, lo que predomina es el efecto de la concentración de reactivos. Por lo tanto, en sistemas diluídos, el control morfológico de los cristales mediante la descomposición controlada de urea está de algún modo limitado. Los estudios de estas muestras mediante TEM confirman que todos las partículas cristalizan en el sistema hexagonal del HA y que son monocristalinas. Además, dichos estudios muestran que, mientras las muestras **PT**, **HX** y **ND** crecen a lo largo del eje *c*, los cristales de **FP** crecen según las direcciones (211) en el caso de las partículas con morfología de lámina fina y (102) para las partículas rectangulares. El HA tiene una tendencia natural a crecer orientado según el eje *c*, por lo que estos resultados son altamente interesantes, pero, al mismo tiempo, sorprendentes.

El módulo elástico y dureza de los cristales con morfología hexagonal **HX**, se determinó mediante nano-indentación. Los resultados obtenidos muestran una anisotropía en

el módulo elástico, obteniendo valores de 62 ± 7.0 GPa para el plano prismático de los cristales (paralelo al eje *c*) y de 68 ± 8.0 GPa en el caso del plano basal (perpendicular al eje *c*). Dichos valores demuestran que los cristales hexagonales de HA son más rígidos que el cemento

C-D36/T48, lo que implica que pueden emplearse como fase de refuerzo del citado cemento.

- ***Obtención y caracterización de los biocomposites***

El cemento **C-D36/T48**, que actúa de matriz, fue reforzado mediante cristales de HA con diversas morfologías sintetizados mediante tratamiento hidrotermal, obteniendo así los biocomposites correspondientes. Todos ellos se transforman en HA puro tras 24 horas de reacción. El estudio de la evolución de la reacción de fraguado mediante XRD muestra que dicha reacción sigue un proceso de nucleación-crecimiento de cristales, el mismo que el cemento puro. Es decir, la presencia de la fase de refuerzo no afecta a la reacción de fraguado de la matriz. Además, los estudios mediante SEM y TEM muestran que el HA obtenido como resultado de la reacción de fraguado del CPC posee las mismas características morfológicas y microestructurales que el cemento puro. Por tanto, se puede concluir que el incremento de las propiedades mecánicas observado para los biocomposites preparados se debe a la "*Regla de las mezclas*" de los composites y no a algún cambio producido en la matriz.

Se observó que la incorporación de cristales de HA con diversas morfologías (esferas, láminas **PT**, hexágonos **HX** o láminas finas **FP**) al cemento puro **C-D36/T48** aumenta la resistencia a la compresión (CS) de los biocomposites correspondientes, independientemente de la forma de dichas inclusiones. Sin embargo, se constató que las distintas morfologías de las inclusiones proporcionan distintos incrementos en la resistencia a la compresión, lo que revela la importancia de la forma y tamaño de las fases reforzantes. La cantidad añadida de fase de refuerzo también resultó un factor clave de las propiedades finales alcanzadas por los biocomposites. El mejor incremento se obtuvo para el biocomposite formado por CPC y un 10% en peso de láminas finas como refuerzo (~50%, CS = 48 MPa). Se cree que el cierto grado de flexibilidad observado para esta morfología es el responsable de este efecto. Así mismo, su pequeño tamaño, comparado con el de los otros cristales, debe de ser otro factor importante. Otra ventaja del biocomposite reforzado con láminas finas es que sus pequeñas dimensiones no afectan de modo significativo las propiedades reológicas del CPC puro, importante para aplicaciones en huesos que no soportan carga pero que necesitan un intervención quirúrgica lo menos invasiva posible, por ejemplo, las vértebras.

El módulo elástico de los biocomposites también depende de la morfología, rigidez y fracción volumétrica de la fase de refuerzo añadida. Cuando se emplean cristales con morfología de lámina fina, más flexibles y probablemente menos rígidos que las inclusiones hexagonales y que la matriz, el módulo elástico se reduce ligeramente (de ~23 a 22 GPa). Sin embargo, los valores obtenidos para estos biocomposites todavía están dentro del rango de valores determinados para hueso humano cortical, lo que implica isoelasticidad entre los compuestos preparados y los huesos, una característica muy importante de los biocomposites.

La dureza de los biocomposites parece estar más influenciada por la fase de refuerzo con morfología de lámina fina, probablemente debido a una mayor área de superficie de estos cristales comparado con las inclusiones hexagonales.

I

RESEARCH MOTIVATION AND BACKGROUND

1.1.- MOTIVATION

Although bones, once they fracture, are able to repair themselves through a natural process, there are some circumstances when bone defects do not heal appropriately or spontaneously. Consequently, bone repair and substitution are common medical practices of increasing value. In fact, bone is the second most frequently transplanted tissue in humans. Therefore, the search of new biomaterials is a very attractive research topic not only with respect to the fabrication of replacement implants, but also with respect to the fundamental study of structure-property relationships, which can lead to discoveries of new families of functional biomaterials with enhanced mechanical, biological and physiological characteristics.

From the viewpoint of biomaterial and biomedical research, calcium phosphate bone-cements (CPCs) are excellent compounds for utilizing in the human body for bone repair and substitution. CPCs also have prospective applications in the field of drug delivery devices. Essentially, all these applications stem from their associated biological and physiological properties –CPCs are highly bioactive, biocompatible and osteoconductive, *i.e.* CPCs are able to be resorbed by biological serum, allowing for progressive substitution by newly formed bone. Generally, all CPCs can be generated by mixing one or several reactive calcium orthophosphate precursors in an aqueous medium. After mixing, a putty-like material/injectable liquid is formed, which is able to set and harden *in vivo*. Therefore, CPCs are promising biomaterials for clinical applications, *e.g.* for filling bone defects during surgery, resulting in reduced patient discomfort in comparison to other techniques currently employed. In addition, most cement formulations result in the formation of Ca-deficient hydroxyapatite after the setting reaction. As-produced hydroxyapatite (HA) is chemically and structurally very similar to biological apatites (the principle inorganic component of mineralized bone tissues), thus exhibiting excellent biological and physiological characteristics for bone graft uses. It is noteworthy that in many cases the rapid conversion of the CPC precursors to HA not only leads to the rise of the appropriate physiological properties, but also results in the strengthening of the mechanical properties. In particular, rapid conversion accelerates achievement of the final compressive strength value, which is almost linearly dependent on the extent of the CPC setting reaction. It should be noted, that during a surgical procedure, the CPC needs to set slowly enough to provide sufficient time for the surgical implantation, but fast enough to minimize the duration of the procedure. Consequently, from a fundamental and an application point of view, it is important to design a

rational synthetic approach to calcium phosphate bone-cement biomaterials with setting time between 10-30 min and a rapid conversion rate to the end product, preferably HA.

Owing to the lower fracture toughness parameters of CPCs in comparison to human bone (~0.6-1.5 *cf.* 2-12 MPa/m^2), the clinical applications of CPCs are nowadays limited to areas where bones are free of dynamic load, *i.e.* for craniofacial and periodontal applications, or as materials for the development of scaffolds in bone tissue engineering. One of the most promising methods to improve the mechanical performance of biomaterials is their reinforcement *via* physical linking by spatially allocated fibrous materials. For example, HA ceramics can be significantly reinforced by various bioinert fibres like SiC, C, Si_3N_4, Al_2O_3 or ZrO_2 (bioinert reinforcement). However, utilization of these fibrous materials leads to a decrease in the bioactivity of the respective composite bioceramics. Hence, research related to bioactive reinforcement, wherein hydroxyapatite particles are applied as a reinforcement phase, has recently received much attention. Particles with plate-like morphologies are the most effective at stiffening isotropic composite materials, followed by fibrous shapes, being the least effective geometry the spherical particles. In this way, HA crystals with desired morphological features are applicable for moderated reinforcement of biomaterials for bone repair and substitution, such as the calcium phosphate bone-cements previously mentioned. Consequently, it is of critical importance for reinforcement applications to develop an effective synthetic route to the phase-pure hydroxyapatite single crystals with controlled morphological features.

Finally, having a complete set of constituent materials –advanced calcium phosphate bone-cement (matrix) and hydroxyapatite crystals with various particle morphologies (fillers)– it is certainly possible to explore a new family of reinforced biocomposite cements. These materials have the advantage that all their components are biocompatible, bioactive and osteoconductive. Another appealing feature of such composite biomaterials is that the filler is mechanically stronger than the matrix, and therefore, being thoroughly embedded in cement, can halt potential crack propagation when applied as bone graft. The shape, size and volume fraction of the hydroxyapatite filler are key parameters that influence the final mechanical performance of such biocomposites, and need to be optimized. Such optimizations, together with an analysis of the correlation between the material properties of the filler and the mechanical performance of the respective reinforced biocomposite cement, can allow the development of new insights into the design of composite biomaterials and allow for new biomedical applications reinforced biocomposite cements.

1.2.- BACKGROUND

The Instituto de Cerámica de Galicia (ICG, Galician Institute of Ceramics) is a relatively young institute of the University of Santiago de Compostela in Spain, which is well known worldwide for its traditionally strong education in the fields of natural sciences. Despite its young "age" ICG is one of the leading institutions involved in ceramics research in Spain. The investigation into original research topics at the institute is realised in close cooperation between the Chemistry, Physics, Materials Chemistry, and Biology departments; a special characteristic of the institute. A remarkable proportion of the research projects at the ICG are devoted to the field of the biomaterials. Since the first study in this research area in 1986, members of the institute have published a series of papers on biomaterials, which have been highly acclaimed within the scientific community. Accordingly, several research projects have been successful carried out on various biomaterials. Specifically, in 1998, the project entitled "Biocompatibility and design of ceramic materials for their application in clinical orthopaedics" (1988-89), was commenced in collaboration with J. Couceiro, M.D., Ph.D, Head of the Orthopaedic Surgery Department of the General Hospital of Galicia and the company Cerámica de Sargadelos.

From then on the ICG has been continuously involved in the design and characterization of calcium phosphate ceramics, mostly hydroxyapatite and tricalcium phosphates in projects such as "Biocompatible materials of hydroxyapatite for their application in clinical orthopaedic" (1990-91), where the syntheses of hydroxyapatite and tricalcium phosphate of high purity were investigated and optimized to obtain dense blocks of different sizes. As a result of these investigations a new project was started, "Design and construction of a pilot plant for the industrial manufacture of biocompatible hydroxyapatite" (1989-91). This research led to the fabrication of these materials at a pilot scale in the factory Cerámica de Sargadelos in Cervo, Lugo (Spain).

In the following years (1991-98), the research carried out by the biomaterials group in the ICG widened to include study of "Bioactive, structural materials of wollastonite-zircon" (1991-93), where bioactivity of a phosphate-free polycrystalline ceramic material, wollastonite, was established for the first time. This was followed up with another project: "Design of wollastonite biomaterials and wollastonite-containing systems" (1995-98). A new material with eutectic structure was developed within the wollastonite-tricalcium phosphate system that transforms *in situ* into a porous HA structure. This new material was named Bioeutectic® and was registered as an international trade mark. These results led to a new

project titled “Design and development of Bioeutectic materials. *In vitro* and *in vivo* studies” (1997-2000)”.

Simultaneously, and continuing with the study of polycrystalline bioceramics, the project “Study, design and fabrication of tricalcium phosphate implants for neurology, dentistry and orthopaedic surgery” (1999-2001) was carried out, where a procedure for the fabrication of tricalcium phosphate implants for those applications was optimized.

In 1999 researchers from the ICG with a group of industrial sponsors founded KERAMAT, Ltd., a company dedicated to the manufacture and marketing of bioceramics of calcium phosphates. This company is part of UNINOVA, a spin-off created by the University of Santiago de Compostela and the City Council to launch innovative academic research projects onto an industrial level. Upon its creation, KERAMAT Ltd. signed with the University of Santiago de Compostela, and in particular, with the Instituto de Cerámica de Galicia, a series of agreements for the transfer of some of the technologies developed in the ICG.

Due to the emergent interest and as a logical consequence to the research in calcium phosphate compounds started in 1986, the ICG initiated in 2000, research on calcium phosphate cements which was soon followed with the project “Design, obtaining and properties of bioceramic mortars for its use in orthopaedic surgery, neurosurgery and maxillofacial surgery” (2003-2007, Spanish Ministry of Education and Science, project MAT2002-03857), in which this dissertation is included.

An important part of the research reflected in this thesis was carried out at the Tokyo Institute of Technology (Materials and Structures Department, Tokyo-Japan) and the Max Planck Institute of Colloids and Interfaces (Biomaterials Department, Potsdam-Germany) which started an ongoing collaboration with the Instituto de Cerámica de Galicia.

II

INTRODUCTION

2.1.- BONES[1-5]

Bone is one of the mineralized tissues found in vertebrates, together with cartilage, dentine, enamel and cementum. Normally, we think of cartilage and bone as skeletal tissues, while enamel, dentine and cementum are considered as dental tissues, since they form part of the endoskeleton or the teeth of vertebrates respectively.

The function of bone is to move, to support, and to protect the various organs of the body; to produce red and white blood cells;[i] and to store minerals –approximately 99% of calcium, ~85% of phosphorous and between 40 to 60% of sodium and magnesium in the human body are stored in bones.

Bone is a composite material consisting of an organic matrix (collagen, ~1/3 of the dry weight) in which are embedded mineral crystals of hydroxyapatite (HA, $Ca_{10}(PO_4)_6(OH)_2$), a calcium orthophosphate. The volume fraction distribution between organic and mineral phase is ~60/40. Its mechanical, chemical and biological properties as composite are considerably different from the characteristics of either component separately. Bone combines the optimal properties of both, stiffness[ii] and toughness.[iii] While HA bone mineral is stiff and brittle,[iv] the protein (collagen) is much softer and tougher, and hence, also more fracture resistant. Additionally, water, bone cells, polysaccharides, proteins and blood vessels are also present in the bone. Water corresponds to 15-25 vol.-% of the bone in mammals.[6]

Bone is considered as a living material. Throughout one's lifetime, bone undergoes constant remodelling to repair microfractures and replace old tissue. Over the course of a ten year period, the entire skeleton is completely reformed. Damaged or old bone is resorbed by osteoclasts[v] and new bone is formed in the resulting cavity by osteoblasts.[vi] As long as the rates of bone resorption and bone formation are balanced, there is no net loss or gain in the amount of bone, and its structural and material properties are maintained.

The properties of the Eiffel tower (constructed in 1889) hold many parallels to those of bone. The structure was designed to withstand wind force and has an open-lattice design (Fig.2.1). The tower was built of iron to be flexible but strong and to resist collapsing. Due to

[i] Red blood cells are the most common type of blood cell and the vertebrate body's principal means of delivering oxygen from the lungs or gills to body tissues via the blood. White blood cells, or leukocytes, are cells of the immune system defending the body against both infectious disease and foreign materials.
[ii] Resistance of a body to elastic deformation by the action of a force.
[iii] Fracture resistance of a material when a force is applied.
[iv] A material is brittle if it is liable to fracture when subjected to a force. Opposite to toughness.
[v] An osteoclast (from the Greek words for "bone" and "broken") is a type of bone cell, located on the bone surface, that removes bone tissue by removing its mineralized matrix. This process is known as bone resorption.
[vi] An osteoblast (from the Greek "bone" and "germ" or embryonic) is a bone cell, present on the bone surface, responsible for bone formation.

the continued repair of weakened material, the Eiffel tower still stands strong over more than a century after its construction.

Fig. 2.1. View of the Eiffel tower (Paris, France)

Nature achieves this task by designing bones that are adapted to the different functions for different parts of the skeleton. According to the laws of physics, the strength of a material is determined by its material and structural properties and is relative to the specific direction of forces applied to it. This means that the strength of a bone is not just determined by its mass, but depends on the materials of which it is made and how they are built up into the overall structure of the bone. In order to serve the differing biomechanical functions of the skeleton, bone must have the following qualities:

- light (for speed of movement)
- strong (for load-bearing)
- stiff (to resist bending under load; to move the body against gravity)
- flexible (to absorb the energy of impacts without fracturing)

2.1.1. Bone constituents and structural hierarchy

2.1.1.1. Bone structure

As discussed above, bone properties are a list of apparent contradictions, strong but not brittle, rigid but flexible, light-weight but solid enough to support tissues, mechanically strong but porous, stable but capable of remodelling, *etc*.

Table 2.1. Mechanical properties of human bones.

Property	Values
Elastic modulus[i] (GPa)[1]	12-20
Hardness[ii] (GPa)[7]	0.52-0.62
Compressive strength[iii] (MPa)[1]	20-205
Tensile strength[iv] (MPa)[1]	53-133
Fracture toughness[v] (MPa/m^2)[8]	2-12

Bone is able to fulfil these opposing requirements by a hierarchical structure going from molecular to macroscopic scale (Fig 2.2). Therefore, its mechanical properties are determined by its structure.

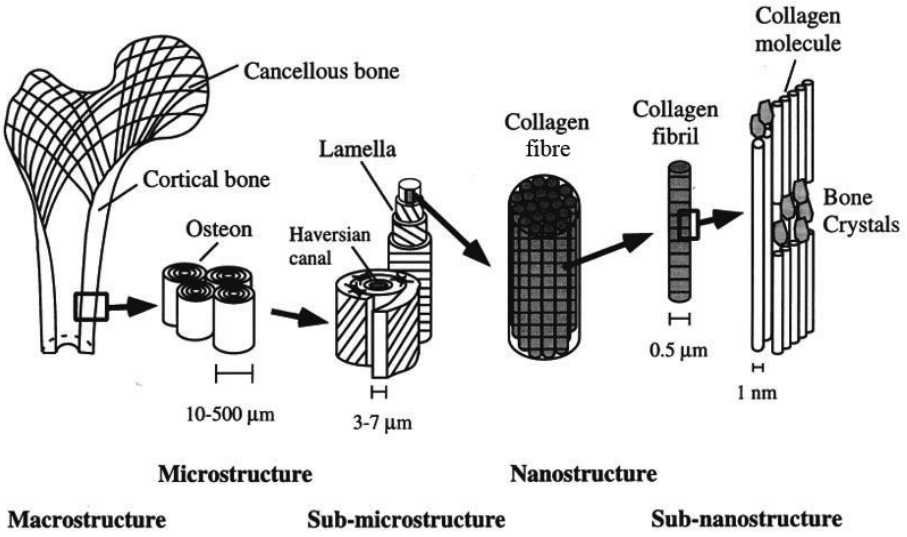

Fig. 2.2. Bone hierarchical structural organization as follows: (a) cortical and cancellous bone, (b) osteons with Haversian systems, (c) lamella, (d) collagen fibres assemblies of collagen fibrils, (e) hydroxyapatite nanocrystals, collagen molecules and non-collagen proteins (after Rho *et al.*).[2]

[i] It is the mathematical description of an object or substance's tendency to be deformed elastically under the action of a load. It is a measure of the stiffness of a material.

[ii] It refers to various properties of matter in the solid phase that gives it high resistance to permanent shape changes when a force is applied. It is related with plastic deformations. In bones, hardness reflects the degree and quality of mineralization of the bone.

[iii] It is the capacity of a material to bear axially directed pushing forces. When the limit of compressive strength is reached, the material fractures.

[iv] It is the resistance of a material to a force tending to tear it apart, measured as the maximum tension the material can withstand without tearing.

[v] It is the ability of a material containing a crack to resist fracture.

The building block of the organic component is the collagen, which is a triple helix with a diameter of ~1.2 nm. These tropocollagens (or collagen molecules) present a periodicity of 67 nm –distance by which adjacent tropocollagens are staggered– and holes (or gaps) of 40 nm between their ends which become filled up with HA nanocrystals (Fig. 2.3A). Therefore, collagen molecules are intercalated with the mineral phase HA forming fibrils that are stabilized by cross-linking (Fig. 2.2, 2.3A). The collagen fibrils are arranged in concentric layers with the biological HA embedded into them (Fig. 2.3A, inset). Many collagen fibrils together make up a collagen fibre, also stabilized by cross-linking. The collagen fibres are in turn organized into sheets, either stacked in parallel arrays (lamella) or wrap in concentric layers (3-8 lamellae) around a central canal to form what is known as an osteon or a Haversian system (Fig. 2.2). The osteon looks like a cylinder ~200-250 μm in diameter running roughly parallel to the long axis of the bone. Each layer of the osteon has its constituent fibrils oriented in alternate directions similar to plywood (Fig. 2.2). On a longer scale, the osteons are grouped together into long bundles that are the basic building block of cortical bone (Fig. 2.2, 2.3B, 2.3C). Finally, at the macroscopic level, each bone has a specific shape and structure so that the skeleton can work as an integrated whole (Fig. 2.2).

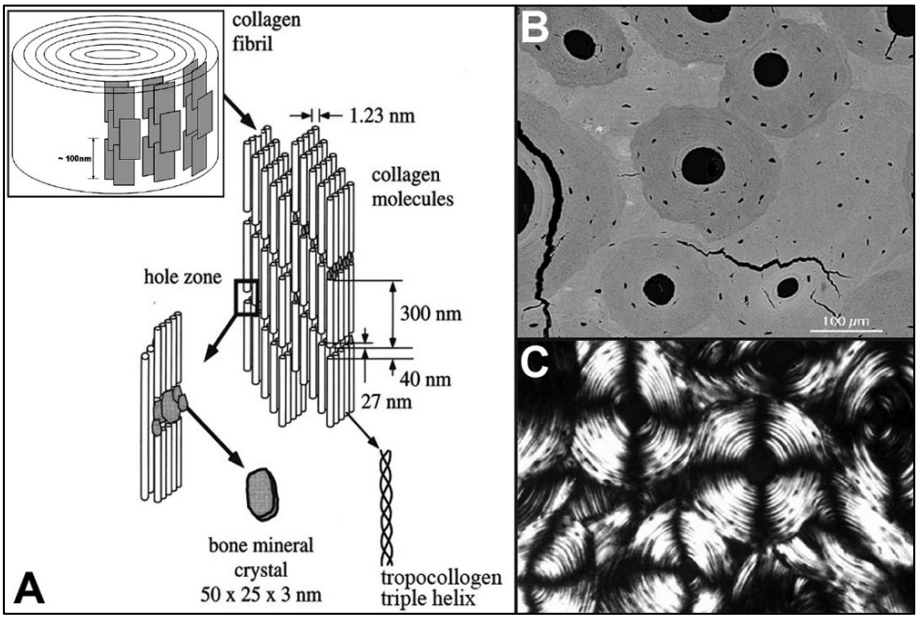

Fig. 2.3. (A) Schematic diagram showing the assembly of collagen fibrils and fibres and hydroxyapatite nanocrystals. The 67 nm periodic pattern results from the presence of adjacent holes (40 nm) and overlaps (27 nm) regions of the assembled molecules (after Rho *et al.*).[2] SEM (B) and polarized light microscope (C) images of a cortical bone showing the grouping of several osteons. The concentric lamellaecan be seen in (C).

2.1.1.2. Bone composition: collagen and hydroxyapatite. Woven and lamellar bone.

The characteristics of HA crystals and of collagen (composition and cross-linking) and the way both component interact is important for bone strength.

Collagen in bone:

About 90% of the collagen present in bone is type I. Bone derives its toughness from collagen, which can stretch like an elastic band and allows bone to deform to a certain extent without fracturing. Bone strength is influenced by the orientation and amount of collagen present and the type and number of cross-links. The degree of longitudinal orientation of collagen fibres is a strong determinant of bending strength and stiffness. Disorientation and random distribution of collagen fibres can be detrimental to bone quality. Therefore, above the level of the collagen fibrils and its associated mineral content, mammalian bone exhibits two distinctive structural forms: *woven bone* and *lamellar bone*.

Woven bone is weaker with respect to lamellar bone but is formed rapidly. It is usually laid down very quickly (> 4 μm per day), most characteristically in the foetus and in the callus that is produced during fracture repair. The collagen is variable and oriented almost randomly. Woven bone is replaced by lamellar bone, highly organized, filled with many collagen fibres parallel to other fibres in the same layer. Lamellar bone laid down much more slowly than woven bone (< 1 μm per day). The fibres run in opposite directions in alternating layers to form a ply-like structure (Fig. 2.2), assisting in the bone's ability to resist torsion forces.

Hydroxyapatite characteristics:

Controlled HA nucleation and growth occurs within the gaps formed by the collagen matrix (Fig. 2.3A). Therefore, the collagen matrix works like a net defining the space of the mineral crystals.

The gaps localize a microenvironment containing free mineral ions and bound side chain groups, with a molecular periodicity that serves to nucleate the mineral phase heterogeneously. The nucleation of the HA nanocrystals within the gaps between the collagen fibrils (Fig. 2.3A) forces the crystals to be discrete and discontinues. HA crystals grow with a specific crystalline orientation – the *c*-axes of the crystals are mostly arranged parallel to each other and to the long axes of the collagen fibrils. On a larger scale, the crystals are aligned in parallel arrays across individual fibrils and sometimes this arrangement is even coherent across several adjacent fibrils. Such a long-range ordering of the collagen matrix and HA crystallites could be responsible for the unusual fracture properties of bone.

Initially, crystals form within the collagen fibrils, but as mineralization of the bone continues they may extend outside the fibrils and fuse with other crystals (Fig. 2.4).

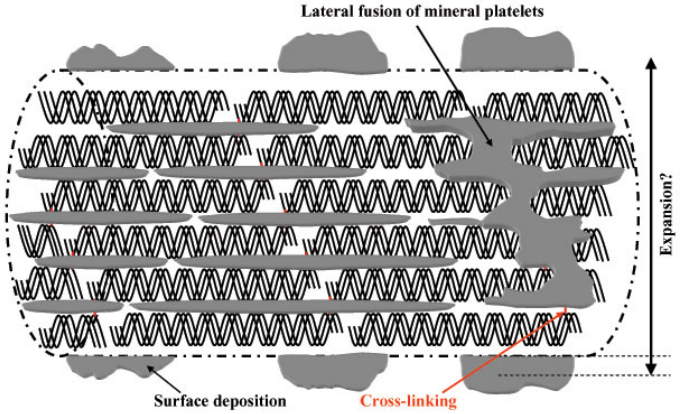

Fig. 2.4. Scheme showing the size increasing of the mineral crystals in mature bone.

It should be noted that although the mineral of bone is often referred as hydroxyapatite, HA in bone is never pure and it contains other ionic species that replace the calcium ions, the phosphate, or the hydroxyl group (Table 2.2). One of the most common occurrences is the partial substitution of phosphate groups by carbonates (3-5 wt.-%),[9] but other ions are also present in the HA crystal structure such as Na^+, Mg^{2+}, Sr^{2+}, F^-, *etc.* The composition of biological HA can be expressed as:

$$(Ca,Sr,Mg,Na,H_2O,[\,])_{10}(PO_4,HPO_4,CO_3,P_2O_7)_6(OH,F,Cl,H_2O,O,\,CO_3[\,])_2$$

where [ ] denotes the presence of lattice defects. Also, the Ca/P molar ratio in bone HA is smaller that the ratio for stoichiometric HA, which shows a Ca/P ratio of 1.67. Therefore, in bones, HA exists as substituted nanosized, poorly crystalline, calcium-deficient carbonated HA.

Table 2.2. Typical composition of the HA in bones in wt.-%.[9]

	Ca^{2+}	PO_4^{3-}	CO_3^{2-}	Na^+	K^+	Mg^{2+}	Sr^{2+}	Cl^-	F^-	$P_2O_7^{4-}$	H_2O	Ca/P ratio
Bone	36.6	17.1	4.8	1.0	0.07	0.6	0.05	0.1	0.1	0.07	10	1.65

2.1.2. Microarchitecture

Bone is not a homogeneously dense material (Fig. 2.5). Each bone is composed of varying amounts of trabecular bone and cortical bone depending on its function, *i.e.*, vertebrae contain a high proportion of trabecular bone, which has a network-like structure composed of trabeculae.

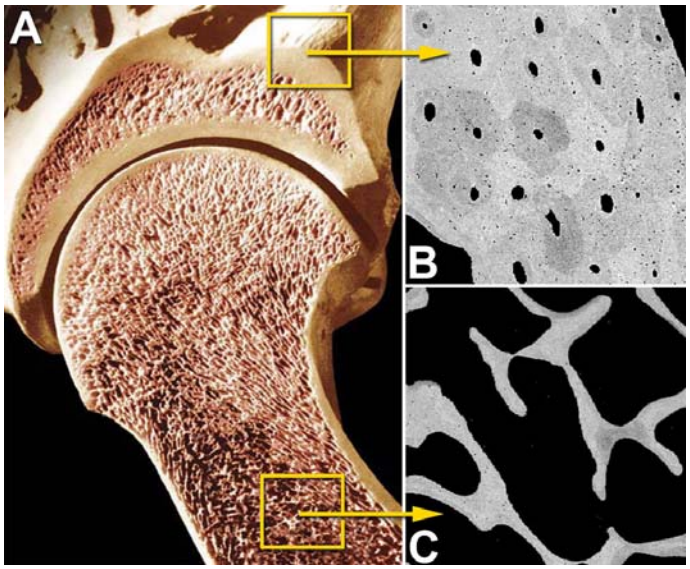

Fig. 2.5. Longitudinal section of the humerus (upper arm bone) (A) showing outer cortical bone (B) and inner trabecular bone (C).

2.1.2.1 Trabecular bone

Trabecular bone (also known as cancellous or spongy bone) is found in the end of long bones, in vertebras and flat bones such as the pelvis, *etc.* Trabecular bone area represents a large surface area within the skeleton (twice than that of cortical bone). However, only ~20 wt.-% of the total skeletal mass consist of trabecular bone, with the remaining 80 wt.-% consisting of cortical bone. This is due to the open, sponge-like structure of trabecular bone (Fig. 2.6A, 2.6B) –only about 20% of the volume is filled with bone material, and the rest is bone marrow.[i] Trabecular bone is made up of small structures called trabeculae (from Latin for small beam), which are generally classified as rods or plates (Fig. 2.6C). Trabeculae are usually less than 200 μm thick and 1000 μm long, and are themselves composed of lamellae structures ~50 μm thick (Fig. 2.6D).

Trabecular bone has several functions:

- To act as a load-bearing tissue
- To transfer loads across joints
- To resist compressive loads
- To act as a shock absorber

The interconnected plates and rods of trabecular bone function like springs to absorb energy and resist compression without cracking. In addition to its structural role, trabecular

[i] The flexible tissue found in the hollow interior of bones. In large bones it produces new blood cells.

bone is also involved in calcium homeostasis.[i] It is also where most of the arteries and veins of bone organs are found.

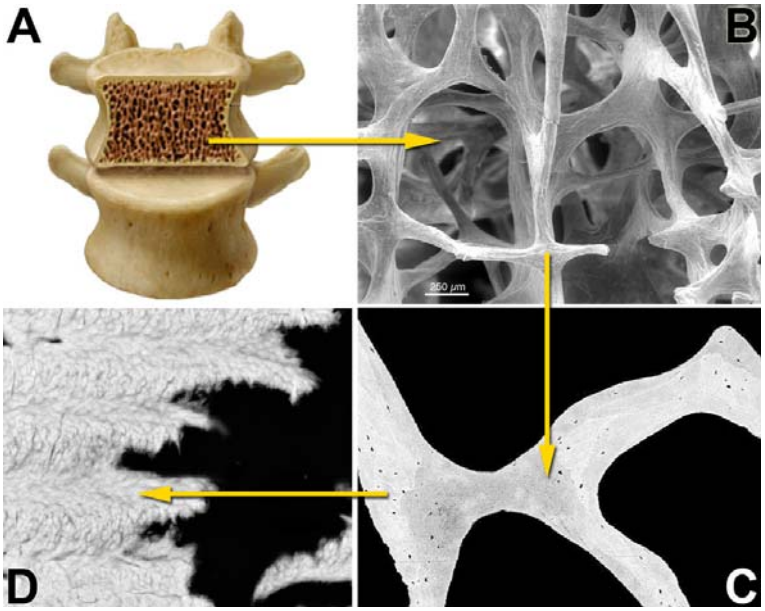

Fig. 2.6. General view of a vertebra (A) showing its microarchitecture –the trabecular bone (B), the trabeculae (C) and lamellae (D).

2.1.2.1 Cortical bone

Cortical bone is found primarily in the shaft of long bones and forms a thin shell around trabecular bone (Fig. 2.5). It is much denser than trabecular bone and has a porosity of less than 15 vol.-% (~80 vol.-% for trabecular bone). Cortical bone is arranged in Haversian systems (also called osteons) (Fig. 2.3B, 2.3C). As discussed before, simple osteons consist of concentric lamellae of bone tissue surrounding a central canal called Haversian canal (Fig. 2.2). This canal is usually 1 to 90 μm in diameter and contains blood vessels, nerves, and a monolayer of bone lining cells on the bone surface. Outside the outermost concentric lamella is a cement line –the first layer of tissue laid down when the Haversian system was being formed. Osteoblasts on the surface of the bone secrete components of the bone matrix, and, once they become trapped in the matrix they secrete, they become osteocytes.[ii] Osteocytes reside in holes filled with extracellular fluid (called lacunae, Latin for a pit) within the bone matrix. Lacunae are interconnected by canaliculi, and the osteocytes remain connected to each other and osteoblasts on the bone surface by cytoplasmic processes that run within the canaliculi. Volkmann's canals run perpendicular to Haversian canals and carry blood vessels

[i] The property of either an open system or a closed system, especially in a living organism, that regulates its internal environment so as to maintain a stable, constant condition.
[ii] They are actively involved in the routine bone resoption through various mechanosensory mechanisms.

into the centre of the bone tissue. Interstitial lamella fills the angular gaps between Haversian systems and parallel circumferential lamella run around the outer diameter of the cortical wall and within the osteons (Fig.2.7).

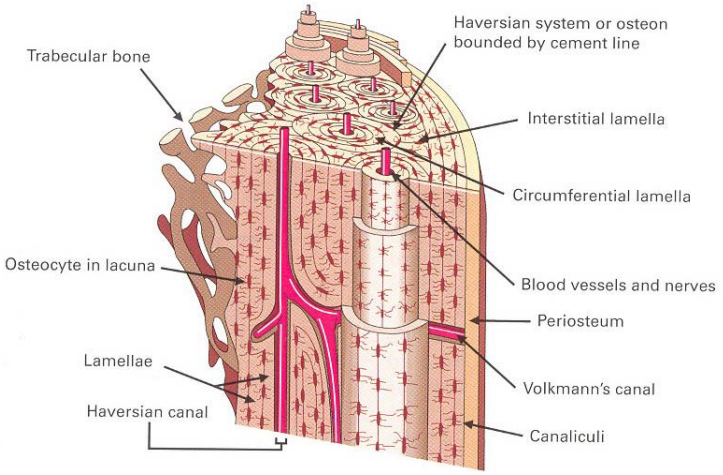

Fig. 2.7. The microarchitecture of cortical bone (after Dempster *et al.*).[3]

Cortical bone provides stiffness and resistance to bending and torsion. Use of this characteristic is made in long bones, which need to resist bending when carrying weight. Long bones consist mainly of cortical bone and only 5% of trabecular bone. At the base of the femoral neck, cortical bone supports 96% of the loading associated with normal human locomotion, while in the middle of the femoral neck, cortical bone supports 50% of stress. The remaining stress in each case is supported by trabecular bone.

2.1.3. Bone shape and function

From a macroscopic point of view, the shape of bones is quite variable; however, a large proportion of bones can be classified into long, short or flat bones (Fig. 2.8). The shape of different types of bone is determinate by cellular differentiation during formation of the embryo and it plays a role in determining its strength. The geometry (including shape) of the bone is adapted to the direction of the normal physiological forces, which will distort the bone within a certain range. Greater than normal forces in unusual directions (as in a fall) that distort the bone beyond this range may fracture the bone.

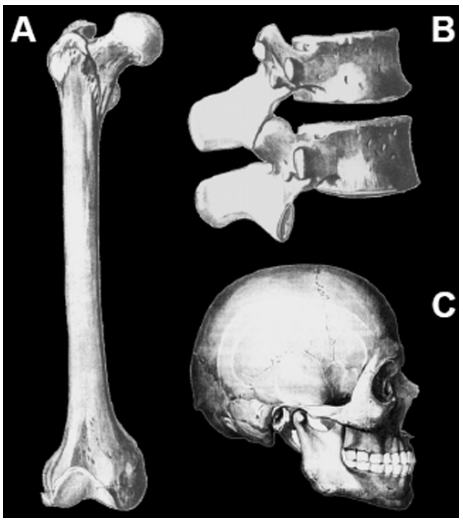

Fig. 2.8. A femur (long bone) (A), vertebras (short bones) (B) and skull (flat bones) (C).

2.1.3.1. Long bones

Long bones, also called tubular bones, such as the humerus, radius, femur, tibia, *etc.*, are elongated in one direction and the section is often circular (Fig. 2.8A). These bones are thick-walled hollow tubes; in their midsection the wall thickness is characteristically about one-fifth of the overall diameter. They are expanded at their ends. Near the ends the central cavity is filled with trabecular bone. Long bones are designed to carry compressive loads and bending moments over reasonably long distances.

2.1.3.2. Short bones

Short bones are bones or parts of bones that are roughly the same size in all directions. Examples are wrist and ankle bones and the central of vertebras (Fig. 2.8B). They tend to have very thin outer layers and to be completely filled with cancellous bone, the trabeculae running from one end to the other. They are designed to carry loads, usually compressive, over short distances. They are not usually subjected to much bending.

2.1.3.3. Flat bones

Flat or tabular bones are bones or, often parts of bones, that are rather flat, so that one dimension is much less than the other two. Examples are the scapular, the iliac blades, bones of skull, *etc.* (Fig. 2.8C). They usually consist of two thin sheets of cortical bone separated by some trabecular bone, but sometimes, as in some scapula, the two cortices are not separate. Flat bones are designed either for protection, as in the vault of the skull, or to provide a base for the origin of extensive muscles, as in the scapula or the iliac blades.

2.1.3.4. Other geometries

Irregular bones do not fit into the above categories. They consist of a thin layer of cortical bone surrounding the interior. They have irregular and complicate shapes, *i.e.,* the bones of the hip.

Sesamoid bones are bones embedded in tendons. Since they act to hold the tendon further away from the joint, the angle of the tendon is increased and thus the force of the muscle is increased. Examples are the patella and the pisiform.

2.1.4. Bone remodelling

Throughout life, old bone matrix is continuously resorbed and replaced by new bone due to the activity of the bone cells osteocytes, osteoclasts and osteoblasts. This process is called remodelling (Fig. 2.9).

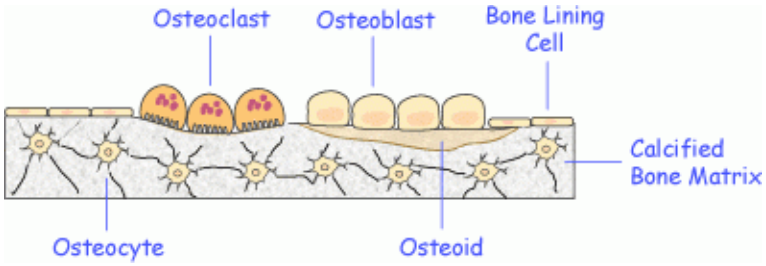

Fig. 2.9. Scheme of the remodelling process in bones.

Osteoclasts remove bone tissue by removing its mineralized matrix (HA nanocrystals) by realising H^+ to decrease the pH from ~7 to ~4 and therefore dissolve the HA. Osteoblasts are responsible for bone formation by the synthesis and secretion of the organic matrix collagen and regularization of HA crystallization. Osteocytes are highly specialized, fully differentiated osteoblasts that act as stress sensors inside the bone. Osteoclasts and osteoblasts are localized on the bone surface.

New, "young" bone is not mineralized and requires time to become fully mineralized. During the bone remodelling cycle, collagen is deposited to form new bone matrix (osteoid) that is subsequently mineralized in two phases by deposition and maturation (growth) of mineral crystals, known as primary and secondary mineralization. As remodelling is a continuous process, this means that any one person, irrespective of their age, has younger (less mineralized) and older (more mineralized) packets of bone basic structural units[i] present

[i] The basic structural units are osteons for cortical bones and trabeculae for trabecular bones. This characterization is based on the fact that trabeculae have similar size ranges as the osteon. Other denotations of the trabecular packet as the basic structural unit of trabecular bone based on the fact that it is the basic remodelling unit of trabecular bone just as the osteon is the basic remodelling unit of cortical bone are also accepted.[10]

at the same time in their bone. Secondary mineralization includes an increase in the size of mineral crystals (Fig. 2.4) and changes to their composition and crystal structure. An imbalance in remodelling in favour of resorption can occur with age, menopause and disease (*i.e.*, as in osteoporosis[i])

Remodelling allows bone to fulfil its structural and metabolic functions, since it permits the repair of damage and the maintenance of the structural integrity of the skeleton (targeted remodelling); and the storage and release of calcium, phosphorous, *etc.*, to maintain the acid-base balance (non-targeted remodelling). It has been estimated that ~30% of remodelling is targeted and that ~70% is non-targeted.

2.1.5. Bone microdamage. Microcracks.

Axial loads able to deform one of the bone dimensions ~1-1.5% causes microdamage in the form of microcracks, which are a means of absorbing energy from the load without causing complete fracture of the bone.

The presence of microcracks stimulated remodelling, and under normal conditions, they are repaired as fast as they are produced. If, however, microcracks form faster than they are repaired, bone strength may be adversely affected, and so, the rate at which microcracks are repaired influences strength. Microcracks accumulate with age in both cortical and trabecular bone, which may be related to the increased fracture risk in elderly persons.

2.1.6. Bone fracture

From a mechanical perspective, fractures represent a structural failure of the bone when the forces applied to the bone exceed its load-bearing capacity or the whole-bone strength.

Bone adapts its size and shape to accommodate the loads to which it is exposed by bone modelling and remodelling (Sections 2.1.3 and 2.1.4), but too high forces or in unusual directions, might result in bone fracture. The ability of a bone to resist fracture depends on the amount of bone (*i.e.*, mass), the spatial distribution of the bone mass (shape and microarchitecture) and the intrinsic properties of the materials that comprise the bone (collagen, HA). Therefore, although many fractures are the result of high force impact or stress, bone fracture can also occur as a result of certain medical conditions that weaken the

[i] In osteoporosis the bone mineral density (a measure of the amount of minerals, mainly calcium, contained in a certain volume of bone) is reduced, bone microarchitecture is disrupted, and the amount and variety of non-collagenous proteins in bone is altered. It makes bones weak and more likely to break.

bones, such as osteoporosis, certain types of cancer or osteogenesis imperfecta[i] or to age due to microcracks accumulation

Also, the emergence of bone fragility with age is the result of the failure of modelling and remodelling adaptive mechanisms, with remodelling imbalance in each basic structural unit producing a decline in the volume of bone formed and an increase in the volume of bone resorbed. Therefore, the rate of remodelling affects the degree of mineralization of bone and microdamage repair. Imbalances in bone resorption and formation, mainly due to the detriment of formation, lead to a reduction in the amount of bone formed and to net bone loss. This has an adverse effect on trabecular and cortical microarchitecture and on bone strength.

The size of the mineral crystals themselves also affects bone strength. The bones of older animals or form osteoporic animal models contain a greater portion of large HA crystals. These bones tend to fracture more easily than bones from younger animals that contain a greater mixture of smaller and larger crystals.

2.2.- TEETH[6, 9, 11]

Teeth consist of a unique composition of the three dental mineralized tissues, namely dentine, enamel and cementum. The three form a complex 3D structure designed to ensure that the tooth as a system can function for a time span of about seven decades, since, in contrast with bone which can undergo self-repair and remodelling, enamel, dentine and cementum are static and cannot be repair by remodelling.

2.2.1. Structure

Innervated soft tissue (dental pulp or tooth's nerve) is totally covered by dentine, which, in turn, forms the core of a tooth. In the upper area of a tooth (crown) the dentine is covered by enamel, harder and more mineralized than dentine. In the root area the outer layer of the dentine is coved by cementum (Fig. 2.10), which anchors the tooth in its socket by inserting Sharpey's fibres.[ii] This combination makes possible that teeth can withstand mechanical forces such as chewing forces up to 800 N, wear (abrasion), chemical or physical interactions such as changes in the pH value or variations in temperature, and biological effects such as bacteria and toxins.

[i] People with this genetic bone disorder either have less collagen than normal or the quality is poorer than normal.
[ii] There are matrixes of connective tissue consisting of bundles of strong collagenous fibres. In the teeth, Sharpey's fibres (also called perforating fibres) are the ends of principal fibres that insert into the cementum.

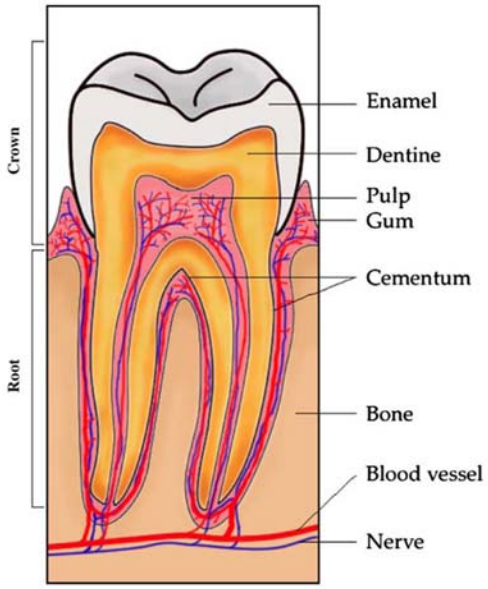

Fig. 2.10. A schematic picture of a tooth (after Dorozhkin).[12]

2.2.1.1. Enamel

Enamel purpose is to protect the tooth from the dangers posed to the teeth by the oral environment. In general, it is vulnerable only to acid attack from excess sugar (dental caries), generalized trauma such as a blow from a hard object, and serious bruxing (the habit of clenching and grinding the teeth) with associated attrition. It is white, but somewhat translucent and allows the colour of the underlying yellow dentine to shine through to a certain extent.

Unlike bone, enamel does not contain collagen. Ninety-six percent of enamel consists of mineral, the mineral being hydroxyapatite rods. Water and organic material compose the rest. Enamel varies in thickness over the surface of the tooth and is often thickest at the cusp, up to 2.5 mm, and thinnest at its border.

An enamel rod is the basic unit of enamel. Measuring ~5 μm wide to ~8 μm high, an enamel rod is a tightly packed, highly organized mass of hydroxyapatite crystals. Enamel rods are found in row along the tooth (Fig. 2.11A, 2.11B). Within each row, the long axis of the enamel rod generally is perpendicular to the underlying dentine. The arrangement of HA crystals within each enamel rod is highly complex. For the most part, the crystals are oriented parallel to the long axis of the rod. The further away the crystals are from the central axis, the more their own orientation diverges.

Each enamel rod is attached to the dentine underneath it. For this reason, cracks in the enamel penetrate only as far as the dentine. This method of attachment makes it impossible for the enamel to separate from the tooth.

2.2.1.2. Dentine

Dentine –which is necessary for the support of the enamel– structure is fairly similar with that of bone but simpler. It contains 30 vol.-% of collagen (90% of which is type I) and 25 vol.-% water, the remainder being HA. One of the major features of dentine is the tubules (microchannels) (Fig. 2.11C, 2.11D). Tubules are originate from the inner surface of the dental pulp and they run approximately parallel to each other and perpendicular from their point of origin throughout the structure of the dentine. They terminate at the under-surface of the enamel. The diameter and density of the tubules are greatest near the pulp. As a result, dentine is a porous material (Fig. 2.11C, 2.11D). Dentine tubules contain cellular structures and a fluid that carries nourishment to the inside. They are surrounded by HA crystals (~0.5-1 μm diameter) arranged in a random fashion. These tubular units are, on their turn, embedded in a composite consisting of a collagen matrix reinforced with HA. This is called the intertubular region.

2.2.1.3. Cementum

Cementum is a specialized calcified substance covering the anatomic root of the tooth. The principal role of cementum within the tooth is to serve as a medium by which the periodontal ligaments can attach to the tooth for stability. Hence, its bottom surface is tangent to the periodontal ligaments running through the jaw (*via* collagen fibres), and the upper portion of the surface is firmly cemented to the dentin of the tooth.

From a chemical point of view, cementum is similar to dentine and bone –it is formed by approximately 45 vol.-% of inorganic material (mainly HA), 33 vol.-% of collagen (mostly type-I) and 22 vol.-% of water. Its coloration is yellowish and, since is less mineralized, softer than either dentin or enamel.

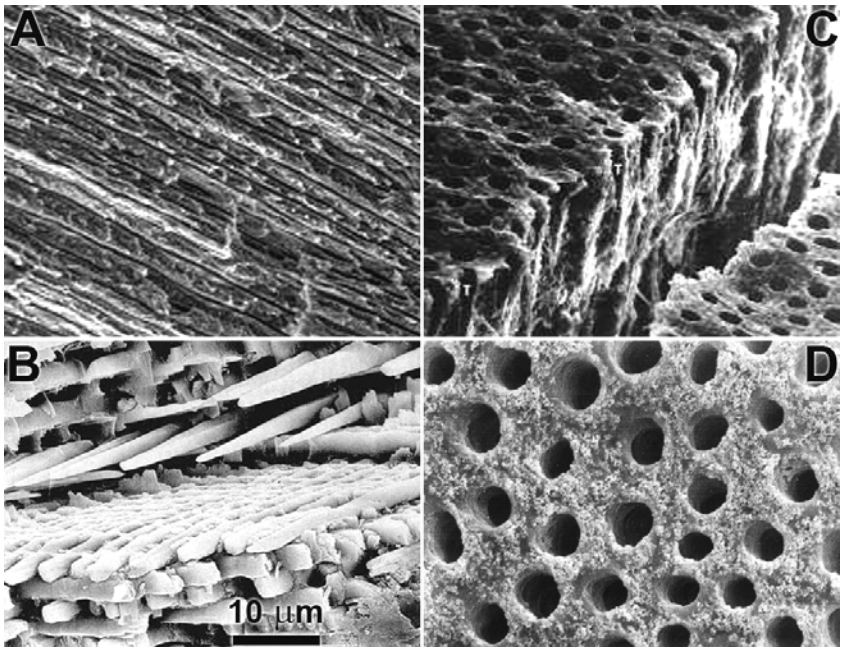

Fig. 2.11. SEM images of the column-like structure of the enamel (A), detailed of the enamel structure showing ordered rods of HA (after Dorozhkin) (B),[12] general view of the dentine (C) and detail of the dentine tubules (D).

2.2.2. Mechanical properties

The toughness of enamel is lower than that of the dentine, hence, dentine possess a higher resistance to fracture under the action of a force than enamel. The converse is the case for the hardness (Table 2.3). Enamel hardness is indeed significant: it is the hardest material in vertebrates (Table 2.3). The hardness of the enamel layer is due to its high degree of mineralization, however, the large amount of minerals in enamel accounts not only for its strength but also for its brittleness. Dentine, less mineralized than enamel, is also less brittle.

Table 2.3. Mechanical properties of teeth.[6]

Property	Enamel	Dentine
Fracture toughness (MPa/m^2)	0.7-1.3	1-2
Elastic modulus (GPa)	60	Perpendicular to tubules: 5-6 Parallel to tubules: 13-17
Hardness (GPa)	4	0.5

The presence of tubules in the dentine confers a considerable degree of anisotropy to its structure, and, therefore, its mechanical properties in general, and toughness in particular, are quite anisotropic (Table 2.3).

Comparing with bone (Table 2.1), teeth are harder and present a higher elastic modulus, thus, they support better elastic deformations. Teeth's fracture toughness is lower than the found for bones.

2.2.3. Hydroxyapatite in teeth

Like in bones (Section 2.1.1.2), HA present in teeth is not pure, and it contains several ions in the crystal structure partially substituting calcium, phosphate groups or carbonate anions. Additionally, although the mineral in all the three dental tissues is basically HA, it chemical composition is different depending on the phase considered (Table 2.4).

The carbonate contain in dentine is similar with the amount present in bone (~5 wt.-%) and significantly higher than that of enamel (~3 wt.-%). The carbonate content of human enamel increases from the surface going inwards. The magnesium content on dentine is also higher than in enamel (~1 and 0.2 wt.-% respectively). Also, dentine is less calcium-deficient than enamel, with a Ca/P molar ratio ~1.66 (very close to the Ca/P ratio for stoichiometric HA, 1.67) and ~1.59 respectively. In enamel, the F^- ion content (~0.01 *vs.* ~0.07 wt.-% in dentine) is sharply peaked at the surface.

Table 2.4. Typical composition of HA in enamel and dentine[i] in wt.-%.[9, 12]

	Ca^{2+}	PO_4^{3-}	CO_3^{2-}	Na^+	K^+	Mg^{2+}	Sr^{2+}	Cl^-	F^-	$P_2O_7^{4-}$	H_2O	Ca/P ratio
Enamel	37.6	18.3	3.0	0.7	0.05	0.2	0.03	0.4	0.01	0.022	1.5	1.59
Dentine	40.3	18.6	4.8	0.1	0.07	1.1	0.04	0.27	0.07	0.10	10	1.66

When the OH^- group of the HA structure is fully replace by F^-, we speak about fluorapatite (FAp, $Ca_{10}(PO_4)_6F_2$) instead of hydroxyapatite. FAp is the most stable and least soluble compound among all calcium orthophosphates. FAp easily forms solid solutions with HA with any desired F/OH molar ratio. Such compounds are called fluorhydroxyapatites (FHA) or hydroxyfluorapatites (HFA) and described with the chemical formula $Ca_{10}(PO_4)_6(OH)_{2-x}F_x$ ($0 < x < 2$). Pure FA never occurs in biological systems. However, due to the ability to form FHA and HFA, an exposure to fluoride (like that contained in toothpaste and city tap water) to turn some of the HA into FHA/HFA (more resistant to damage caused by acids) is probably the most effective cavity prevention treatment available today.

[i] Numerical values were not found in the literature for the cementum, but they should be similar to those for dentin.

2.3.- BONE REPAIR AND SUBSTITUTION

2.3.1. Bone defects

Although bones repair themselves when they fracture through a natural remodelling process (Section 2.1.4), there are some circumstances when bone defects do not heal spontaneously. These situations frequently result from trauma, an increasingly aged population, pathological degeneration, congenital abnormities, infections or tumour resection of the bone tissue.[13] Hence, filling of the resulting defect is a common practice with an increasing value in the re-establishment of the musculoskeletal system to promote bone healing,[13] and, in fact, bone is the second most frequently transplanted tissue in humans.[14]

Currently, repairing osseous deficiencies involves various medical surgical techniques, including autogenous grafts, allografts, internal and external fixation devices, electrical stimulation, alloplastic implants,[i] *etc.*[13] The goal of bone replacement is to bridge a bone defect over healing procedures stable and durable without having to accept new problems or complications in order to restore form and function to patients.

In general, bone-grafting materials can be divided into two main groups, natural and synthetic bone grafts.

2.3.2. Natural bone grafts. Autogeneous, allogeneous and xenogeneous implants

Natural materials used as bone graft materials can be divided into autograft, allograft and xenograft.[13, 15]

- Autogenous grafting involves harvesting healthy bone from one anatomical site and implanting the graft material in a defect site of the same individual. The tissue is usually collected from the iliac crest, but also from the distal femur and proximal tibia.
- Allografts are taken from donors or cadavers and implanted into another individual of the same specie.
- Xenografts refer to bone tissue collected from one species and implanted into a different one, *i.e.* ivory or bovine bone.

Since von Walter described as early as 1821 the successful clinical application of an autogenous bone transplant for the first time in Germany,[13] autogenous bone grafting became the 20th century standard for bone repair and regeneration as its additional functions of serving as a mechanical bridge and providing a scaffold for the ingrowth of new bone became clear.[16]

[i] It refers to inorganic materials implanted in living tissue.

Essentially, autografts possess the advantages of an absence of immunogenic reaction[i] after surgery and very good biological performance[17] in terms of osteogenicity, [ii] osteoinductivity[iii] and osteoconductivity.[iv] However, although autologous bone graft meets many requirements for successful bone regeneration, their use is also associated with some important drawbacks. Harvesting the graft requires an additional invasive surgical procedure that may lead to donor site morbidity (it occurs in ~20% of all cases),[15] chronic post-operative pain, extra blood loss from the donor site, infection and cost.[17, 18] Furthermore, autografting is ineffective when the defect volume exceeds the volume of healthy graft material. Additionally, a second invasive procedure is contraindicated for geriatric or pediatric patients in a compromise state.[18] Another important drawback of the use of autografts is limited availability.

Unlike autologous bone, allogeneic and xenogeneic grafts are widely available and do not require additional surgery on the patient. However, nowadays xenogeneic tissues find rather infrequent application in bone grafting owing to concerns with immunogenicity and disease transmission.[18]

Allogeneic bone has to undergo processing techniques such as lyophilization, irradiation or freeze-drying to remove all immunogenic proteins, in order to avoid any risk of immunogenic reaction. In turn, these processing techniques have a negative effect on the osteoinductive and osteoconductive potential of the allografts, which consequently decreases their biological performance as compared to autografts.[17] However, despite the extensive testing of the donor and the bone obtained, a risk of both bacterial and viral transmission from the donor material to the host remains.[15, 19] Also in some areas of the world, the practice of cadaveric bone transplantation is culturally unacceptable. Allografts fail more frequently than autografts.[18] Nevertheless, use of the various forms of allogenic bone grafts has become commonplace in a wide range of orthopaedic procedures. In fact, the demand for these materials has risen dramatically over the past decade and it is believe that the supply of cadaveric bone graft will become incapable of meeting the epidemiologically driven demand.[16]

[i] Immunogenicity is the ability of a particular substance (antigen), to provoke an immune response; a collection of mechanisms within an organism that protects against disease by identifying and killing pathogens.
[ii] It is the supply of bone-forming cells by the marrow of the harvested bone.
[iii] Associated to the process whereby implanted proteins and growth factors induce new bone to grow.
[iv] Osteoconduction refers to the ability of some materials to serve as a scaffold on which bone cells can attach, grow and divide. In this way, the bone healing response is "conducted" through the graft site. They promotes bone apposition on its surface or down into pores or channels functioning in part as a receptive scaffold to facilitate enhanced bone formation.

Because of the above-mentioned drawbacks of natural bone grafts, large number of synthetic grafts has been developed as a promising alternative to traditional bone grafting.[15-18]

2.3.3. Synthetic bone grafts: Biomaterials

2.3.3.1. What is a biomaterial?

Despite the benefits of both autografts and allografts, the limitations of each have necessitated the development of synthetic materials for bone repairs and replacements. We speak, then, of biomaterials used as bone graft.

A biomaterial is an artificial material capable of being implanted in the body. They are *used to make devices to replace a part or a function of the body, in safe, reliable, economic and physiologically acceptable manner*.[20] A variety of devices and materials used in the treatment of disease or injury include such commonplace items as sutures, needles, catheters, plates, tooth fillings, *etc*. Over the years, various definitions of the term biomaterials have been proposed. For example, a biomaterial can be simply defined as *a synthetic material used to replace part of a living system or to function in intimate contact with living tissue*.[21] Williams defined biomaterials in 1987 as "*a nonviable material used in a medical device, intended to interact with biological systems*".[22] Other definitions have included "*materials of synthetic as well as of natural origin in contact with tissue, blood and biological fluids, and intended for use for prosthetic, diagnostic, therapeutic and storage applications without adversely affecting the living organism and its components*"[23] and "*any substance (other than drugs) or combination of substances, synthetic or natural in origin, which can be used for any period of time, as a whole or as a part of a system which treats, augments, or replaces any tissue, organ or function of the body*".[24]

By contrast, a biological material is a material, such as skin or artery, produced by a biological system.

Artificial materials that simply are in contact with the skin, such as hearing aids and wearable artificial limbs are not included in the biomaterials definition since the skin acts as a barrier with the external world.

2.3.3.2. Hystorical background

In 1931, it was found at the Ulúa valley (Honduras) a fragment of a Mayan girl jaw dated from 600 A.D. where three pieces of a shell shaped as teeth were replacing three lost lower incisisors.[25] This fact shows that the use of *foreigner* materials for the replacement and care of damaged parts of the human body is not new.

The use of biomaterials did not become practical until the advent of an aseptic surgical technique developed by Dr. J. Lister in the 1869s.[21] Earlier surgical procedures, whether they involved biomaterials or not, were generally unsuccessful as a result of infection. The earliest successful implants, as well as a large fraction of modern ones, were in the skeletal system. The first documented use of synthetic bone grafts was reported in 1892 by Dreesman, who treated large-bone defects with calcium sulphate hemihydrate or gypsum ($CaSO_4 \cdot 0.5H_2O$, also called plaster of Paris).[16] Metallic bone plates were introduced in the early 1900s to aid in the fixation of long bone fractures, but many of these early plates broke as a result of unsophisticated mechanical design. Also, materials such as vanadium steel corroded rapidly in the body and caused adverse effects on the natural healing process.[21] Better designs and materials soon followed, as the use of stainless steels and cobalt-chromium alloys in the 1930s, when the first joint replacement surgeries were performed.[21] During the 1940s, polymethylmetacrylate was first used for corneal or damaged skull bones replacement. Following further advances in materials and surgical technique, blood vessel replacements were tried in the 1950s and heart valve replacements and cemented joint replacements in the 1960s.[21] Dr. W. J. Kolff implanted the first artificial heart in 1982. The role of biomaterials has been influenced considerably by advances in many areas of biotechnology and science.

2.3.3.3. Requirements of biomaterials. Biocompatibility, bioactivity and bioresorbability

As discussed before, biomaterials function physically and/or biologically in intimate contact with living tissue. Therefore, the success of biomaterials in the body depends on factors such as the material properties, design and biocompatibility of the material used. Other factors include the technique used by the surgeon and the health, activities and condition of the patient.[21] Biocompatibility involves the acceptance of an artificial implant by the surrounding tissues and by the body as a whole. Biocompatible materials do not irritate the surrounding structure, do not provoke a sustained inflammatory or toxic response, do not incite allergic or immunologic reactions and do not cause cancer.[21] Other compatibility characteristics which may be important in function of an implant device made of biomaterials include *(i)* and adequate mechanical properties such as strength, stiffness and fatigue properties, *(ii)* appropriate optical properties of the material is to be used in the eye, skin or tooth and *(iii)* appropriate density. Sterilizability and appropriate design are also to be considered.[21]

Also, it is now known that clinical success of a biomaterial implant requires the simultaneous achievement of a stable interface with connective tissue (bone bonding).[8]

Bone bonding, or the ability of bone tissue to bond to the surface of a synthetic material, was first introduced by Hench in 1970 following experimental findings on tissue bonding to bioactive glasses.[26] When exposed to an aqueous medium simulating body fluid, a layer of carbonated HA was formed on the glasses' surface. This superficial carbonated HA is chemically equivalent to the mineral phase in bone. Hench studies have demonstrated that for a bond with host tissues to occur, this layer of carbonated HA must form, being the equivalence between both phases the responsible for interfacial bonding.[26] This is true in the case of all bioactive graft materials. In many cases the interfacial strength of adhesion is equivalent to (or greater) than the cohesive strength of the implant material or the tissue bonded to the bioactive implant.[8]

Based on the tissue response, biomaterials can be divided as follows:[8]

- Toxic: the surrounding tissue dies.
- Non-toxic but biologically inactive (nearly inert): a fibrous tissue of variable thickness forms producing the encapsulation of the implant.
- Non-toxic and biologically active (bioactive): an interfacial bond forms.
- Non-toxic and resorbable: the surrounding tissue replaces the implant.

When a biomaterial is nearly inert and the interface is not chemically or biologically bonded, there is relative movement and progressive development of a non-adherent fibrous capsule in both soft and hard tissues. Movement at the biomaterial-tissue interface eventually leads to deterioration in function of the implant or the tissue at the interface or both.[8]

A bioactive material is one that draws out a specific biological response at the interface of the material, which results in the formation of a bond between the host tissues and the material.[26]

Resorbable biomaterials are designed to gradually degrade with time being replaced by the natural host tissue.

Taking into account the mentioned above, the important properties of a biomaterial can be summarized as follows:[27]

- The biomaterial should be biocompatible and bioactive.
- It should have acceptable shelf live.[i]
- It should present appropriate mechanical properties for the indicated application.
- It should have appropriate permeability and processibility for the intended application.

If additionally, the employed biomaterial is biodegradable (resorbable):

[i] It is the length of time a product may be stored without becoming unsuitable.

- The degradation time of the material should match the healing or regeneration process.
- The variation in mechanical properties with degradation should be compatible with the healing or regeneration process.
- The degradation products should be non-toxic, and able to get metabolized and cleared from the body.

2.3.3.4. Biomaterials for bone repair

Despite the benefits of both autografts and allografts, the limitations of each have necessitated the pursuit of alternatives (Section 2.3.2). Although the ideal substitute has not yet been developed, a number of promising products have been described and a large number is, nowadays, commercially available.[15, 28]

As aforementioned (Section 2.1), bone forms complex arrays, possess a hierarchical structure and has more than one function in the vertebrates. Hence, is more complex than synthetic materials. An important challenge in the field of bone regeneration is the development of synthetic bone graft substitutes that fulfil the following requirements:[29]

a) They can readily take part in bone remodelling (*i.e.*, osteoconduction). They are bioactives.
b) They can cause the formation of bone tissues (*i.e.*, osteinduction), even if is not in interfacial contact with natural bones.
c) They maintain their mechanical strength even during the intermediate stages of cellular (*i.e.* osteoclast) or active resorption.
d) They are gradually but fully replaced, within 48 to 52 weeks, by new bone at the implantation site (*i.e.* osseointegration). The benefit of having the implant completely resorbed is that the body is able to repair the tissue with no foreign bodies remaining.[15] The current trend predict that in the near future, many of the permanent prosthetic devices used for temporary therapeutic applications will be replaced by biodegradable (resorbable) devices.[30]

Unfortunately, until now, there are no synthetic biomaterials which simultaneously satisfy all of these criteria, but several successful artificial bone grafts have been developed by using the three basic criteria of a successful graft: osteoconduction, osteogenicity and osteoinduction.[15] Based on their chemical composition, synthetic bone grafts can be divided into four main groups:

- metallic implants, such as titanium and its alloys, stainless steel or cobalt-chromium alloys;

- polymers, such as polymethylmethacrylate, polyurethane, ultra-high molecular weight polyethylene or polylactide;
- ceramics, such as calcium phosphates, alumina, carbon or glass ceramics; and
- composites of the first three groups, such as calcium phosphate-ceramic coatings on metallic implants or polymer-ceramic composites. Composites are formed to improve the properties of existing materials, resulting in a superior material for the intended application by combining the advantages of the composite phases.

2.3.4. Metallic biomaterials

Metals are used as biomaterials in bones due to their excellent mechanical properties, and in fact, they are the most used group of biomaterials for implants that need to bear high tension loads.

They are used as passive substitutes for hard tissue replacement such as total hip and knee joints, for fracture healing aids as bone plates and screws (Fig. 2.12), spinal fixation devices and dental implants. Some metallic alloys are used for more active roles in devices such as vascular stents, guide wires, orthodontic archwires or cochlea implants.[31]

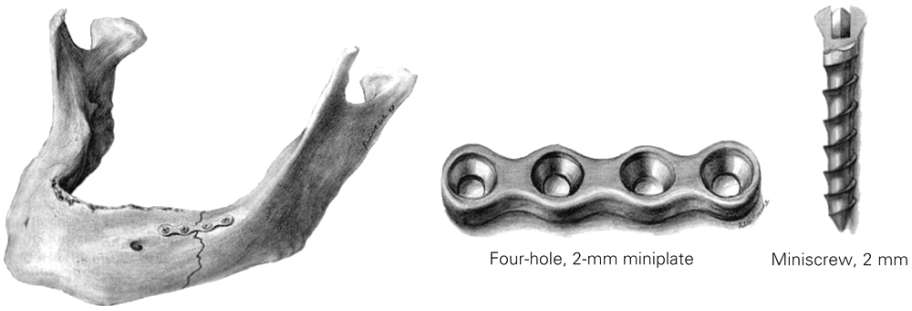

Fig. 2.12. From left to right: bone plate for repair of a broken human jaw and detail of the plate and the screw (after Machado and Savi).[32]

The biocompatibility of the metallic implant is of considerable concern because these implants can corrode in an *in vivo* environment. Body fluids contain various amino acids and proteins that influence metallic corrosion because they are electrolytes.[33] In addition, the concentration of dissolved oxygen is 1/4 that of air in venous blood and 1/80-1/4 that of air in intercellular spaces, which accelerates the corrosion of metallic materials.[33] The cell is also a kind of charging body that may influence the corrosion of metallic materials.[33] The consequences of the corrosion are the disintegration of the implant material *per se* –which will weaken the implant– and the harmful effect of corrosion products on the surrounding tissues and organs.

Adequate mechanical properties such as toughness, high fatigue strength or an elastic modulus similar to that of the human bone (isoelastic implant) are also essential properties for metallic materials.[33, 34]

These specific requirements placed upon metals to be used as biomaterials –corrosion resistance and biocompatibility– restrict the metals or alloys which can be employed to *(i)* stainless steel, *(ii)* cobalt-chromium alloys, *(iii)* titanium or some titanium alloys (*i.e.* Ti6Al4V), *(iv)* niobium or *(v)* tantalum.[34] Among them, Ti and specially developed Ti alloys have an outstanding position due to their combination of strength, elasticity and biocompatibility.[34]

Requirements for highly loaded endosseous (intra-bone) implants such as hip prostheses (Fig. 2.13A) include, in addition to sufficient mechanical properties, a good load transfer from the implant into the bone in order to stimulate the formation of new bone, leading to a good and long-term integration.[i] A metal with an elastic modulus similar to that of the bone will provide this isoelastic behaviour. This can be achieved by production of a suitable alloy (*i.e.*Ti30Ta) and/or porous sintered surfaces.[34] To avoid the metal corrosion, it is also possible to develop tailored materials by coating the metals by a bioactive ceramic material such as HA.[8] Additionally, due to the osteoconductive effects of HA, non-bioactive metals can be "transform" in bioactive at the surface in contact with the host tissue, and therefore, a large number of implants coated with HA are available nowadays (Fig. 2.13B).[34] HA coating of metal surfaces enhances ingrowth and direct bonding of bone to porous surface (Fig. 2.13C),[35] therefore, it eliminates the encapsulation of the implant by the tissue, typical of bioinert materials (Section 2.3.3.3).

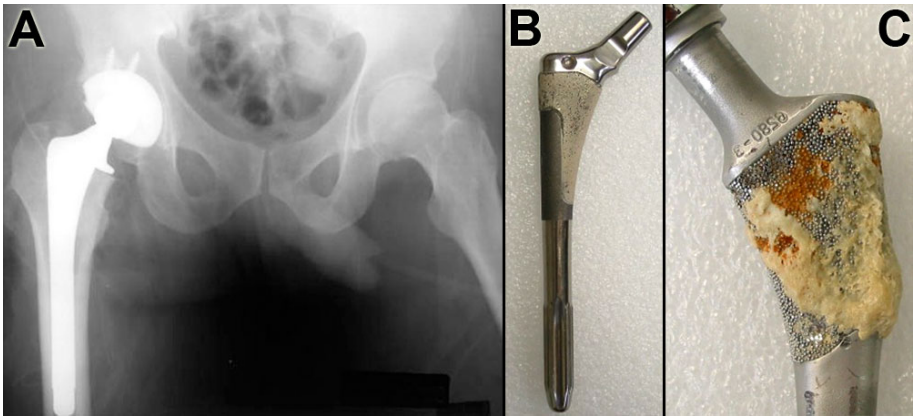

Fig. 2.13. (A) X-ray image showing a metallic hip prosthesis, (B) image of a HA-coated hip prosthesis with porous surface and, (C) the same HA-coated implant after *in vivo* testing showing the bone ingrowth on the HA-coated surface.

[i] If metals used as implants are much stiffer than bone, they shield the nearby bone from mechanical stress. Stress shielding results in a kind of disuse atrophy: the bone resorbs. Therefore, the integrity of the bone/implant interface is compromised.

To provide high shear strength[i] of the HA/metal-interface a heat treatment is necessary, which, due to an interdiffusion process, produces a chemical ceramic-metal bonding.[34] However, these coatings can be used on implants with relatively simple surface geometry. This means that it is difficult to coat implants with complex surface geometry. Also, the use of excessive high temperatures implies that no biologically active agents can be added to the coating during the spraying process.[35]

Tantalum can be fabricated as metallic foam-like structure with interconnecting pores, which allows exceptionally rapid and complete ingrowth.[35]

Other employed strategy to make the surface of the metallic implant bioactive is the chemical surface modification. The case of Ti is a distinguished example of this bioactive surface functionalization. Titanium metal is immersed in aqueous solution of NaOH to form a thin layer of bioactive Na_2O-TiO_2 phase on its surface, which is functionally graded on the metal substrate without phase discontinuity. The titanium metal after this modification reveals calcium phosphate-forming ability *in vivo* and *in vitro*.[36]

As seen, a variety of porous metal surfaces and coatings have been used as surfaces for bone ingrowth intended to fix prosthetic joint replacement components to bone. However, metallic implants are not resorbable, and thus, they do not give way to new bone growth. Therefore the value of the graft is as good as the bond between itself and the host bed.[16]

2.3.5. Polymeric biomaterials

Even though the biomedical applications of enzymatically degradable natural polymers such as collagen dates back thousands of years, the application of synthetic biodegradable polymers started only in the later half of 1960s, with the employment of polymethylmethacrylate (PMMA) for prosthetic fixation.[37] However, the past two decades saw the development of a range of new generation synthetic biodegradable polymers and analogous natural polymers specifically developed for biomedical applications. The driving force is, in part, due to the emergence of novel biomedical technologies including: tissue engineering, regenerative medicine, gene therapy, controlled drug delivery and bionanotechnology, all of which require biodegradable platform materials to build on.[30]

The main advantages of the polymeric biomaterials compared to metal or ceramic materials are ease of manufacturability to produce various shapes (latex, film, sheet, fibres,

[i] It is the resistance to the deformation when the stress (amount of force exerted per unit area) is parallel or tangential to a face of the material.

etc.), ease of secondary processibility, reasonable cost and, in the case of biodegradable polymers, replacement by newly formed tissue.[38]

Given the complexity and the range of applications polymeric biomaterials are currently used, there is not just one polymeric system available that could be considered as an ideal biomaterial. This underlines the need for developing a wide range of biodegradable materials available for implant fabrication that can appropriately match the specific and unique requirements of each individual medical application. As an example, synthetic polymeric materials have been widely used in medical disposable supplies, prosthetic materials, dental materials, extracorporeal devices, encapsulants, polymeric drug delivery systems, *etc.*[38] Non biodegradable polymeric cements, such as PMMA, have been utilized for decades as a bone substitute to fill defects and in the reconstruction of complex fractures or for scaffold development.[16, 39] However, there are not reabsorbed and therefore the new bone is not replaced at the site of the defect. Additionally, it has been shown that non-resorbable polymers may even inhibit new bone growth and normal healing. Therefore, biodegradable polymers that will degrade after a certain period of time of implantation in non-toxic products are nowadays receiving much attention.[16, 30, 39] Examples are polylactide, polyglycolide, poly(glycolide-*co*-lactide), poly(dioxanone), poly(carbonate), *etc.*[38]

Bioresorbable (biodegradable) polymers are degraded by hydrolysis or enzymatically, and may be of synthetic or natural origin –*i.e.* several useful biocompatible polymers of microbial origin are being produced from natural sources by fermentation processes.[40] Non-toxic alcohols, acids and other low molecular products, easily eliminated by the body, are formed as a result of hydrolysis *in vivo* of biodegradable polymers.[40]

Biodegradable polymeric materials are being investigated in developing therapeutic devices such as temporary prostheses, three-dimensional porous structures as scaffolds for tissue engineering and for pharmacological applications, such as drug delivery. Some of the current biomedical applications of biodegradable polymeric materials include *(i)* large implants, such as bone screws (Fig. 2.14), bone plates and contraceptive reservoirs, *(ii)* small implants, such as staples, sutures and nano- or micro-sized drug delivery vehicles, *(iii)* plain membranes for guided tissue regeneration and *(iv)* multifilament meshes or porous structures for tissue engineering.[30]

Current efforts in biodegradable polymer synthesis have been focused on custom designing and synthesizing polymers with tailored properties for specific applications by *(i)* developing novel synthetic polymers with unique chemistries to increase the diversity of polymer structure, *(ii)* developing biosynthetic processes to form biomimetic polymer

structures and *(iii)* adopting combinatorial and computational approaches in biomaterial design to accelerate the discovery of novel resorbable polymers.[30]

Polymeric biomaterials are less stiff and hard than bones, and therefore, they cannot be used in load-bearing implants. In order to increase their mechanical properties, polymers can be mixed with a reinforcement phase such as, *i.e.*, carbon fibres[41] or ceramics granules such as HA[42] or bioactive glass.[43]

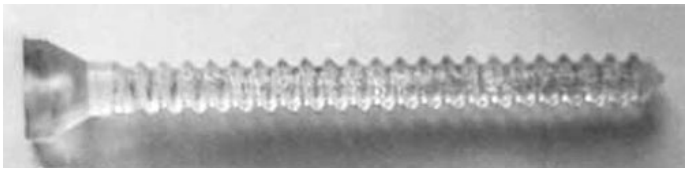

Fig. 2.14. A poly(glycolide-*co*-lactide) bone screw (after Jan and Grzegorz).[41]

2.3.6. Ceramic biomaterials

Unlike metals and polymers, ceramics are difficult to shear plastically due to the ionic or covalent nature of the bonding and minimum number of slip systems.[i] These characteristics make the ceramics non-ductile[ii] and are responsible for almost zero creep[iii] at room temperature.[44] Consequently ceramics are very susceptible to notches or microcrakcs because instead of undergoing plastic deformation they fracture elastically on initiation of a crack, thus, they are brittle. This is also the reason ceramics have low tensile strength compared to compressive strength. Ceramic are generally hard, *i.e.*, alumina (Al_2O_3) shows a hardness of 9 in the Mohs' scale.[iv] Other characteristics of ceramics are their high melting temperatures and low conductivity of electricity and heat due to the nature of their bonding.

In recent years, humans have realized that ceramics and their composites can be used also to augment or replace various parts of the body, particularly bone. Thus, the ceramics used for the latter purposes are classified as bioceramics. Also, their relative inertness to the body fluid, high compressive strength and esthetical pleasing appearance led to the use of ceramics in dentistry as dental crows. Some carbons have found use as implants especially for blood interfacing applications such as heart valves. Due to their high specific strength as fibres, ceramics are also being used as reinforcing components of composite implant materials[41-43] and for tensile loading applications such as artificial tendons and ligaments.[44]

[i] Slip is the process by which plastic deformation is produced by a dislocation (a crystallographic defect, or irregularity, within a crystal structure motion). By an external force, parts of the crystal lattice glide along each other, resulting in a changed geometry of the material.
[ii] A ductile material is capable of withstanding a certain amount of force, by changing its form, before fracturing or breaking (related with plastic behaviour).
[iii] It is a deformation under a constant load.
[iv] At the Mohs scale, talc $Mg_3Si_4O_{10}(OH)_2$ is the softest ceramic with a Mohs hardness of 1 and diamond is the hardest (value of 10). Apatite has a Mohs value of 5.

Other applications of bioceramics are as carriers for enzymes, antibodies and antigens –non-resorbable porous glasses– since they have several advantages, notably resistance to microbial attack, pH changes, solvent conditions, temperature, *etc.*[8]

However, due to bioceramics' inherent brittleness, susceptibility to microcracks, low tensile and impact strength and poor fracture toughness, their use for applications requiring significant load-bearing, torsion bending or shear stress, *etc.*, seems impracticable at present.[8]

From a structural point of view, biocompatible ceramic materials used in fabricating implants can be classified as:

- crystalline solids (ceramics),
- amorphous solids (glasses),
- amorphous solids with crystallization nuclei (glass-ceramics),

which can in turn be considered as (Section 2.3.3.3):[8]

- non-resorbable (relatively bioinert): not able to bond with the host tissue,
- bioactive or surface reactive (semi-inert): able to physically bond directly to the living host bed,
- resorbable (non-inert) bioceramics : able to bond with living tissues and to be replaced by the natural host tissue.

2.3.6.1. Non-resorbable bioceramics

Non-resorbable bioceramics have almost no influence in the surrounding living tissue and maintain their physical and mechanical properties while in the host. They resist corrosion and wear.[i] Examples are dense and porous alumina (Al_2O_3), zirconia (ZrO_2) and titania (TiO_2) ceramics and single-phased calcium aluminates (xCaO.$y$$Al_2O_3$). Because they do not bond to bone, their application is limited to repairs that will not encounter sheering or torque[ii] forces.[16] They are typically used as dental implants (Fig. 2.15A) (because of its combination of excellent corrosion and high wear resistance), structural-support implants (*i.e.*, bone plates, bone screws, Fig. 2.15B), or for long-bone defects (because of their excellent compressive strength). Examples of non structural support uses are ventilation tubes, sterilization devices and drug delivery devices.[45]

[i] In materials science, wear is the erosion of material from a solid surface by the action of another solid.
[ii] Torque is a vector that measures how much a force acting on an object causes that object to rotate.

Fig. 2.15. Images showing a bioceramic dental implant (A) and a bone screw (B).

2.3.6.2. Bioactive bioceramics

Upon implantation in the host, bioactive bioceramics form strong bonds with adjacent tissue. Surface reactive bioceramics are, *i.e.*, HA ceramics, hydroxyapatite/wollastonite[i] glass-ceramics and certain compositions of silicate-based glasses (bioactive glasses).[8] Bioactive glasses developed for implantation are, mainly SiO_2-CaO-Na_2O-P_2O_5 and Li_2-ZnO-SiO_2 systems.[44]

Bioactive ceramics have many applications, primarily in the areas of bone repair and bone regeneration *via* tissue engineering, such as:

- synthetic bone graft materials for general orthopaedic, craniofacial, maxillofacial and periodontal repair (Fig. 2.16),
- cochlear implants, or
- bone tissue engineering scaffolds (porous bioceramics).

Fig. 2.16. X-ray image of a dog's periodontal bone defect before (A) and after (B) filling with a bioactive glass.

[i] $CaSiO_3$

Also, bioactive ceramics are employed to obtain bioactive composites. As an example, bioactive glass has been used in combination with PMMA to form a bioactive bone cement, and HA and glasses are used as a coating to form a layer on metallic implants' surface that eases the chemical bonding of the implant to the surrounding bone tissue (Section 2.3.4).[8, 15]

A common characteristic of bioactive glasses and bioactive ceramics is a time-dependent, kinetic modification of the surface that occurs upon implantation into living bone tissue. The surface forms a biologically active carbonated HA layer, which provides the bonding interface with osseous tissues (bone bonding), and is chemically and structurally equivalent to the mineral phase in bone. It is that equivalence which is responsible for interfacial bonding (Section 2.3.3.3).[8]

2.3.6.3. Resorbable bioceramics

Resorbable bioceramics degrade upon implantation in the host and the resorbed material is replaced by endogenous tissues,[i] being this its principal advantage. The rate of degradation varies from material to material. Almost all bioresorbable ceramics, except biocoral ($CaCO_3$) and gypsum ($CaSO_4 \cdot 0.5H_2O$), are variations of calcium orthophosphates, including aluminium-calcium-phosphorous oxide, ferric-calcium-phosphorous oxide, zinc-calcium-phosphorous oxides, zinc-sulphate-calcium-phosphorous oxides, tricalcium phosphate (TCP, $Ca_3(PO_4)_2$) and HA.[44]

Fig. 2.17. Examples of calcium orthophosphate-based bone substitution materials (granules and scaffolds) (after Dorozhkin).[12]

As for non-resorbable or bioactive bioceramics, the mechanical behaviour of resorbable bioceramics strongly influences their use as implants, and therefore, they must be shielded from loading forces until bone ingrowth has occurred. Rigid stabilization of

[i] Endogenous substances are those that originate from within an organism, tissue, or cell. It is the opposite of exogeneous.

surrounding bone and non-weight bearing are required during this period because ceramics can only tolerate low bending and torque load before failing, unless they are used in sites of relatively low mechanical stress or when forces are basically compressive.[16]

Applications include dental implants, percutaneous devices, periodontal treatment, drug delivery devices, alveolar ridge augmentation, orthopaedic and maxillofacial surgery, otolaryngology, spinal surgery, bone defect filling, excised tumour and diseased bone loss, scaffolds (Fig. 2.17), *etc.*

Although gypsum –or plaster of Paris– was used already in 1892 as bone substitute,[16] the concept of using synthetic resorbable ceramics as bone grafts was introduced in 1969.[46]

Gypsum biocompatibility, bioactivity and resorbability make it a desirable candidate for bone graft substitutes, but its degradation time –between 30 and 60 days– is too short for bone repair. Also, there is significant loss of mechanical properties upon degradation, so it does not provide internal strength or support. Therefore it can only be used to fill small bone defects such as those resulting from cyst curettage.[15, 16] Nevertheless, calcium sulphate has recently seen resurgence in use with the recent marketing of this material in the form of tablets for use in filling osseous defects.[16]

Calcium orthophosphates make up the majority of ceramic-based bone graft substitutes currently available on the market, namely TCP, hydroxyapatite or the combination of both.[15, 28] Calcium orthophosphate-based bioceramics have been in use in medicine and dentistry for nearly forty years, mainly with bone repair purposes.[8] The first *in vivo* use of calcium orthophosphates was performed in 1920; that time the researchers implanted TCP into animals to test its efficacy as a bone substitute.[47] In 1951, HA was tested *in vivo* for the first time. However, it was already the 1970s, when other calcium orthophosphates were synthesized, characterized, investigated, and tried in medicine.[47]

An advantageous property of these ceramics, particularly HA, is that they are osteoconductive and they bond well to the host bone (osseointegration).[i] Additionally, although these ceramics do not contain intrinsic osteoinductive properties, the bond between host and graft provides sufficient affinity for local or exogenous[ii] growth factors[iii] that serve in the regeneration process.[16] Like HA, TCP is biocompatible, bioactive and bioresorbable, but its resorption rate is 10-20 times faster than the HA one.[48] When a biphasic calcium

[i] It is the direct structural and functional connection between living bone and the surface of an artificial implant.
[ii] In biology, an exogenous factor is any factor that is present and active in an individual organism or living cell but that originated outside of that organism. It is the opposite of endogenous.
[iii] Growth factor refers to a naturally occurring protein capable of stimulating cellular differentiation and maturation. For example, bone morphogenic proteins stimulate bone cell differentiation.

orthophosphate ceramic, consisting of HA and β-TCP, was compared with a pure HA ceramic with similar macro- and microstructure, more bone was found in the TCP more soluble phase. This suggests that the more soluble calcium orthophosphate phases are more osteoinductive than less soluble ones.[17] However, implantation of highly soluble carbonated apatite ceramic did not result in bone induction, suggesting that a relatively stable surface is needed for facilitation of bone formation.[17] Therefore, a combination of a mixture of both HA and TCP phases might be clinically favorable.[16]

HA and TCP bioceramics are obtained by sintering calcium orthophosphate salts at high temperatures (1000-1500°C) to produce a powder that can then be moulded into the desired shape by high-pressure compaction.[8, 16] There is little control over the porosity of this material, and hence, the ceramic remains stable (not resorbed) for long periods of time due to its high density –radiographic findings demonstrate a continued presence of the calcium orthophosphate ceramic for a prolonged period of time due to the failure of complete remodelling.[16]

Osteoconduction is a 3D process that is observed when porous structures are implanted into or adjacent to bone. Porosity alone, however, is not adequate for bone ingrowth. Open porosity –connected to the outside surface– with interconnectivity is the most essential prerequisite. This is based on the 3D interconnections between the lacunae in the bone that provide intercellular communication (Section 2.1.2.1).[35] Hence, open porosity is critical to the integration of tissue into the ceramics, and porous calcium orthophosphate bioceramics are widely studied.[8, 28, 44] The consensus of research indicates that the requisite pore size for bone ingrowth into porous implants is 100 to 500 μm and the interconnections must be larger than 100 μm.[8, 16, 35] However, when designing a porous resorbable bioceramic, it should be take into account that, with increased porosity, the graft exhibitss significantly less compressive strength and fatigue resistance.[8]

Recently, it was predict that calcium orthophosphate bioceramics designed to mimic the bone mineral and intended for use as implants *in vivo* should not possess steps of heating/firing/calcination at or above 650°C in any phase of their processing, manufacturing and/or shaping operations.[29] The reason is that at, or above, this temperature, carbonate ions which may be present in the HA structure are opt to readily leave the materials. The same also applies to the case of HPO_4^{2-} ions. Both CO_3^{2-} and HPO_4^{2-} ions are present in biological HA (Section 2.1.1.2), and therefore, researches should incorporate them when preparing bioceramics grafts in order to prepare materials that will resemble biological HA to the most possible extent.[29] Na^+, K^+ and Mg^{2+}, which altogether amount to a value greater than 1 wt.-%

in the bone HA (Section 2.1.1.2), must also be consider in preparing synthetic bioceramic bone substitute materials.[49]

In sharp contrast to the aforementioned sintered bioceramics, calcium orthophosphates are also used as biomaterials for bone repair and substitution in the form of calcium phosphate bone-cements –a mixture of calcium orthophosphates that reacts in an aqueous medium at room temperature to form HA or dicalcium phosphate dihydrate (DCPD, $CaHPO_4 \cdot 2H_2O$). They are biocompatible, bioactive and resorbable.

2.4.- CALCIUM ORTHOPHOSPHATES

Diverse combinations of oxides of calcium and phosphorus (both in the presence of water and without it) provide a large variety of compounds which are distinguished by the type of the phosphate anion: ortho- (PO_4^{3-}), meta- (PO_3^-), pyro- ($P_2O_7^{4-}$) or polyphosphate ($(PO_3)_n^{n-}$). In the case of multi-charged anions (orthophosphates and pyrophosphates), calcium phosphates are also differentiated by the number of hydrogen ions present in the anion. Examples include mono- ($Ca(H_2PO_4)_2 \cdot H_2O$), di- ($CaHPO_4$), tricalcium phosphate ($Ca_3(PO_4)_2$) or calcium pyrosphosphate ($Ca_2P_2O_7$). All these varied compounds form the family of the calcium phosphates.

With the exception of calcium pyrophosphate, calcium phosphates used in medical applications are namely calcium orthophosphates.[48] By definition, all calcium orthophosphates consist of three major chemical elements: calcium (oxidation state +2), phosphorus (+5) and oxygen (–2). In addition, the chemical composition of many calcium orthophosphates includes hydrogen, either as an acidic orthophosphate anion (for example, HPO_4^{2-} or H_2PO^{4-}), and/or as incorporated water (for example, $CaHPO_4 \cdot 2H_2O$). In the ternary system $Ca(OH)_2$-H_3PO_4-H_2O there are eleven known non-ion-substituted calcium orthophosphates with the Ca/P molar ratio within 0.5 and 2.0 (Table 2.5).

It should be noted that in literature occasionally one could find brief notes on the 12th calcium orthophosphate, namely oxyapatite ($Ca_{10}(PO_4)_6O$). A mixture of oxyapatite and HA might be prepared by dehydration of HA at temperatures exceeding ~900°C (*i.e.*, during plasma spray of HA) only in the absence of water vapour. It also might be crystallized in glass-ceramics. Oxyapatite is very reactive and transforms to HA in contact with water vapour. It is still very poorly known; however, data on the solubility constant and crystal structure are available.[12]

Table 2.5. The members of the calcium orthophosphate family with their respective Ca/P ratio and pH stability range in aqueous solutions at 25°C.

Common name	Acronym	Formula	Ca/P	pH range[12]
Monocalcium phosphate anhydrous	MCPA	$Ca(H_2PO_4)_2$	0.5	[e]
Monocalcium phosphate monohydrate	MCPM	$Ca(H_2PO_4)_2 \cdot H_2O$	0.5	0.0-2.0
Dicalcium phosphate anhydrous[a]	DCPA	$CaHPO_4$	1.0	[e]
Dicalcium phosphate dihydrate[b]	DCPD	$CaHPO_4 \cdot 2H_2O$	1.0	2.0-6.0
Amorphous calcium phosphate	ACP	$Ca_xH_y(PO_4)_z \cdot nH_2O$ n = 3-4.5; 15-20% H_2O	1.2-2.2	~5-12[f]
Octacalcium phosphate	OCP	$Ca_8(HPO_4)_2(PO_4)_4 \cdot 5H_2O$	1.33	5.5-7.0
α-Tricalcium phosphate	α-TCP	α-$Ca_3(PO_4)_2$	1.5	[g]
β-Tricalcium phosphate[c]	β -TCP	β -$Ca_3(PO_4)_2$	1.5	[g]
Calcium deficient hydroxyapatite	CDHA	$Ca_{10-x}(HPO_4)_x(PO_4)_{6-x}(OH)_{2-x}$ $(0 < x < 1)$	1.5-1.67	6.5-9.5
Hydroxyapatite	HA	$Ca_{10}(PO_4)_6(OH)_2$	1.67	9.5-12
Tetracalcium phosphate[d]	TTCP	$Ca_4(PO_4)_2O$	2.0	[g]

[a]– mineral: monetite; [b]– mineral: brushite; [c]– mineral: whitlockite; [d]– mineral: hilgenstockite; [e]– stable at temperature above 100°C; [f]– always metastable; [g]– cannot precipitate from aqueous solutions.

The most important parameters at the calcium orthophosphates are the molar Ca/P ratio, basicity/acidity and solubility. These parameters strongly correlate with the solution pH. The lower the Ca/P molar ratio is, the more acidic and water-soluble the calcium orthophosphate is.[9] Hence, MCPM is both the most acidic and water-soluble calcium orthophosphate and TTCP is the most basic. However, TTCP solubility in water is higher than that of HA ($\log(K_s)_{25°C}$ = 38-44 *vs.* 116.8, respectively).[12] TTCP is not very stable in aqueous solutions –it hydrolyses[50] to HA and $Ca(OH)_2$. The vast majority of calcium orthophosphates are sparingly soluble in water;[9] however, all of them are easily soluble in acids but insoluble in alkaline solutions.

Chemically pure calcium orthophosphates are crystals of white colour and moderate hardness. However, natural minerals of calcium orthophosphates are always coloured due to impurities. The atomic arrangement of calcium orthophosphates is built up around a network of PO_4^{3-} groups, which gives stability to the whole structure.[51]

2.4.1. Solubility phase diagram

As mentioned above, calcium orthophosphates comprises eleven known non-ion-substituted compounds. Each of them can be synthesized at different conditions, *i.e.* those with $H_2PO_4^-$ ions only form under rather acidic conditions.[9] Due to the triprotic (three protons) equilibrium that exists within orthophosphate-containing solutions (Eq. 2.1), variations in the pH solution alter the relative concentrations of the four orthophosphoric acid polymorphs and, thus, both the chemical composition and the amount of the calcium orthophosphates that forms by direct precipitation.[52]

$$H_3PO_4 \overset{k_1}{\longleftrightarrow} H_2PO_4^- \overset{k_2}{\longleftrightarrow} HPO_4^{2-} \overset{k_3}{\longleftrightarrow} PO_4^{3-} \qquad \text{(Eq. 2.1)}$$

where[12] $k_1 = 7.5 \cdot 10^{-3}$; $k_2 = 6.2 \cdot 10^{-8}$ and $k_3 = 1.7 \cdot 10^{-12}$.

Solubility diagrams show the thermodynamically stable phases at given conditions, and provides an indication of the likely conditions required for the synthesis of a determinate calcium orthophosphate. The solubility diagram[53] for the ternary system $Ca(OH)_2$-H_3PO_4-H_2O at 25°C is given in Fig. 2.18.

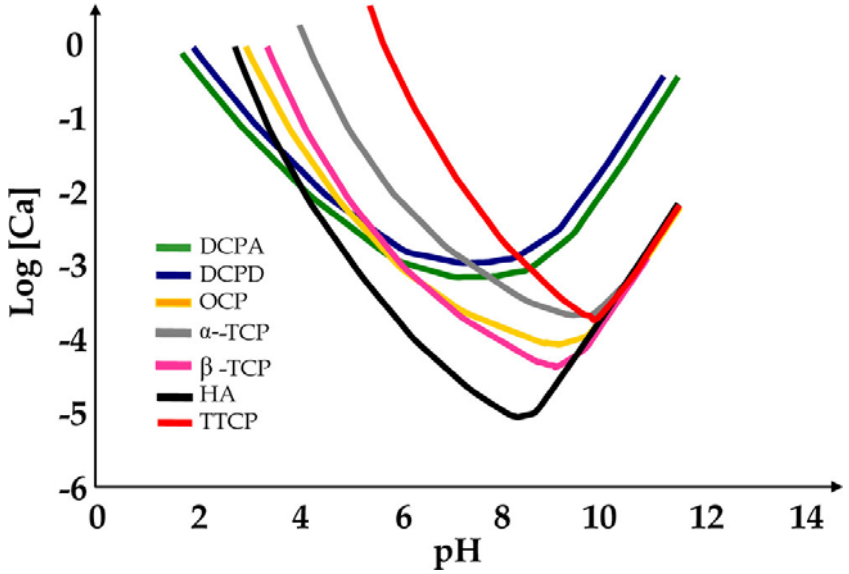

Fig. 2.18. Diagram of solubility isotherms of calcium orthophosphates phases in the ternary system $Ca(OH)_2$-H_3PO_4-H_2O at 25°C.[53]

Gibbs' phase rule (Eq. 2.2) is the fundamental rule on which phase diagrams are based. It provides the number of degrees of freedom of a system for a given thermodynamic condition, that is, how many control variables (pressure, temperature, composition, *etc.*) can be altered while maintaining this condition. Mathematically, this number is:

$$F = 2 - P + C \qquad \text{(Eq. 2.2)}$$

where F is the degrees of freedom, P is the number of phases that coexist in the equilibrium (solid, liquid, gas, *etc.*) and C is the number of components in the system. The number two

arises from the two main thermodynamic control parameters, usually temperature and pressure. If other variables such as magnetic, electric or gravitational fields are considered, the numerical value two will increase by the number of new variables considered.

According to Gibbs' phase rule, a ternary system as $Ca(OH)_2$-H_3PO_4-H_2O with a single phase, *i.e.* liquid (solution), has two degrees of freedom at a fixed temperature and pressure; that is, two variables (pH, concentration, composition, *etc.*) can be altered while keeping this condition. Hence, the composition of any solution in this system is defined by fixing, *i.e.*, pH and calcium concentration [Ca], or pH and [P], or [Ca] and [P]. The solubility diagram at Fig. 2.18 represents the pH *vs.* [Ca] diagram of the calcium orthophosphates at a fixed pressure and temperature.

According to this diagram, HA is the phase thermodynamically stable at pH ~4.5-10, and therefore, it will be the calcium orthophosphate precipitated in this pH range. However, it should be take into account that the actual phase that forms under any given conditions is often also influenced by kinetic considerations.[9]

The solubility diagram also reflects the fact that all calcium orthophosphate compounds are more soluble as the pH decreases. The slope of the isotherm is an indication of how fast the solubility of the salt increases with decreasing pH. Since, for a given drop in pH, the solubility of a basic salt would increase more than would an acidic salt, the slope of the isotherm is related to the alkalinity of the salt. Consequently, the more acidic salts, DCPD and DCPA, have smaller negative slopes than do the more basic salts TTCP, HA and the two TCPs.

At the invariant or singular points (point where two solubility isotherms across), three phases coexist in equilibrium. As an example, DCPD-TTCP invariant point occurs at ~8.5 pH. This equilibrium is characterized by a continuous saturation[i] of the liquid phase with respect to DCPD and TTCP, which are equally stable at this solution composition. However, their relative stabilities are different –DCPD is more stable than TTCP at pH below 8.5 and *vice versa*. At this invariant point, the solution is supersaturated[ii] with regards to HA (the thermodynamically stable phase at this pH). Thus, HA will precipitate under these conditions while DCPD and TTCP will keep in solution. As long as DCPD and TTCP are present in excess, the solution pH will remain close to the DCPD-TTCP singular point. Therefore, the

[i] Is the point at which a solution of a substance can dissolve no more of that substance.
[ii] It is a solution that contains more of the dissolved material than could be dissolved by the solvent under normal circumstances.

solution will stay at a quasi-constant pH and composition, allowing the HA formation to progress at a steady rate.

2.4.2. Biological occurrence and medical uses

Natural calcium orthophosphates are the principal raw material for phosphorus-containing fertilizers,[12] while biologically formed calcium orthophosphates are the major component of all mammalian mineralized tissues (Table 2.6). From the family of calcium orthophosphates, only DCPD, ion-substituted ACP, OCP and ion-substituted CDHA can be found in humans in normal and/or pathological calcifications (Table 2.6). Additionally, fluorapatite, another member of the calcium orthophosphates were all OH^- groups of the HA structure are substituted by F^- ($Ca_{10}(PO_4)_6F_2$), is also found in teeth in solid solutions with HA (Section 2.2.3).

Table 2.6. Biological occurrence of calcium orthophosphates in humans and its medical use.[12]

Compound	Biological occurrence	Medical use
MCPA	None	In calcium phosphate bone-cements
MCPM	None	None
DCPA	None	In calcium phosphate bone-cements
DCPD	– Pathological calcifications (dental and urinary calculi, chondrocalcinosis,[i] *etc.*) and some carious lesions – Intermediate in both bone mineralization and dissolution of enamel in acids (dental erosion)	– In calcium phosphate bone-cements – As intermediate for tooth remineralization
ACP	Containing Na^+, Mg^{2+}, CO_3^{2-}, and $P_2O_7^{4-}$ is found in soft-tissue pathological calcifications (*i.e.*, heart valve calcifications of uremic[ii] patients)	– In calcium phosphate bone-cements – As a filling material in dentistry
OCP	– One of the stable components of human dental and urinary calculi. – Proposed to participate as the initial phase in enamel and bone mineral formation. – It plays an important role at *in vivo* formation of apatitic biominerals. – Precursor phase to biological apatite found in natural and prosthetic heart valves	Implantation into bone defects
α-TCP	None	Occasionally for calcium phosphate bone-cements
β -TCP	None	– As bioceramic (Section 2.3.6) – In calcium phosphate bone-cements
CDHA	The ion-substituted CDHA (by Na^+, K^+, Mg^{2+}, Sr^{2+} for Ca^{2+}; CO_3^{2-}, HPO_4^{2-} for PO_4^{3-} or F^-, Cl^-, CO_3^{2-} for OH^-) plus water forms biological HA, the main inorganic component of vertebrates normal (bone, teeth) and pathological calcifications (Section 2.1.1.2)	Very promising compound for synthetic bone substitutes due to its similarity with biological HA
HA	None	As bioceramic (Section 2.3.6)
TTCP	None (not very stable in aqueous solutions)[50]	In calcium phosphate cements

[i] It is a rheumatologic disorder with varied clinical manifestations due to precipitation of DCPD crystals in the connective tissues.
[ii] It is a term used to loosely describe the illness accompanying renal failure.

ꕥ *MCPM* is never found in biological calcifications due to its high acidity and solubility. Moreover, pure MCPM is not biocompatible with bone. However, in medicine it is used as a component of several self-hardening calcium phosphate bone-cements.[12] Like MCPM, *MCPA* never appears in calcified tissues and is not biocompatible due to its acidity. There is no current application of MCPA in medicine. Due to the similarity with MCPM, in many cases MCPA might be used instead of MCPM; however, the highly hydroscopic properties of MCPA reduces its commercial application.[12]

ꕥ *DCPD* is of biological importance because it is often found in pathological calcifications, urinary stones and some carious lesions. In medicine is used in calcium phosphate bone-cements and as intermediate for tooth remineralization.[12] Like DCPD, *DCPA* is used in calcium phosphate bone-cements, but it never occurs neither in normal not in pathological calcifications.

ꕥ *ACP* is often encountered as a transient phase during the formation of calcium orthophosphates in aqueous systems. Biologically, ACP (often containing Na^+, Mg^+, carbonate and pyrophosphate ions) is found in soft-tissue pathological calcifications.[12] In medicine, ACP is used in calcium phosphate bone-cements and as a filling material in dentistry.[12]

ꕥ *OCP* is often found as an unstable transient intermediate during precipitation of the thermodynamically more stable calcium orthophosphates (Fig. 2.18). OCP is of a great biological importance (Table 2.6).[54] In surgery, OCP is used for implantation into bone defects.

ꕥ *β-TCP* cannot be precipitated from aqueous solutions. It is a high temperature phase of calcium orthophosphates, which only can be prepared by thermal decomposition, *i.e.* of CDHA at temperatures above 800ºC.[9] At temperatures above 1125ºC, it transforms into *α*-TCP, another polymorphous modification of TCP.[9] Being the stable phase at room temperature, *β*-TCP is less soluble in water than *α*-TCP.[12] Pure *β*-TCP never occurs in biological calcifications. Only the Mg-substituted form (β-$(Ca,Mg)_3(PO_4)_2$) is found in dental calculi and urinary stones, dentinal caries, salivary stones, arthritic cartilage, as well as in some soft-tissue deposits.[12] In medical practice, *β*-TCP is used in calcium phosphate bone-cements. In combination with HA, *β*-TCP forms a biphasic calcium phosphate (BCP). Both *β*-TCP and BCP are widely used as a bone substitution bioceramics.[16] *α-TCP* is more reactive in aqueous systems, has a higher specific energy and it can be hydrolyzed to a mixture of other calcium phosphates. It never occurs in biological calcifications but in medicine, chemically pure *α*-TCP is occasionally used in calcium phosphate bone-cements.[12]

ꕥ Stoichiometric pure *HA* does not exist in biological systems. Biological HA is, in fact, ion-substituted *CDHA* (Section 2.1.1.2). Biological HA is the main inorganic component of vertebrates' mineralized tissues. For medical practice, CDHA is a very promising compound for industrial manufacturing of artificial bone substitutes, and due to the great similarity to bone and teeth mineral (Sections 2.1.1.2 and 2.2.3), HA is widely used as a coating on orthopaedic and dental implants (Section 2.3.4).

ꕥ Like β-TCP, *TTCP* is another high temperature phase of calcium orthophosphates. In aqueous solutions it hydrolyses to HA and $Ca(OH)_2$.[50] Consequently, TTCP is never found in biological calcifications. However, it is widely use for calcium phosphate bone-cements.[12]

2.5.- CALCIUM PHOSPHATE BONE-CEMENTS

As mentioned before, recently it was pointed out the necessity of calcium orthophosphate bioceramics that do not include steps of heating/firing/calcination at or above 650°C if they are designed to mimic the biological HA present in bones (Section 2.3.6).[29]

Calcium phosphate bone-cements or calcium phosphate cements (CPCs)[i] are a very promising alternative to bioceramics since they also are biocompatible,[55] bioactive,[56] resorbable and osteoconductive[57], but additionally, they do not imply any high temperature step for their use as biomaterial for bone repair and substitution. Their name stems from its suitability for repair, augmentation and regeneration of bones.

Put in a simply way, CPCs are essentially a mixture of calcium orthophosphates that react in an aqueous/physiological medium at room/body temperature to form (precipitate) DCPD or HA. The reaction that takes places is called setting reaction, since the precipitation of the final product makes the mixture hard. These products are easy to handle. After the powder(s) and the solution are mixed together, a viscous and mouldable paste is formed that sets to a firm mass within a few minutes. Therefore, in sharp contrast with bioceramics, they can be shaped to fit irregular defects of the bone and they establish good prospects for minimally invasive surgical techniques –less aggressive than the classical surgical methods.

[i] It should be noted that although the common name of this product is calcium phosphate (bone)-cements, they are entirely or essentially formed by a mixture of calcium orthophosphates (Section 2.4). However, the prefix ortho- is commonly omitted when referring to CPCs.

All CPCs are made of an aqueous solution and fine powders of one or several calcium orthophosphate(s). Here, dissolution of the initial calcium orthophosphates and mass transport appear to be the primary functions of the aqueous environment, in which the dissolved reactants form a supersaturated microenvironment with regard to precipitation of the final products.[47] The relative stability and solubility of various calcium orthophosphates is the major driving force for the setting reactions that occur in these cements (Section 2.4.1). Therefore, mixing of a dry powder with an aqueous solution induces various chemical transformations, where crystals of the initial calcium orthophosphate(s) rapidly dissolve(s) and precipitate(s) into crystals of CDHA or DCPD with possible formation of intermediate precursor phases (*i.e.* ACP or OCP). During precipitation, the newly formed crystals grow and form a web of intermingling microneedles or microplatelets of the final products, thus provide a mechanical rigidity to the hardened cements. In other words, entanglement of the newly formed crystals is the major reason of setting.

As the paste is set and hardened at room or body temperature, direct application in healing of bone defects became a new and innovative treatment modality in the end of the 20th century. Moreover, calcium orthophosphate cements can be injected directly into fractures and bone defects, where they intimately adapt to the bone cavity regardless its shape.[58]

The discovery of CPCs has been ascribed to Brown and Chow for an abstract published in 1983.[59] However, several authors worked before with similar reactions. For example, Kingery looked at formulations based on CaO and H_3PO_4 in 1950.[60] In the 1970's Driskell *et al.*[61] described the possibility to obtain a monolithic calcium orthophosphate ceramic at ambient or body temperature. Also in the 1970's, Monma and Kanazawa described the hydraulic properties of α-TCP.[62] In 1982, LeGeros *et al.* published an abstract on apatitic CPCs setting at physiological conditions.[63] The first reports on the clinical use of CPCs came out in the mid 1990's.[64, 65]

The major advantages of the CPCs include (Table 2.7):

- it is a self-hardening process (setting reaction),
- the setting reaction proceeds *in situ* at room or body temperature,
- the defect site does not have to be adapted to the graft material,
- there is no appreciable volume contraction during setting.

Table 2.7. Major advantages and disadvantages of CPCs.[47, 66, 67]

Advantages	Disadvantages
• Self-setting ability *in vivo*.	• Mechanical weakness: limited use due to potential collapse of material followed by soft-tissue formation instead of bone formation. Until cements with adequate shear strength are available, most complex fractures that can be repaired with cement also will require metal supports.
• Good injectability that allows cement implantation by minimally invasive surgical techniques, which are less damageable than the traditional surgical techniques.	• Can be washed out from surgical defect if excess of blood.
• Good osteoconductivity and occasional osteoinductivity: the initial biological properties of the hardened cements are similar to those of CDHA or DCPD.	• Lack of macroporosity (especially interconnected pores), which prevents fast bone ingrowth. The cements degrade layer by layer form the outside to the inside only.
• Can be replaced by newly formed bone after a period of time.	• The *in vivo* biodegradation of many formulations is slower than the growth rate of a newly formed bone.
• Excellent biocompatibility and bioactivity.	
• No toxicity.	
• Low cost.	
• Ease of preparation and handling.	
• Setting at body temperature.	
• Form chemical bonds to the host bone.	
• Clinically safe materials in their powder components.	
• Can be used to deliver antibiotics, anti-inflammatory drugs, bone morphogenic proteins,[i] *etc.* at local sites, which are able to stimulate certain biological responses.	

Therefore, the cements are more versatile in handling characteristics than prefabricated calcium orthophosphate granules or blocks. Besides, like any other bioceramics, calcium orthophosphate cements provide the opportunity for bone grafting using alloplastic materials, which are unlimited in quantity.

[i] It refers to a naturally occurring protein capable of stimulating and promote cellular differentiation and maturation, which varies between growth factors. Bone morphogenic proteins stimulate bone cell differentiation (they induce the formation of bone and cartilage).

Hence, CPCs are becoming of increasingly great importance in the field of biomaterials, in particular, as bone substitutes and repair (Fig. 2.19).[68] CPCs also have prospective applications in the field of drug delivery devices.[67] Because of their remarkable insertion properties, CPCs and related biomaterials have been studied intensively over the last twenty five years and, as a result, a number of different formulations have been established that are currently used in medical practice.[69] Consequently, several reviews covering the preparation, properties and applications of CPC biomaterials are available,[47, 67-72] as well as more than a dozen commercial CPC formulations.[69]

However, it should be emphasized that owing to the lower fracture toughness parameters of CPCs[73] in comparison to human bone[8] (~0.6-1.5 *cf.* 2-12 MPa/m^2), the clinical applications of CPCs are limited to areas where bones are free of dynamic load, *i.e.* for non-load bearing as well as craniofacial and periodontal applications,[74] or as materials for the development of scaffolds in bone tissue engineering.[75] (Table 2.7)

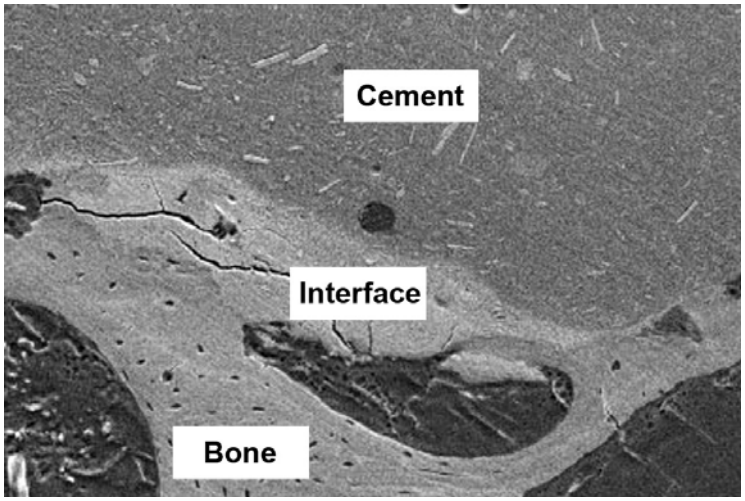

Fig. 2.19. SEM image illustrating CPCs application for bone repair (after Ni *et al.*)[76]

2.5.1. Types of calcium phosphate cements

As mentioned before, generally, all CPCs can be generated by mixing one or several reactive calcium orthophosphate precursors in an aqueous medium. After mixing, a putty-like material/injectable liquid is formed, which is able to set and harden *in vivo*. Consequently, CPCs are widely applicable in clinical practice, *i.e.*, for filling bone defects during surgery, resulting in reduced patient discomfort in comparison to other techniques currently employed.[77]

In 1990s, it was established that there were about fifteen different binary combinations of calcium orthophosphates which gave pastes upon mixing with water or aqueous solutions, so that the pastes set at room or body temperature into a solid cement.[47] From these basic systems, secondary formulations could be derived containing additional or even non-reactive compounds, but still setting like cements.[55, 57]

Most of the cement formulations after the setting reaction result in the formation of CDHA, while the remaining cement formulations give DCPD (brushite) as the end product,[70] since at body temperature only these two calcium orthophosphates are stable in contact with aqueous media such as body fluids.[i] DCPD is the stable phase a pH < 4.2, whereas at pH > 4.2 HA is the stable phase (Table 2.5, Fig. 2.18).[53] A striking difference between these two types of CPCs (called apatitic or brushite CPCs) is that the solubility at physiological pH of the brushite cements is approximately two times higher compared with the HA cements,[78] resulting in their enhanced resorption by biological serum.[57] However, DCPD is a metastable phase which can hydrolyses to apatite *in vivo* and thus may potentially generate biocompatibility problems.[79] In addition, upon examination of the literature related to brushite CPCs, it is apparent that overall they exhibit a lower mechanical strength compared to the apatite CPCs.[80] Other advantages of the apatite CPCs are: thermodynamic stability,[71] reasonable setting time with respect to surgeons' requirements[70] and the formation of CDHA as the end product[72] –the inorganic component of mineralized bone tissues. As-produced apatite CPCs are chemically and structurally very similar to biological apatites, exhibiting excellent biological and physiological characteristics.

For the majority of apatite cements, water is not a reactant in the setting reaction. Therefore, the quantity of water actually needed for setting of apatite cements is very small.[81] However, for brushite cements, water always participates in the chemical transformations because it is necessary for DCPD formation. Due to this reason, brushite cements are always hydraulic,[ii] while usually this term is not associated with apatite cements.

Despite their very large number, the most studied CPC formulations are based on the following reactions (Eq. 2.3 to 2.5):[70]

$$\beta\text{-}Ca_3(PO_4)_2 + Ca(H_2PO_4)_2{\cdot}H_2O + 7H_2O \rightarrow 4CaHPO_4{\cdot}2H_2O \qquad \text{(Eq. 2.3)}$$

[i] ACP and OCP appear in humans as precursor in the initial phase of enamel and bone mineral formation. However, they appear as an unstable transient intermediate phase (Section 2.4.1.1).

[ii] Hydraulic cements are materials that set and harden, after being combined with water, as a result of chemical reactions with the mixing water.

It is an acid-base reaction, where β-TCP acts as base an MCPM as acid. They react to form DCPD, a neutral calcium orthophosphate

$$2Ca_4(PO_4)_2O + 2CaHPO_4 \rightarrow Ca_{10}(PO_4)_6(OH)_2 \qquad \text{(Eq. 2.4)}$$

In this acid-base reaction TTCP (basic character) reacts with DCPA (neutral) to form HA (slightly basic).

$$3\alpha\text{-}Ca_3(PO_4)_2 + H_2O \rightarrow Ca_9(HPO_4)(PO_4)_5(OH) \qquad \text{(Eq. 2.5)}$$

The slightly basic α-TCP hydrolyzes to CDHA (slightly basic) *via* a dissolution-precipitation process without pH change.

Therefore, all existent CPC formulation reacts, well by an acid-base reaction (Eq. 2.3 and 2.4), well by a conversion (Eq. 2.5) to give as the end-product either DCPD or HA (Ca-deficient or stoichiometric).

2.5.2. Control of the setting reaction. Cohesion and setting time

Generally, CPC reaction rate must be well controlled: the CPC must react slowly enough to provide enough time to the surgeon for implantation, and fast enough to prevent delaying the operation. In the clinical situation, the surgeon needs to place the CPC paste into the prepared surgical site and then wait for the paste to sufficiently set before closing the wound. Otherwise the soft paste could be deformed easily to lose its geometrical shape by the stress generated in closing the wound, or even be disintegrated and fail to set into a cohesive implant.[82] Thus, from a fundamental and an application point of view, it is important to design a rational synthetic route to CPC biomaterials with setting time between 10-30 minutes.[47, 70]

The *setting time* of a CPC is divided in initial (*I*) and final (*F*) setting time. The initial one marks the onset of hardening after water has been added, while the final one refers to the fact that, after this time, the setting reaction has proceeded to an extent that the manipulation of the CPC will not deteriorate its mechanical properties. Clinically, it states that the cement paste should be implanted before time *I* and that the wound can be closed after time *F* (Fig. 2.20). A cement should not be deformed between times *I* and *F* because in that stage of the setting process any deformation could induce cracks.[57] The following handling requirements (in minutes) have been formulated for CPCs: $3 \leq I < 8$; $F \leq 20$.[47]

Another requirement of CPCs is that the *cohesion time*[i] (CT) must be at least 1 min before the initial setting time so that a clinician has at least 1 min to apply and to mold the material. As the mixing in a mortar is about 1 min, the shortest CT that can be allowed is about 2 min, so that a clinician has at least 1 min to collect the paste from the mortar and put it on the pallet knife or in the syringe with which it is to be transferred to the wound after CT and before *I* (Fig. 2.20).[47]

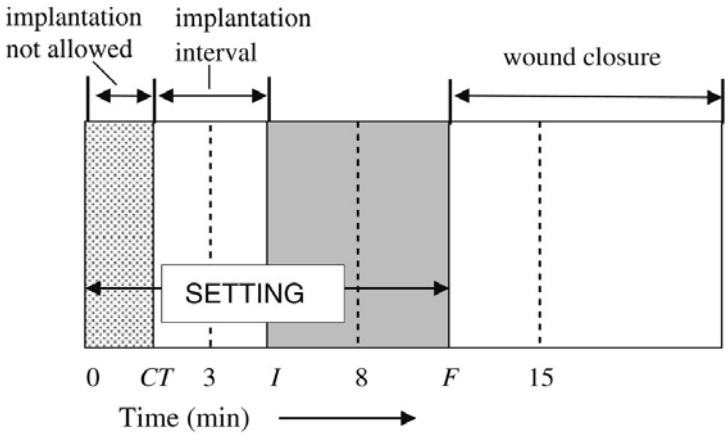

Fig. 2.20. Diagram of the setting parameters relevant for a CPC: CT – cohesion time; *I* – initial setting time; *F* – final setting time (after Dorozhkin).[47]

Additionally, it is noteworthy that in many cases the rapid conversion of the CPC precursors to HA not only leads to the rise of the appropriate physiological properties, but also results in the strengthening of the mechanical properties. In particular, rapid conversion accelerates achievement of the final compressive strength value, which is almost linearly dependent on the extent of the CPC setting reaction.[83] Therefore, a rapid conversion rate to the end product might be also desirable.

The setting reaction of CPCs consists of three stages, namely, *(i)* dissolution of reactants, *(ii)* nucleation of crystals, and *(iii)* growth of crystals.

Therefore, the strategies to modify the setting reaction of CPCs have been targeted to these three stages of the setting process.[70] Table 2.8 gathers the approaches and the employed tactics to modify CPCs reactivity. [70]

[i] It is the time from which a cement no longer disintegrates when immersed in an aqueous phase.

Table 2.8. Strategies and approaches of the employed tactics to modify CPCs' setting reaction rate.[70]

Strategy	Approach	How?
Dissolution rate	Change contact area between reagent and mixing liquid	– Milling of reactants – Use nano/micro powders
	Change solubility in the mixing liquid	– Use more/less soluble phase – Change of reaction pH
	Change mixing liquid saturation	Use a liquid phase containing Ca^{2+} and/or phosphate ions
	Use dissolution inhibitors in the mixing liquid	
	Modify reagent surface	– Chemical change (pre-reaction) – Physical change (dissolution pits)
Nucleation rate	Use seeds	
	Change the saturation of the reaction product in the mixing liquid	– Change of saturation – Change of end-product solubility
	Use of nucleation inhibitors	
Growth rate	Change the saturation of the reaction product in the mixing liquid	Change of saturation
	Use crystal growth inhibitors	– Change of saturation – Change of end-product solubility

2.5.2.1. Dissolution rate of reactants

Experimental studies have revealed that the setting reactions based on Eq. 2.4 and 2.5 are initially controlled by surface reactions, and then by diffusion.[84, 85] In brushite CPCs (Eq. 2.3), the very strong effect of β-TCP specific surface area on β-TCP–MCPM–water CPCs suggests that a surface reaction is also the limiting factor, at least at the start of the brushite CPCs setting reaction.[70] Therefore, the control of the reagent dissolution rate is a very important aspect of the overall CPC setting reaction. The dissolution rate of reactants can be modified by various means (Table 2.8):[70]

- Increasing the surface area between reagent and liquid phase,
- Changing the reagent solubility in the liquid phase,
- Changing the saturation of the liquid phase towards the reagent,
- Using dissolutions inhibitors,
- By surface modification (passivation or activation of the surface).

- The surface area between reagent and liquid phase can be increase by milling of the reagents or by using nano/micro powders. Unfortunately, nano-powders tend to agglomerate, and therefore a large amount of water is required to wet the powder.[70] On the other hand, by milling, the particle size of the starting powder does not decrease further than a few micrometers.[50] Beyond this point, powder amorphization occurs.[50, 86]

- The solubility of the reagent in the mixing liquid can be varied, either by choosing a more (or less) soluble reagent, or by changing the mixing liquid composition. For example, the replacement of β-TCP by the more soluble α-TCP, or the less soluble HA in β-TCP–MCPM–water cements can lead to much shorter or much longer reaction times.[87] The dissolution rate of CPC reagents can also be modified with a shift of the pH value of the mixing liquid. However, it should be taken into account that HA and DCPD only form at specific pH values.

- The saturation of the liquid phase towards CPC reagents can be significantly increase using a liquid which already contains phosphate ions (*i.e.* $(NH_4)H_2PO_{4(aq)}$, $NaH_2PO_{4(aq)}$, $KH_2PO_{4(aq)}$).[88] However, the use of a liquid phase saturated with phosphate ions is somewhat limited owing to the incorporation of foreign ions (*i.e.* NH_4^+, Na^+, K^+) into the crystal lattice of the end product. Additionally, such CPC systems have an excess of non-participant reactive ions (*i.e.* phosphate) and the low or high initial pH of the mixture is also prone to forming intermediate phases.[71, 72] These effects can potentially create biocompatibility problems with as-prepared CPCs as well as slow their conversion rate.

- The use of inhibitors that allow controlling the dissolution rate of reagents can also modify CPCs setting reaction. As an example, HA dissolution is inhibited by the presence of compounds such as bisphosphonates.[89]
- Recently it was suggest that the nucleation of dissolution pits at the material surface is a very important factor controlling material dissolution.[90] As an example, an approach to reduce the dissolution rate via surface modification is to partially react the powders to form a dissolution barrier.[70]

2.5.2.2. Nucleation rate

The nucleation rate of new HA or DCPD crystals during the CPC setting reaction can be modified by (Table 2.8):

- The addition of nuclei (seeds) in the cement paste,
- The modification of the saturation of the mixing liquid,
- The use of nucleation inhibitors.

- By adding crystal nuclei as seeds into the CPC formulation, it is possible to accelerate its nucleation rate.[91]
- By using more soluble reagents or by adding predissolved calcium and phosphate ions in the mixing liquid, nucleation can also be modified. For example, since fluoroapatite is less soluble than HA, the presence of fluoride ions in the mixing liquid of an apatite CPC accelerates the whole setting reaction.[70]
- The use of nucleation inhibitors strongly reduces the nucleation rate (*i.e.*, Mg^{2+} ions in apatitic CPCs).[85, 92]

2.5.2.3. Growth rate

Since the means to change growth and nucleation rate are the same, the tactics employed to control the growth rate are very similar with the used to modify the nucleation rate. Among all substances affecting apatite crystal growth, several are of particular importance due to their relevance in mineralization, for example Mg^{2+} ions[85, 92] and carbonate ions[70] which are known to inhibit hydroxyapatite growth and also prolong the setting reaction of α-TCP-based CPCs.

It should be noted that strategies that increase the dissolution rate of CPC reagents can have a negative influence on the rate of crystal nucleation and growth.[88]

2.5.3. Future developments of calcium phosphate bone-cements[47, 70]

The discovery of CPCs has already opened up new perspectives in synthesis of bioceramic scaffolds possessing sufficient mechanical properties. In the past, such scaffolds could only be manufactured by the sintering route at elevated temperatures. Therefore, until recently it was impossible to produce resorbable preset low-temperature hydrated 3D ceramics for various applications, *i.e.* scaffolds and granules from low-temperature calcium orthophosphate phases, such as ACP, DCPA, DCPD, OCP and CDHA. Now, using the appropriate techniques, open macroporous 3D scaffolds consisting of the aforementioned low-temperature phases (currently, excluding ACP and OCP) can be produced *via* a cementation reaction, thus noticeably widening the application of these calcium orthophosphates as biomaterials. This type of materials could be very promising for tissue engineering applications. Among them, CDHA is of a special interest due to its chemical similarity to bone material and a large specific surface area.

As CPCs and cement-based composites represent an intriguing group of new materials for bone augmentation and reconstruction, there is a great potential for further improvement of their properties, in which the ideal characteristics (Table 2.7) should be achieved by manipulations with the chemical composition, powder particle size and distribution, as well as by means of various additives. Few commercial apatite cements are currently approved for clinical use.[69] New formulations of both apatite and brushite cements are expected to appear in the market soon. New formulations will include *(i)* injectable and open macroporous formulations to optimize their osteoconduction, *(ii)* formulations containing only one calcium orthophosphate (single-phase cement powders), and *(iii)* drug-loaded and hormone-loaded cements for the treatment of bone diseases. The former two directions deal with both chemistry and material science, while the last direction is more related to tissue engineering and medicine.

The most promising direction of the future developments of CPCs is obviously seen in their functionalization by incorporation or impregnation of various hormones, growth factors, drugs or other biorganic compounds; as well as incorporation of living cells and other tiny biological objects. The initial attempts have already been performed but without a great success yet. For example, researchers have already found that unset CPCs might have toxic effects when placed on cell monolayers, while the set cements are biocompatible for the same type of cells.

Stability (insolubility) in normal physiological fluid environment and resorbability under acidic conditions produced by osteoclasts are also among the most important *in vivo*

characteristics of modern CPCs. For some clinical applications, such as cranioplasty, a relatively slow resorption and replacement by bone is quite acceptable, whereas in other applications, such as periodontal bone defects repair, sinus lift, *etc.*, the ability of the hardened cement to be replaced quickly by bone is crucial. Experimental results suggest that a number of parameters of CPCs, such as Ca/P ratio, carbonate content, ionic substitution, crystallinity, *etc.*, might affect the dissolution characteristics of the cements in slightly acidic solutions. This gives an opportunity to formulate cements possessing different resorption rates, which are suited for different applications.

Finally, besides the aforementioned chemical, material, and biomedical improvements of CPCs, one should not forget on a better design of both the mixing equipment and delivery (injection) techniques.

2.6.- REINFORCEMENT OF BIOCERAMICS AND CALCIUM PHOSPHATE CEMENTS

Bones are stiff and tough because they combine the "good" properties of the collagen (tough but not stiff) and HA (stiff but not very tough) present in their structure (Section 2.1). However, compared with bones, bioceramics and CPCs used for their repair and substitution are brittle, with both a low impact resistance and a low-tensile strength, *i.e.*, fracture toughness for synthetic HA[73] with respect to bones[8] is 0.6-1.5 *vs.* 2-12 MPa/m^2, respectively. They are strong enough only at compression strength. Consequently, the use of HA ceramics and CPCs for clinical practice is at present limited to low-load bearing areas. Therefore, numerous studies have been developed to investigate the reinforcement of bioceramics materials, and improvements in strength have been reported due to the use of various additives –*i.e.* phosphate[88] or chitosan;[93] by increasing the solid to liquid ratio in CPCs;[94] by a previous thermal treatment of the CPC precursors;[95] by using fibres to reinforce the cement matrix;[47] *etc.* The use of fibres also increase the fracture toughness of the final products.[96] Increasing of pressure during the sintering step also improve the strength and fracture toughness of HA ceramics.[97]

When a reinforcement phase is mixed with bioceramics or CPCs, we speak about biocomposites.

2.6.1. What is a composite?. Biocomposites

Composite materials are solids which contain two or more distinct constituent materials or phases on a scale larger than the atomic and in which properties are significantly altered in comparison with those of a homogeneous material.[98] Composite materials offer a variety of advantages in comparison with homogeneous materials, as in the case of bone (a natural composite,[i] Section 2.1) or HA-coated metallic implants (Section 2.3.4).

The properties of a composite material depend very much upon structure, *i.e.* bone hierarchical structure (Section 2.1.1.1). In particular, they depend upon the shape of the heterogeneities, the volume fraction occupied by them and upon the interface among the constituents.[98]

The shape of the heterogeneities in a composite material can be *(i)* particles with no long dimension (spherical, ellipsoidal, polyhedral or irregular), *(ii)* fibres[ii] and *(iii)* platelets.[iii] In isotropic systems,[iv] stiff platelet inclusions are the most effective in creating a stiff composite, followed by fibres. The least effective geometry for stiff inclusions is the spherical particles.[98] On the contrary, when the inclusions are more compliant that the matrix, spherical particles reduce the stiffness the least and platelet particles reduce it the most.[98] Soft spherical inclusions are used intentionally as crack stoppers to enhance the toughness of polymers such as polystyrene with a small sacrifice in stiffness.[98]

Apart from the mechanical properties of the reinforcing material, the orientation of the incorporated fibres and the matrix-fibre interface are also of great importance for the resulting mechanical properties of the composite.

In biomaterials, it is important for each constituent of the composite to be biocompatible. Moreover, the interface between constituents should not be degraded by the body environment.[98] Composites employed as biomaterials are often called *biocomposites*.

2.6.2. Fibrous reinforcement concept

The idea behind reinforced ceramics is simple: if a strong filler is present in the matrix, it might stop crack propagation.

The concept of using fibres as reinforcement for brittle materials is not new. Fibres have been used as reinforcement since ancient times, when straw was used in mud huts to improve structural integrity. Today, this technique has advanced considerably in the

[i] Other natural composites include dentine (Section 2.2.1.2), cartilage, skin and wood.
[ii] Particles with one long dimension.
[iii] Particles with two long dimensions.
[iv] They have identical values of a property in all crystallographic directions.

construction industry, and steel, glass and synthetic fibres such as polypropylene are used in concrete to improve its mechanical properties (Fig. 2.21).

Fig. 2.21. Concrete reinforced with steel fibres.

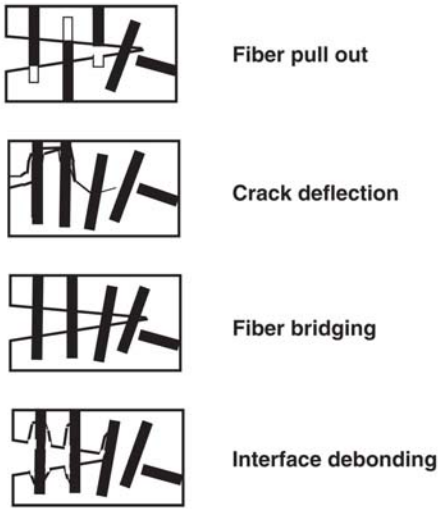

Fig. 2.22. Mechanisms for improving the fracture toughness in short fibre reinforced ceramics (after Dorner-Reisel *et al.*).[96]

It should be taken into account that, while unidirectional fibre composites can be made very strong in the axial direction, they are weaker than the matrix alone when loaded transversely. Therefore, if stiffness and strength are needed in al directions, the fibres may be oriented randomly.[98]

Several toughening mechanisms contribute to the increase of fracture toughness of ceramic materials, namely *(i)* fibre breakage, buckling or pull out, *(ii)* crack deflection, *(iii)* fibre bridging or *(iv)* interface fibre-matrix debonding (Fig. 2.22).[98] For example, during the pull out, energy that would normally cause crack propagation is partially expended by debonding and by friction as the whisker slides against adjacent microstructure features.

Hence, whiskers[i] and fibres are nowadays required in the development of modern composites materials, including ceramic-based biomaterials.

2.6.3. Fibrous reinforcement of calcium orthophosphates

As mentioned before, the mechanical properties of CPCs and bioceramics (both ceramic materials) severely limit their use to non-load bearing implants. Among the various employed methods for increase the strength of these biomaterials, and therefore enlarge their applications to minor load bearing implants, the use of fibre as reinforcement phase improves not only their strength, but also their fracture toughness.[96] Fibre length, fibre volume fraction and the mechanical properties of the reinforcing material were found to be key microstructural parameters that controlled the mechanical properties of calcium orthophosphate composites.[99] Additionally, the orientation of the incorporated fibres, regular or random, appears to be crucial for the resulting flexural strength and modulus of elasticity. Random orientations led to a preserved modulus at a slight strength increase whereas a regular fibre orientation led to increased strength at decreased modulus.[100]

However, it should be taken into account when adding fibres that the presence of non-resorbable fillers always reduced the porosity of the composite, thus affecting negatively bone ingrowth into pores (Section 2.3.6.3).

Discussions about carcinogenic effect of fibrous materials exist. However, they suffer from insufficient experimental data. Some early investigations show that carcinogenic effects of fibres depend on their geometry, and therefore, fibres with a diameter below 1 μm and a length above 10 μm need to be prevented.[101, 102] Further systematic research is certainly necessary.

In ceramics, actual problems in reaching a sufficient reinforcing effect with improved fracture toughness are mainly of two origins.[96] Firstly, there is insufficient optimization of the fibre-matrix interface. Secondly, defects can exist within the ceramic matrix, like crack or porosity.

Various types of materials have been used to improve the mechanical properties of bioceramics and CPCs (ceramics, metals or polymers). Since the resultant composites are employed as biomaterials (biocomposites), the chemical species (chemical composition) constituting these materials should be biocompatible (Section 2.3.3.3).

[i] Fibrous single crystals with no dislocations usually grown at high temperatures and with great aspect ratio (length/diameter), thus, with small diameters and big lengths.

2.6.4. Bioinert reinforcements

2.6.4.1. Metallic and ceramic reinforcements

Metallic fibres have been successfully used to reinforce bioceramics and CPCs. For example, it was shown that the addition of 20 vol.-% Fe-Cr alloy fibres increase the strength and fracture toughness of a pure HA ceramic by a factor of ~2 and ~6 respectively.[103]

One of the requisites of these composites is low or, preferably, no reactivity at all between the ceramic and the metal.[103] Due to the sintering step of bioceramics, elements from the matrix (Ca, P) appear to diffuse into some metallic short fibres, like stainless steel and Ti fibres. The extend of diffusion depends strongly on the sintering conditions.[104] Also, there is an immense difference between the thermal expansion coefficient of hydroxyapatite and metallic fibres. This drastic difference might lead to a crack net in the composites with metallic fibres, thus decreasing their mechanical properties.[96] This effect due to a high difference between the thermal expansion coefficient was shown for a ceramic composite with carbon fibres after hot pressing up to 1150°C.[105] In addition, the elastic modulus of these composites needs further consideration. Metals possess a much higher elastic modulus than bones, and an increase of elastic modulus in the final composite results in bone stress shielding (Section 2.3.4).

As for metallic implants, other important problems of metal fibres-reinforced ceramics are related to corrosion, wear and/or negative tissue reaction of the metallic fibres. Therefore, only metals with good corrosion properties as Ti or its alloys should be employed as fibrous reinforcement[34] (Section 2.3.4).

Bioinert ceramics such as SiC,[106] C,[106] Al_2O_3,[104] ZrO_2,[107] Al_2O_3/ZrO_2 combinations,[108] *etc.* have also been used in bioceramics to improve its reliability. A major advantage of ceramics with respect to metals as implant materials is their corrosion, wear resistance, and minimal host tissue reaction (Section 2.3.6). Also, there is not reactivity between the ceramic matrix and the ceramic reinforcement, *i.e.*, no diffusion zone was detected between bioinert Al_2O_3 short fibres and HA after sintering.[104]

Carbon nanotubes have been successfully tested to reinforce CPCs,[109] and Xu *et al.* reported that incorporation of 5.7 vol.-% long carbon fibres increases ~100 times the toughness if compared to un-reinforced CPC. The reinforcement mechanisms were found to be crack bridging and fibre pullout.[110] Although carbon fibres used in composites are known to be inert in aqueous environments (even seawater), and carbon itself has been successfully used as a biomaterial for heart valves,[44] they do not have a track record in the biomaterials setting and more *in vivo* studies should be perform.[98]

Bioinert reinforcements are biocompatible, but, as their name states, they do not interact with the surrounding host tissue. Thus, the bioactivity of reinforced HA ceramics or CPCs with bioinert materials is expected to be much lower than that of un-reinforced ones.[111] This, and its non-resorbability, are the main disadvantages of this kind of reinforcements for bioceramics. Bioceramic reinforcements with bioactive fibres seem to be especially advantageous in regard to biocompatibility.[96] Bioresorbable reinforcements might facilitate bone ingrowth due to an increase in porosity.

2.6.4.2. Polymeric reinforcements

Polymeric resorbable fibres such as polyglactin, polyacrylic acid, polyvinyl alcohol, *etc.*, are also use to reinforce CPC.[47] Their main advantage is that, when implanted in vivo, bioresorbable fibres would provide initial strength and then dissolve to form interconnecting macroscopic channels, which could facilitate bone ingrowth into the implant.[82, 112] For example, interconnected macropores were formed in a CPC-absorbable mesh composite after 84 days of immersion in a physiological solution.[112]

A higher strength might help extending the use of CPCs to larger stress-bearing repairs, while the macropores might facilitate tissue ingrowth and integration of the cement with an adjacent bone. However, an increase in the porosity leads to a decrease in the composite strength. To overcome this situation, several types of fibres with different rates of bioresorbability might be simultaneously incorporated into a cement formulation.[47] Additionally, polymers are less stiff than metals or ceramics, and thus, the final reinforcement of the composite will be lower *cf.* metallic or ceramic fibres (Section 2.6.2).

2.6.5. Bioactive reinforcements

Bioactive β-TCP[113] and, especially, HA fibres[111, 114] are also used to successfully reinforce CPC and bioceramics. They main advantage is their bioactivity, and therefore, they receive the name of bioactive reinforcements. The obtained composites consist only of calcium orthophosphates.

The first biphasic composition consisting of a hardened DCPD matrix filled with β-TCP granules was introduced in 1992.[115] Unfortunately, neither the mechanical nor the rheological properties of this composite have been disclosed. At physiologic pH, the solubility of DCPD is approximately 8 times higher than β-TCP.[47] Therefore, new bone forms in the space left after resorption of the DCPD matrix, while β-TCP granules act as guiding structures.

The idea behind is similar to the use of resorbable polymeric fibres (Section 2.6.4.2), although this feature of the cement should be considered an inverse scaffolding effect.[116]

The use of HA has the advantage of its compositional similarity to the cement matrix and to bone and tooth mineral (Sections 2.1.1.2, 2.2.3). Therefore, fibrous HA should act both as bioactive phase and as reinforcement and, nowadays, the investigation of HA with rod-like morphology received much attention.[117]

It should be also mentioned that calcium orthophosphates powders, granules or fibres are also used as reinforcement phase in polymers[42] or glass ionomer[i] cement[118] used for bone repair. The calcium orthophosphates presented in these formulations act as fillers, which are necessary to improve the mechanical properties and to impart bioactivity; they do not participate in the hardening mechanisms.

2.7.- HYDROXYAPATITE CRYSTALS

2.7.1. Apatite

Apatite is, in fact, three different minerals depending on the predominance of fluorine, chlorine or hydroxyl species in the crystal structure. The names of the individual minerals are fluorapatite (FAp), chlorapatite (ClAp) or hydroxyapatite (HA) respectively.

The formula for apatite is written as $Ca_{10}(PO_4)_6(OH,F,Cl)_2$ while the formulae of the individual minerals are thus written as $Ca_{10}(PO_4)_6(OH)_2$, $Ca_{10}(PO_4)_6F_2$ and $Ca_{10}(PO_4)_3Cl_2$, respectively.[ii] Hence, they belong to the family of calcium orthophosphates (Section 2.4.1). All three modifications are generally present in naturally occurring apatite, and therefore, they are usually considered together due to the difficulty in distinguishing them by ordinary methods. Nevertheless, although less common, pure natural specimens also exist.

As a mineral specie, apatite was first recognized by the German geologist Abraham Gottlob Werner (1750-1817) in 1786 and named by him from the Greek *απατώ* (apato), to mislead or to deceive, because it had previously been mistaken for other minerals, such as beryl $Be_3Al_2(SiO_3)_6$, olivine $(Mg,Fe)_2SiO_4$, amethyst SiO_2, *etc.*[12] All chemically pure calcium orthophosphates are white crystalline materials. Nevertheless, naturally occurring calcium orthophosphate is always coloured due to impurities, the most widespread of which are iron

[i] A ionomer is a polyelectrolyte that comprises copolymers containing both electrically neutral repeating units and a fraction of ionized units. Glass ionomer cements are derived from aqueous polyalkenoic acid –such as polyacrylic acid– and a glass component that is usually a fluoroaluminosilicate. When the powder and liquid are mixed together, an acid-base reaction occurs. As the metallic polyalkenoate salt begins to precipitate, gelation begins and proceeds until the cement sets hard. They are commonly used in dentistry.

[ii] Instead of $Ca_5(PO_4)_3(OH,F,Cl)$ to denote that the crystal unit cell comprises two molecules.

and rare earth elements.[i] Therefore, natural apatite is typically green, but also yellow, blue, reddish brown or purple (Fig. 2.23). However, apatite is not frequently used as a gemstone due to its softness (5 hardness in the Mohs' scale),[12] that limits it's appeal for use as a decorative stone in jewellery applications.

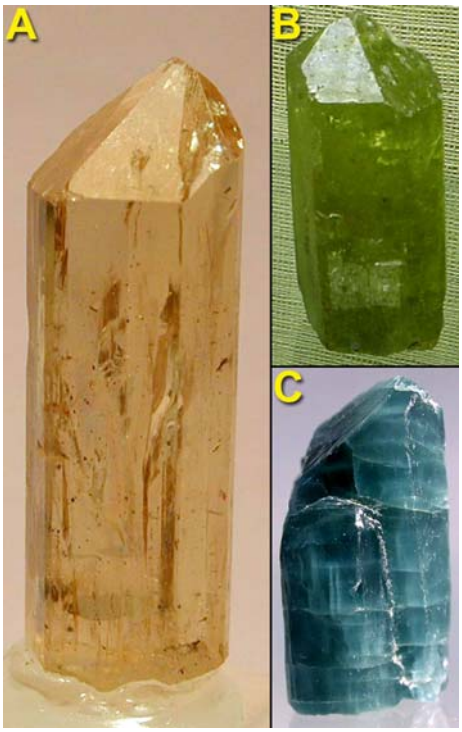

Fig. 2.23. View of natural coloured apatite's crystals. (A) and (B), single crystals from Durango-Mexico, (C) polycrystalline specimen from Russia.

The basic apatite crystal structure is hexagonal with space group $P6_3/m$ (bypiramidal hexagonal) and approximate lattice parameters $a = b = 9.4$ Å and $c = 6.9$ Å.[9] The atomic arrangement of calcium orthophosphates is built up around a network of orthophosphate (PO_4^{3-}) groups, which gives stability to the structure.[9]

From a geological point of view, apatite is the most common phosphate mineral (mainly FAp and carbonated apatite, dahllite), and is the main source of the phosphorus utilised by plants. Nowadays, phosphorous is extracted from enormous deposits of apatite-rich rock. Thus, apatite is essential in the manufacture of phosphate fertilizers.

Non-stoichiometric, Ca-deficient HA is the main inorganic component of bone and teeth (Sections 2.1, 2.2). Biological interest in FAp, and more particularly solid solutions of FAp and HA, arises from the reduction in the incidence of dental caries observed in areas where water supplies are fluoridated (Section 2.2.3). Bone can also accumulate large amounts

[i] Taking into account the common impurities of natural apatite, its general chemical formula can be expressed as $A_{10}(BO_4)_6X_2$, where A = Ca^{2+}, Sr^{2+}, Ba^{2+}, Fe^{2+}, Pb^{2+}, Cd^{2+} and many rare earth elements; BO_4 = PO_4^{3-}, VO_4^{3-}, SiO_4^{4-}, AsO_4^{3-}, CO_3^{2-}; X = OH^-,Cl^-,F^-, CO_3^{2-}. Water exists in different forms.

of F^- ion (Section 2.1.1.2). ClAp, substituted- and non-stoichiometric-ClAp are of interest as model compounds for studying the crystal chemistry of apatites because single crystals are easily grown. Biological apatites also contain Cl^- ions (Section 2.1.1.2).

2.7.2. Hydroxyapatite

2.7.2.1. Crystal structure. Differences in surface reactivity.

The formula for hydroxyapatite[i] can be represented as $Ca_5(PO_4)_3(OH)$, but is usually written as $Ca_{10}(PO_4)_6(OH)_2$ to denote that the crystal unit cell comprises two molecules.

Chemically pure, stoichiometric HA crystallizes in the monoclinic space group $P2_1/b$ with lattice parameters $a = 9.4320$, $b = 2a$, $c = 6.8810$ Å , $\gamma = 120°$.[9] However, at temperatures above 250°C, there is a monoclinic to hexagonal phase transition in HA[9] (space group $P6_3/m$, bypiramidal hexagonal, $a = b = 9.4320$, $c = 6.8810$ Å, Fig. 2.24).[12] Some impurities, such as the partial substitution of hydroxide by fluoride or chloride anions, stabilize the hexagonal structure of HA at ambient temperature. For this reason, the very rare single crystals of natural HA always exhibit a hexagonal space group.[12] The hexagonal structure is the form encountered most frequently and involved in bone formation, because it allows for much easier exchange of OH^- groups with other anions, such as F^-, Cl^- and CO_3^{2-}. Therefore, we will focus on hexagonal HA (Fig. 2.24). However, from the thermodynamic aspect, the monoclinic form is more stable.[119]

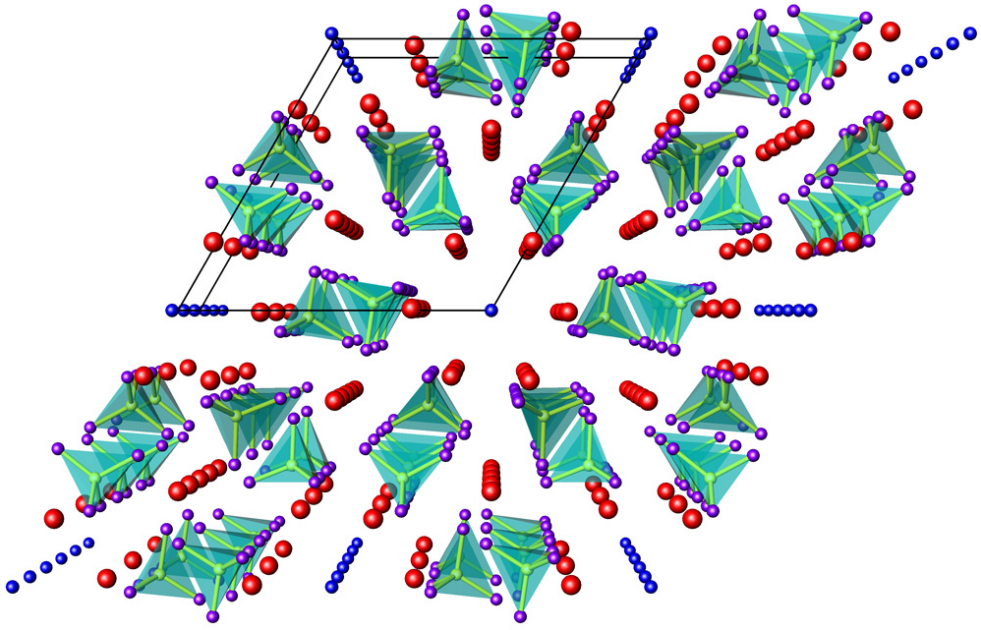

Fig. 2.24. Schematic representation of the hydroxyapatite $Ca_{10}(PO_4)_6(OH)_2$ structure along the [001] axis (hexagonal, a=9.4320 Å, c=6.8810 Å, space group $P6_3/m$ (No. 176)). Ca atoms: red, P atoms: yellow; O atoms belonging to PO_4 tetrahedra: violet; O atoms from hydroxyl groups: blue.

[i] The chemically correct name would be hydroxylapatite or hydroxidapatite, while hydroxyapatite is the common name employed by the medical and material communities.

In the monoclinic phase, the OHs occur in columns on the screw axis,[i] pointing upward and downward in alternate, nearest-neighbour dyads (Fig. 2.25). The hexagonal form of HA can be derived from the monoclinic form by allowing the OHs to become statistically disordered about the associated Ca ion triads, centred on the screw axis.

However, within the $P6_3/m$ space group, is not possible to simulate the hexagonal HA because of the non-physical duplication of each OH^- group by the *m* plane (Fig. 2.25). To avoid this situation, many studies on the HA hexagonal structure reduce the symmetry to a $P6_3$ space group that assumes only one OH^- group per Ca ion triangle.[119, 120] Within the $P6_3$ group, all the OH^- groups maintain the same alignment in each column within the HA structure (Fig. 2.25); other structural features remain very similar.

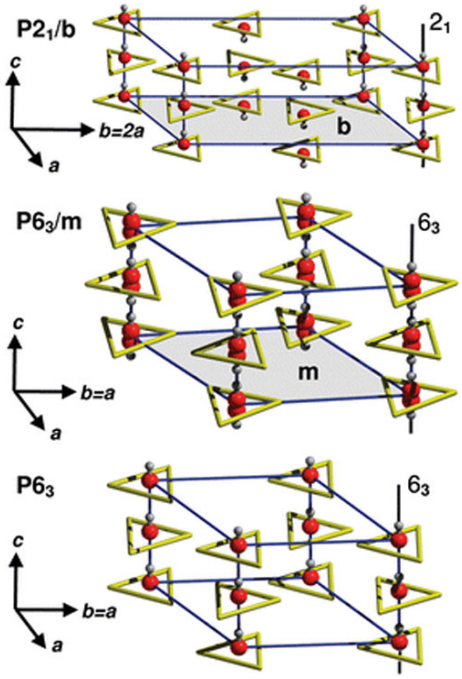

Fig. 2.25. Scheme showing the different HA structures: monoclinic $P2_1/b$ (top), experimental hexagonal $P6_3/m$ (middle) and theoretical adopted hexagonal $P6_3$ (bottom) unit cells. P, O and Ca atoms not relevant for the scheme have been omitted for clarity. Ca atoms are at the vertices of triangles around each hydroxyl group (after Corno *et al.*).[119]

The optimized structure of hexagonal $P6_3$ HA is characterized by two formula units per cell and contains 44 atoms per unit cell. As a consequence of lowering symmetry, there are three types of Ca ions inside the cell instead of two (as in the case of $P6_3/m$ space group), indicated by Ca1, Ca2 and Ca3, in which Ca1 has three oxygen atoms as first neighbours, Ca2 has six, and Ca3 has four. The OH^- group is linked to three Ca3 ions, which form an equilateral triangle in the *ab* plane with the hydroxyl in the centre (Fig. 2.25). Two ions of

[i] In crystallography, a screw axis is a symmetry operation describing how a combination of rotation about an axis and a translation parallel to that axis leaves a crystal unchanged.

type Ca1 and two of Ca2 are present in the cell and involved in an octahedral arrangement and, as for phosphates groups, there are six of them inside the unit cell, all equivalent for symmetry. Finally, there are two OH^- groups per cell, oriented in the same direction along the *c*-axis and defining internal channels.

HA crystal structure planes are differently charged. The basal plane[i] (or *c*-surface) is calcium-rich and therefore, positively charged; while the prismatic plane[ii] (or *a*-surface) is phosphate- and hydroxyl-rich and hence, negatively charged (Fig. 2.26).[120] Owing to this intrinsically different surface reactivity, HA exhibits selective adsorption of various ions, organic compounds and proteins, and can therefore be used in numerous chromatographic applications.[121]

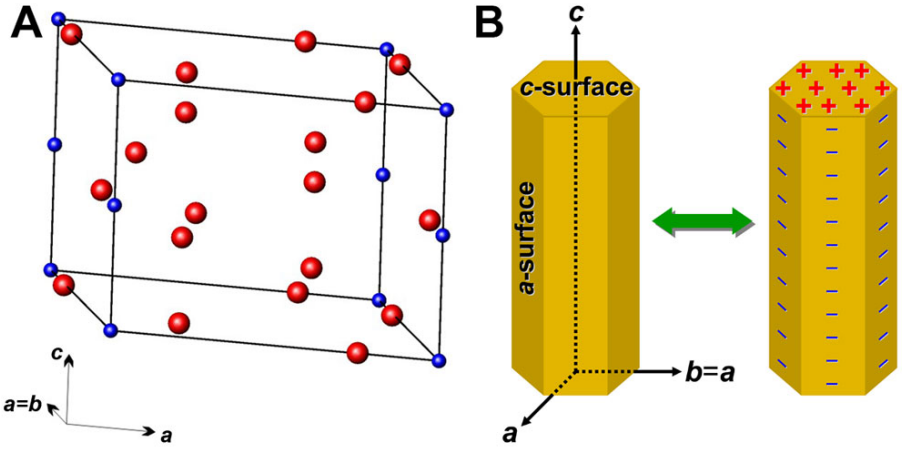

Fig. 2.26. A part of the crystal structure of the hexagonal HA is shown in (A), wherein PO_4 tetrahedra are omitted for clarity. A unit cell is shifted to (0; 0; ¼). (001) plane contains (1 + 4/2) Ca atoms and only 4/4 hydroxyls' oxygen atoms, hence having ratio Ca:O = 3:1, and therefore discussed surface will be charged positively. In contrast, (100) plane contains equal amounts of Ca and hydroxyl groups, (1 + 2/2) and (4/4 + 2/2), respectively. Additionally, Ca atoms are slightly shifted out of plane to ± 0.06 Å, resulting in the enrichment of (100) plane with hydroxyl and phosphate groups. Therefore this surface will be charged negatively. Schematic representation of HA crystal growing along *c*-axis is displayed in (B). Such crystal growth leads to the development of the negatively charged prism-faceted *a*-surface (*a*- and *b*-surfaces are equivalent).

2.7.2.2. Hydroxyapatite applications

Additionally to its wide uses in chromatography, synthetic HA is used nowadays in several other applications, *i.e.* as fertilizer,[122, 123] in catalysis[124], or as a way of effectively sequestering heavy metal species in contaminated soils and/or ground water.[125, 126] Also, HA is particularly important in medicine, and is widely used as a biomaterial in clinical

[i] It is the plane which is perpendicular to the *c*-axis of the hexagonal structure.
[ii] It is the plane which is parallel to the *c*-axis of the hexagonal structure.

applications such as a replacement material in bone repair and substitution, as a substrate for the development of scaffolds in bone tissue engineering, as a drug delivery system, *etc*. HA medical applications derive from the fact that it is chemically similar to the inorganic component of bones and teeth.

Nevertheless, as a result of functional irregularities, vertebrates can produce HA pathologically (ectopic calcification), resulting in the formation of renal and bile stones, calcifications of cartilages, basal ganglia, *etc.*[127] Hence, synthetic HA crystals can provide a unique tool towards understanding these biomineralization phenomena.[128]

In addition to it's peculiar physico-chemical and physiological properties, the material properties of HA such as: particle size, dimensional anisotropy, morphology, real microstructure, *etc*., are also of critical importance for its application and can be optimized. There are numerous applications in which material properties HA crystals play a significant role. For example, plate-like and fibrous HA particles exhibit enhanced adsorption properties due to the charging surface efficiency.[129] Also, it is well known that crystals with plate-like morphologies are the most effective in stiffening isotropic composite materials, followed by those of fibrous morphology, with the least effective geometry being spherical (Section 2.6.1).[98] From this we can conclude that HA crystals with the desired morphological features are candidates for the moderated reinforcement of biomaterials used in bone repair and substitution, such as calcium phosphate bone-cements, biocomposites, *etc.*[114, 130]

2.7.2.3. Overview of the synthetic routes to hydroxyapatite crystals

The first synthesis of apatite was that of Daubreé[131] in 1851 who obtained HA by passing phosphorus trichloride vapour over red hot lime.[i] Since then, interest in HA continued growing and already in 1951 the first review on methods for the preparation of HA was reported.[132]

Several approaches have been used to synthesize phase-pure, well-defined HA crystals with controlled materials properties. The techniques employed include, hydrothermal routes, molten salts syntheses, precipitation, and, to a lesser extent, growth in a gel system or liquid-solid-solution synthesis.[9, 111, 133-137] Depending upon the technique, materials with various morphologies, stoichiometries, sizes and levels of crystallinity can be obtained (Table 2.9).

[i] A naturally occurring mineral predominately composed of carbonates, oxides and hydroxides of calcium.

Of all the methods employed to synthesize HA crystals, hydrothermal is one of the most promising and convenient due to it's successful application for the one-pot synthesis of a desired phase under gentle reaction conditions.[111] Remarkably, hydrothermal technique is also well known as an efficient approach to synthesized defect-free single crystals of high crystallinity.[138] Because the reactions are solution-mediated, particle size and morphology can be controlled by experimental strategies that regulate nucleation, growth and aging processes.[138] The powder prepared by hydrothermal technique is highly pure and not agglomerated.

Hydrolysis of TCP, DCPA, DCPD or OCP requires low temperatures (usually below 100°C) and results in HA needles or blades in the micron range. However, in most cases, the hydrolysis product is highly non-stoichiometric (Ca/P ratio in the range of 1.50–1.71).[111]

Molten salts synthesis (a solid state reaction) usually give a stoichiometric and well-crystallized product, but they require relatively high temperatures and long heat-treatment times.[111, 134] Moreover, they incorporate K^+ ions from the reactants into the HA crystal lattice and show a sensitive dependence on the preparation conditions.[134]

In the case of precipitation, where the temperature does not exceed 100°C, nanocrystals are obtained. They have shapes of blades, needles, rods, or equiaxed particles. Their crystallinity and Ca/P ratio depend strongly upon the preparation conditions and are in many cases lower than that of well-crystallized stoichiometric HA.[9, 135]

HA fibres grown in the gel system do not have high mechanical strength. Additionally, they show a strong dependence on the synthesis conditions and their crystallinity and thermal stability are relatively inferior.[111, 136] Liquid-solid-solution syntheses are also dependent on the preparation conditions.[137]

Table 2.9. Preparation techniques for hydroxyapatite crystals.

Technique	Synthetic conditions	Comments
Hydrothermal[111]	Homogeneous precipitation using urea (85-95°C)	• High degree of crystallinity. • Ca/P ratio ~1.67. • Controlled morphology. • Controlled particle size (from nm to mm).
	Homogeneous precipitation using chelates (90-200°C)	• High degree of crystallinity. • Ca/P ratio ~1.67. • Controlled morphology. • Controlled particle size (from nm to mm).
Hydrolysis of calcium orthophosphates[111, 133]	≤ 100°C	• Needles or blades. • Micro-particles. • Ca/ P ratio ~ 1.50-1.71.
Molten salts synthesis[134]	850-1190°C	• Well crystallized product. • Ca/P ratio ~1.67. • Size of several micrometers. • Single crystals with hexagonal morphology. • Incorporation of K^+ to the crystal structure. • Requires high temperatures.
Precipitation[9, 135]	≤ 100°C	• Inhomogeneous nanocrystals. • Needles, blades or equiaxed particles. • Variable crystallinity and Ca/P ratio.
Gel system[111, 136]	Room temperature	• Polycrystalline crystals. • Sensitive dependence on the preparation condition. • Inferior thermal stability.
Liquid-solid-solution synthesis[137]	Use of templates (90-180°C)	• Sensitive dependence on the preparation condition. • Nanocrystals.

Hence, hydrothermal routes appear to be well suited for the development of an inexpensive synthesis method for crystalline HA, which focuses on precise control of particle size, morphology and chemical composition. For this reason, hydrothermal is nowadays the most commonly employed method to synthesize HA crystals.[111, 139] Fibres prepared by hydrothermal method have a more controlled and better morphology, and are more uniform in size, purity and composition compared to HA produced by other methods.[138]

Many research groups have prepared HA crystals with various morphologies by hydrothermal routes. In the majority approaches reported, the phase-pure HA products are commonly characterized by either rod-like[111, 136, 137] or plate-like[137, 140, 141] particle morphology. In addition, hydrothermally-produced HA powders have been reported to exhibit hexagonal prism-like,[129, 134, 142, 143] elliptical-like,[133, 144] or ribbon-like[145] particle shapes. Despite this variety of morphological features, all synthesized crystals growth along the *c*-axis of the hexagonal structure, the natural tendency of HA.

2.7.3. Hydrothermal approaches to hydroxyapatite crystals

2.7.3.1. Hydrothermal technique. Definition.

The term hydrothermal is purely of geological origin. It was first used by the British geologist Sir Roderick Murchison (1792–1871) to describe the action of water, at elevated temperature and pressure, in bringing about changes in the earth's crust leading to the formation of various rocks and minerals.[139] The largest single crystal formed in nature (beryl crystal of >1.000 kg) is of hydrothermal origin.

Hydrothermal processing can be defined as *any homogeneous (nanoparticles) or heterogeneous (bulk materials) reaction in the presence of aqueous solvents or mineralizers under high pressure and temperature conditions to dissolve and recrystallize materials that are relatively insoluble under ordinary conditions*.[139] Byrappa and Yoshimura define hydrothermal as *any homogeneous or heterogeneous chemical reaction in the presence of a solvent (whether or non-aqueous) above the room temperature and at pressure greater than one atmosphere in a closed system*.[138] However, chemists prefer to use the term *solvothermal* when these chemical reactions take place in the presence of organic solvents. There are several other terms like *glycothermal*, *alcothermal*, *ammonothermal*, *carbonothermal*, *etc.* used sometimes to further specify the employed non-aqueous solvent.

In hydrothermal, it is possible to work under supercritical fluid [i] conditions. Supercritical solvents (the most commonly used are H_2O or CO_2) are now regularly used to carry out a wide range of chemical reactions replacing organic solvents in a number of chemical processes, including nanoparticles fabrication, extraction, chemical manufacturing, waste treatment, recycling, *etc.*[139]

2.7.3.2. Hydrothermal method. Historical background[111, 138, 139]

In 1839, the German chemist R. W. Bunsen contained aqueous solutions in thick-walled glass tubes at temperatures above 200°C and at pressures above 100 bars. The crystals of barium carbonate and strontium carbonate that he grew under these conditions mark the first use of hydrothermal aqueous solvents as media. Another early report of the hydrothermal crystal growth was by E.T. Schafhäult, who in 1845 prepared fine particles of quartz in a Papin's digester.[ii] In 1905 G. Spezzia published reports on the growth of macroscopic crystals. By 1900 more than 150 mineral species had been synthesized by hydrothermal methods, including diamond. Commercial application of the hydrothermal technique began in 1908 when K.J. Bayer leached bauxite mineral under hydrothermal conditions to obtain aluminium. This opened up a new avenue for hydrothermal research in the area of metallurgy. This was subsequently followed by the synthesis of various minerals and, during the 1940s, bulk crystal growth, phase equilibria studies, *etc.*

The focus of hydrothermal technology in the earlier days was exclusively on the growth of bulk single crystals, since it was technologically important to produce big, pure and defect-free single crystals. The earliest material to be grown was quartz,[iii] followed by a wide range of mineral species in the bulk form such as ruby, corundum and various other silicates, carbonates, phosphates, sulphates, *etc.* Over 5.000 kg of quartz single crystal can be produced in one experimental run in a single large autoclave. So far no other crystal growth technique can match the size and quantity of quartz produced in a single experimental run using the hydrothermal technique.

Today much of the commercial production of bulk single crystals using hydrothermal technology is devoted to quartz, gems –*i.e.* emerald, corundum, ruby or alexandrite– and other

[i] A supercritical fluid is any substance at a temperature and pressure above its thermodynamic critical point.
[ii] The Papin's digester (also known as a steam or bone digester) is a high-pressure cooker invented by French physicist Denis Papin in 1679. It is a device for extracting fats from bones in a high-pressure steam environment, rendering them brittle enough to be easily ground into bone meal. It is the forerunner of the autoclave and the domestic pressure cooker.
[iii] With a melting point of 1670 °C and high chemical resistance, quartz crystals would be very difficult to form by either melt or flux techniques.

single crystals with commercial value. Additionally, nowadays hydrothermal method is regularly used for processing a wide range of materials not only as bulk crystals, but particles ranging from fine crystallites to nanoparticles with controlled size and morphology. Also, hydrothermal methods have proved to be extremely efficient both in the search for new compounds with specific physical properties and in the systematic physico-chemical investigation of intricate multicomponent systems at elevated temperatures and pressures.

2.7.3.3. Hydrothermal advantages in comparison with other conventional techniques

The aforementioned hydrothermal methods allow the synthesis of defect-free single crystals of high crystallinity and purity with controlled morphology and narrow particle size distribution. The reaction takes places under gentle conditions in one step. Additionally, this method offers several other advantages *cf.* other conventional techniques:[138]

i) compounds with elements in oxidation states that are difficult to obtain, can be synthesized in a closed system by hydrothermal methods (*i.e.*, ferromagnetic chromium(IV) oxide).
ii) it is useful for so-called low temperature phases, *i.e.* α-quartz.
iii) it is possible to synthesize metastable compounds, such as subiodides of tellurium, Te_2I.

Hydrothermal method has a range of other advantages such as: a high reaction rate for powders, homogenous dispersion in the liquid phase, almost pollution free, does not require very expensive and highly sophisticated equipment, energy saving processing and, in many cases, it is possible to produce new phases with no natural analogue inaccessible via other methods.[138] Also, since hydrothermal fluids offer higher diffusivity, lower viscosity, facilitate mass transport and higher dissolving power, reaction kinetics can be enhanced *cf.* conventional techniques.[139]

Table 2.10. Comparison of various powder synthesis methods.[139]

Parameter	Solid state reactions	Co-precipitation	Sol-gel	Hydrothermal
Cost	Low to moderate	Moderate	High	Moderate
Compositional control	Poor	Good	Excellent	Good/excellent
Morphology control	Poor	Moderate	Moderate	Good
Powder reactivity	Poor	Good	Good	Good
Purity (%)	<99.5	>99.5	>99.9	>99.5
Annealing step	Yes	Yes	Yes	No
Milling step	Yes	Yes	Yes	No

2.7.3.4. Principles of the crystal growth under hydrothermal conditions

The grow of a single crystal into the seed can proceed in two ways:[138]

- recrystallization of the solid substance, including its dissolution in the liquid phase, followed by convective[i] mass transfer of the dissolved part of the substance to the growth zone or seed.
- dissolution of the mixture of nutrient components with the help of their convective mass transport into the growth zone and interaction of the dissolved components of the seed surface.

The methodology of the growth of single crystals on a seed is the establishment of growth conditions in which the process is represented by the sum of macro- and micro-processes occurring between the interface boundary of the solution and the crystal. The composition and concentration of the solution, temperature and pressure, hydrodynamic conditions and surface contact of the phases are some of the basic physical and chemical parameters which determine the regime and rate of the dissolution of the nutrient, mass transport and the possibility of the formation of new phases.[138]

Typically, hydrothermal syntheses mainly result in the formation of the thermodynamically favourable product under certain conditions. However, kinetics also plays an important role. As an example, in the case of ZnO the presence of NH_4^+ ions in the solution produces a marked increase in the growth rate of the prismatic faces, which under ordinary conditions, does not exceed hundredths of a millimetre per day.[138]

2.7.3.5. Hydrothermal synthesis of hydroxyapatite crystals

Hydrothermal preparation techniques of HA crystals can be divided into two main groups (Table 2.9):

i) Methods using urea as precipitation agent[146-149]

ii) Methods using chelating agents[150-152]

Both techniques involve a homogeneous precipitation of the HA crystals with a slow reaction rate, a relatively easy procedure for obtaining uniform HA particles.

The first method is based on the thermally-induced decomposition of urea $(NH_2)_2CO$. Essentially, at the temperature range 80-95°C, $(NH_2)_2CO$ smoothly decomposes to form carbon dioxide and aqueous ammonia species according to the Eq. 2.6 and 2.7:

[i] Convective transport occurs when a constituent of the fluid (mass, energy, a component in a mixture) is carried along with the fluid. The flux is determined by its concentration and the fluid velocity.

$$CO(NH_2)_{2(aq)} \xrightarrow{T\geq 80^\circ C} NH^+_{4(aq)} + CON^-_{(aq)} \qquad (2.6)$$

$$CON^-_{(aq)} + 3H_2O \rightarrow NH^+_{4(aq)} + 2OH^-_{(aq)} + CO_{2(g)} \qquad (2.7)$$

In turn, the $NH_{3(aq)}$ released *in situ* generates a gradual increase of the reaction solution pH to the values at which HA is the more thermodynamically stable (less-soluble) calcium orthophosphate compound, and is thus formed (Fig. 2.18).[53] Upon heating a urea solution, the change in pH will be uniform throughout if the temperature is the same and no local excess of the reagent exist at any point. Consequently, HA precipitates slowly and uniformly throughout the solution. Additionally, because urea is very soluble in water and its rate of decomposition –relatively slow– is dependent upon the temperature and duration of heating, good control of the solution pH is possible.[153] Also, since no urea decomposition takes place below 80°C, the generation of NH_3 can be halted at any time by simply cooling the system.[153]

In the second method, ethylenediaminetetraacetic acid, lactic acid or citric acid are used as chelating agents. During the heat treatment, the chelated Ca^{2+} complexes generated by these agents decompose at elevated temperatures (T ~ 90-200°C). Hence, Ca^{2+} is slowly released to the medium and reacts with PO_4^{3-} ions to produce, at the appropriate pH, HA.[111] In isothermal conditions the Ca^{2+} complexes will decompose homogeneously throughout the system and HA will precipitate uniformly in the solution.

2.8.- OBJECTIVES AND STRATEGIES

2.8.1. Research objectives

As it follows from the current state of the art described above, calcium phosphate bone-cements are among of the most promising class of biomaterials for bone repair and substitution. Consequently, **one of the main tasks of the current work is to prepare bioactive calcium phosphate bone-cement**, which sets within 10-30 minutes and exhibits rapid conversion to hydroxyapatite as a final product.

The second main objective of the work is to develop a facile hydrothermal route to hydroxyapatite powders for use in reinforcement applications. By varying the synthesis conditions, defect-free hydroxyapatite single crystals with controlled particle morphology should be synthesized.

Obtained advanced cement and hydroxyapatite crystals are expected to be crystalline solids and should be comprehensively characterised with **the main objective of determining**

their structure, composition and physico-chemical properties. Various techniques ranging from convenient powder X-ray diffraction to nano-indentation probing should be used for that.

A consequent research direction should be towards reinforcement of the advanced calcium phosphate bone-cement using the hydroxyapatite crystals **to explore new family of reinforced biocomposite cements**.

Finally, by judicious tailoring of the shape, size and volume fraction of the hydroxyapatite reinforcement crystals, **new functional biomaterials with enhanced mechanical, biological and physiological properties should be discovered**.

2.8.2. Research strategies

2.8.2.1. Calcium phosphate bone-cement

Dicalcium phosphate dihydrate (DCPD) and tetracalcium phosphate (TTCP) were selected as precursors for the preparation of the CPC, since they react to from hydroxyapatite as final product and their invariant point ~8.5 pH is close to the physiological pH. Decreasing of CPC precursors' crystal sizes *via* mechanochemical grinding was the selected strategy to accelerate cement setting and conversion rates, since it has been observed that increasing the saturation of the liquid phase using a phosphate-containing liquid phase demonstrates some limitations. Specifically, this preparative technique is limited owing to the incorporation of foreign ions into the crystal lattice of the end product. Additionally, such CPC systems have an excess of non-participant reactive ions and the low or high initial pH of the mixture is also prone to forming intermediate phases. These effects can create biocompatibility problems with as-prepared CPCs as well as slow their conversion rate. In contrast, finer ball-milled DCPD and TTCP powders exhibit a high dissolution rate and, accordingly, facilitate the rate of CPC setting reactions.

2.8.2.2. Hydroxyapatite crystals

Hydrothermal technique was the selected approach to synthesize hydroxyapatite crystals due to it successful application for the one-pot synthesis of a desired phase under gentle reaction conditions. The hydrothermal method with water as solvent at elevated temperatures is environmentally benign because the reactions are carried out in a closed system and the contents can be recovered and reused after reaction. Remarkably, hydrothermal technique is also well known as an efficient approach to synthesized defect-free single crystals of high crystallinity with relatively narrow particles size distribution and distinct morphological features.

Hydroxyapatite crystals with different morphological features were synthesized *via* direct hydrothermal reaction between calcium nitrate tetrahydrate and diammonium hydrogen phosphate, using urea as a homogeneous precipitation agent. Urea decomposes uniformly in the low temperature range of 80-95°C releasing $NH_{3(aq)}$ to the medium, which in turn increases the pH to values at which HA becomes less-soluble, and thus, precipitates. Urea is very soluble in water and it's thermal decomposition kinetics are dependent upon the temperature and duration of heating. Therefore, by judicious variation of the hydrothermal treatment conditions it was possible to control the pH of the reaction solution, and consequently, generate HA single crystals with various controlled particle morphologies.

2.8.2.3. Biocomposites

In order to generate a family of reinforced biocomposite cements, the produced optimal calcium phosphate bone-cement was reinforced *via* physical linking by HA single crystals, a bioactive filler. The idea behind was that the presence of a mechanically strong filler (HA crystals) can prevent possible crack propagation as well as comprehensively enhance the mechanical performance of these biocomposites; being extremely important steps in the development of new biomaterials for bone repair and substitution. The influence of the shape, size and volume fraction of the hydroxyapatite reinforcement crystals on the mechanical properties of the respective biocomposite cements was thoroughly investigated and optimized to give a functional biomaterial.

III

MATERIALS AND METHODS

3.1.- STARTING MATERIALS

- Acellular simulated body fluid solution (SBF) having pH 7.25. Prepared according to Kokubo *et al*.;[154]
- Acetone (CH_3COCH_3, SC grade, Wako);
- Benzoylperoxid (for synthesis, 25% H_2O, Merck);
- Calcium carbonate ($CaCO_3$, 98.0% Wako);
- Calcium dihydrogenphosphate monohydrate ($Ca(H_2PO_4)_2 \cdot H_2O$, 90.0% Kanto);
- Calcium hydrogenphosphate ($CaHPO_4$, 98.0% Wako);
- Calcium nitrate tetrahydrate ($Ca(NO_3)_2 \cdot 4H_2O$, 98.5% Wako);
- Diammonium hydrogen phosphate ($(NH_4)_2HPO_4$, 99.0% Wako);
- Distilled water
- Isopropanol ($CH_3CH_2(OH)CH_3$, 99.5% anhydrous, Sigma-Aldrich);
- Methylmethacrylate (99% Merck);
- Nitric acid (HNO_3, 63% Wako);
- Nonylphenylpolyethylenglycol acetate (for synthesis, Fluka);
- Potassium bromide (KBr, for IR, Wako);
- Sodium hexametaphosphate ($(NaPO_3)_n \cdot Na_2O$, 96% Aldrich);
- Urea ($(NH_2)_2CO$, 99.0% Wako).

3.2.- CHARACTERIZATION METHODS

3.2.1. Powder X-ray diffraction

The structure and composition of the products were characterized by powder X-ray diffraction (XRD) using a Rigaku RINT 2000 diffractometer with Ni-filtered CuK_α radiation (λ = 1.54178 Å), operating at 200 mA and 50 kV. Data were collected in the 2θ range of 3º to 80º, with a scan speed of 1º/min and a step width of 0.02º. Processing of X-ray diffraction data was performed using the STOE powder diffraction software package[155] WinX^{POW} and the phases were identified by comparison with the data reported in the Joint Committee of Powder Diffraction Standards (JCPDS) database.

XRD analysis was also applied in order to investigate the conversion rate of the fastest setting DCPD/TTCP-based CPC to HA. For this purpose, CPC was prepared from equimolar amounts of ball-milled DCPD and TTCP powders (total 0.6 g) using 0.3 mL of distilled water as a liquid phase (S/L ratio: 2 g/mL). The resultant putty-like paste was rapidly shaped into a

rod, divided into several pieces and allowed to set for 1 hour. Each piece was separately incubated in distilled water at 37°C for a specific period of time. Immediately prior to the XRD analysis, the CPC test sample was very quickly ground in warm acetone using a hot agate mortar and pestle (80°C), in order to remove the rest of the water and, to some extent, suspend the reaction process. Diffraction patterns were collected in the 2θ range of 8º to 38º, with a scan speed of 4º/min. All rest of the XRD experimental parameters were maintained the same as in the case of the XRD analysis described above. The conversion of CPC precursors to HA was roughly estimated by employing a technique reported by Fukase *et al.*[156] and improved by Ishikawa and co-workers.[88] Simply put, this approach is based on the fact that the intensity diffracted by a crystalline phase is essentially proportional to the quantity of the diffracting compound. Although this technique is found to be a reasonable and valid method for the rough estimation of CPC conversion, it is not very accurate owing to the line broadening effect and low intensities distinctive for apatite CPC systems.

The extents of the cement setting reactions ($\%_{conv}$) were calculated according to Eq. 3.1:[88]

$$\%_{conv} = \frac{\dfrac{I_{HA(t)}}{I_{HA(\infty)}} + \dfrac{1-(I_{DCPD(t)}/I_{DCPD(0)})+1-(I_{TTCP(t)}-I_{TTCP(0)})}{2}}{2} \times 100 \qquad \textbf{(3.1)}$$

where $I_{HA(t)}$, $I_{DCPD(t)}$ and $I_{TTCP(t)}$ are intensity values of the (002) diffraction peak of HA (JCPDS No. 72-1243), the sum of the intensities of the (020) and (021) diffraction peaks of DCPD (JCPDS No. 9-77) and the sum of the intensities of the (013) and (040) diffraction peaks of TTCP (JCPDS No. 70-1379), respectively, at specific times of setting reaction t = 0.5, 1, 2, 3, 4, 5, 6, 7, or 8 hours. $I_{DCPD(0)}$ and $I_{TTCP(0)}$ are intensity values of the same characteristic diffraction peaks from DCPD and TTCP, respectively, but for the unreacted CPC specimen at the starting time (t = 0). Since the dissolution-precipitation reaction between the fastest setting combination of CPC precursors resulted in phase-pure HA already after 6 hours and no significant product advantages were observed from longer reaction times, the value $I_{HA(\infty)}$ –peak intensity of HA in the fully converted CPC– can be consistently chosen as the intensity of the (002) diffraction peak of HA at t = 8 hours. In a typical data processing step, firstly the background was removed from each XRD spectrum using the PeakFit software program and then the resulting I data (three replicates) were averaged. All used diffraction peaks were free of overlapping.

3.2.2. Spectroscopic product analyses

3.2.2.1 Energy-disperse X-ray spectroscopy

Energy-dispersive X-ray spectroscopy investigations (EDX) for semiquantitative Ca and P content determination were performed with EDAX DX-95 spectrometry system using commercial hydroxyapatite powder (HW-003, Mitsubishi Chemicals) as a standard sample (molar ratio Ca/P = 1.67).

3.2.2.2 Diffuse reflectance infrared Fourier-transform spectroscopy

The room temperature diffuse reflectance infrared (IR) Fourier-transform spectra were recorded on a Jeol JIR-7000 spectrometer with a resolution of 4 cm^{-1} and a number of scans 100. The crystalline products (~4 mg) were thoroughly ground with potassium bromide powder (~200 mg) in an agate mortar and pestle to give a fine mixture and subjected to IR analysis. For the background spectrum, a finely ground KBr powder was used.

3.2.2.3 Raman scattering

The room temperature Raman scattering measurements were carried out on a confocal Raman microscope WITEC CRM200 with linear polarized laser light (λ = 532 nm) as the excitation source. The laser beam was focussed on the sample surfaces with the aid of an optical microscope unit equipped with a Nikon 10x objective and numerical aperture of 0.25.

3.2.3. Electron microscopy product analyses

3.2.3.1 Scanning electron microscopy

The morphology was studied by scanning electron microscopy (SEM) and field-emission environmental scanning electron microscopy (FE-ESEM) using Hitachi S-4500 and FEI Quanta 600F microscopes operating at 15 and 5 kV, respectively.

3.2.3.2 Transmission electron microscopy

The fine microstructure and phase purity of the samples were investigated by transmission electron microscopy (TEM), electron diffraction (ED) and high-resolution TEM (HRTEM) using Hitachi H-8100 and Jeol 4000EX microscopes operating at 200 and 400 kV, respectively. The samples for TEM were crushed or dispersed in methanol and deposited on a carbon mesh grid. Computer-simulated HRTEM images for different defocus and different thickness were obtained using the Mac Tempas and Crystal Kit software programs.

3.2.4. Particle size distribution estimation

Average particle sizes and particle size distributions (PSD) of the raw DCPD and TTCP powders were determined using sedimentation analysis on a Micrometrics SediGraph 5100 particle size analyser. For the measurement, 2 g of the test sample was dispersed by vigorous stirring for 2 hours in 50 mL of 0.075% aqueous solution of sodium hexametaphosphate (dispersant).

Particle size characteristics of the ball-milled DCPD and TTCP samples were monitored using dynamic light-scattering (DLS) technique on a Malvern Instruments Zetasizer Nano-ZS (λ = 633 nm, 3 runs, run duration of 10 seconds). For DLS measurements, a small amount of the powder was fully dispersed in water using high-power ultrasonication and subjected to the DLS analysis.

3.2.5. Thermo-gravimetric and differential thermal analyses

Thermo-gravimetric and differential thermal analyses (TGA/DTA) were performed using a Mac Science Type-2020 TG-DTA thermoanalyser. The heating profile was a 10°C/min linear ramp from room temperature to desired temperature usually 1300°C. Measurements were realized in a static air atmosphere using platinum crucibles and alumina powder as reference material.

3.2.6. Elemental analysis

Carbon content was determined quantitatively by combustion bulk elemental analysis using a Fisons EA 1108 elemental analyzer. In this technique, a sample is burned in an excess of oxygen, and the weight of traps collect carbon dioxide is used to calculate carbon content.

3.2.7. Porosity evaluation

3.2.7.1 Adsorption-desorption of nitrogen

Nitrogen adsorption-desorption measurements were performed at liquid nitrogen temperature on a Quantachrome Autosorb-1 automated gas sorption system. Prior to measurement, the samples were outgassed in vacuum at 150°C for 2 hours. Total surface area was calculated according to the multipoint Brunauer-Emmett-Teller method (BET). Pore volumes and size distributions were determined by the Barrett-Joyner-Halenda method (BJH).

3.2.7.2 Mercury porosimetry

Porosity was also evaluated by mercury porosimetry in a Micromeritics AutoPore II 9220 porosimeter. Prior to analysis, the samples were degassed at 0.001 psia to remove physisorbed gases. The penetrometer was filled with mercury and the low pressure analysis started at 1.5 psia and terminated at 15 psia. The penetrometer was then transferred to the high pressure chamber and the analysis with mercury intrusion (15-60000 psia) followed by mercury extrusion (60000-15 psia) was conducted.

3.2.8. pH measurements

The pH measurements were carried out using a Mettler Toledo InLab®413 SG pH-meter with combination polymer electrode. Prior to each measurement, the pH-meter was calibrated with the standard buffer solutions pH = 6.86 and pH = 4.01 (Wako).

For the CPCs samples, 1 g of the CPC powder was mixed with 20 mL of distilled water under vigorous stirring for 5 seconds, and then the pH of the suspension was monitored every 30 seconds with continuous stirring.

3.2.9. Final setting time determination

Final setting time (ST) of the as-prepared cements was determined according to the American Dental Association specification No. 9. For this purpose, equimolar amounts of ball-milled DCPD and TTCP powders (total 0.6 g) were thoroughly mixed in an agate mortar and pestle and placed inside a latex finger cot. After this, an appropriate amount of distilled water (0.3 mL) was added to the mixed powders using a micropipette. The used solid to liquid (S/L) ratio was 2 g/mL. This mixture was hand kneaded for 1 min and the resultant putty-like material was placed inside a polytetraflouroethylene (PTFE) mold of 6 mm diameter and 3 mm deep.

The Vicat needle technique (Fig. 3.1) was used to determinate the final setting time (Section 2.5.2). ST was considered to be reached when the tested CPC specimen bore the weight of the Vicat needle (weight = 453.6 ± 0.5 g, tip diameter = 1.06 ± 0.05 mm) without appreciable indentation on the surface. All values are the average of at least six replicates.

Fig. 3.1. Vicat needle tool used for the estimation of the ST of the CPCs.

3.2.10. In vitro test

In vitro test was performed in the optimal CPC in order to investigate its bioactivity. Bioactivity studies were carried out using an acellular simulated body fluid (SBF) solution reported by Kokubo *et al.*[154] SBF is almost identical to human blood plasma in terms of its ion concentrations, but it does not contain organic substances such as proteins (Table 3.1).

Table 3.1. Ions concentration at human blood plasma and employed SBF.

	Ions concentration, mM						
	Na^+	K^+	Mg^{2+}	Ca^{2+}	Cl^-	HCO_3^{2-}	PO_4^{2-}
Human blood plasma[157]	142.0	5.0	1.5	2.5	103.0	27.0	1.0
SBF	142.0	5.0	1.5	2.5	148.8	4.2	1.0

Nevertheless, the soaking of bioactive materials in SBF can reproduce the apatite formation seen on such materials in the living body. Therefore, it is a useful tool for evaluating the bone-bonding bioactivity of materials by simply examining the ability of apatite to form on the surface of these materials (Section 2.3.3.3).[158]

The specimens, in the form of pellets, were prepared, as for the ST determination, by mixing equimolar amounts of the ball-milled DCPD and TTCP powders (total 0.2 g) with 0.067 mL of distilled water (S/L ratio: 3 g/mL). The mixture was kneaded by hand in a latex finger cot for 1 minute and the resulting putty-like material was placed into a cylindrical mold assembly of 6.9 mm diameter. The sample was pressed under 5.3 MPa (20 Kg/cm^2) for 1 minute using a pressure-loading device. The specimen was removed from the mold and kept

for 1 hour at ambient conditions to set. The test samples were then placed into a polystyrene bottle (V = 5.7 mL) previously washed with 1M HCl and water, filled with 3 mL of SBF and incubated at 37°C. The polystyrene bottle and SBF solution were refreshed every 3 days. After soaking for 3, 7 and 10 days, the CPC specimens were collected, their surfaces were washed with acetone and finally dried in ambient conditions before further analysis. The *in vitro* tested samples were studied by XRD, IR, TGA/DTA and SEM characterization techniques in order to investigate the formation of hydroxyapatite on their surfaces.

3.2.11. Mechanical properties measurements

3.2.11.1 Compressive strength testing

For the compressive strength (CS) measurements, the CPC specimens were prepared in a similar manner as in the case of *in vitro* test, the difference being that three times more TTCP and DCPC precursors were used (S/L ratio: 3 g/mL), resulting in the specimen with an aspect ratio of 2. It has to be noted here that the applied pressure may not be applicable for clinical practice, but in the current study it was selected with the aim of obtaining reproducible results in a well-defined and systematic way for comparison purposes.

Biocomposite pellets were prepared in a similar way. In a typical procedure, equimolar amounts of ball-milled DCPD and TTCP powders were thoroughly ground together using an agate mortar and pestle. Next, the desired amount of HA crystals with various morphology were well-dispersed using a hand spatula in the CPC precursors mixture, followed by gentle mixing in an agate mortar. The resulting fine powder (total 0.6 g) was placed inside a latex finger cot and an appropriate amount of distilled water was added to the composite CPC precursor using a micropipette. This amount of liquid phase was calculated to maintain a solid to liquid (S/L) ratio of 2, on the basis of the DCPD and TTCP cement precursors, with the reinforced phase being not considered. The mixture was hand kneaded for 1 minute and then placed into a cylindrical mold assembly of 6.9 mm diameter. The batch was pressed under 5.3 MPa (20 Kg/cm^2) for 1 min using a pressure-loading device. After pressing, the biocomposite specimen was removed from the mold and kept for 1 h at ambient conditions to set before being incubated in acellular simulated body fluid solution at human body temperature of 37°C for 23 hours.

Furthermore, the samples were placed into a polystyrene bottle (V = 5.7 mL) filled with 3 mL of simulated body fluid solution (SBF) and incubated at 37°C for 23 hours. Finally, the wet specimens were subjected to compressive strength measurements on a Universal Testing Machine (Shimadzu Autograph AG-I) with a crosshead speed of 0.5 mm/min until

fracture. The compressive strength value was determined as the critical force divided by the loaded area. All values are the average of at least six replicates.

3.2.11.2. Nano-indentation measurements

The hardness (H) and elastic modulus (E_s) of the optimal CPC specimen were probed at the sub-micro/micro level by means of the nano-indentation technique. E_s is a measure of the inherent material stiffness –material resistance against suffer permanent deformations (elastic) by an applied force, while H is related with the material resistance to various kinds of shape change when a force is applied, and thus, related to plastic deformation.

Experiments were performed on a Hysitron TriboScan UBI-1 nanohardness tester in conjunction with a Digital Instruments Nanoscope III atomic force microscope (AFM). A Berkovich diamond indenter tip with regular triangle pyramid geometry and nominal radius of 300 nm was used.

The system calibration and data evaluation were performed using the method of Oliver and Pharr.[159] Thermal drift is corrected in the Hysitron TriboScan software by automatically measuring the drift for up to 20 seconds before starting each indent. The reduced indentation modulus (E_r) and the hardness were calculated from the load-displacement curve according to the Eq. 3.2 and 3.3, respectively:

$$E_r = \frac{\sqrt{\pi}}{2}\frac{S}{\sqrt{A(h_C)}} \qquad \textbf{(3.2)}$$

$$H = \frac{P_{\max}}{A(h_C)} \qquad \textbf{(3.3)}$$

where S is the slope of the fitted unloading curve at the point of initial unloading (20%-95% of the unloading curve was used for fitting); $P_{\max}$ is the peak load and $A(h_C)$ is the projected contact area at the peak load –*i.e.* area of the indentation at the contact depth of the residual indentation h_C (Fig. 3.2).

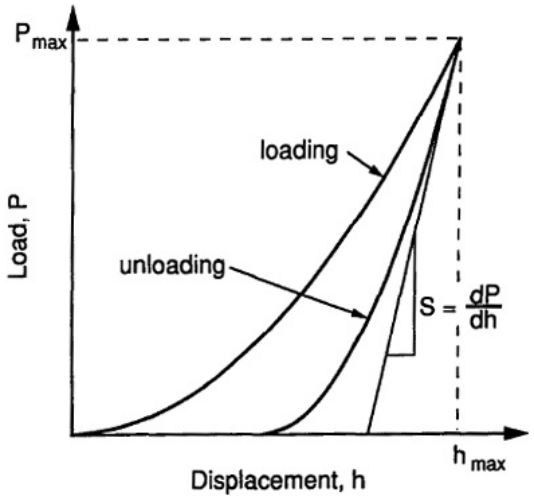

Fig. 3.2. Schematic illustration of an indentation load *vs.* displacement plot showing quantities used to determine the reduced indentation modulus and hardness from the obtained curve.

The reduced modulus (E_r) is related to the elastic modulus (E_s) of the test specimen through the Eq. 3.4:

$$\frac{1}{E_r} = \frac{(1-\nu_i^2)}{E_i} + \frac{(1-\nu_s^2)}{E_s} \qquad \textbf{(3.4)}$$

where ν_i is the Poisson's ratio for the diamond tip (0.07),[160] ν_s is the Poisson's ratio for synthetic HA (0.28)[161] and E_i is the diamond elastic modulus (1141 GPa).[160]

Two loading functions were employed:

(i) Peak load of 1 mN, loading rate of 0.2 mN/s, holding time 60 seconds, unloading to 0.05 mN with rate of 0.2 mN/s, holding 20 seconds at 0.05 mN and unloading back to 0 mN with rate of 0.5 mN/s;

(ii) Peak load of 5 mN, loading rate of 1 mN/s, holding time 60 seconds, unloading to 1 mN with rate of 0.4 mN/s, holding at 1 mN for 20 seconds and unloading back to 0 mN with rate of 0.5 mN/s.

The first loading function was used to probe E_s and H in HA single crystals with hexagonal prism-like particle morphology (Chapter V). The second one was employed for nano-indentation testing of CPCs (Chapter IV) and biocomposites (Chapter VI) systems. One hundred fifty indents were randomly performed in order to obtain average values for CPC' and composites' E_s and H.

For the nano-indentation test on the optimal CPC and composites (optimal CPC reinforced by 10 wt.-% and 15 wt.-% of fine-plate and hexagonal HA crystals respectively), a pellet was prepared in a similar manner as for the CS investigation. Then, the specimen was

embedded in a solution formed by 77.0 wt.-% of methylmethacrylate and the polymerization initiators –1.4 wt.-% of benzoylperoxid and 21.6 wt.-% of nonylphenylpolyethylenglycol acetate. In order to fill up the pores in the CPC pellet, a slow polymerization of methylmethacrylate to polymethylmethacrylate at a moderated low temperature profiles [(39°C, 12 h) → (48°C, 12 h) → (55°C, 12 h)] was performed. Then, the section for nano-indentation was cut in parallel to the pellet base, polished by a set of abrasive papers of decreasing size of grit followed by polishing with 1 μm diamond powder suspended in water and subjected to nano-indentation test.

IV

PREPARATION OF CALCIUM PHOSPHATE BONE-CEMENTS

4.1.- EXPERIMENTAL PART

4.1.1. Synthesis of dicalcium phosphate dihydrate

Dicalcium phosphate dihydrate powder (DCPD, $CaHPO_4 \cdot 2H_2O$) was prepared by a precipitation reaction according to Eq. 4.1:[162]

$$Ca(H_2PO_4)_2 \cdot H_2O_{(s)} + CaCO_{3(s)} + 2H_2O_{(aq)} \xrightarrow{25°C} 2CaHPO_4 \cdot 2H_2O_{(s)} + CO_{2(g)} \quad \textbf{(4.1)}$$

Typically, $CaCO_3$ (0.25 mol) was slowly added under vigorous stirring to a suspension of $Ca(H_2PO_4)_2 \cdot H_2O$ (0.25 mol) in 850 mL of distilled water. After complete mixing, the resultant suspension was stirred for a further 15 minutes. The product of the precipitation reaction was collected by vacuum filtration, washed once with distilled water and twice with acetone. The as-produced white DCPD powder –sample **D-raw**– was dried under ambient conditions and stored in a refrigerator in order to avoid dehydratation.

4.1.2. Synthesis of tetracalcium phosphate

Tetracalcium phosphate (TTCP, $Ca_4(PO_4)_2O$) powder was prepared from $CaCO_3$ and $CaHPO_4$ by solid-state reaction according to Eq. 4.2:[163]

$$2CaCO_{3(s)} + 2CaHPO_{4(s)} \xrightarrow{1500°C,6h} Ca_4(PO_4)_2O_{(s)} + 2CO_{2(g)} + H_2O_{(g)} \quad \textbf{(4.2)}$$

Briefly, stoichiometric amounts of reactants (each 0.043 mol) were weighed and thoroughly ground using an agate mortar and pestle to increase homogeneity. The resulting powder was placed into a platinum crucible (Fig. 4.1). The crucible was placed into a high temperature lift furnace (SPM-6512 Electric Furnace, Marusho Electro-Heat Co., Ltd.) and heated at 1500°C. The treatment involved a 2 hours ramping up to the final temperature and holding at this level for 6 hours. After the heat treatment, the product was air-quenched in order to avoid partial hydrolysis of TTCP during the cooling process.[164] The as-synthesized slightly green TTCP powder –sample **T-raw**– was thoroughly ground in an agate mortar and pestle and finally stored in a moisture-free desiccator.

Fig. 4.1. Images of the platinum crucible before (A) and after (B) a high temperature solid-state reaction of TTCP synthesis showing the shrinkage of the precursors' mixture.

4.1.3. Mechanochemical grinding

In order to decrease the grain sizes of as-derived DCPD and TTCP, the powders were subjected to a wet rolling ball-mill process utilizing a 5 wt.-% silica-doped alumina pot (V = 300 mL). For DCPD milling, distilled water was used as the wet grinding medium, while in case of TTCP, anhydrous isopropanol was chosen in order to prevent hydrolysis of TTCP to hydroxyapatite.[9] To tailor the grain sizes of TTCP and DCPD in the course of mechanochemical process, three different ball sizes were used; namely, zirconia balls with diameters of 9.6 and 4.8 mm and silicon nitride balls with diameters of 3.6 mm (Table 4.1).

In a typical ball-milling procedure, one third of the pot was filled with the selected type of balls. Then, 15 g of the DCPD or TTCP was placed inside the pot together with 60 mL of the desired liquid. The ball-milling was performed at 135 rpm for 24 hours. The resulting DCPD suspension was vacuum filtrated, washed twice with acetone, dried at the ambient conditions, ground and stored in a refrigerator. The obtained TTCP slurry was also vacuum filtrated, but dried at 80°C for 6 h in air, ground and stored in a moisture-free desiccator.

Table 4.1. Comparison of the grinding media specifications. A 5 wt.-% silica-doped alumina pot (V = 300 mL) was used for a wet rolling ball-mill process at 135 rpm for 24 hours.

No.	Balls' material	Number used for grinding	Balls' Diameter (mm)	Specific gravity	Vickers hardness HV (kgf/mm^2)
1	High Purity ZrO_2	215	9.6	6.0	1280
2	High Purity ZrO_2	1730	4.8	6.0	1280
3	Si_3N_4	4100	3.6	3.2	1400-1500
Balls' view					
					

4.1.4. Preparation of the bone cements

Calcium phosphate bone-cement (CPC) was synthesized by the dissolution-precipitation reaction between DCPD and TTCP according to Eq. 4.3.[165] Normally, this reaction results in the formation of Ca-deficient HA as the end product.[85, 166, 167]

$$2CaHPO_4 \cdot 2H_2O_{(s)} + 2Ca_4(PO_4)_2O_{(s)} \xrightarrow{H_2O} Ca_{10}(PO_4)_6(OH)_{2(s)} + 4H_2O_{(aq)} \qquad \textbf{(4.3)}$$

In a typical procedure, equimolar amounts of ball-milled DCPD and TTCP powders (total 0.6 g) were thoroughly mixed in an agate mortar and pestle and placed inside a latex finger cot. After this, an appropriate amount of distilled water (0.3 mL) was added to the mixed powders using a micropipette. The used solid to liquid (S/L) ratio was 2 g/mL. This mixture was hand kneaded for 1 minute and the resultant putty-like material (Fig. 4.2) was rod-shaped, allowed to set for 1 hour (if applicable) and finally incubated for the desired period of time in distilled water or in acellular simulated body fluid solution at human body temperature of 37°C.

Fig. 4.2. Putty-like CPC paste.

Throughout this work, a set of acronyms is used (Tables 4.2, 4.3). The first letter indicates the desired **D**CPD, **T**TCP or **C**PC (**D**, **T** or **C**) while the number indicates the size of the balls (multiplied by 10 for clarity, *i.e.* **36**, **48** and **96** instead of 3.6, 4.8 and 9.6 mm), utilized for mechanochemical grinding.

4.2.- RESULTS

4.2.1. DCPD and TTCP products analysis

The summary of the phase compositions and crystal sizes of the raw and ball-milled CPC precursors are presented in Table 4.2. Raw DCPD is produced from $Ca(H_2PO_4)_2{\cdot}H_2O$ and $CaCO_3$ by a precipitation reaction (Eq. 4.1), while raw TTCP is synthesized from $CaCO_3$ and $CaHPO_4$ by a high temperature solid-state reaction (Eq. 4.2) followed by air-quenching. According to the phase analysis data, these preparation routes lead to the formation of the phase-pure monoclinic DCPD and TTCP, respectively (Fig. 4.3A, 4.4A).

Table 4.2. Comparison of the phase compositions and average crystal sizes of the CPC precursors that were mechanochemically-derived using balls of three different diameters.

Sample	XRD phase composition [a]	Balls' diameter (mm) [b]	Average crystal size (μm) [c]	FWHM (μm) [d]
D-raw	DCPD	—	5.96 [e]	—
D-96	DCPD	9.6	3.66	1.72
D-48	DCPD	4.8	1.69	0.52
D-36	DCPD	3.6	1.13	0.41
T-raw	TTCP	—	6.79 [e]	—
T-96	TTCP	9.6	2.96	1.11
T-48	TTCP	4.8	1.52	0.61
T-36	TTCP	3.6	1.33	0.51

[a] References: JCPDS card numbers 9-77 and 70-1379 for DCPD and TTCP, respectively.
[b] Ball-milling was performed at 135 rpm for 24 hours.
[c] DLS analysis results.
[d] Full width at half maximum of the PSD data estimated by DLS analysis.
[e] Sedimentation analysis results.

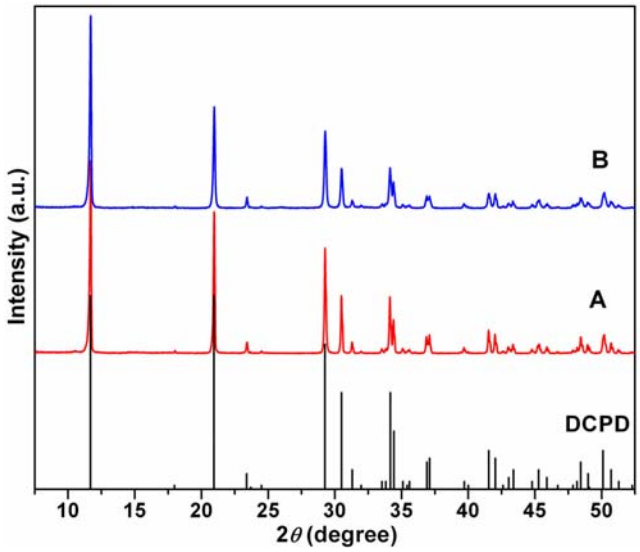

Fig. 4.3. XRD patterns for DCPD powder prepared by precipitation reaction (A) following by mechanochemical grinding using balls with diameter of 3.6 mm (B). Tick marks below the patterns correspond to the positions of the Bragg reflections expected for the monoclinic DCPD ($CaHPO_4 \cdot 2H_2O$, JCPDS No.9-77).

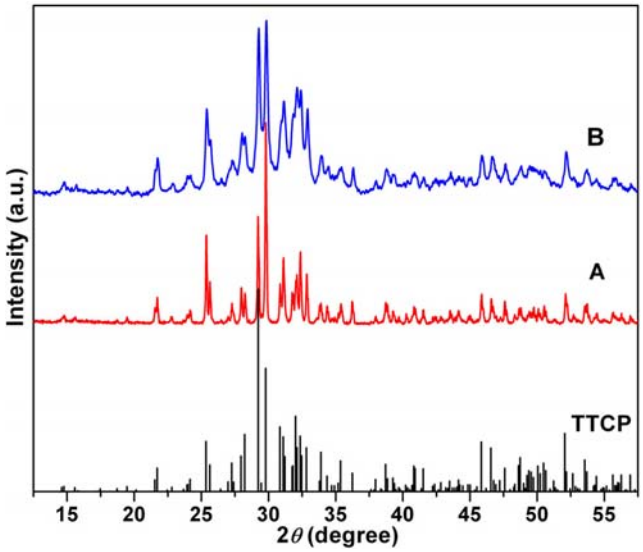

Fig. 4.4. XRD patterns for TTCP powder prepared by solid-state reaction (A) following by mechanochemical grinding using balls with diameter of 4.8 mm (B). Tick marks below the patterns correspond to the positions of the Bragg reflections expected for the monoclinic TTCP ($Ca_4(PO_4)_2O$, JCPDS No. 70-1379).

In order to decrease the crystal sizes of as-prepared **D-raw** and **T-raw**, the powders were subjected to a wet rolling ball-mill process (Tables 4.1, 4.2). IR analysis of the ball-milled DCPD and TTCP products (see Annexe II, Fig. AII.1) confirm the absence of residual acetone and isopropanol from the ball-milling procedures. According to the powder XRD, mechanochemical grinding does not lead to changes in the phase composition and all as-prepared samples were found to be phase-pure TTCP and DCPD (Table 4.2). As an example, we show phase analysis results for **D-36** and **T-48** products (Fig. 4.3B, 4.4B). XRD reveals that the milling of **D-raw** and **T-raw** using balls with diameters of 3.6 and 4.8 mm results in the pure dicalcium phosphate dihydrate and tetracalcium phosphate (samples **D-36** and **T-48**), respectively. It should be noted that for the ball-milled TTCP products, a broadening of the XRD peaks is observed. This is likely due to the comminution of agglomerates, reduction of crystallites sizes and crystal structure deformation from the ball-milling procedure, overall resulting in partial amorphization of the ball-milled material,[86] in good agreement with reported data for TTCP.[50]

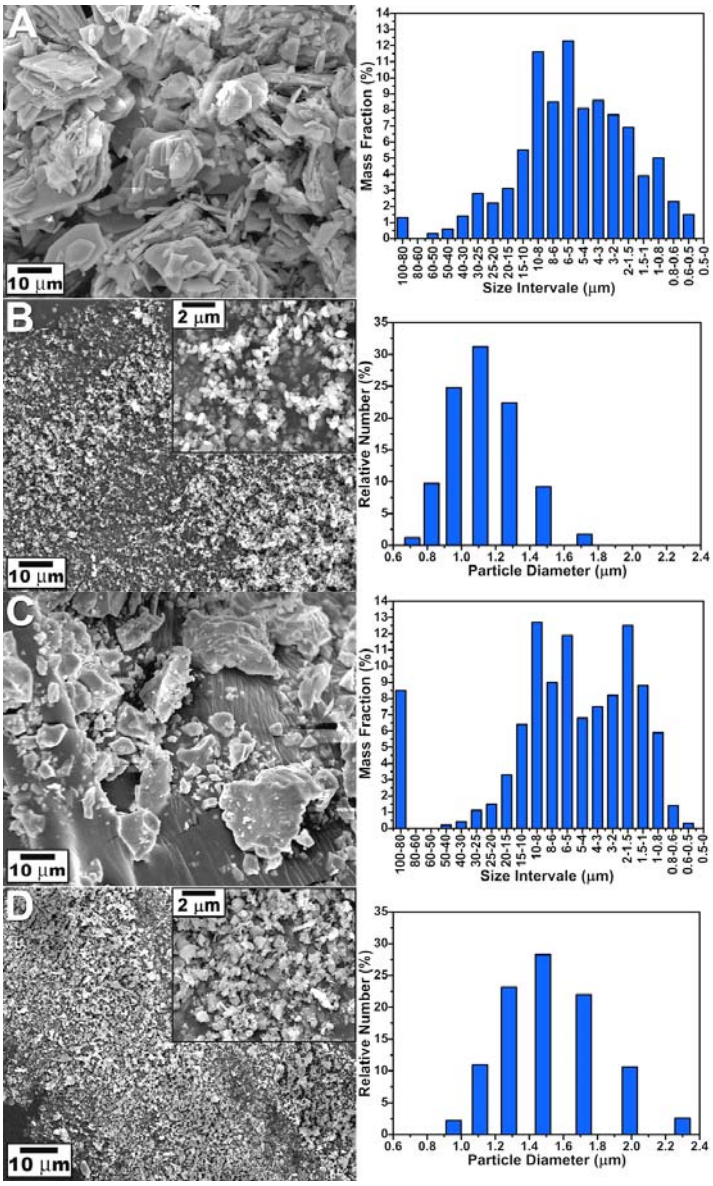

Fig. 4.5. SEM and PSD characterizations of CPC precursors illustrating the considerable reduction of the primary particle's and aggregate's sizes after ball-milling. (A) – the overall morphology of the DCPD powder (left panel) synthesized by a precipitation reaction together with the PSD, determined by sedimentation analysis (right panel); (B) – morphology of the same sample (left panel, inset: high magnification SEM) after mechanochemical grinding using balls with diameter of 3.6 mm in conjunction with the PSD, determined by DLS technique (right panel); (C) – the overall morphology of the TTCP powder (left panel) prepared by solid-state reaction together with the PSD, determined by sedimentation analysis (right panel); (D) – morphology of the same sample (left panel, inset: high magnification SEM) after mechanochemical grinding using balls with diameter of 4.8 mm in conjunction with the PSD, determined by DLS technique (right panel).

The SEM morphologies of polycrystalline raw DCPD and TTCP are shown in Fig. 4.5A and 4.5C (left panels), respectively. The sample **D-raw** consists of relatively large aggregates formed by faceted particles with plate-like morphology, while the **T-raw** product exhibits a less well-defined microstructure. The morphologies of the raw samples, as determined by SEM, are micrometer-sized particles with typical sizes in the range of several micrometers to several tens of micrometers.

Particle size distributions (PSD) of the **D-raw** and **T-raw** samples were estimated using sedimentation analysis (Fig. 4.5A, 4.5C (right panels)) and obtained values are in good agreement with the SEM observations. According to the PSD analysis, the as-prepared DCPD exhibits a non-uniform size distribution with particles sizes ranging from ~0.5 μm to ~100 μm. The average particle size for **D-raw** was established to be ~6 μm (Table 4.2). The latter value most likely corresponds to the overall sizes of the particles in **D-raw** powder, while the presence of grains with size up to ~100 μm appears to be attributed to the overall sizes of the particle agglomerates. According to the PSD analysis, sample **T-raw** is also characterized by a non-uniform size, with particles sizes ranging from ~0.6 μm to ~100 μm, which is quite typical for the powder prepared by solid-state reaction followed by thorough grinding in an agate mortar and pestle. The average particle size for **T-raw** was determined to be ~7 μm (Table 4.2).

A wet rolling mechanochemical grinding of the raw DCPD and TTCP powders with three different types of balls (Table 4.1) leads to significant changes of the microstructure, particles size and PSD (Table 4.2). As an example, we show SEM results in conjunction with the PSD data, determined by dynamic light-scattering technique, for **D-36** and **T-48** samples (Fig. 4.5B, 4.5D, respectively). In sharp contrast to the morphologies of the raw materials, even at low magnification, the ball-milled **D-36** and **T-48** products show drastic reduction in particle sizes and narrowing of the PSD. Higher magnifications of these powders reveal almost non-aggregated sub-micrometer-sized particles with typical sizes in the range of several hundred nanometers to several micrometers (Fig. 4.5B, 4.5D (left panels, insets)).

It can be expected that the use of three different ball diameters (3.6, 4.8 and 9.6 mm) in the course of a wet rolling mechanochemical grinding would provide a useful variable to tailor the grain sizes. To investigate the PSD evolution with respect to the variation of the grinding media, DLS analysis was applied and a summary of the results is presented in Fig. 4.6 and Table 4.2.

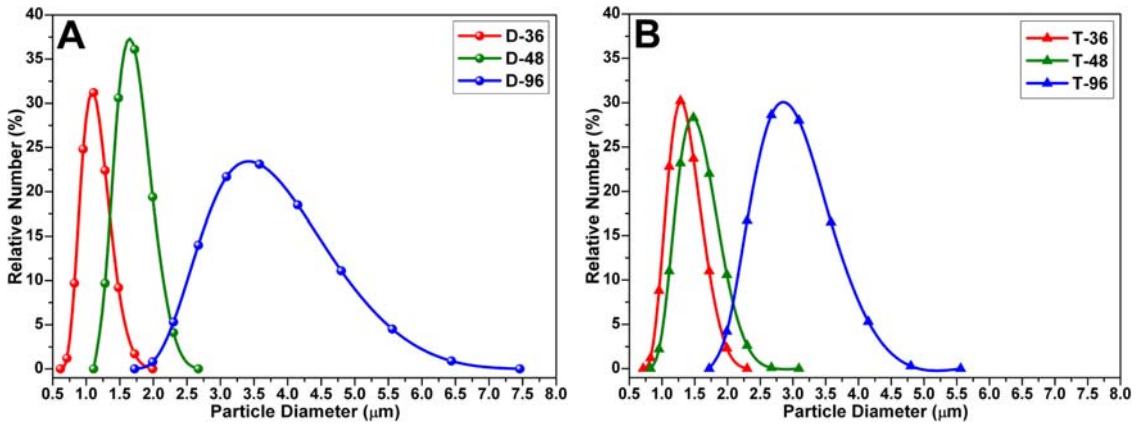

Fig. 4.6. Comparison of the particle size distributions data, determined by DLS technique, for ball-milled DCPC (A) and TTCP (B) cement precursors.

According to the PSD analysis, samples **D-96** and **T-96** posses quite broad peaks centred approximately at 3.66 and 2.96 μm with full width at half maximum (FWHM) of 1.72 and 1.11 μm, respectively; samples **D-48** and **T-48** have a rather narrow peaks centred approximately at 1.69 and 1.52 μm with FWHM of 0.52 and 0.61 μm, respectively; while the samples **D-36** and **T-36** exhibit quite narrow peaks at about 1.13 and 1.33 μm with FWHM of 0.41 and 0.51 μm, respectively (Fig. 4.6, Table 4.2). It should be noted that ball-milled **D-36** and **T-48** particles do not posses any shape anisotropy (Fig. 4.7) and, consequently, the spherical approximation employed by DLS technique to estimate the particles' diameters, can be considered to be a reliable estimation.

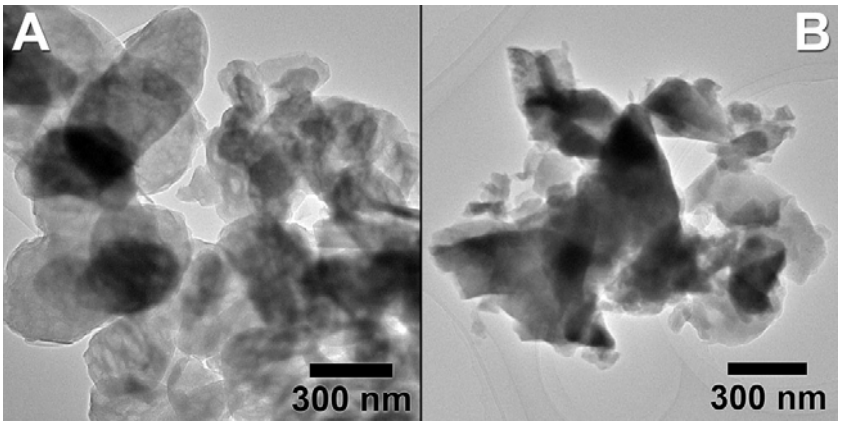

Fig. 4.7. Low-magnification TEM images of the DCPD (A) and TTCP (B) powders after mechanochemical grinding using balls with diameters of 3.6 mm and 4.8 mm, respectively.

4.2.2. Bone cements synthesis and CPCs comparison: selection of the optimal cement

Different CPCs were synthesized from ball-milled dicalcium phosphate dihydrate and tetracalcium phosphate *via* a dissolution-precipitation reaction (Eq. 4.3). Table 4.3 compares the final setting time, phase composition and conversion data for the CPCs produced by a combinatorial method utilizing DCPD and TTCP of various crystal sizes as precursors.

Table 4.3. Final setting time, phase composition and conversion date for CPCs produced by combinatorial method utilizing DCPD and TTCP precursors of various particle sizes. The used solid to liquid ratio was 2 g/mL.

Sample	CPC precursors combination		Final setting time (min) [a]	XRD phase composition [b]	CPC conversion to HA (%) [c]
	DCPD	TTCP			
C-D96/T96	D-96	T-96	40 ± 4	HA	—
C-D96/T48	D-96	T-48	53 ± 4	HA	—
C-D96/T36	D-96	T-36	25 ± 2	HA	16.4 ± 1.6
C-D48/T96	D-48	T-96	47 ± 3	HA	—
C-D48/T48	D-48	T-48	35 ± 3	HA	11.8 ± 1.1
C-D48/T36	D-48	T-36	31 ± 2	HA	10.9 ± 1.2
C-D36/T96	D-36	T-96	42 ± 3	HA	—
C-D36/T48	D-36	T-48	22 ± 2	HA	33.3 ± 3.1
C-D36/T36	D-36	T-36	37 ± 3	HA	12.9 ± 1.4

[a]– Final setting time data estimated by Vicat needle technique (Fig. 3.1).
[b]– XRD analysis results after 24 hours of setting reaction. Reference: JCPDS card number 72-1243.
[c]– Conversion data after 3 hours of setting reaction calculated by Eq. 3.1.

The powder XRD patterns of nine derived cements after 24 hours of setting reaction (1 hour setting at ambient conditions and 23 hours of incubation in distilled water at 37°C) exhibit low intensities and very broad peaks (Fig. 4.8). This observation would suggest that these samples are essentially amorphous, however, as established by TEM investigation, these samples are crystalline (*vide infra*). Hence, aforementioned features of the powder X-ray diffraction patterns are most likely caused by the nanocrystalline nature and defective HA structure of the as-synthesized cements. The XRD patterns of all samples are very similar to each other and most of the relatively sharp peaks closely resemble hexagonal hydroxyapatite (JCPDS No. 72-1243). According to the powder XRD, the peaks related to the presence of separate DCPD and/or TTCP phases are not detected, indicating that all nine as-prepared cements are totally converted to phase-pure HA already after 24 hours of setting reaction (Fig. 4.8, Table 4.3).

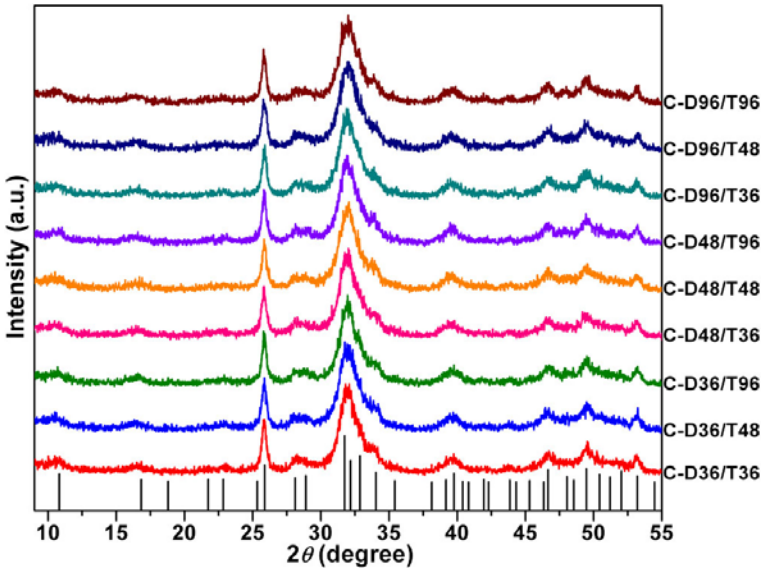

Fig. 4.8. Comparison of the nine CPC products after 24 hours of setting reaction by powder XRD. The samples were combinatorially prepared from stoichiometric amounts of DCPD and TTCP precursors of various crystal sizes (Table 4.2). The as-produced CPCs were allowed to set for 1 hour at ambient conditions and then incubated in distilled water for 23 hours at 37°C. Tick marks below the patterns correspond to the positions of the Bragg reflections expected for the hexagonal HA phase (JCPDS No. 72-1243). Note the similarity between powder XRD patterns of all CPCs as well as their entire conversion to HA after 24 hours of setting reaction.

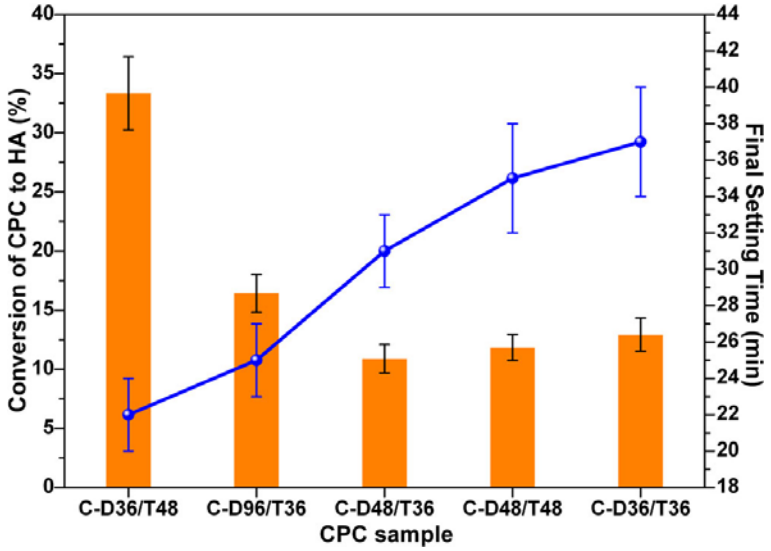

Fig. 4.9. Comparison of the conversion data after 3 hours of setting reaction (columns) and setting time (dots) for the selected cements. Solid line connects setting time data for visual clarity. The conversion percentages of CPCs to HA phase were calculated according to Eq. 3.1. Note the higher conversion rate and shortest setting time for the **C-D36/T48** CPC.

Owing to the lack of structural differences amongst all combinatorially-derived CPC samples after 24 hours of setting reaction, setting time measurements were performed. The ST data are compared in Table 4.3. The CPCs show quite varied values of ST, ranging from ~22

to 53 minutes for the samples **C-D36/T48** and **C-D96/T48**, respectively. But only several of the cements, namely **C-D96/T36**, **C-D48/T48**, **C-D48/T36**, **C-D36/T48** and **C-D36/T36**, exhibit setting time values which are suitable with respect to surgeons' requirements (Section 2.5.2).[70] Additionally, only these CPCs result in the formation of the required easy to handle putty-like materials when mixed with water (S/L ratio: 2 g/mL) (Fig. 4.2).

For further comparison of these CPCs, their conversion rate to HA at a moderated reaction time of 3 hours (1 hour setting at ambient conditions and 2 hours incubation in distilled water at 37°C) were investigated. Fig. 4.9 shows the conversion percentages of the selected CPCs to HA. The calculated values are also enlisted in Table 4.3. Analysis of the obtained data reveals that the cement **C-D36/T48** possesses the highest percentage conversion to HA after 3 hours (~33 %). Taking into account the quickest achievement of setting and fastest conversion rate, **C-D36/T48** cement has been chosen as the *optimal* one amongst all the combinatorially prepared CPCs. Consequently, in the research described below, **C-D36/T48** cement is used to realize further investigations by different characterization methods.

4.2.3. Phase composition evolution during setting reaction

C-D36/T48 cement phase composition evolution during the setting reaction at the selected times of 0, 0.5, 1, 2, 3, 4, 5, 6, 7 and 8 hours is shown in Fig. 4.10A.

According to XRD, this cement at t = 0 (unreacted **D-36** and **T-48** powders mixture) consists of, as expected, DCPD and TTCP (JCPDS No. 9-77 and 70-1379, respectively). Further phase analysis reveals total consumption of **D-36** already at t = 4 hours, while **T-48** is fully exhausted at t = 6 hours. At this time of reaction (t = 6 hours), **C-D36/T48** cement product consists of only phase-pure HA (JCPDS No. 72-1243). The powder XRD patterns of this cement at t = 6, 7, 8 and 24 hours as well as after 1 and 3 weeks of incubation are very much similar and no distinction in phase composition, patterns shapes and positions/intensities of Bragg reflections of an apatite phase are detected. This indicates that the conversion rate of **C-D36/T48** CPC to HA appears to be very high and the dissolution-precipitation reaction is fully complete already after 6 hours of cement setting.

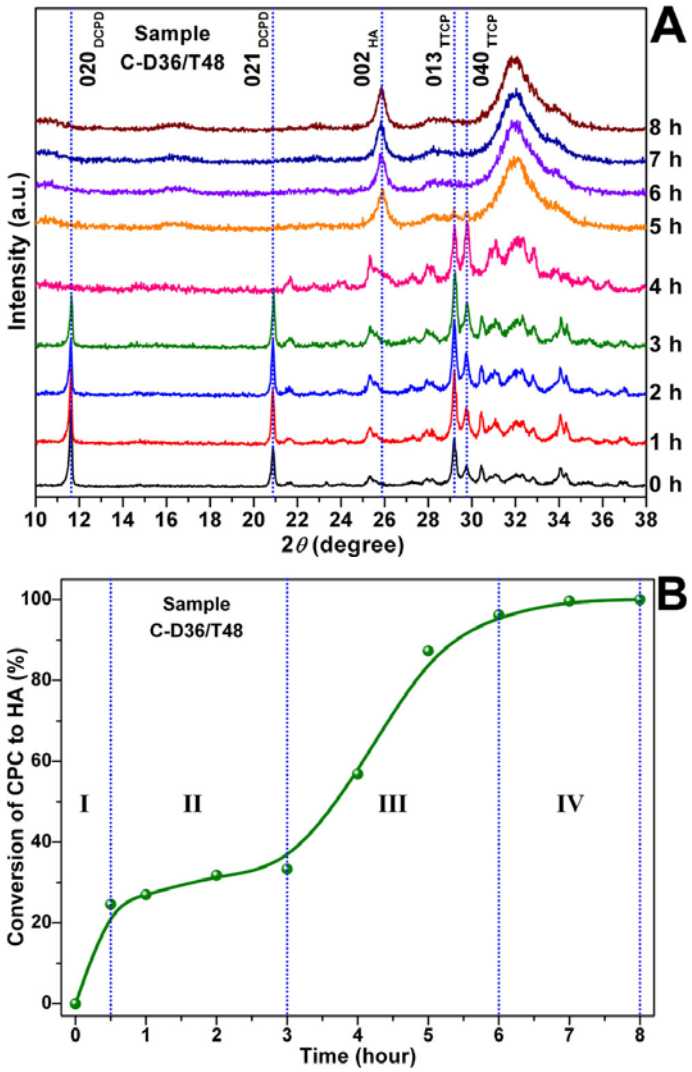

Fig. 4.10. Comparison of the X-ray powder diffraction patterns at different times of setting reaction (A) together with estimated conversion data (B) for the optimal **C-D36/T48** cement sample. The dotted lines in (A) correspond to the diffraction peaks of DCPD, TTCP and HA used for the calculation of the conversion percentages of this CPC to HA phase by Eq. 3.1, presented in (B). Note the disappearance of DCPD and TTCP diffraction peaks already after 4 and 6 hours of setting reaction, respectively.

Fig. 4.10B shows the **C-D36/T48** to HA conversion data determined according to Eq. 3.1, considering the disappearance of the strongest DCPD and TTCP diffraction peaks – (020), (021) and (013), (040), respectively; and the appearance of the HA (002) diffraction peak. This curve clearly shows that the CPC setting reaction does not follow a linear progression and it exhibits four distinct stages during the dissolution-precipitation reaction. The first (I) stage (up to half hour) is most likely attributed to the wetting and initial dissolution of the **D-36** and **T-48** cement precursors.[91] The following stages resemble a sigmoidal curve, which is typically assumed to be a result of the rate-limiting process of the formation and growth of nuclei.[168] Hence, the second (II) stage between approximately a half

and three hours is probably owing to the induction period of the reaction. At this time, no change in the extent of reaction is occurs. As the reaction proceeds, it shifts towards a proliferation period, caused by the rapid increasing of the reaction extent per unit of time (stage III, ~3–6 hours). Finally, the fourth (IV) stage (tapering off period, ~6–8 hours) indicates that the rate of transformation decreases appreciably until it finally reaches the total conversion.[168] Overall, it is apparent that after the wetting and initial dissolution of the **D-36** and **T-48** precursor powders (stage I), the processes involving nucleation and nucleus growth takes place, resulting in a sigmoid-like plot of conversion rate *versus* time (stages II to IV, Fig. 4.10B).

4.2.4. Spectroscopic CPC product analysis

4.2.4.1. Energy-dispersive X-ray spectroscopy

The semiquantitative Ca and P content of the 24 hour-derived optimal cement **C-D36/T48** was determined by EDX. The average atomic percent of the calcium and phosphorous elements are 34.3% and 65.7%, providing the average molar ratio of the calcium to phosphorous elements (Ca/P) ~ 1.49. The molar ratio of calcium and phosphorous elements in stoichiometric HA is 1.67, indicating that **C-D36/T48** cement is Ca-deficient HA. Ca-deficient HA can be expressed as $Ca_{10-x}(HPO_4)_x(PO_4)_{6-x}(OH)_{2-x}$, with $0 \leq x \leq 2$, where the Ca/P molar ratio varies between 1.67 ($x = 0$, stoichiometric HA) and 1.33 ($x = 2$, Ca-deficient HA).[169] Hence, the EDX data reveals a rough composition $Ca_{8.94}(HPO_4)_{1.06}(PO_4)_{4.94}(OH)_{0.94}$ for the 24 hour-derived **C-D36/T48** cement product.

4.2.4.2. Diffuse reflectance infrared Fourier-transformed spectroscopy

The chemical and structural composition of **C-D36/T48** CPC was studied by IR, a useful technique for determining the incorporation of anions like CO_3^{2-} and/or HPO_4^{2-} into the structure of the as-prepared cement, since HA possesses a strong ability to incorporate different ions into its crystal lattice.[9]

Fig. 4.11 displays a representative spectrum for the 24 hour-derived **C-D36/T48** cement product. Peaks centred near 3568 and 634 cm^{-1} are assigned to the stretching (ν_S) and librational modes (ν_L) of the hydroxyl groups respectively. Their harmonic overtones and/or combination bands are also detected[135] at ~2085 and 1996 cm^{-1}. Peaks observed at ~2358 and 2339 cm^{-1} correspond[170] to the atmospheric $CO_{2(g)}$. The set of characteristic bands representing apatitic PO_4^{3-} groups appear at ~1095, 1070 (shoulder) and 1043 cm^{-1} (triply

degenerated asymmetric stretching mode of the P-O bond, v_3); ~962 cm^{-1} (symmetric stretching mode, v_1); ~604, 577 (shoulder) and 567 cm^{-1} (triply degenerated bending mode of the O-P-O bond, v_4); and ~472 cm^{-1} (double degenerated symmetric bending mode of O-P-O, v_2).[135] The broad peak at ~3406 cm^{-1} reflects the physisorbed water, while the appearance of the H–O–H deformation band[170] at ~643 cm^{-1} suggests the existence of free water molecules trapped in the crystal lattice of the **C-D36/T48** HA cement product (Fig. 4.11). The latter observation is consistent with the non-stoichiometry of this cement seen by EDX, since water molecules can be incorporated only into the crystal structure of non-stoichiometric HA.[171] There are also bands that confirm the incorporation of CO_3^{2-} anions into the structure of hydroxyapatite, which indicate that the obtained HA cement is not only Ca-deficient, but carbonated HA. This fact is proved well by the representative combustion bulk elemental analysis, which shows that **C-D36/T48** cement contained approximately 0.55 wt.-% of carbon after 24 hours of setting reaction. These carbonate anions are believe to come from the synthesis procedures, namely, from the atmospheric/water CO_2 and/or from tiny impurity of the $CaCO_3$ phase (if any) utilized for the DCPD and TTCP synthesises. According to the assignation of the bands owing to CO_3^{2-} groups (1462, 1419 and 875 cm^{-1}), **C-D36/T48** can be referred as B-type carbonated HA, *i.e.*, with the CO_3^{2-} ions occupying PO_4^{3-} positions in the HA structure.[172]

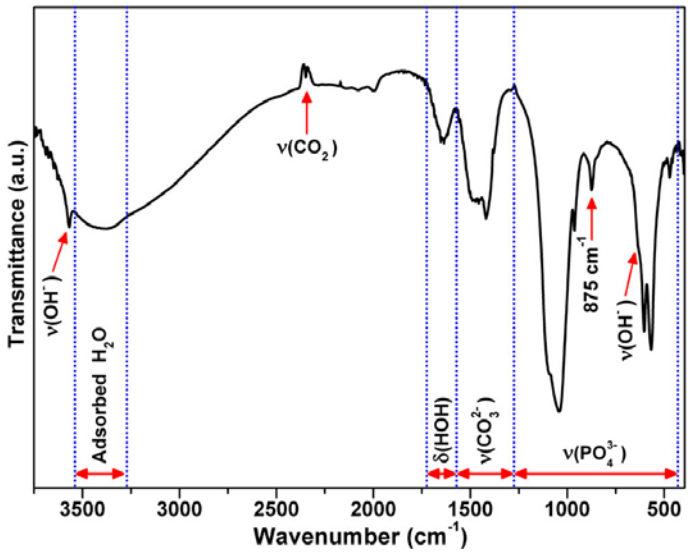

Fig. 4.11. IR spectra collected from the 24 hour-derived **C-D36/T48** cement product.

It should be emphasized that the band at ~875 cm^{-1} can also be assigned to the symmetric stretching mode of P-O(H) bond in the HPO_4^{2-} groups present in Ca-deficient HA.[135] This characteristic band of HPO_4^{2-} anions normally appears near 870 cm^{-1}, where it is

overlapped with the strong band of CO_3^{2-} groups (Fig. 4.11) and cannot be sharply detected. Taking into account that the other two characteristic vibrational bands of HPO_4^{2-} anions[173] centred near 980 and 1080 cm^{-1} also coincide with the region of the strong v_3 stretching mode of the PO_4^{3-} groups, a straightforward assignation of the bands representing HPO_4^{2-} groups can not be performed with full confidence, but at the same time their presence should not be excluded.

4.2.4.3. Raman scattering

The existence of the HPO_4^{2-} anions present in the as-prepared Ca-deficient HA cement was studied by Raman scattering, since here its characteristic band[174] at ~875 cm^{-1} is not overlapped by any peak due to the CO_3^{2-}. Therefore, Raman scattering becomes an essential study to be performed.

The Raman spectrum of the 24 hour-derived **C-D36/T48** CPC is shown in Fig. 4.12 and the assignation of the observed characteristic bands is given in Table AI.1 (see Annexe I). The set of observed bands and spectrum features agree fairly well with the reported Raman data for hydroxyapatite.[135] The spectrum shows a very strong characteristic peak at ~969 cm^{-1} due to the symmetric stretching mode $v_1(PO_4^{3-})$. Apart from this v_1 mode, the other stretching modes of the PO_4^{3-} groups are also observed, namely, v_2 in the 391-502 cm^{-1} region, v_4 in the 559-646 cm^{-1} region and v_3 in the 1002–1110 cm^{-1} region.[135] The band at ~3576 cm^{-1} corresponds to the stretching vibration of the OH^- groups.[135] The set of bands representing HPO_4^{2-} groups[135] appear centred at ~395 (O-P-O bending mode, v_2), 893 (sharp) and 1134 cm^{-1} (P-O stretching modes, v_1 and v_3 respectively) (Fig. 4.12). Another expected band of the HPO_4^{2-} anions[175] at ~985 cm^{-1} is not observed due to the overlapping with the strong v_1 mode from the phosphate group, but confirmed to exist at 981 cm^{-1} by second derivation of the Raman spectra.

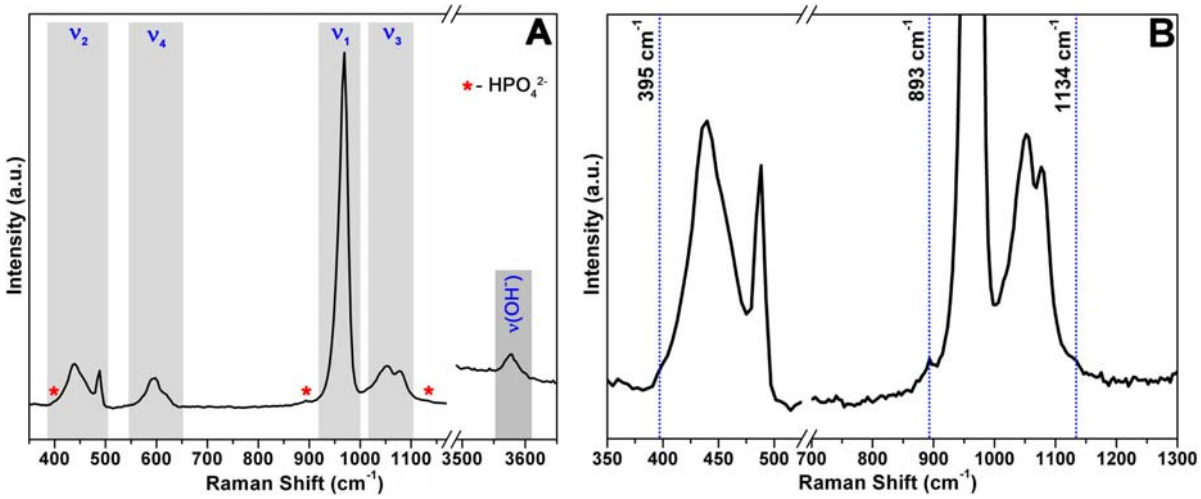

Fig. 4.12. (A) Raman scattering spectra collected from the 24 hour-derived **C-D36/T48** cement product. The characteristic v_1, v_2, v_3 and v_4 stretching modes attributed to the apatitic PO_4^{3-} groups as well as the characteristic OH^- stretching mode are marked by grey regions. The positions of the observed characteristic bands of the HPO_4^{2-} groups attributed to the Ca-deficient HA are shown by asterisks. (B) Detail of the region where the bands due to HPO_4^{2-} anions are expected (dotted blue lines).

4.2.5. Thermal stability of CPC product

Thermo-gravimetric and differential thermal analyses was performed to investigate the thermal behaviour of 24 hour-derived **C-D36/T48** and representative results of TGA/DTA measurements are shown in Fig. 4.13. The TGA curve demonstrates a continued weight loss and the maximum value of weight loss between 25 and 1300 °C is recorded to be ~7.9 wt.-%.

Based on our observations, the total weight loss of **C-D36/T48** cement product consists of five contributions. The first step (up to 280°C), exhibiting a strong weight loss of approximately 6 wt.-%, is probably attributed to the endothermic desorption of physically adsorbed water. The second step between 280 and 375°C can be mostly related to the liberation of the crystal water.[176] The third step (375-550°C) is likely owing to the loss of chemically bounded hydroxyl groups, as well as to the thermal decomposition of the HPO_4^{2-} anions to pyrophosphate $P_2O_7^{4-}$ anions.[9] The fourth step (550-880°C) is most likely related to the CO_2 release during the endothermic decomposition of CO_3^{2-} anions.[9] Finally, the weight loss above 880°C indicates partial transition of Ca-deficient HA to tricalcium phosphate $Ca_3(PO_4)_2$ through the following solid-state reactions: Ca-deficient HA → stoichiometric HA → *β*–tricalcium phosphate (*β*–TCP) → *α*–tricalcium phosphate (*α*–TCP).[9] This is supported by the presence of an exothermic peak at around 1130°C in the DTA curve (Fig. 4.13), indicating phase transition of *β*–TCP to *α*–TCP,[9] as well as by the powder XRD analysis of the **C-D36/T48** product after TGA/DTA experiment (see Annexe II Fig. AII.2).

Stoichiometric HA is relatively stable above 1000°C, *e.g.* it is showed that after heat treatment at 1100°C for 2 hours it does not even partially transform to any calcium orthophosphates phases,[177] while Ca-deficient HA during heat treatment already at ~800°C exhibits transformation to TCP/HA phases mixture.[147] The changes in phase composition of **C-D36/T48** CPC during TGA/DTA experiment additionally prove that 24 hour-derived cement is Ca-deficient HA, in agreement with EDX, IR and Raman scattering analyses.

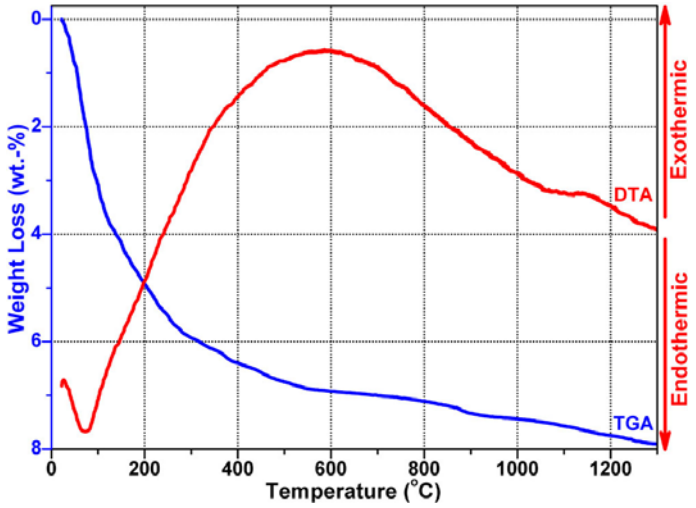

Fig. 4.13. TGA/DTA plot of **C-D36/T48** cement acquired using a heating ramp of 10°C/min in air.

4.2.6. Textural properties of CPC

BET/BJH analysis was used to characterize the textural properties of the optimal CPC. Fig. 4.14 shows the nitrogen adsorption-desorption isotherms and pore size distribution curves of the 24 hour-derived **C-D36/T48** cement powder.

According to the IUPAC classification, the observed isotherm shape is type IV, possessing a monolayer-multilayer adsorption and a type H2 hysteresis loop at a relative pressure above P/P_0 = 0.4. This is associated with capillary condensation taking place in a disordered mesopore range.[178] BET/BJH investigations reveal a high specific surface area of ~169 m^2/g and a total pore volume of ~0.41 cm^3/g for the as-prepared **C-D36/T48** powder, exhibiting a mesopore system of relatively small pores with average diameter of ~55 Å (Fig. 4.14, inset).

Along with the BET/BJH analysis –which gives a total pore volume for the pores with diameter less than ~0.32 μm– the porosity ranging from 3 nm to 360 μm of **C-D36/T48** cement product was also monitored by mercury porosimetry. The specific surface area and total pore volume of 24 hour-derived **C-D36/T48** were established to be 147 m^2/g and 0.19 cm^3/g, respectively, which is relatively low *cf.* BET/BJH analysis. According to the

mercury porosimetry analysis, bulk and skeletal densities of this cement are 1.878 and 2.877 g/cm^3 respectively, while the density of crystalline HA at room temperature is 3.146 g/cm^3 (JCPDS No. 72-1243). The fact that the skeletal density of the **C-D36/T48** cement product after 24 hours of setting reaction is lower than the crystalline HA is consistent with the non-stoichiometry of the as-produced apatite CPC, observed by EDX, IR, Raman scattering and TGA/DTA. The bulk density value indicates that this cement product possess ~35 % porosity. Mercury porosimetry also reveals the presence of only mesopores with average pore diameter of ~50 Å, in good agreement with BJH data. However, the observed mesoporosity is unlikely to cause ~35 % porosity only by itself.

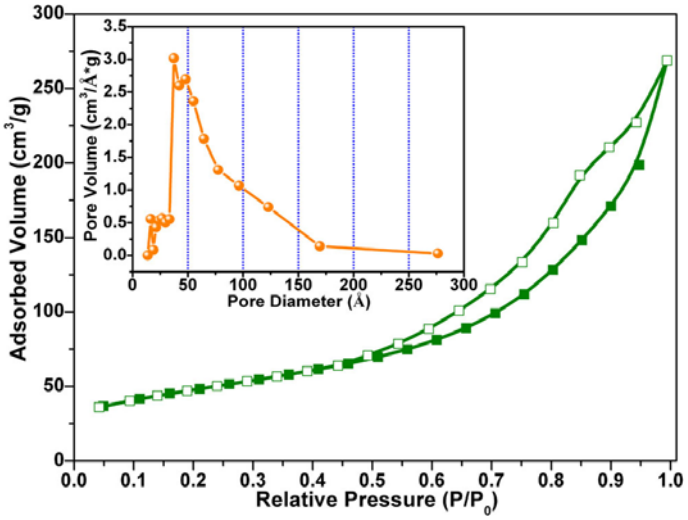

Fig. 4.14. N_2 adsorption (■) – desorption (□) isotherm (inset: pore size distribution) for the 24 hour-derived **C-D36/T48** cement.

4.2.7. CPC product morphologies and microstructure

SEM investigation of the morphology evolution during the setting reaction of **C-D36/T48** cement reveals significant differences in the product morphologies through the duration of the reaction. A SEM image of **C-D36/T48** after 1 hour of setting reaction is shown in Fig. 4.15A. It displays a highly aggregated microstructure with visible alteration of the facets of the ball-milled **D-36** and **T-48** precursors, *i.e.* owing to the smoothing of edges, the grains become less faceted *cf.* primary morphologies (Fig. 4.5B, 4.5D, left panels). Since the CPC precursors were used as faceted, sub-micrometer-sized and almost non-agglomerated powders, the above results support the proposition that the partial dissolution of the precursors already occurs at this stage of the reaction (t = 1), consistent with the conversion rate study (Fig. 4.10).

The SEM image of 24 hour-derived **C-D36/T48** powder reveals the highly associated microstructure of this cement with clearly visible macropores (Fig. 4.15B), in agreement with

the ~35 % porosity established by mercury porosimetry. SEM observations also show the lack of the particulate structure regions in as-synthesized cement. Furthermore, the surface of this cement is free of any crystal faceting. These data support that the dissolution-precipitation reaction between **D-36** and **T-48** precursors with faceted morphology and, accordingly, **C-D36/T48** cement formation process is complete. This is consistent with conversion data on the **C-D36/T48** CPC that exhibits rapid conversion to HA already after 6 hours (Fig. 4.10B).

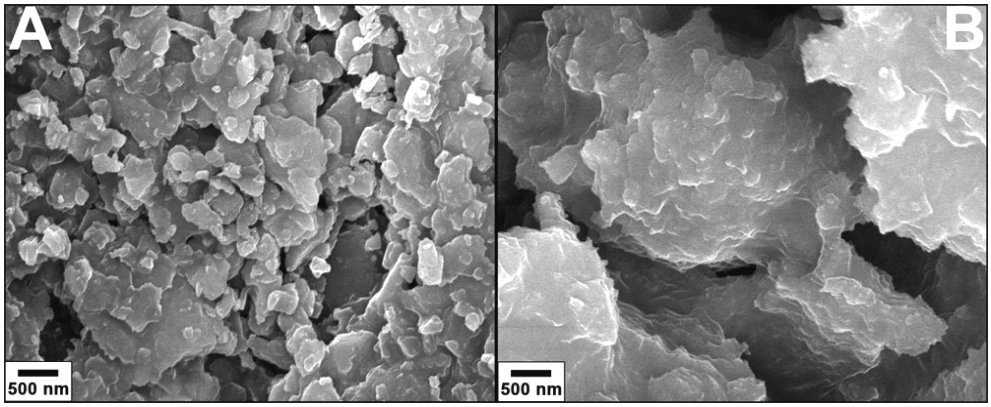

Fig. 4.15. SEM analysis of the cement (sample **C-D36/T48**). Comparison of the morphologies of the cement products at different times of setting reaction: (A) – 1 hour and (B) – 24 hours.

In order to understand the fine microstructure of the optimal cement; TEM, ED and HRTEM measurements of the 24 hour-derived **C-D36/T48** were carried out. Low-magnification and high-resolution TEM images of this product are shown in Fig. 4.16. The sample consists of interlocking nanoscaled platelet crystals with well-developed crystal structure (Fig.4.16A). The compact packaging of the nanocrystallites is subsequently confirmed to be a common feature of 24 hour-derived **C-D36/T48** which is consistent with the SEM observations (Fig.4.15B). The crystallite' size lies within the range of 10-15 nm and the surfaces are free of any amorphous or secondary phase (Fig.4.16A). These results indicate that the line broadening effect and low intensity of the cements' patterns, recorded by powder XRD (Fig. 4.8), are likely related to the nanocrystalline nature of the CPC products and not associated with an amorphous character of the as-produced cements. From analysis of N_2 adsorption-desorption, mercury porosimetry and TEM results, the mesoporous structure of the prepared powders can be attributed to a random assembly of precipitated cement nanocrystals which leads to the formation of a disordered porous system in the mesopore-size region.[179]

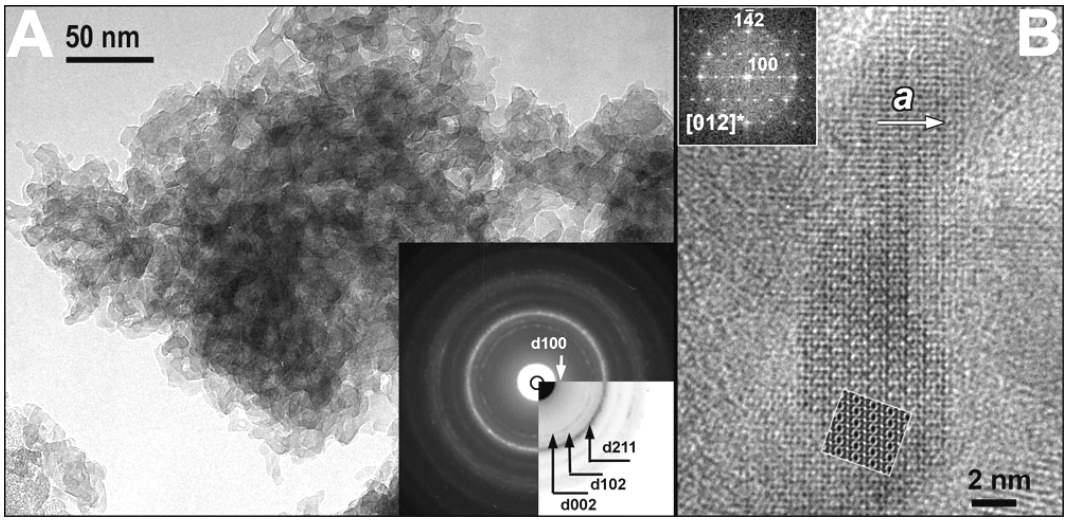

Fig. 4.16. TEM analysis of the cement **C-D36/T48**: (A) – a low-magnification TEM image and corresponding electron diffraction pattern (given as insert); (B) – HRTEM image of single nanocrystal along [012] zone axis for the 24 hour-derived **C-D36/T48** cement product. The Fourier transform (FT) pattern is shown as a top insert in (B). A simulated (112) HRTEM image (t = 5 nm, Δf = –30 nm), calculated on the basis of the hexagonal $P6_3/m$ structure along corresponding direction, is given as a main panel inset in (B). TEM investigation clearly confirms that the cement is formed by strongly interlocked HA nanocrystallites, generating the structural solidity of the as-prepared CPC.

Electron diffraction of the as-prepared sample shows a very dense ring pattern, exhibiting a lack of distinct diffraction spots, typical for a nanocrystallite clustering (Fig. 4.16A, inset). The ED pattern closely resembles the hexagonal HA phase of JCPDS No. 21-1272 (hexagonal, $P6_3/m$, a = 9.432 Å, c = 6.881 Å). The rings of the ED pattern can be indexed using the characteristic d-spacings of the hexagonal HA phase (d_{211}, d_{102}, and d_{002}) determined from powder X-ray diffraction of this **C-D36/T48** cement product. The very weak intensity of the d_{100} and d_{101} rings representing large d spacing in the ED pattern (Fig. 4.16A, inset) is related to the platelet shape of the nanocrystals resulting in a preferential orientation of the nanocrystallites. As determined by HRTEM, the nanocrystallites in the as-synthesized sample are rarely oriented with their a- and b-axes perpendicular to the electron beam. Nevertheless, a [012] HRTEM image of this uncommon crystal orientation is shown in Fig. 4.16B. The corresponding Fourier transform (FT) of the nanocrystallite is shown as the top inset in Fig. 4.16B. This pattern can be indexed according to the hydroxyapatite structure. The computer-simulated HRTEM image, based on the hexagonal $P6_3/m$ HA structure, is in good agreement with the experimental image (given as inset in Fig.4.16A). The intense black dots represent the columns of the calcium atoms and the intense bright dots correspond to the structural channels. Furthermore, there are several interesting aspects concerning the phase composition of 24 hour-derived **C-D36/T48** cement resulting from the TEM investigation. A

direct measurement of the d_{100} spacing on the HRTEM image (Fig.4.16B), gives a slightly smaller distance (~7.4 Å) than a similar measurement for the ideal hexagonal HA structure (~8.2 Å). The calculated ED pattern for hexagonal HA does not fit perfectly with the FT pattern (given as inset in Fig.4.16B). These experimental data suggest that **C-D36/T48** cement does not crystallize in the ideal HA structure; the observed discrepancy can be explained by the non-stoichiometry of the as-synthesized **C-D36/T48** CPC $Ca_{8.94}(HPO_4)_{1.06}(PO_4)_{4.94}(OH)_{0.94}$, as determined by EDX analysis.

4.2.8. In vitro bioactivity test of CPC product

To the first approximation, the bioactivity of the optimal **C-D36/T48** cement was evaluated by means of the *in vitro* test using soaking in an acellular simulated body fluid solution at the human body temperature of 37°C. Fig. 4.17A shows low and high magnification SEM images of the **C-D36/T48** specimen's surface after soaking in water at 37°C for 10 days. The sample exhibits solid microstructure with porous surface. According to SEM analysis, for the **C-D36/T48** sample soaked in SBF at 37°C the first isolated morphologies of precipitated apatite crystals occur already after three days of incubation, whereas after ten days an extensive formation of sub-micrometer-sized scaly-like apatite crystals is observed (Fig. 4.17B). Closer examination of the surface of the present specimen by cross section SEM confirms the apatite crystal growth, as well as shows the presence of knoll-like aggregates, which together generate a continuous layer on the sample surface (Fig. 4.17C).

The phase purity of the **C-D36/T48** cement immersed in SBF at 37 °C for ten days was confirmed by powder X-ray diffraction (Fig. 4.18). IR spectroscopy and TGA/DTA analysis of the 10 days SBF-derived **C-D36/T48** (see Annexe II Fig. AII.3, AII.4) do not reveal any significant differences *cf.* IR and TGA/DTA data for the 24 hours water-derived **C-D36/T48** cement product (Fig. 4.11 and 4.13, respectively), thus additionally indicating phase purity of the **C-D36/T48** after soaking in a SBF solution.

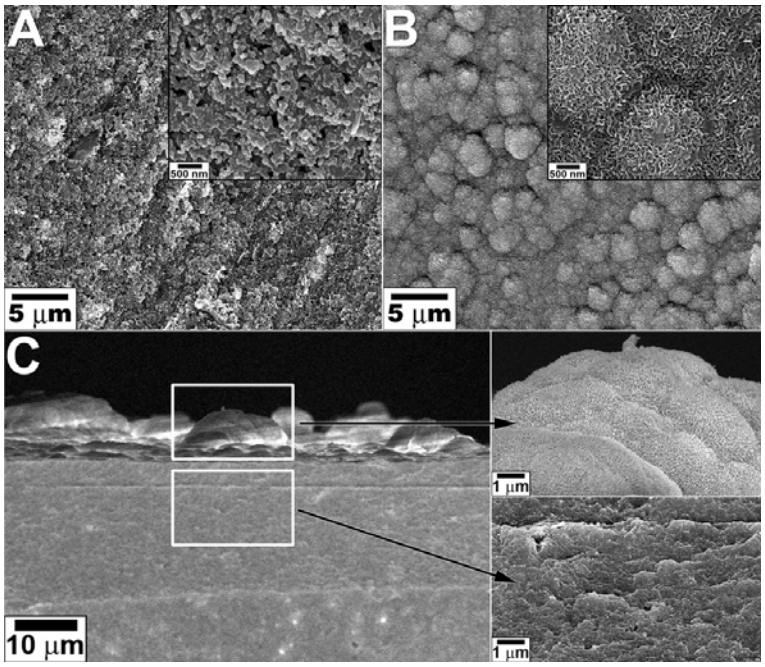

Fig. 4.17. Scanning electron microscopy results for the *in vitro* test of the **C-D36/T48** cement, illustrating the extensive formation of HA phase on the surfaces of SBF incubated specimen. Comparison of the low magnification (main panel) and high magnification (right panel) SEM images from the surface of the **C-D36/T48** sample soaked in distilled water (A) and in SBF (B) at 37°C for 10 days. The SEM images (B) clearly confirm the growth of hydroxyapatite crystals forming a continuous layer on the surface of the cement. A low magnification (left panel) and high magnification from selected regions (right top and right bottom panels) cross section SEM images (C) are provided for clarification of the HA crystal growth on the surface of the **C-D36/T48** CPC immersed in SBF.

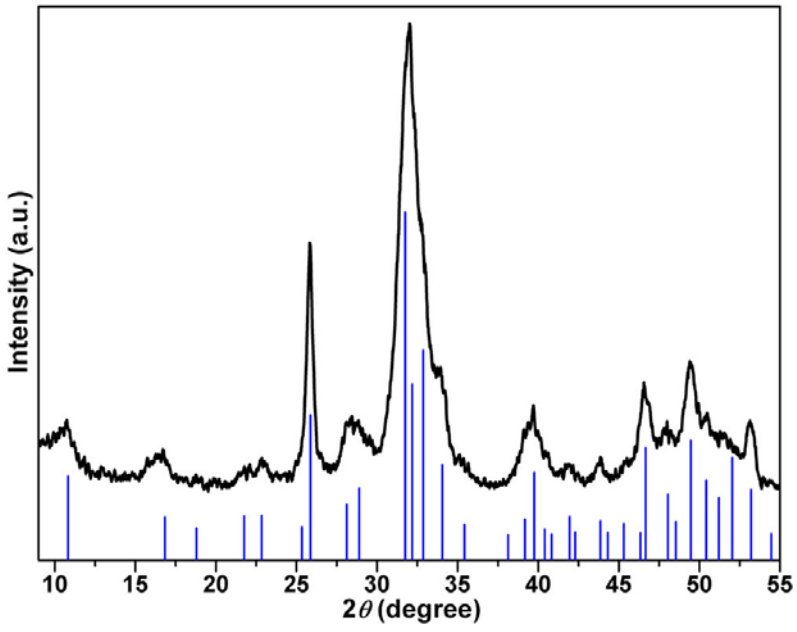

Fig. 4.18. Powder X-ray diffraction pattern of the **C-D36/T48** specimen incubated in a SBF solution at 37°C for ten days. Tick marks below the pattern correspond to the positions of the Bragg reflections expected for the hexagonal HA ($Ca_{10}(PO_4)_6(OH)_2$, JCPDS No. 72-1243). Note the absence of the XRD peaks related to the other phases, confirming the phase purity of the *in vitro* tested CPC.

4.2.9. Mechanical properties of the optimal CPC

Compressive strength measurements were applied to investigate the mechanical properties of the optimal **C-D36/T48** specimen, obtaining a value for CS of 25 ± 3 MPa. The local material properties elastic modulus (E_s, related to elastic deformations) and hardness (H, related to plastic deformations) of the **C-D36/T48** specimen were estimated by means of the nano-indentation technique. A representative nano-indentation load *vs.* displacement profile is shown in Fig. 4.19A. This load-displacement curve smoothly follows the loading function without any discontinuities or pop-in marks, confirming that no cracks arise during nano-indentation.[180] According to the displacement profile, the peak load of 5 mN results in residual indentation depths ranging from approximately 250 to 300 nm. The average elastic modulus and hardness of the **C-D36/T48** cement were calculated to be 23.1 ± 2.6 and 0.73 ± 0.2 GPa, respectively. The inset in Fig. 4.19A shows a typical FE-ESEM image of the **C-D36/T48** specimen surface after nano-indentation, which, as a whole, exhibits clearly visible macropores, in good agreement with the above-mentioned mercury porosimetry and SEM analyses. The nano-indentation probing expectedly generates equilateral triangle-shaped microindent impressions with typical sides' lengths of approximately 4.5 μm. No cracks are observed by FE-ESEM (Fig. 4.19A, inset), consistent with the load-displacement curve (Fig. 4.19A).

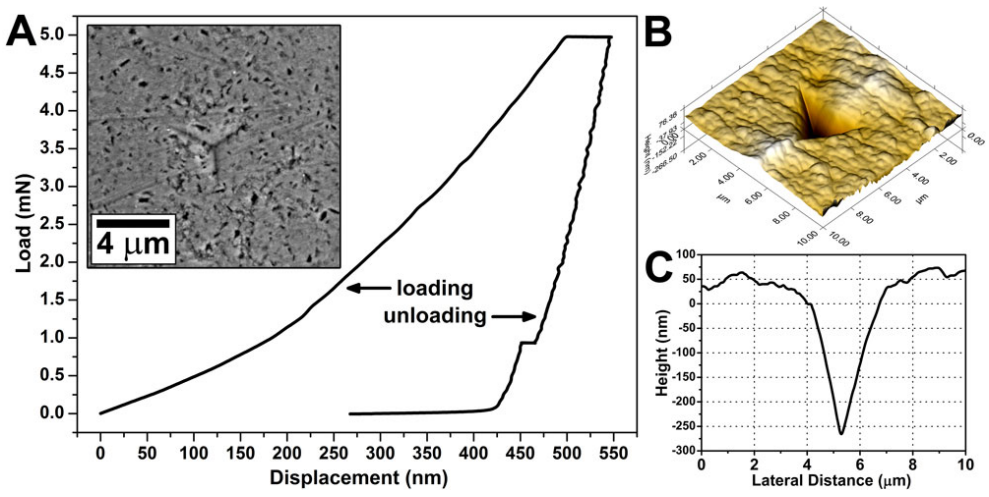

Fig. 4.19. A representative load versus depth curve acquired by nano-indentation probing (peak load: 5 mN) of the **C-D36/T48** cement (A). The inset is a typical FE-ESEM image of a specimen surface after nano-indentation, showing the microindent impression. AFM three-dimensional topography view (B) along with the corresponding height profile (C) from the microindent impression on a cement surface (lateral size: 10 μm by 10 μm; height: from 76.36 nm to 266.50 nm).

A view of the microindents can be observed more closely from the AFM topography imaging, owing to the higher spatial resolution of this technique, and a representative 3D AFM image of the regular triangle pyramid faceted impression is shown in Fig. 4.19B. The AFM thickness profile of the microindent (Fig. 4.19C) reveals that the surface exhibits a residual indentation depth consistent with the one observed in the load-displacement curve (Fig. 4.19A). According to the AFM observations, the appearance of pile-up around the microindents is not detected.

4.3.- DISCUSSION

In the current study, the dissolution-precipitation reaction between DCPD (basic character) and TTCP (acid character) has been chosen to generate hydroxyapatite calcium phosphate bone-cements (Eq. 4.3). This setting reaction occurs most readily when both precursors exhibit high solubility, since the reaction initially takes place at the surface before becoming limited by diffusion.[70] Consequently, the dissolution rate of the CPC precursors becomes a key factor that accelerates cement setting and conversion rates. It is reasonable to expect that the solubility of the DCPD and TTCP will increase with decreasing of their crystal sizes that, accordingly, will facilitate the formation of respective cements. On the basis of this concept, we pursued a strategy that includes several stages to explore advanced HA cement biomaterial. The initial stage involves the convenient synthesis of the phase-pure DCPD and TTCP crystalline compounds –samples **D-raw** and **T-raw** respectively. Next, these raw materials are mechanochemically treated using three different grinding media to reduce and to tailor the size of the particles. Further, a set of calcium phosphate bone-cements are generated, *via* a combinatorial approach, from the ball-milled DCPD and TTCP powders. At the latter stage, the optimal cement is selected with respect to the quickest setting time and the fastest conversion rate after 3 hours of setting reaction. Finally, this optimal CPC is subjected to detailed characterization studies employing various techniques.

In our investigation, sample **D-raw** is a product of the precipitation reaction (Eq. 4.1), while sample **T-raw** is synthesized by high temperature reaction (Eq. 4.2). As a result, phase-pure compounds dicalcium phosphate dihydrate and tetracalcium phosphate were produced (Fig. 4.3A, 4.4A, Table 4.2). The SEM and PSD examination of DCPD and TTCP clearly show that these powders are composed of micrometer-sized crystals and aggregates (Fig. 4.5A, 4.5C, respectively), which are expected to exhibit relatively low dissolution rates. In order to improve the precursors contact and to enhance their reactivity, the primary crystal

sizes of the **D-raw** and **T-raw** were reduced by mechanochemical grinding. XRD data reveals that all six CPC precursors prepared by a wet rolling ball-mill process are phase-pure powders and no by-products/admixtures were found in the samples (Fig. 4.3B, 4.4B, Table 4.2). SEM and DLS analyses clearly confirm that ball-milling serves to effectively break up the large crystals and aggregates of TTCP and DCPD raw materials (Fig. 4.5B, 4.5D), while PSD data obviously indicates that employing smaller grinding media promotes the formation of finer particles with narrowing particle size distributions (Table 4.2, Fig. 4.6).

Many research groups have previously investigated the preparation of the cement biomaterials based either on dicalcium phosphate dihydrate or dicalcium phosphate anhydrous (DCPA) and tetracalcium phosphate precursor systems.[88, 94, 156, 165, 166, 181-185] The starting TTCP materials were normally approximately 10 times greater in crystal sizes than the DCPD or DCPA ones,[88, 94, 156, 165, 181, 182, 185] since originally Chow and Takagi stated that CPC can only be solidified with this particular size ratio of starting compounds.[181] In contrast, in other reports, HA CPCs were successfully prepared by varying the crystal sizes of both precursors[183, 184] or exclusively the dicalcium phosphate precursor while the size of tetracalcium phosphate crystals remained constant.[185] In these efforts, the common trend of a progressive decrease in the setting times with decreasing orthophosphates crystal sizes was observed, showing that the TTCP size effect is predominant.[183] Additionally, Otsuka *et al.* reported that the crystal sizes of both precursors affected the CPCs' compressive strength performance, wherein the optimal results were obtained when both precursors have the crystal sizes of about 1 μm.[184]

It should be stressed that upon examination of the literature related to HA CPCs on the basis of the dicalcium and tetracalcium phosphates (particle size of TTCP larger than DCPD ~10 times), it is apparent that the TTCP precursors were not entirely converted to the apatitic cements after 24 hours of setting reaction and in all cases the as-produced CPCs still contained unreacted TTCP.[88, 94, 156, 165, 182, 185] The biocompatible disadvantage of such cements with a non-homogeneous composition is clear. It is believed that unconsumed TTCP is related to the greater size of TTCP crystals *cf.* DCPD ones and also can be connected to the formation of HA layer on the surface of the reactants.[186] The results of all reviewed studies demonstrate that only Greish and Brown have reported before a cement formulation which is totally converted to HA after approximately 24 hours of setting reaction.[166] This was achieved by using a liquid phase containing phosphate ions, which significantly increased the saturation of the liquid phase with PO_4^{3-} ions compared to traditional water mixing liquid.[88]

However, as-prepared CPC exhibits a high pH for a long period of time (~7 days), prone to generating cell damage when employed *in vivo*.[166]

In the current investigation of CPCs synthesis, a combinatorial approach, utilizing equimolar amounts of ball-milled DCPD and TTCP powders with different crystal sizes, was used (Table 4.3). In sharp contrast to the published data, after 24 hours of setting reaction, all nine as-prepared CPCs have very similar powder X-ray diffraction patterns and show only evidence for nanocrystalline hydroxyapatite (Fig. 4.8), *i.e.* the conversion reaction is complete after one day. One potential reason for this is that the mechanochemically-derived powders are sub-micrometer sized and usually characterized by storing a certain amount of the received mechanical energy, therefore, exhibiting enhanced reactivity owing to their capability to consume this extra energy in different ways.[86] The setting time and conversion rate studies of the nine combinatorially-derived cements indicate that it is **C-D36/T48** CPC which exhibits the quickest achievement of setting (~22 minutes, Table 4.3) and the highest percentage conversion to HA (~33 %) at a moderated setting reaction time of 3 hours (Fig. 4.9). It is noteworthy that this setting time fulfils the medical[47] requirements' (Section 2.5.2) and that it was achieved by using exclusively water as the liquid mixing phase, *i.e.* without any of the setting accelerators widely used in cement formulations[88] that may potentially generate biocompatibility problems.[71, 72] The insert data conclusively support that **C-D36/T48** cement, prepared from **D-36** and **T-48** powders with average crystal sizes of ~1.13 and ~1.52 μm, respectively, is the optimal one among the nine combinatorially-derived CPCs (Table 4.3). Furthermore, it was established that **C-D36/T48** is entirely converted to HA already after 6 hours of setting reaction (Fig. 4.10). To our knowledge, this is the highest reaction rate observed for CPCs based on dicalcium and tetracalcium phosphates, an important step toward enhanced biological and physiological characteristics.

According to the published data, complete hydrolysis of dicalcium phosphate to HA can only be achieved in very dilute suspensions (S/L ratio ~0.01),[187] whereas tetracalcium phosphate with particles size of about 1.4 μm (similar to our **T-48**) is only partially hydrolysed to HA after 24 hours of incubation at 37°C (S/L ratio : 2 g/mL).[50] Therefore, it is believed that the observed rapid formation of HA during **C-D36/T48** setting is a result of a straightforward reaction between ball-milled **D-36** and **T-48** (Eq. 4.3) and not product of their hydrolysis.

Although we have not attempted to investigate the kinetics of the optimal cement formation, a qualitative understanding of the reaction pathway can be deduced from the pH

evolution as a function of the reaction's duration (Fig. 4.20). It should be emphasized that the solubility of TTCP is higher than that of DCPD in acidic and neutral pH[71] and, as expected, at the beginning of the dissolution-precipitation reaction, the suspension pH rises up very quickly to a value of 11.4, presumably due to the release of OH^- ions during TTCP dissolution evolving water (Eq. 4.4). However, at pH higher than ~8.5, tetracalcium phosphate becomes progressively less soluble than dicalcium phosphate dehydrate (Fig. 2.18).[53] Hence, at highly alkaline pH, DCPD starts to dissolve at a greater rate over TTCP (Eq. 4.5), leading to the reduction of the pH owing to the release of H^+ ions (Eq. 4. 6).

$$Ca_4(PO_4)_2O_{(s)} + H_2O_{(aq)} \xrightarrow{H_2O} 4Ca^{2+}_{(aq)} + 2PO_4^{3-}{}_{(aq)} + 2OH^-_{(aq)} \qquad \textbf{(4.4)}$$

$$CaHPO_4 \cdot 2H_2O_{(s)} \xrightarrow{H_2O} Ca^{2+}_{(aq)} + HPO_4^{2-}{}_{(aq)} + 2H_2O_{(aq)} \qquad \textbf{(4.5)}$$

$$HPO_4^{2-}{}_{(aq)} \rightarrow H^+{}_{(aq)} + PO_4^{3-}{}_{(aq)} \qquad \textbf{(4.6)}$$

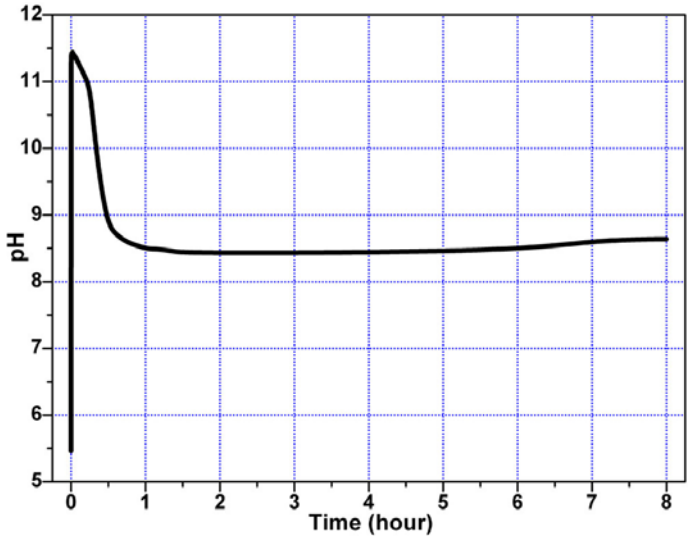

Fig. 4.20. pH *versus* time curve for the **C-D36/T48** cement (S/L ratio : 0.05 g/mL).

As a result of DCPD (predominant) and TTCP co-dissolution, after approximately one and a half hours, the suspension pH reaches the value of ~8.45 (Fig. 4.20), which remains constant until the end of the **C-D36/T48** CPC setting reaction (t = 6 hours).

The observed steady-state pH value is consistent with the pH value of ~8.5 representing DCPD-TTCP invariant (singular) point (Fig. 2.18),[53] suggesting that a pseudo-metastable equilibrium is established in the suspension for the remaining period of time. This equilibrium is characterized by a continuous saturation of the liquid phase with respect to dicalcium dihydrate and tetracalcium phosphates and supersaturation with regards to hydroxyapatite, thus providing the driving force toward the nucleation and growth of a

more thermodynamically stable (less-soluble) calcium phosphate compound (HA) under these conditions (Fig. 2.18).[53]

As long as DCPD and TTCP are present in excess and their rates of dissolution are greater than the rate of HA precipitation, the liquid phase of the cement will remain near the DCPD-TTCP singular point. Therefore, the solution will stay at a quasi-constant pH and composition, allowing the HA formation to progress at a steady rate. However, with the exception of stage I (Fig. 4.10B), the conversion of **C-D36/T48** to HA does not occur at a constant rate (zero-order reaction), indicating that the kinetic effects have profound influence on **C-D36/T48** setting. The observed sigmoid-like plot for the conversion (Fig. 4.10B) suggests that the formation and growth of HA nuclei is the rate-limiting process of the setting reaction.[168] Furthermore, according to our conversion data, **D-36** is consumed faster than **T-48** (Fig. 4.10A), which is consistent with most previous reports on the dicalcium-tetracalcium phosphates CPC systems.[88, 94, 156, 182, 185, 188] Although more data are needed to be certain, it is believed that, in our case, the enhanced dissolution rate of **D-36** is associated with an intrinsic capacity of $CaHPO_4{\cdot}2H_2O$ for *in situ* releasing of H_2O during dissolution, thus, taking advantage over **T-48**. Specifically, *in situ* released water facilitates the dissolution of dicalcium phosphate dihydrate, while the dissolution rate of tetracalcium phosphate is likely to be limited by the diffusion of water to the TTCP crystals; therefore **D-36** and **T-48** are consumed at different rates. One important feature of this data is that the **C-D36/T48** setting should result in the formation of Ca-deficient HA, since it is expected that stoichiometric HA would form directly only when the reactants are consumed at similar rate.

With regards to the application of CPC in the human body for bone repair and substitution, whereby it should be similar to biological apatites, it is also beneficial to investigate the structural, textural and mechanical properties, as well as bone-bonding capacity of the selected optimal cement. Therefore, detailed characterization studies were carry out on the **C-D36/T48** CPC.

According to XRD, the 24 hour-derived **C-D36/T48** sample is phase-pure nanocrystalline hydroxyapatite (Fig. 4.8). EDX study clearly confirms that this sample is Ca-deficient HA, having an average Ca/P molar ratio of ~1.49. This result is consistent with the different CPC precursors' dissolution rate (Fig. 4.10A). Also, the obtained CPC present a partial substitution of the PO_4^{3-} anions by HPO_4^{2-} and CO_3^{2-} anions in the HA crystal structure, as established by IR spectroscopy (Fig. 4.11), combustion bulk elemental analysis, Raman scattering (Fig. 4.12) and TGA (Fig. 4.13). IR spectroscopy also confirms water incorporation into the crystalline CPC product. Based on these data, the complex formulation

$Ca_{10-x-y}(HPO_4)_x(CO_3)_y(PO_4)_{6-x-y}(OH)_{2-x-y}(H_2O)_z$ is a possible representation of 24 hour-derived **C-D36/T48** CPC, however the exact formula was not established in the current study. It is worth noting that the Ca-deficient HA is more similar to bone mineral than stoichiometric HA and, consequently, exhibits better osteogenic and osteoconductive properties.[189] Moreover, biological apatite contains 3-5 wt.-% carbonate groups,[9] thus prepared carbonated Ca-deficient HA CPC is the requirement rather than a problem for its application in medical practice.

BET/BJH and mercury porosimetry studies of the 24 hour-derived **C-D36/T48** sample reveal some remarkable features related to the textural properties of this cement. The as-prepared sample possesses a relatively high specific surface area (~169 m^2/g), high total pore volume (~0.41 cm^3/g) and average mesopore size ~55 Å, as estimated by BET/BJH methods (Fig. 4.14). It should be noted that CPCs are normally characterized by developed macroporous structure owing to the water diffusion during the setting reaction.[190] Clear evidence for macroporosity in **C-D36/T48** cement can be found from SEM and FE-ESEM images (Fig. 4.15B and Fig. 4.19A, inset). According to the mercury porosimetry analysis, the 24 hour-derived **C-D36/T48** CPC possesses ~35 % porosity, however only the presence of mesopores with an average diameter of ~50 Å was determined for this cement. From these data, it can be deduced that macroporous structure observed by SEM and FE-ESEM is likely not mechanically stable at the relatively high pressure of mercury porosimetry experiment (up to 60000 psia), leading to the shrinkage of the CPC structure. Therefore, the presence of macropores was not detected by this technique.

According to the SEM data, **C-D36/T48** CPC setting reaction results in a closely associated microstructure (Fig. 4.15B). Detailed TEM, ED and HRTEM studies on the 24 hour-derived **C-D36/T48** reveal that the sample has the HA crystal structure, devoid of other impurity phases (Fig. 4.16). TEM clearly confirms that the close-packed microstructure of this CPC is generated by strongly interlocked nanocrystallites (Fig. 4.16A) and it appears that namely such spontaneous assembly *via* interlocking of the precipitated nanocrystals results in the structural solidity of the as-prepared CPC biomaterial. The materials exhibit mesoporosity due to voids in between the interlocked nanocrystals. HRTEM results also demonstrate that those nanocrystallites do not tend to orient with their axis along *a*- and *b*-axes, indicating that the precipitated Ca-deficient HA nanocrystals exhibit a much higher tendency to grow along the *c*-axis, the natural tendency of HA.

The potential bioactivity of the optimal **C-D36/T48** cement –ability to form a direct chemical bond with surrounding bone tissue– was explored *via* soaking in SBF at the human

body temperature of 37°C. This bone-bonding capacity was evaluated by analyzing the formation of an apatite layer on the surface of the test sample, revealing the **C-D36/T48** apatite-inducing ability. The results of the *in vitro* tests on the **C-D36/T48** CPC clearly demonstrate a widespread formation of apatite crystals already after soaking in a SBF solution for ten days at 37°C. Furthermore, the crystals tend to generate a relatively thick and persistent apatitic layer on the specimen surface, as it can be seen in Fig. 4.17, thus proving the potentially high bone-bonding ability of the Ca-deficient HA **C-D36/T48** CPC.[191]

Compressive strength performance of the CPCs on the basis of dicalcium and tetracalcium phosphates is described in the literature.[91, 94, 95, 156, 167, 183, 190, 192-194] In preparative chemistry of CPCs, there are several key factors that have essential influences on the CS values: (*i*) synthesis with lower solid to liquid ratio (S/L) leads to an increasing in the porosity, resulting in low compressive strength and *vice versa*;[94, 167, 192] (*ii*) products derived from precursors with reduced crystal sizes are normally characterized by higher CS values;[183] (*iii*) the use of HA crystal seeding in the preparation course of the calcium phosphate bone-cements results in the rise of the compressive strength;[91, 183] (*iv*) the DCPD or DCPA to TTCP ratio,[192] the stoichiometry of tetracalcium phosphate[94] and the variety of the incubating solutions[75] also might alter the CS characteristics of the final products. Moreover, some aspects of the specimens' fabrication for the compressive strength measurements, such as applying a compaction pressure,[75, 94, 167, 192] thermal treatment of the CPC precursors[95, 193] or the specimen's aspect ratio,[195] are shown to have a great impact on the final CS value. Hence, the reported CS values for the cements obtained from dicalcium and tetracalcium phosphates vary essentially from ~10 MPa[156] to 174 MPa,[167] depending upon the CPCs composition and experimental aspects. As an example, a value of ~174 MPa was achieved using a S/L ratio of 9 g/mL and a compaction pressure of 70 MPa.[167] However, based on our experience, such a S/L ratio does not result in CPCs with putty-like behaviour, as it required in medical practice.

The ultimate compressive strength value of the optimal **C-D36/T48** specimen was determined to be 25 ± 3 MPa, indicating that as-prepared cement is able to bear ~255 kg/cm^2. It should be noted that larger CS values can be achieved for **C-D36/T48** CPC by increasing the S/L ratio, pressure and/or compaction time in the course of the specimens' fabrication for the CS measurements. However, in the current study, the objective was to obtain a CPC under experimental conditions that closely mimic those in clinical practice, ensuring the possibility of CPC *in situ* shaping at low pressure for a short period of time.

In addition to the compressive strength, elastic modulus and hardness of **C-D36/T48** sample were estimated using nano-indentation. According to nano-indentation experiments, it

was established that **C-D36/T48** cement exhibits an elastic modulus of 23.1 ± 2.6 GPa and a hardness of 0.73 ± 0.2 GPa and does not possess any crack or pile-up behaviour.

The lack of literature related to nano-indentation probing of CPCs on the basis of the dicalcium and tetracalcium phosphates, did not allow us to compare the observed results with reported data. In contrast, few reports have been published where test samples include HA in their complex composition.[42, 76, 196, 197] E_s and H values of 15.2 and 0.59 GPa, respectively, were achieved when a TTCP/DCPA-based CPC was used as a filler component of a resin matrix, along with SiC whiskers as reinforcement phase.[196] These values are lower *cf.* **C-D36/T48** cement. Additionally, it is known that fibrous SiC decreases the bioactivity of calcium phosphate composite biomaterials.[106] Without SiC whiskers, lower E_s and H values of 11.8 and 0.41 GPa, respectively, were observed.[196] When a Sr-HA CPC was used as a filler component of a resin matrix, along with 5 wt.-% SiO_2 as reinforcement phase, E_s values ranging from ~3.3 to 5.2 GPa were obtained,[76, 197] which are essentially lower than E_s of **C-D36/T48** CPC. The low values of E_s and H reported for the aforementioned biomaterials[76, 196, 197] seem likely to be associated with the presence of a resin, which, possess lower elastic modules than ceramics. When the content of HA increases (from 5 to 40 vol.-%) in a composite with polyetheretherketone resin, elastic modulus raises significantly (from ~2 to ~11 GPa), indicating a high influence of the crystalline phase on E_s.[42]

Compared to human bones, the elastic modulus of **C-D36/T48** cement is slightly higher than in human trabecular bones[7] (15.0-19.4 GPa) and lies in the range of human cortical bones[198] (20.0-25.8 GPa). Following E_s trend, the hardness of this cement is also higher than in human trabecular bones[7] (0.52-0.62 GPa) and in consistency with H of human cortical bones[7] (0.62-0.74 GPa). Overall, the observed results clearly demonstrate a high mechanical similarity (both elastic and plastic) between the as-prepared cement biomaterial and human bone, an important requirement for biomaterials used for bone repair and substitution. Biomaterials with elastic modulus higher than bone produce stress shielding to the bone (Section 2.3.4).

4.4.- CONCLUDING REMARKS

Nine calcium phosphate bone-cements were efficiently synthesized from ball-milled DCPD and TTCP powders of different crystal sizes *via* a combinatorial method. This approach yield CPCs products exhibiting overall transformation to apatite after 24 hours of setting reaction, but markedly different setting times and conversion rates. We have shown that the optimal cement sets in ~22 minutes and entirely converts to the end product already after 6 hours of setting reaction. Detailed experimental studies conclusively support that this cement biomaterial is indeed porous, nanocrystalline and potentially bioactive Ca-deficient carbonated hydroxyapatite, demonstrating essential mechanical performance.

As-produced advanced **C-D36/T48** CPC was further used as a benchmark for reinforcement by hydroxyapatite crystals with various morphologies (Chapter V) in order to prepare biocomposite cements with enhanced mechanical properties (Chapter VI).

V

HYDROTHERMAL SYNTHESIS OF HYDROXYAPATITE CRYSTALS WITH VARIOUS MORPHOLOGIES

5.1.- EXPERIMENTAL PART

5.1.1. Hydrothermal syntheses of hydroxyapatite

Hydroxyapatite crystals with different morphology were synthesized via direct hydrothermal reaction between calcium nitrate tetrahydrate $Ca(NO_3)_2{\cdot}4H_2O$ and diammonium hydrogen phosphate $(NH_4)_2HPO_4$ using urea $(NH_2)_2CO$ as a homogeneous precipitation agent. Briefly, stoichiometric amounts of $Ca(NO_3)_2{\cdot}4H_2O$ and $(NH_4)_2HPO_4$ (Ca/P molar ratio of 1.67) together with an appropriate amount of urea were mixed with 25 mL of distilled water under vigorous stirring in a 40 mL polytetrafluoroethene (PTFE) vessel (Table 5.1).

Table 5.1. Summary of synthetic conditions and results from selected hydrothermal reactions.

Sample	Concentration, M			Applied temperature profile	pH_{final}	XRD phase composition	SEM particles' morphology
	$[Ca^{2+}]$	$[PO_4^{3-}]$	[Urea]				
PT	0.1670	0.10	0.50	Scheme I	8.5	HA	Plates
HX	0.1670	0.10	0.50	Scheme II	8.1	HA	Hexagonal prisms
ND	0.1670	0.10	0.50	Scheme III	8.4	HA	Needles
FP	0.0835	0.05	0.25	Scheme IV	8.4	HA	Fine-plates

Fig. 5.1. A hydrothermal setup: stainless steel autoclave, a low-density porous polytetrafluoroethene (PTFE) hyper-sheet® gasket (GORE-TEX®), as well as PTFE cover and cell.

The suspension pH was then adjusted to be ~3 by 0.5 M nitric acid HNO_3 aqueous solution using a Mettler Toledo InLab®413 SG pH-meter, and the resulting mixture was stirred for further 15 min. Afterwards, the pH was subsequently readjust to 3.00 ± 0.05 under

constant stirring and the solution volume was complete to 35 mL with distilled water. The vessel was capped by a PTFE cover and charged into a stainless steel autoclave. A 1.5 mm thick, low-density (0.6 g/cm^3) HYPER-SHEET® gasket (GORE-TEX®) with porous structure of PTFE polymer (Fig. 5.1) was placed between the vessel and the cover. Such gasket is semipermeable to gaseous products under elevated temperatures, thus enabling gradual release of the CO_2 forming during the urea temperature decomposition.[199]

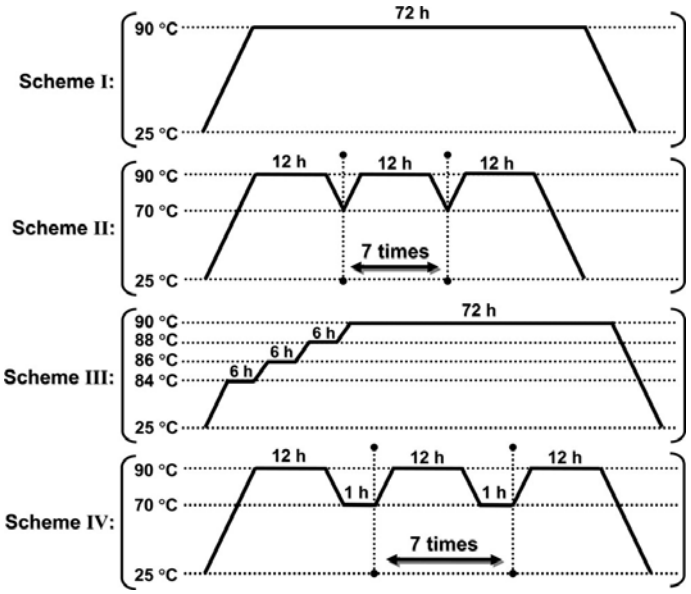

Fig. 5.2. Schematic representation of controlled temperature profiles applied during the hydrothermal treatments. Heating and cooling rates of 0.5°C/min were used.

The autoclave was then sealed and subjected to a controlled heat treatment (T_{max} = 90°C, Table 5.1, Fig. 5.2), with subsequent cooling to room temperature. In this way, intensive, stepwise, slow, and interrupted thermal decomposition of urea were achieved applying temperature profiles of Scheme I, II, III and IV, respectively (Fig. 5.2). The products of hydrothermal synthesis were obtained in two forms; namely, an abundant cotton-like suspension (Fig. 5.3A) and secondary wall-product firmly attached to PTFE vessel's walls (if exist) (Fig. 5.3B). Both crystalline materials were carefully separated, collected by filtration, washed with distilled water and ethanol, and finally dried at 80°C. Throughout this work, a set of acronyms is used (Table 5.1), wherein the first two letters mean the obtained sample morphology in form of plates (**PT**), hexagonal prisms (**HX**), needles (**ND**) and fine-plates (**FP**).

Fig. 5.3. Photo of two types of hydrothermal synthesis products: an abundant cotton-like suspension (A) and secondary wall-product (B).

5.1.2. Nano-indentation sample preparation detail

For the nano-indentation tests, HA crystals were firstly embedded in the advanced calcium phosphate bone-cement **C-D36/T48** (Chapter IV). More specifically, equimolar amounts of sub-micrometer-sized, ball-milled dicalcium phosphate dihydrate and tetracalcium phosphate powders (total 0.51 g) were thoroughly ground together in an agate mortar and pestle. Next, 15 wt.-% of a well-dispersed hydrothermally-derived powder (sample **HX**), consisting of HA particles with sharply faceted hexagonal prism-like morphology, was added to the CPC precursors followed by gentle mixing in an agate mortar and pestle. The resulting fine powdered mixture (total 0.6 g) was then placed inside a latex finger cot. After this, 0.19 mL of distilled water was added to the composite CPC precursor using a micropipette. This mixture was hand kneaded for 1 minute and then placed into a cylindrical mold assembly of 6.9 mm diameter. The batch was then pressed under 5.3 MPa for 1 min using a pressure-loading device. Afterwards, the specimen was removed from the mold, kept for 1 h at ambient conditions to set and then incubated in distilled water at 37°C for 23 h. After this stage, the CPC precursor mixture is entirely reacted, thus generating Ca-deficient HA cement pellet containing 15 wt.-% of spatially-dispersed HA crystals of **HX**, as illustrated schematically in Fig. 5.4.

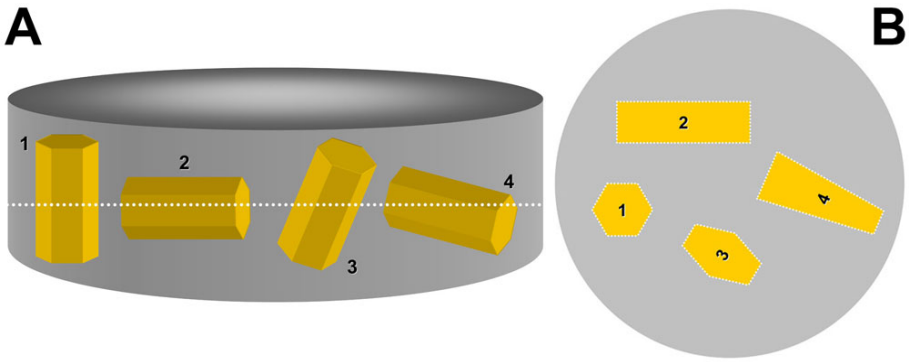

Fig. 5.4. Schematic representation of the cement-embedded HA single crystals with sharply faceted hexagonal prism-like morphology (A) together with expected top view of the pallet surface (B) after cutting along white dotted line in (A).

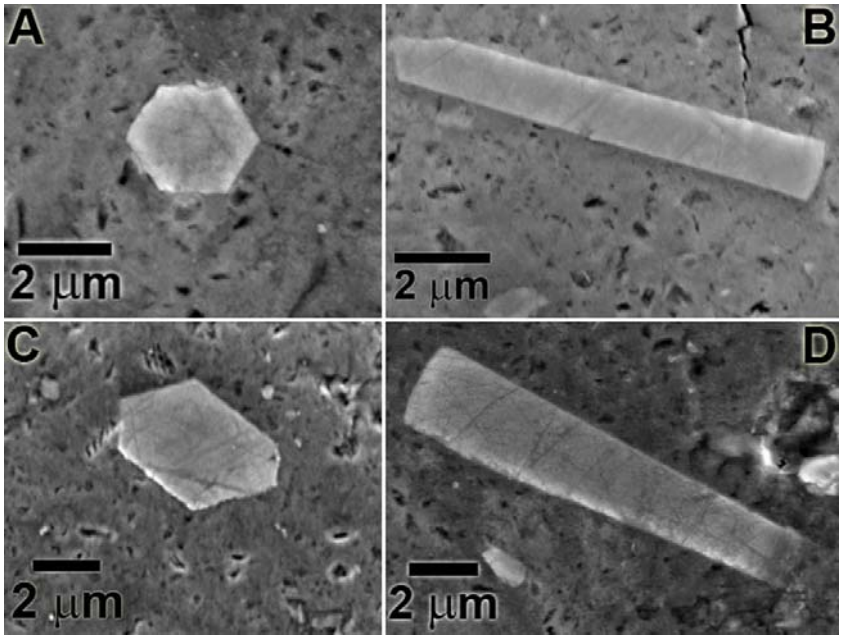

Fig. 5.5. A representative micrographs imaged by FE-ESEM from the surface of nano-indentation test sample, illustrating the shape variety of the cement-embedded HA single crystals after polishing. Only nearly regular in shape basal-faceted (A) and prism-faceted (B) HA crystals were subjected to NI measurements, while the crystals exhibiting irregular shapes (C and D) were omitted.

The specimen was then embedded in PMMA (Section 3.2.11.2), cut in parallel to the pellet base, as schematically indicated by white dotted line in Fig. 5.4A, and polished (Section 3.2.11.2). Owing to the spontaneous spatial allocation of the HA crystals inside cement matrix, after cutting and polishing, the shape of the cement-embedded crystals is expected to exhibit different geometrical features at the surface, as represented schematically in Fig. 5.4B. Therefore, prior to NI, the surface of the test sample was carefully investigated using field-emission environmental scanning electron microscopy (FE-ESEM), and exclusively *a*-surface exposed (*i.e.*, prism-faceted) and *c*-surface exposed (*i.e.*, basal-faceted) HA single crystals

were subjected to NI measurements. Specifically, only nearly uniform in shape basal-faceted and prism-faceted HA particles (Fig. 5.5A, 5.5B) were probed, while the crystals exhibiting irregular shapes (Fig. 5.5C, 5.5D) were deemed to be inappropriate for NI, and accordingly were not tested. The measured elastic modulus E_s and hardness H values are the average of at least thirty NI experiments for each surface.

5.2.- RESULTS

5.2.1. Analysis of hydroxyapatite hydrothermal synthesis

Hydroxyapatite crystals with various controlled morphologies were prepared by the direct reaction between $Ca(NO_3)_2{\cdot}4H_2O$ and $(NH_4)_2HPO_4$ under gentle hydrothermal conditions (T_{max} = 90°C). The precursors were chosen to avoid contamination of the precipitate by incorporation of foreign ions such as K^+, Na^+, *etc.* Also, the larger ionic size of NO_3^- ions prevents their substitution for OH^- groups in the crystalline structure of HA. Urea was used as a homogeneous precipitation agent. At elevated temperatures, $(NH_2)_2CO$ smoothly decomposes releasing carbon dioxide and aqueous ammonia species to the medium (Section 2.7.3.5). In turn, this *in situ* released $NH_{3(aq)}$ generates a gradual increase of pH in the reaction solution to the range wherein HA is the more thermodynamically stable (less-soluble) calcium orthophosphate compound, and is thus formed (Fig. 2.18).[53] Our attempts to use a closed hydrothermal reaction system for the synthesis of the title compound were unsuccessful due to the high autogenous pressure of CO_2, which is additionally poorly soluble in water under elevated temperatures, thereby suppressing the driving force for urea decomposition. This drawback was successfully overcome by using a porous PTFE gasket, semipermeable to gaseous products (Fig. 5.1).[199]

Several parameters of the hydrothermal synthesis were varied in order to study their influence on the phase composition and morphology of the products, namely, the temperature profile, and the Ca^{2+}, PO_4^{2-}, urea and HNO_3 concentrations. The optimal initial concentrations of starting reagents, post-synthesis reaction solution pH, phase composition and overall particle morphology of the hydrothermally derived products are given in Table 5.1, while Tables AI.2 and AI.3 (Annexe I) summarize all the hydrothermal reactions conducted in the study. The four applied temperature profiles are presented in Fig. 5.2.

The analysis of the primary synthetic data reveals that the initial pH is of great importance in obtaining phase-pure HA. Therefore, the optimal pH value was investigated using Scheme I (Fig. 5.2). It was found that only when the initial solution pH is ~3 is it possible to obtain phase-pure HA. Also, the most favourable values of temperature and time were found to be T = 90ºC, t = 72 h. All our attempts to reduce the temperature and/or duration of the hydrothermal treatment does not result in the phase-pure HA products.

The concentration of the reactants is also crucial to the phase composition of the prepared samples (see Annexe I, Tables AI.2 and AI.3). Despite the mild temperature profile, using higher reactant concentrations prevented the formation of phase-pure HA (see Annexe I, Table AI.2). It was found that hydrothermal syntheses with the lower reactant concentrations in all cases lead to phase-pure HA with fine-plate morphology (see Annexe I, Table AI.2). The concentration of nitric acid used for adjusting the solution pH did not affect the particle morphology of the synthesized powders (see Annexe I, Table AI.2).

Interestingly, a minimum urea concentration of 0.375 M is required in order to obtain phase-pure HA (see Annexe I, Table AI.3). Hydrothermal syntheses using an excess of urea (0.50 M (Scheme II) or 0.75 M (Scheme III)) do not lead to the formation of significant amounts of HA and OCP was established to be the predominant resulting phase. This observation was not due to the low values of the final pH, since using urea concentration higher than 0.25 M results in post-synthesis pH values of around 8 (see Annexe I, Tables AI.2 and AI.3), sufficient for phase-pure HA formation. Therefore, the appearance of OCP as a main product is likely related to the high pressure of CO_2. Specifically, thermal decomposition of urea with the increased concentrations leads to a release of NH_3 to the reaction medium, providing appropriate solution pH, but also, to an increased amount of CO_2. Although PTFE gaskets with porous structure were used in order to release resulting CO_2, it is appears to be that during the syntheses with increased urea concentrations, all the released CO_2 cannot be liberated from the reaction media through such a gasket. This process generates reaction conditions wherein the formation of the phase-pure HA is prevented due to kinetic reasons.

The shape of the particles is also affected by urea concentration (see Annexe I, Table AI.3). For HA phase-pure samples, a mixture of two morphologies (plates and needles) are obtained at concentrations higher (Scheme II) or lower (Scheme III) than 0.5 M. Conversely, the concentration of HNO_3 used to adjust the solution pH affects neither the shape nor the purity of the produced samples (see Annexe I, Table AI.2).

The samples originating from the vessel's walls (Fig. 5.3B) are inhomogeneous but typically composed of huge aggregates, predominantly formed by crystals with hexagonal prism-like particle morphology (Fig. 5.6, see Annexe I Table AI.2). Therefore, taking into account the significant yield of the products recovered from the cotton-like suspension (Fig. 5.3A) as well as their fine homogeneity in comparison to the wall-products, the research described below is devoted only to the powdered samples originating from the cotton-like suspension.

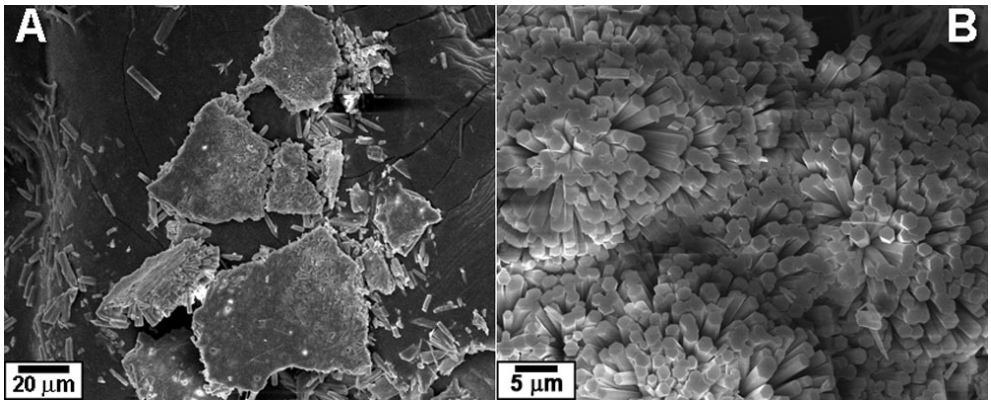

Fig. 5.6. The overall morphology of the hydrothermal synthesis products recovered from walls of PTFE vessel (see Fig. 5.3B) as imaged by SEM; in particular, two representative micrographs of agglomerated HA crystals showing the interfacial region (A) and region of the crystal growth (B).

5.2.2. Powder X-ray diffraction product analysis.

The powder XRD patterns of the synthesized samples are presented in Fig. 5.7A, indicating overall crystalline nature of the products. According to the phase analysis, samples **PT**, **HX**, **ND** and **FP** are phase-pure HA $Ca_{10}(PO_4)_6(OH)_2$ (JCPDS No. 72-1243, hexagonal, a=9.4320 Å, c=6.8810 Å, space group $P6_3/m$). Whereas XRD pattern of **FP** powder closely resemble the diffraction peaks with the reported in JCPDS database, the ones from **PT**, **HX** and **ND** products are very similar to each other and clearly exhibit inconsistencies in the intensity *cf.* Bragg reflections reported in JCPDS database (Fig. 5.7B). The latter observation most likely corresponds to the shape anisotropy (*i.e.*, textured microstructure) of the particles in as-synthesized products, indicating that the crystals in these samples grew along the c-axis (Fig. 5.7B, inset). Such crystal growth develops the a-plane of hexagonal HA (Fig. 2.26), hence, the observed (300) XRD reflection representing a-plane is more intense than the reported one in JCPDS database (Fig. 5.7B).

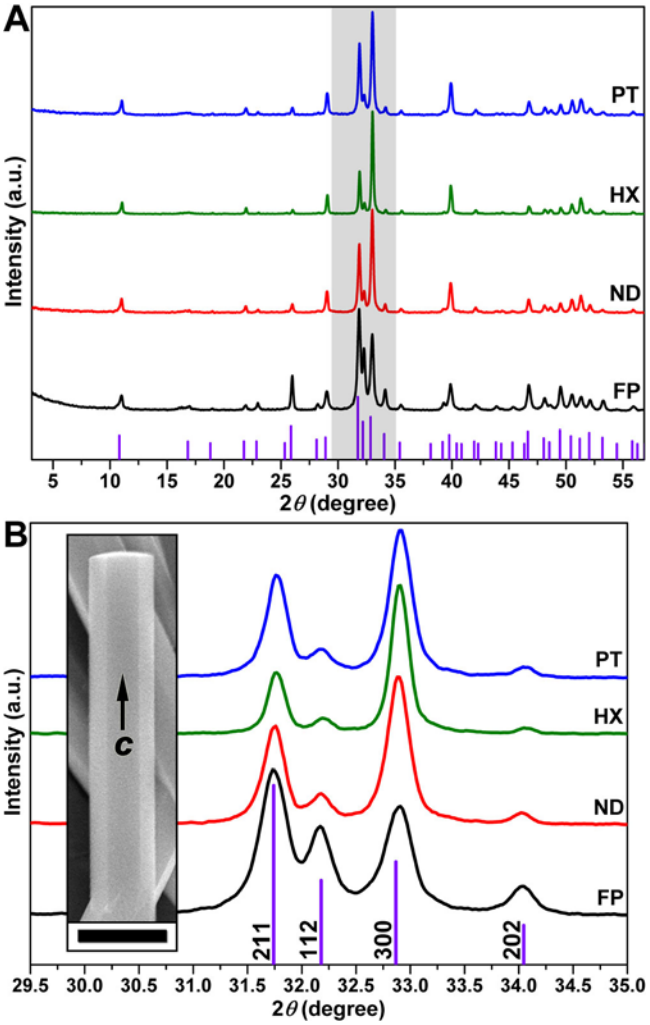

Fig. 5.7. (A) – XRD patterns from the hydrothermally-derived **PT**, **HX**, **ND** and **FP** samples. Tick marks below the patterns correspond to the positions of the Bragg reflections expected for the hexagonal HA (JCPDS No. 72-1243). (B) – The angular region of the XRD patterns from 29.5° < 2θ < 35.0° marked by grey region in (A) where (211), (112), (300) and (202) peaks of HA phase are expected to be. In the inset, SEM image of HA crystal (sample **HX**) exhibiting shape anisotropy and crystal growth along the *c*-axis is displayed (scale bar 5 μm).

5.2.3. Spectroscopic hydroxyapatite product analysis

5.2.3.1. Diffuse reflectance infrared Fourier-transformed spectroscopy

Fig. 5.8A displays IR spectra collected from hydrothermal synthesis products. The assignments of the observed bands were accomplished according to the literature data,[135, 170, 172] the summary of the assignments and IR wavenumber is presented in Table AI.4 (see Annexe I). The set of observed bands and spectra features agree fairly well with the reported IR data for phase-pure HA.[135] The set of characteristic bands representing apatitic PO_4^{3-} groups are observed at ~1104, 1064 and 1028 cm^{-1} (ν_3, triply degenerated asymmetric stretching mode of the P-O bond) and ~960 cm^{-1} (ν_1, symmetric stretching mode of the

P-O bond). Additional expected bands representing v_4 triply degenerated bending mode of the O-P-O bond (~604, 578 and 563 cm^{-1}) are also observed in the low wavenumber region.[135] The intense peak at ~3570 cm^{-1} and the weak one at ~632 cm^{-1} are assigned to the stretching (v_s) and librational modes (v_L) of the structural hydroxyl anions, respectively.[135] Moreover, their harmonic overtones and/or combination bands are also observed[135] in the region between 2171 and 1923 cm^{-1}.

The broad weak peak at ~3327 cm^{-1} (distinct for **ND** and **FP** samples) is assigned to the physisorbed water.[170] Peaks observed in the 2400-2287 cm^{-1} range correspond to the atmospheric $CO_{2(g)}$.[170] The inspection of the 1630-1194 cm^{-1} region clearly shows the existence of the distinctive bands attributed to the carbonate groups (Fig. 5.8A),[135] indicating their incorporation into the crystal structure of HA. In particular, the peaks observed at ~1544 and 879 cm^{-1} represent CO_3^{2-} anions partially occupying OH^- positions (A-type), while the bands detected at ~1451, 1420 and 874 cm^{-1} reflect partial PO_4^{3-} substitution (B-type).[172] Hence, all four hydrothermally-derived samples are AB-type carbonated HA. These carbonate anions are believe to come from the urea decomposition. This fact is very consistent with the representative combustion bulk elemental analysis, which demonstrates that the **PT**, **HX**, **ND** and **FP** samples contained approximately 0.61, 0.90, 0.70 and 0.80 wt.-% of carbon, respectively. Although $CO_{2(g)}$ is mostly released from the hydrothermal system through the porous PTEF gasket, it is also partially dissolved in the water and consequently, due to the strong ability of HA to include different ions into its crystal structure,[9] easily incorporated into the synthesized products.

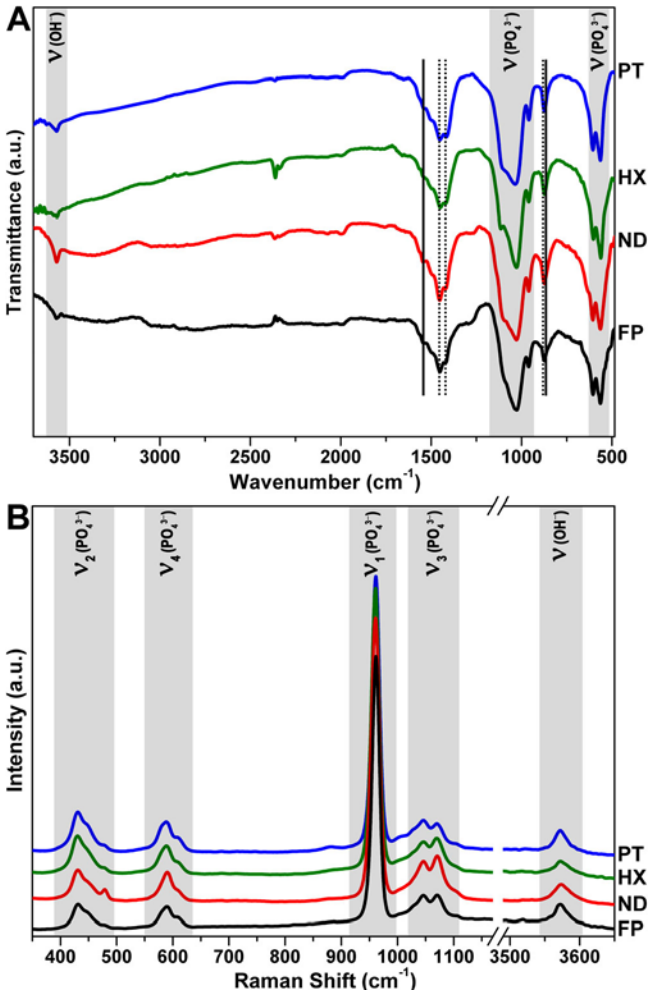

Fig. 5.8 Comparison of IR (A) and Raman scattering (B) data for the hydrothermally-derived **PT**, **HX**, **ND** and **FP** powdered products. The characteristic stretching modes attributed to the apatitic phosphate PO_4^{3-} and hydroxyl OH^- groups are marked by grey regions. Solid and dotted lines are drawn in (A) at the positions of CO_3^{2-} anions vibrations to indicate A-type (carbonate replacing hydroxyl) and B-type (carbonate replacing phosphate) of carbonated HA, respectively.

5.2.3.2. Raman scattering

Fig. 5.8B shows Raman scattering spectra from the powdered **PT**, **HX**, **ND** and **FP** samples. The summary of the assignments and Raman scattering wavenumber is presented in Table AI.5 (see Annexe I). The band positions for hydrothermally-derived HA phases are in good agreement with published data on bulk HA powder.[135] The spectra show a very intense characteristic peak at ~962 cm^{-1} owing to the symmetric stretching mode $v_1(PO_4^{3-})$. Apart from this v_1 mode, the other stretching modes of the PO_4^{3-} groups are also observed; namely, v_2 in the 391-502 cm^{-1} region, v_4 in the 559-646 cm^{-1} region and v_3 in the 1002-1110 cm^{-1} region.[135] The band at ~3572 cm^{-1} corresponds to the stretching vibration of the hydroxyl groups.[135] Additionally, in contrast to the **C-D36/T48** CPC (Section 4.2.4.3), the bands

representing HPO_4^{2-} anions –present in Ca-deficient HA– are absent in the Raman spectra of hydrothermally-prepared samples.[135]

5.2.3.3. Energy-dispersive X-ray spectroscopy

The semiquantitative calcium and phosphorous content in the prepared samples was determined by EDX. The average molar ratios of the Ca to P elements (Ca/P) are ~1.76, 1.74, 1.75 and 1.76 for the **PT**, **HX**, **ND** and **FP** samples, respectively. Overall, these values are in good agreement with the Ca/P ratio for stoichiometric HA (Ca/P = 1.67), as well as with the initial molar ratio of the precursors used for the hydrothermal synthesis (Table 5.1). Slightly higher Ca/P ratio values obtained for the hydrothermal products in comparison with stoichiometric HA could be ascribed to the partial substitution of PO_4^{3-} and OH^- groups in the HA lattice by CO_3^{2-} anions, in agreement with IR and bulk elemental analyses.

5.2.4. Hydrothermally-derived hydroxyapatite thermal stability

Representative results of TGA/DTA measurement of hydrothermally-derived **HX** are shown in Fig. 5.9. The values of weight loss between 25 and 1200°C are recorded to be approximately 5-6 wt.-% for all powders synthesized by hydrothermal route. TGA curve exhibits a continuous weight loss, overall, owing to the desorption of physically adsorbed water, loss of chemically bounded hydroxyl groups and CO_2 release during the decomposition of CO_3^{2-} anions, in consistent with IR, elemental analysis and Raman scattering. In contrast to the CPC (Section 4.2.5), the powder XRD analysis of the **HX** product after TGA/DTA experiment does not reveals partial transform of HA to any calcium orthophosphates phases (see Annexe II, Fig. AII.5). This fact additionally supports that hydrothermally-derived HA products are thermally stable stoichiometric HA.[9]

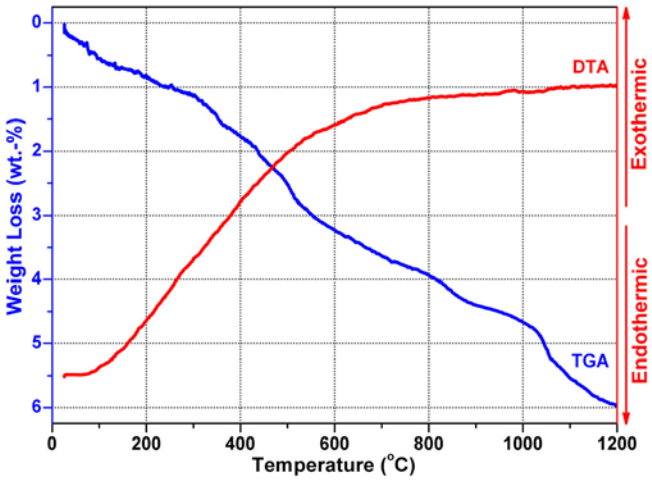

Fig. 5.9. TGA/DTA plot for hydrothermally-derived **HX** product acquired using a heating ramp of 10°C/min in air in the 25-1200°C temperature range.

5.2.5. Hydroxyapatite particle morphologies

Overall morphology of the synthesized HA powders, observed thorough by SEM measurements, are enlisted in Table 5.1 and also shown in Fig. 5.10. **PT** sample mostly consists of particles with plate-like morphology exhibiting a non-uniform size distribution. Crystal sizes in the as-prepared powder range from a few micrometer to a few tenths of a micrometer. Hydrothermal synthesis applying temperature profile of Scheme II (sample **HX**) leads to a distinct morphology. SEM observations of **HX** sample reveal an overwhelming quantity of elongated micrometer-sized particles with sharp faceted hexagonal prism-like morphology, which exhibit a relatively uniform size distribution: a width of about 1.5-2.1 μm and a length in the range from 9.5 to 15.5 μm (Fig. 5.10B). Using the same synthetic route but applying temperature regime of Scheme III (sample **ND**), continuous crystals with needle-like shape can be synthesized readily (Fig. 5.10C). The as-prepared **ND** particles exhibit a non-uniform size distribution with sizes ranging from several tenths of a micrometer to a few hundreds of a micrometer. In sharp contrast to the described **PT**, **HX** and **ND** products, synthesis using twice less amount of Ca and P precursors as well as applying temperature profile of Scheme IV (sample **FP**) generates HA crystals exhibiting considerable smaller sizes with less well-defined overall microstructure (Fig. 5.10D). According to SEM analysis, **FP** powder mostly consists of crystals exhibiting fine-plate-like (predominant) and rod-like particle morphology with typical sizes in the range from a few hundreds of a nanometer to several micrometers.

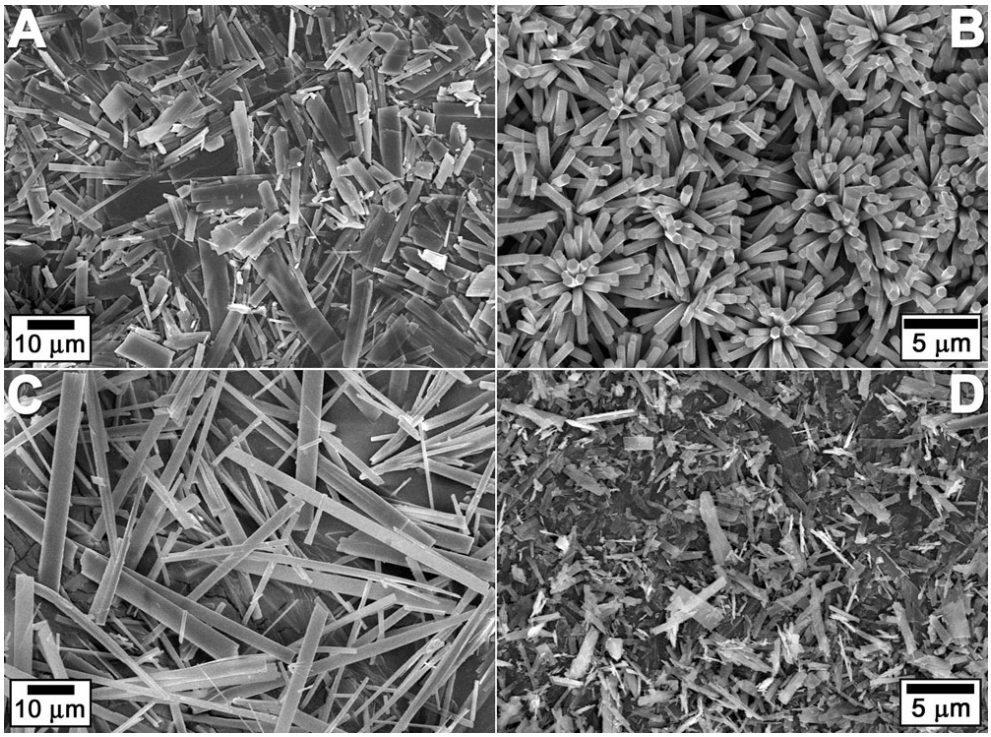

Fig. 5.10. Comparison of the morphological features of hydrothermally-derived products as imaged by SEM from **PT** (A), **HX** (B), **ND** (C) and **FP** (D) samples.

5.2.6. Hydroxyapatite particle microstructure

Main panel in Fig. 5.11A shows a representative low-magnification TEM image of **HX** product. This sample mostly consists of elongated micrometer-sized particles, in good agreement with the SEM observations (Fig. 5.10B). The corresponding [010]* electron diffraction pattern is displayed as right top inset in Fig. 5.11A, wherein all major diffraction spots can be completely indexed in the hexagonal $P6_3/m$ space group, using the HA phase unit cell parameters of JCPDS No. 21-1272. According to a careful ED study, the particles of **HX** are exclusively oriented with their axis along [010], indicating the crystal growth along the *c*-axis, which is consistent with texturing effect observed by XRD (Fig. 5.7B). Moreover, ED analysis reveals the same geometry of ED patterns along the *c*-axis, manifesting that each HA particle is a single crystal. All ED reflections are also very distinct and sharp, indicating the perfection of the as-prepared HA crystals. A representative HRTEM image along [010] zone axis from **HX** sample is given as right bottom inset in Fig. 5.11A, which exhibits extended, defect free lattice fringes, thus, along with ED, confirming nearly perfect HA structure of **HX** sample.

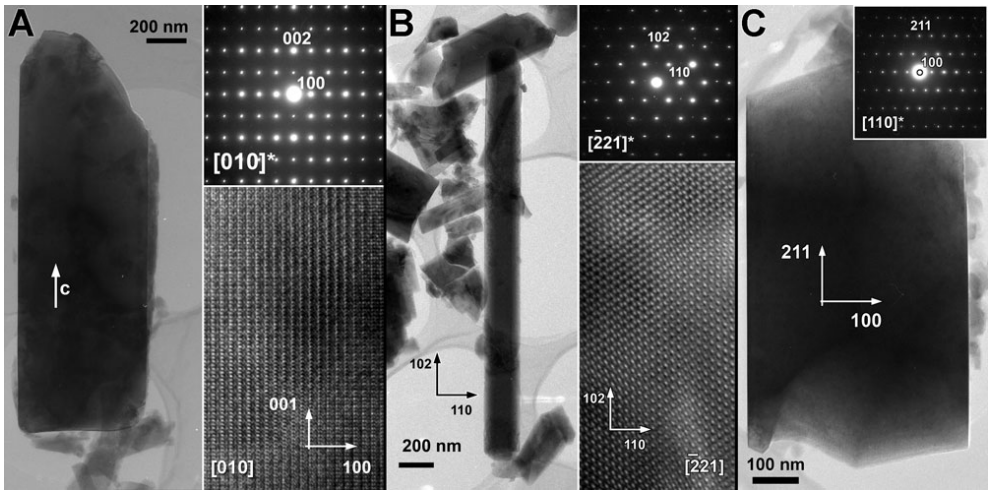

Fig. 5.11. A low-magnification TEM images (main panels) together with corresponding ED patterns (right top insets) and HRTEM images (right bottom insets) along most prominent growth directions of HA crystals: along (001) in sample **HX** (A) as well as along (102) and (211) in sample **FP** (B, C).

In contrast to **HX** sample, TEM shows the presence of two types sub-micro/micrometer-sized well-crystallized particles in hydrothermally-derived **FP** product (Fig. 5.11B, 5.11C, main panels) –thin and long rod-like and nearly rectangular predominant plate-like crystals. According to the ED analysis (Fig. 5.11B, 5.11C, right top insets), both these morphologies are phase-pure HA particles possessing different growth directions;

namely, rods exhibit [$\bar{2}$21] orientation, while the plates are [110] oriented, growing along the (102) and (211) directions, respectively. ED also reveals the single-crystalline nature and structural perfection of these characteristic HA structures of **FP**, which is subsequently confirmed by HRTEM investigations. The right bottom inset in Fig. 5.11B displays a representative HRTEM image from HA single crystal along [$\bar{2}$21] zone axis. Close inspection of individual crystals on a largely scale reveals the absence of any types of structural defects throughout the particles, proving their nearly ideal real microstructure.

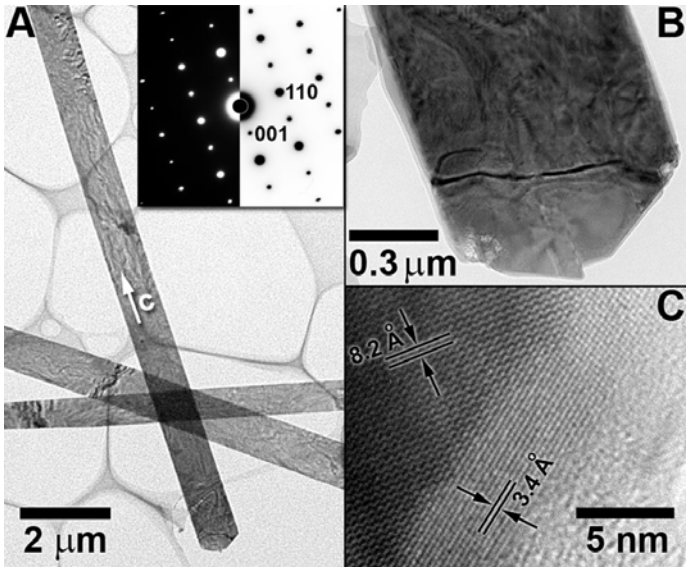

Fig. 5.12. (A) – A low-magnification TEM image and corresponding ED pattern (inset) of HA needle of sample **ND**; (B) – TEM image of the terminal end of HA needle in (A); (C) – HRTEM image of an edge area of the lamellar terminal end of HA needle in (B), with (210) and (002) lattice planes visible.

Fig. 5.12A shows a representative low-magnification TEM image and corresponding ED pattern (Fig. 5.12A, inset) of the as-prepared **ND** powdered product. The sample mostly consists of well defined and sharp faceted needles-like crystals, in good agreement with the SEM data (Fig. 5.10C). ED investigation reveals overall phase-purity, single crystals with high crystallinity of the needles-like crystal in **ND** sample. The terminal end of HA needle in Fig. 5.12A is shown on Fig. 5.12B, which demonstrates the presence of local deformations in the as-synthesized **ND** particles, *i.e.* the crystal surface in not smooth in nanoscale. HRTEM analysis (Fig. 5.12C) of an edge area of the terminal end of HA needle also indicates that the needle is highly crystalline and planar defect-free. The crystal lattice can be estimated to be about 8.2 and 3.4 Å, corresponding to the (210) and (002) planes of the hexagonal crystal structure of HA, respectively, indicating that the needles in **ND** hydroxyapatite product grow along the *c*-axis, which is in good agreement with XRD data, described above (Fig. 5.7A).

5.2.7. Direct probing of the mechanical properties of hydroxyapatite single crystals

The mechanical properties of phase-pure, structurally nearly perfect HA single crystals with well-defined hexagonal prism-like morphology (sample **HX**) were studied using nano-indentation. Two representative load *versus* displacement curves collected on both prism- and basal-faceted crystal's planes are shown in Fig. 5.13A. These load-displacement profiles smoothly follow the loading function without any discontinuities or pop-in marks, confirming that no cracks arise during NI measurements.[180] According to the displacement profiles, the peak load of 1 mN generates residual indentation depths in the 15-20 nm range. The elastic modulus E_s and hardness H values of the HA single crystals were calculated to be about 62.1 ± 7.0 GPa and 5.9 ± 0.8 GPa for the prism-faceted plane and 68.3 ± 8.0 GPa and 5.7 ± 0.9 GPa for the basal-faceted plane, respectively. Nevertheless, the calculated hardness values are established to be not significantly different statistically (Mann-Whitney rank sum test (P = 0.359)).

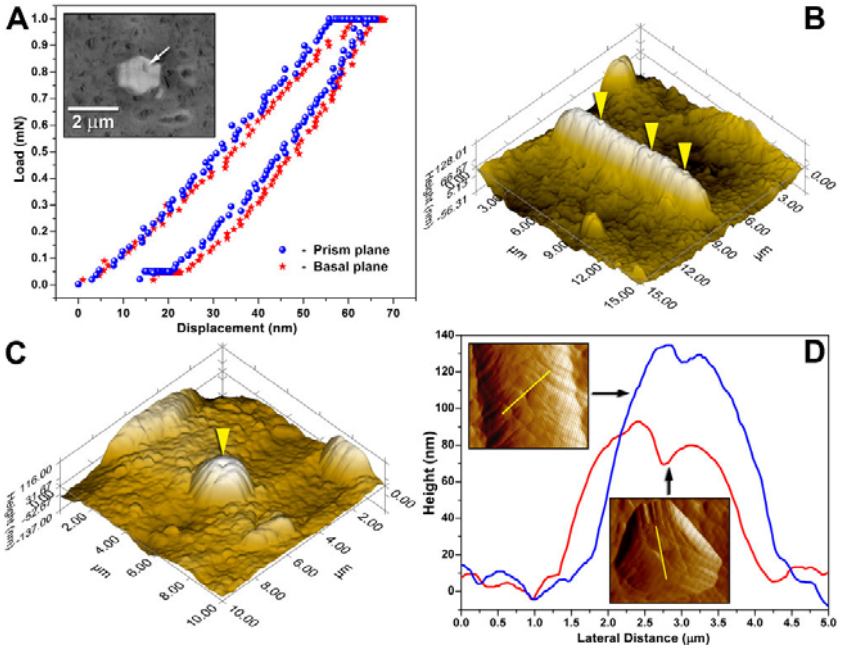

Fig. 5.13. Representative load *versus* displacement curves (A) together with 3D AFM topography view of the indentation impressions (marked by yellow arrows) acquired by NI probing on the prism-faceted (B) and basal-faceted (C) planes of HA crystals having well-defined hexagonal prism-like particle morphology. The inset in (A) is FE-ESEM image of a specimen surface after NI measurement, also showing the nanoindent impression. Cross-sectional highness profiles are compared in (D) with respect to the probed *a*- and *c*-surface exposed HA crystals.

The inset in Fig. 5.13A shows a representative FE-ESEM image of the surface of nearly regular in shape basal-faceted HA crystal after nano-indentation. The NI probing expectedly results in nearly equilateral triangle-shaped indent impressions with typical sides'

lengths of ~0.4 μm. No cracks are observed by FE-ESEM, which is in good agreement with the behavior of the load-displacement curves (Fig. 5.13A). A view of the nanoindents can be observed more closely from the AFM topography imaging owing to the higher spatial resolution of this technique in comparison to the electron microscopy. Representative 3D AFM images of the nearly regular triangle pyramid-faceted impression from the *a*- and *c*-surface exposed HA crystals are displayed in Fig. 5.13B and 5.13C, respectively. According AFM observations, the probed crystals have diameters of 1.5 to 2.0 μm and lengths in the range from 10 to 15 μm. Their surfaces appear to be relatively curved in nanoscale, but exhibiting lack of any inappropriate nanostructuring. All measured HA crystals are found to be well-fixed in the calcium phosphate bone-cement matrix (Section 5.1.2), since the dragging of cement-embedded particles by the Berkovich tip is not detected. In Fig. 5.13D, the thickness profiles of the nanoindents from two different planes, obtained from the sections marked in the respective images, are shown. These profiles reveal that both probed crystal planes exhibit the residual indentation depths of about 12-16 nm, which is consistent with those ones deduced from the load-displacement curves (Fig. 5.13A). Moreover, the asymmetry of these profiles at the top clearly highlights the flow of the material above the edges of the nanoindents during probing, so-called pile-up (Fig. 5.13D) –a characteristic feature of single-crystalline particles. This observation is consistent with TEM study.

5.3.- DISCUSSION

Many research groups have previously investigated the preparation of HA with different materials properties, in particular, morphological features. In the majority of the reported approaches, the phase-pure HA products are commonly characterized by either rod-like (whiskers, needles, wires, fibres, *etc.*)[111, 136, 137] or plate-like[137, 140, 141] particle morphology. In addition, few reports have been published where HA powders exhibit hexagonal prism-,[129, 134, 142, 143] elliptical-,[133, 144] or ribbon-like[145] particle shape. Despite morphological difference, the as-derived HA crystals typically grow along the [001] of the hexagonal structure, the natural tendency of HA as, *i.e.*, in bones (Section 2.1.1.2). Hence, the synthesis of differently oriented HA crystals still remains a challenge. It should be emphasized, that the application for most of aforementioned synthetic procedures is somewhat limited owing to the utilization of different additives (coordinating ligands,

surfactants, *etc.*)[137, 141, 143-145] or incorporation of foreign ions into the crystal lattice of the end products.[134, 145] Additionally, most of the reported syntheses are not well developed in terms of high-yield, homogeneity of materials properties and feasibility of large-scale production.

In the current investigation, a direct hydrothermal reaction between $Ca(NO_3)_2{\cdot}4H_2O$ and $(NH_4)_2HPO_4$ has been chosen to generate HA powders at the low temperature of 90°C (Table 5.1). All the samples were prepared using urea as a homogeneous precipitation agent, which exhibits an intrinsic capacity for *in situ* releasing of ammonia species due to its hydrolytic thermal decomposition (Eq. 2.6, 2.7). Respective increasing of $NH_{3(aq)}$ amounts results in a gradual increasing of the solution pH, eventually providing a proper basic aqueous media for the thermodynamically favourable formation of the phase-pure HA (Fig.2.18).[53] The main advantage of urea-assisted approach is that urea hydrolyzed homogeneously –if the reaction medium is uniform with respect to the concentrations and temperature– thereby generating the driving force toward the nucleation and growth of the HA crystals under moderated supersaturation conditions. Since the decomposition of $(NH_2)_2CO$ is a thermally-induced, temperature-dependent process,[153] herein, we attempt to governed its decomposition rate, and accordingly the saturation of the reaction solution, applying different temperature profiles in the course of hydrothermal treatment.

According XRD and Raman scattering, all as-synthesized samples are phase-pure hexagonal hydroxyapatite (Fig. 5.7A, 5.8B, respectively). Additionally, XRD patterns reflect a textured microstructure of **PT**, **HX** and **ND**, indicating *c*-axis orientation of the crystals in these samples, whereas this texturing trend was not observed for **FP** product (Fig. 5.7B). The latter observation corresponds to the overall smaller size of the **FP** crystals and their various orientations (TEM). EDX studies clearly confirm that all as-prepared HA samples are slightly non-stoichiometric HA, having Ca/P molar ratio of ~1.75. As established by IR spectroscopy, the observed non-stoichiometry resulted from partial substitution of the OH^- and PO_4^{3-} anions by CO_3^{2-} groups in the HA crystal structure (Fig. 5.8A). Thus produced HA are of AB-type carbonated hydroxyapatite. This is consistent with the elemental analysis, showing ~0.75 wt.-% carbon content in the synthesized HA products. It is worth noting that biological apatite contains 3-5 wt.-% carbonate groups.[9] It should be noted that, in contrast to calcium phosphate bone-cement, the presence of the HPO_4^{2-} anions –existing in Ca-deficient HA– was not observed by IR, Raman scattering or TGA/DTA analysis, indicating the regularity of the Ca sublattice in hydrothermally-derived HA products.

According to the SEM data, samples with different particle morphology were generated (Fig. 5.10) depending upon applied temperature profile and initial concentrations of starting compounds (Table 5.1). When the hydrothermal synthesis is conducted at the constant temperature of 90°C (Scheme I), the urea is intensively decomposed providing enhanced supersaturation, which should generate a large number of nuclei, and consequently, preferably smaller crystals should formed. However, in our case, synthesis by Scheme I yielded highly crystalline HA powder, which is predominantly composed of elongated, plate-like crystals with different size on a micrometer scale (sample **PT**, Fig. 5.10A). In general, the synthesis of HA is proceed through the formation of octacalcium phosphate $Ca_8H_2(PO_4)_6{\cdot}5H_2O$ (OCP), which acts as precursor for the final HA formation.[9] Overall, OCP crystals are characterized by the plate-like particle morphology.[200] Therefore, it is believed that the plate-like shape and large size of **PT** crystals are due to a kinetic effect, in particular, a result of the epitaxial transformation from transitory existed intermediate OCP phase to HA.[200] This is possible owing to the structural similarity between both calcium orthophosphates.[54] A non-uniform size distribution of as-derived **PT** plate-like crystals is presumably related to the differing rates of the plate-like crystal growth during hydrothermal synthesis.

The resulting morphology of a stepwise decomposition of urea (Scheme II in Fig. 5.2) is very different than aforementioned one for kinetically-determined intensive decomposition (Scheme I). SEM reveals that the hydrothermal synthesis by Scheme II efficiently extended the overall particle morphology to a well-defined hexagonal prism-like shape, thus mimicking the crystal habit of the HA hexagonal-bipyramidal class (sample **HX**, Fig. 5.10B). This indicates that the reaction under gentle supersaturation conditions is shifted toward the formation of the thermodynamically favourable product, thereby excluding the intensive epitaxial growth of HA from the OCP template in form of plates. TEM, ED and HRTEM analyses confirm that the micrometer-sized particles of **HX** are indeed HA single crystals devoid of any structural defects and oriented along *c*-axis (Fig. 5.11A). The as-prepared hexagonal prism-like HA particles should possess an increased selectivity toward adsorption of negatively charged acidic proteins due to the well-developed *a*-surface (Section 2.7.2.1, Fig. 2.26).

SEM examination of hydrothermally-derived **ND** powder clearly demonstrates that this HA product is composed of sharply faceted microcrystals having needle-like particle morphology (Fig. 5.10C). This is consistent with controlled slow decomposition of urea *via* Scheme III (Fig. 5.2), wherein small numbers of nuclei are generated, resulting in large crystals size. TEM investigation proves that the needle-like particles in the sample **ND** are

planar defect-free HA single crystals growing along *c*-axis (Fig. 5.12). Existence of local deformations in hydrothermally prepared whiskers was also revealed by TEM (Fig. 5.12A, 5.12B).

Our attempts to further slowdown the thermal decomposition of urea applying temperature profile of Scheme IV (Fig. 5.2), maintaining the rest of the experimental parameters the same, were failed. The powder XRD analysis of the as-derived product shows that such interrupted urea decomposition pathway does not results in the formation of significant amount of HA, and OCP was found to be a predominant phase. In the same time, a single phase HA product without any admixture is formed readily (samples **FP**, Fig. 5.7A) when 2 times less concentration of the initial components was used for the hydrothermal synthesis by Scheme IV (Table 5.1). The as-derived powdered sample is composed of the particles with fine-plate-like (predominant) and rod-like appearance, as imaged by SEM (Fig. 5.10D). In addition, the particles size of **FP** product is much smaller than that of **PT**, **HX** and **ND** samples.

Further, the influence of the concentration of the starting reagents on the nature of the product was also investigated. The syntheses by Scheme I, II and III started from 2 times less concentrations of starting compounds lead to the single phase HA samples, exhibiting practically the same particle shape and size as the **FP** sample derived by Scheme IV (see Annexe I, Table AI.2). This highlights that the morphological characteristics of the product under certain hydrothermal conditions are affected primarily by the concentration. Hence, despite the applied temperature profile, an effective morphology control of HA particles *via* governed thermal decomposition of urea is limited in the diluted precursor system.

Detailed TEM, ED and HRTEM studies (Fig. 5.11B, 5.11C) confirm that the particles in **FP** sample have hexagonal HA crystal structure. Besides a predominant formation of fine-plate crystals with their axis oriented along [110], TEM indicates also formation of rod-like particles oriented along $[\bar{2}21]$, thereby growing along the (211) and (102) directions, respectively. This is somewhat surprising, because HA particles exhibit a natural tendency to grow along the *c*-axis, *i.e.* as observed for **HX** sample (Fig. 5.11A) or in bones (Section 2.1.1.2). The as-synthesized rarely oriented HA particles can exhibit promising selective adsorption properties.[121] ED and HRTEM also prove the single-crystalline nature and largely planar defect-free crystal structure of the particles in **FP** (Fig. 5.11B, 5.11C), thus demonstrating nearly ideal fine microstructure of the HA crystal originated from hydrothermal synthesis.

Recently, HA exhibiting various morphological features is among the more promising class of compounds to reinforce the mechanical properties of the bioceramics and calcium phosphate bone-cements, used in medical practice as grafts. In addition, HA based composite materials are also intensively used to mimic and investigate the mechanical behaviour of bone. Therefore, it is beneficial to study the mechanical properties of the HA single crystals, which might lead to further understanding of mechanistic behaviour of the biocomposites materials. Carrying out direct measurements of the mechanical properties on HA micrometer single crystal is nontrivial process; however recent development of nano-indentation technique has enabled researchers to characterize mechanical properties at the nano level. Owing to the appropriate crystals size and shape, phase-purity, well-defined hexagonal prism-like particle morphology, single-crystalline nature and absence of structural defects, the hydrothermally-derived **HX** product has been chosen to realize NI investigation.

Both prism-faceted and basal-faceted planes representing *a*-surface and *c*-surface exposed HA crystals were probed (Fig. 5.5A, 5.5B). It was established that the respective *a*- and *c*-surface of the HA single crystals exhibit a very small deformation under a constant applied load, so-called creep (Fig. 5.13). This fact is due to the single-crystalline nature of the probed HA particles, related with the degree of orientation and regularity in the structure leading to a minimum number of slip systems in HA single crystals. In addition, AFM observations reveal the appearance of piles-up, a typical feature of single crystals (Fig. 5.13D). Therefore, these date together with TEM investigation mark one of the most remarkable point of our NI experiments, confirming that we have been able to investigate mechanical properties of single crystals.

According to NI experiments, it was established that prism-faceted and basal-faceted planes possess elastic modulus of 62 ± 7.0 GPa and 68 ± 8.0 GPa, respectively (peak load 1 mN). This NI result shows that *c*-axis orientation is ~11.5% stiffer than *a*-axis one, indicating an anisotropy for HA elastic properties, most likely due to a more close packed nature of *c*-surfaces (Section 2.7.2.1).[120] The similar anisotropic elasticity trend was also observed by Viswanath *et al*. in HA single crystals prepared by molten salt synthesis,[201] and the reported differences in elasticity between basal-faceted and prism-faceted planes were ~7% or ~27%, depending upon the employed NI load function.[201] Nevertheless, they measured E_s values of ~130 GPa which are reasonably higher than that of the present **HX** hydroxyapatite crystals, but at the same time, in good agreement with NI results on HA ceramics (~122 GPa).[202] In

contrast, Teraoka *et al*. reported a E_s value of ~64 GPa for the *a*-surfaces of HA crystals synthesized by hydrothermal method at moderate temperature (200-300°C).[203] This value match well with that of the respective surface of **HX** hydroxyapatite crystals. Interestingly, the E_s values of the synthesized phase-pure HA agrees with elastic modulus of biological HA from tooth enamel (~60 GPa).[204] Therefore, it certainly appears that the observed difference in E_s values is due to the influence of preparation technique on elastic modulus. In terms of synthesis, HA crystals prepared by molten salt[201] and HA ceramic obtained by sintering[202] were generated at high temperatures (T > 1000°C). Owing to the annealing of the lattice impurities and defects, such high-temperature synthetic procedures lead to the formation of HA products structurally very close to the ideal HA. Thereby, high E_s values were observed, which are almost attain E_s value calculated for basal-faceted plane of a HA perfect single crystal (~138 GPa).[205]

NI probing reveals that the prism-faceted and basal-faceted planes of single-crystalline HA with hexagonal prism-like particle morphology exhibit hardness of 5.9 ± 0.8 GPa and 5.7 ± 0.9 GPa, respectively (peak load 1 mN). However, in contrast to the published data,[201] these two values are found to be a like within one standard deviation. The lack of difference between H values for *a*- and *c*-surfaces most likely stem from technical limitations. Specifically, the crystal surface appears to be slightly curved (Fig. 5.13B, 5.13C, 5.13D), while performing measurements using a peak load of 1 mN generates indentation depths in the order of nanometers. Consequently, estimating the contact area from the contact depth can lead to significant errors when the surface exhibits such an uneven surface at the nanoscale. Hence, a difference of hardness from the prism-faceted and basal-faceted planes of **HX** crystals can not be excluded.

5.4.- CONCLUDING REMARKS

The hydroxyapatite powdered samples were successfully synthesized on a gram scale through urea-assisted hydrothermal reaction between $Ca(NO_3)_2{\cdot}4H_2O$ and $(NH_4)_2HPO_4$ at a low temperature of 90°C. The results demonstrate that the particle morphology of the HA crystals can be easily controlled by judiciously varying the decomposition kinetics of urea and concentration of initial components in the course of hydrothermal process. Detailed experimental studies clearly demonstrate that as-derived products are composed of single-crystalline, structural defect-free, carbonated hydroxyapatite crystals, exhibiting plate-like,

hexagonal prism-like, needle-like and fine-plate-like particle morphology. Furthermore, we have been able to probe mechanical properties of the hydroxyapatite single crystals by nano-indentation, and the obtained data conclusively highlight that the hardness and elastic modulus are determined by the crystal orientation and synthetic route.

Hydrothermally as-synthesized high-quality HA crystals with four different particle morphologies were further used for the reinforcement of advanced **C-D36/T48** cement (Chapter IV) in order to generate biocomposite cements with enhanced mechanical properties (Chapter VI).

VI

BIOCOMPOSITES

6.1.- EXPERIMENTAL PART

6.1.1. Preparation of reinforced biocomposite cements

In order to generate a family of biocomposite cements, nanocrystalline, bioactive calcium phosphate bone-cement **C-D36/T48**, which exhibited the quickest curing onset and the fastest conversion rate (Chapter IV), was reinforced with hydrothermally-derived hydroxyapatite crystals of various particle morphologies (Chapter V). The influence of the shape, size and volume fraction of the HA reinforcement crystals on the biocomposites' mechanical properties was investigated.

In a typical procedure, equimolar amounts of ball-milled DCPD and TTCP powders were thoroughly ground together using an agate mortar and pestle. Next, the desired amount (Table 6.1) of HA crystals with plate-like (**PT**), needle-like (**ND**), hexagonal (**HX**) or fine-plate (**FP**) morphology were well-dispersed using a hand spatula. This was followed by gentle mixing in an agate mortar (Fig. 6.1). Commercial HA (**SP**) composed of spherical aggregates (Fig.6.2) was also examined for the reinforcement (HAP, Mitsubishi Chemical Co., Ltd). The resulting fine powder (total 0.6 g) was placed inside a latex finger cot and an appropriate amount of distilled water was added to the composite CPC precursor using a micropipette. This amount of liquid phase was calculated to maintain a solid to liquid (S/L) ratio of 2, on the basis of the DCPD and TTCP cement precursors, with the reinforced phase being not considered. The mixture was hand kneaded for 1 minute and then placed into a cylindrical mold assembly of 6.9 mm diameter. The batch was pressed under 5.3 MPa for 1 min using a pressure-loading device. After pressing, the biocomposite specimen was removed from the mold and kept for 1 h at ambient conditions to set before being incubated in acellular simulated body fluid solution at human body temperature of 37°C for 23 hours. Finally, the as-derived biocomposite cements were subjected to detailed characterization studies employing different techniques.

Throughout the current work, a set of acronyms is used (Table 6.1). The first three letters **CPC** indicate advanced **C-D36/T48** calcium phosphate bone-cement matrix, the numbers show weight percentages **wt.-%** of the respective reinforcement phase, while the last two letters reflect the particle morphology of the reinforcement phase: **SP** – spherical aggregates, **PT** – plate-like, **HX** – hexagonal prism-like, **ND** – needle-like, **FP** – fine-plate.

Fig. 6.1. The hydrothermally-derived HA powdered product (top left panel), the reinforcement phase during and after hand spatula dispersing (top right and bottom left panels, respectively), the reinforcement phase and the CPC precursors (TTCP and DCPD) at the agate mortar (bottom central panel), and the resulting fine powders mixture after gentle grinding.

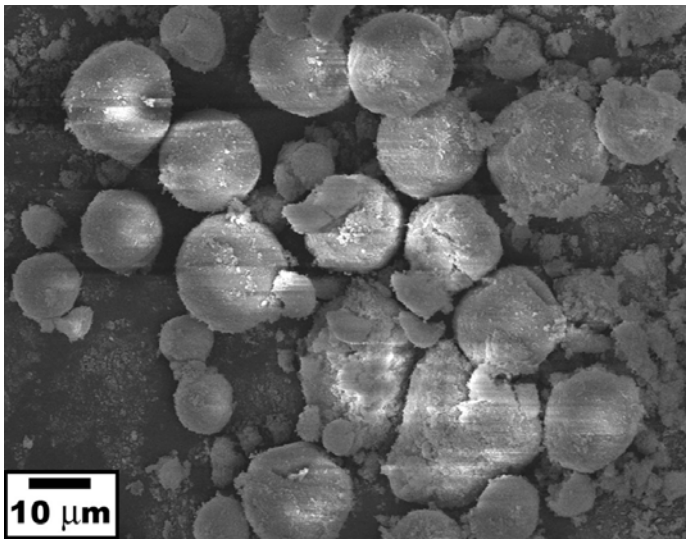

Fig. 6.2. Typical SEM image of the spherical aggregates in the commercial hydroxyapatite HAP purchased from Mitsubishi Chemicals Co., Ltd.

Table 6.1. Specification, phase composition and compression strength of reinforced biocomposite cements.

Sample [a]	Overall morphology of the HA reinforcement phase	Amount of the HA reinforcement phase		XRD and Raman phase composition [c]	Compression strength (MPa) [c]
		wt.-%	vol.-% [b]		
Selection of the optimal particle morphology					
Pure CPC	—	—	—	HA	25 ± 3
CPC-10%SP	Spherical aggregates	10	7	HA	28 ± 0.3
CPC-10%PT	Plate-like	10	7	HA	27 ± 1
CPC-10%HX	Hexagonal prism-like	10	7	HA	30 ± 3
CPC-10%ND	Needle-like	10	7	HA	28 ± 2
CPC-10%FP	Fine-plate-like	10	7	HA	37 ± 3
Selection of the optimal volume fraction					
CPC-5%HX	Hexagonal prism-like	5	3	HA	31 ± 3
CPC-10%HX		10	7	HA	30 ± 3
CPC-15%HX		15	10	HA	33 ± 2
CPC-20%HX		20	14	HA	27 ± 0.6
CPC-30%HX		30	22	HA	26 ± 4
CPC-5%FP	Fine-plate-like	5	3	HA	31 ± 4
CPC-10%FP		10	7	HA	37 ± 3
CPC-15%FP		15	10	HA	29 ± 4
CPC-20%FP		20	14	HA	23 ± 1
CPC-30%FP		30	22	HA	20 ± 0.3

[a] – **CPC** is advanced **C-D36/T48** calcium phosphate bone-cement, developed in the present work (Chapter IV).; [b] – volume percentages were calculated assuming density of 3.146 g/cm^3 for the reinforcement phase (crystallographic density of hydroxyapatite) and bulk density of 1.878 g/cm^3 for the **C-D36/T48** pure cement (mercury porosimetry results, see Section 4.2.6); [c] – estimated after 24 h of setting reaction (1 h setting at ambient conditions and then immersed in SBF for 23 h at 37°C).

6.2.- RESULTS

6.2.1. Phase composition product analysis

The summary of the specification, phase composition and compression strength of all prepared reinforced biocomposite cements are presented in Table 6.1.

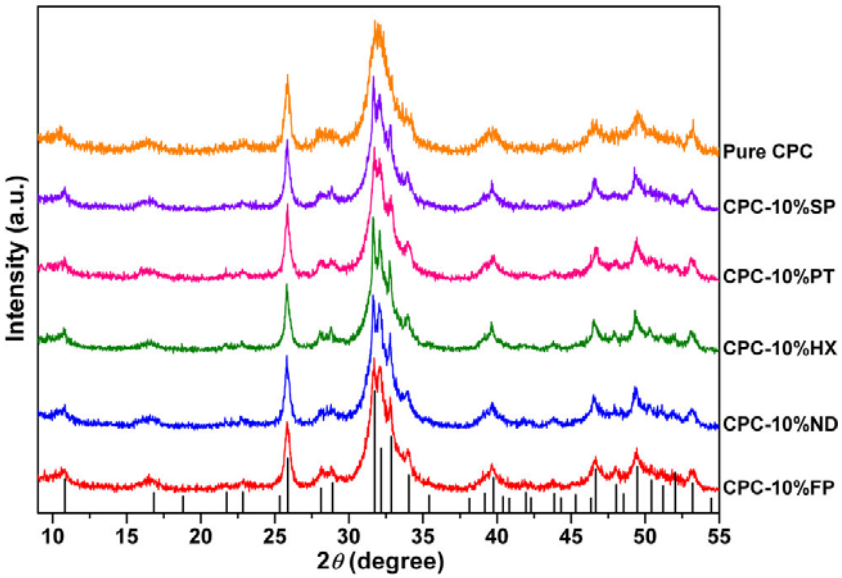

Fig. 6.3. Comparison of the reinforced and pure cements products (Table 6.1) by powder XRD. The as-produced CPCs were allowed to set for 1 hour at ambient conditions and then incubated in distilled water for 23 hours at 37°C. Tick marks below the patterns correspond to the positions of the Bragg reflections expected for the hexagonal HA phase (JCPDS No. 72-1243). Note the similarity between powder XRD patterns of all reinforced biocomposite cements as well as their entire conversion to HA after 24 hours of setting reaction.

According to the powder X-Ray diffraction analysis, all prepared composite samples closely resemble phase-pure HA (JCPDS No. 72-1243). Fig. 6.3, shows the XRD patterns of biocomposite cements reinforced with 10 wt.-% of HA crystals of various particle morphologies derived over 24 hours with 1h setting time at ambient conditions that have subsequently been soaked in SBF for 23 h at 37°C. All biocomposites exhibit very similar diffraction patterns, which are also closely similar to the pattern derived from pure **C-D36/T48** CPC. The resolution of the XRD reflections from the composite cements is higher due to the presence of well crystallised HA filler. However, the XRD patterns are still characterized by low intensities and very broad peaks; this is a result of the nanocrystalline nature and defective HA structure of the pure cement matrix (Section 4.2.7).

In accordance with the trend seen in the XRD analysis, all 24 hour-derived reinforced biocomposite cements show very similar Raman spectra. As an example, Raman spectra collected from the **CPC-10%HX** and **CPC-10%FP** samples are presented in Fig. 6.4 and the

assignments of the observed characteristic bands are given in Table AI.6 (see Annexe I). The band positions are in good agreement with published data on bulk hydroxyapatite[135] as well as with Raman scattering results observed in the present work (Section 5.2.3.2), indicating the phase purity of all composite products (Table 6.1). It should be noted that the set of bands resulting from HPO_4^{2-} anions present in pure Ca-deficient HA cement (Section 4.2.4.3) is not observed for the biocomposites. This can be ascribed to the presence of a highly crystalline HA reinforcement phase which exhibits high intensity, thus making impracticable the resolution of the weak bands attributed to the cement matrix.

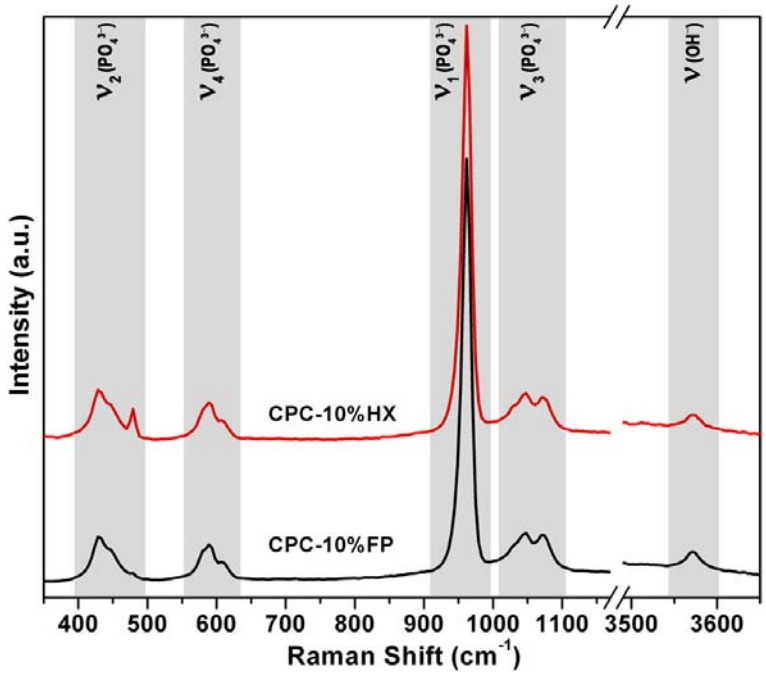

Fig. 6.4. Comparison of the Raman scattering data for the 24 hour-derived **CPC-10%HX** and **CPC-10%FP** biocomposites products. The characteristic stretching modes attributed to the apatitic phosphate PO_4^{3-} and hydroxyl OH^- groups are marked by grey regions.

6.2.2. Biocomposite morphology and microstructure

Investigation of the biocomposite setting reaction using SEM illustrates remarkable differences in the product morphologies throughout the setting reaction. As an example, SEM images of **CPC-10%FP** and **CPC-15%HX** before and after 24 hours of setting reaction are presented in Fig. 6.5. The SEM images of both unreacted biocomposites show reasonably exaggerated sub-micrometer-sized particles of DCPD and TTCP cement precursors (Fig. 6.5A, 6.5C), consistent with previous SEM results (Section 4.2.1). The SEM analysis of these samples also reveals the presence of well-dispersed, micrometer-sized HA filler crystals with visible fine-plate- and hexagonal prism-like particle morphologies (Fig. 6.5A and 6.5C,

respectively). This is also in agreement with previous SEM data for hydrothermally-derived HA (Section 5.2.5). However, SEM studies of the 24 hour-derived **CPC-10%FP** and **CPC-15%HX** products demonstrate that the precipitated nanocrystals, originating from the cement matrix, thoroughly cover the surface of the reinforcement HA crystals (Fig. 6.5B and 6.5D, respectively). A high magnification SEM image (Fig. 6.5D, inset) from selected region also reveals that the cement nanocrystallites exhibit close physical contacts with the surface of respective filler as expected.

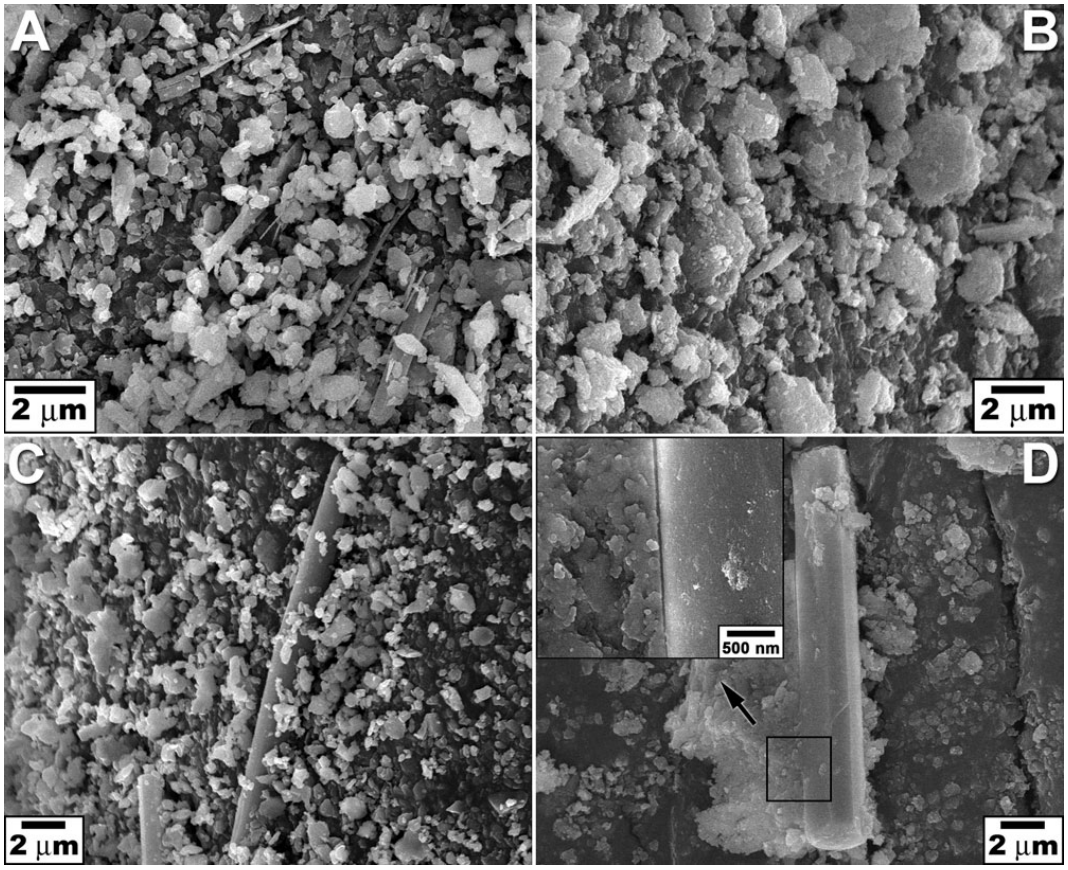

Fig. 6.5. Comparison of reinforced biocomposite cements' morphologies. SEM images of the unreacted DCPD, TTCP and HA filler powders mixture: (A) and (C) – samples **CPC-10%FP** and **CPC-15%HX**, respectively. (B) and (D) – SEM images (inset: high magnification SEM) of the same composite biomaterials after 24 h of setting reaction, respectively.

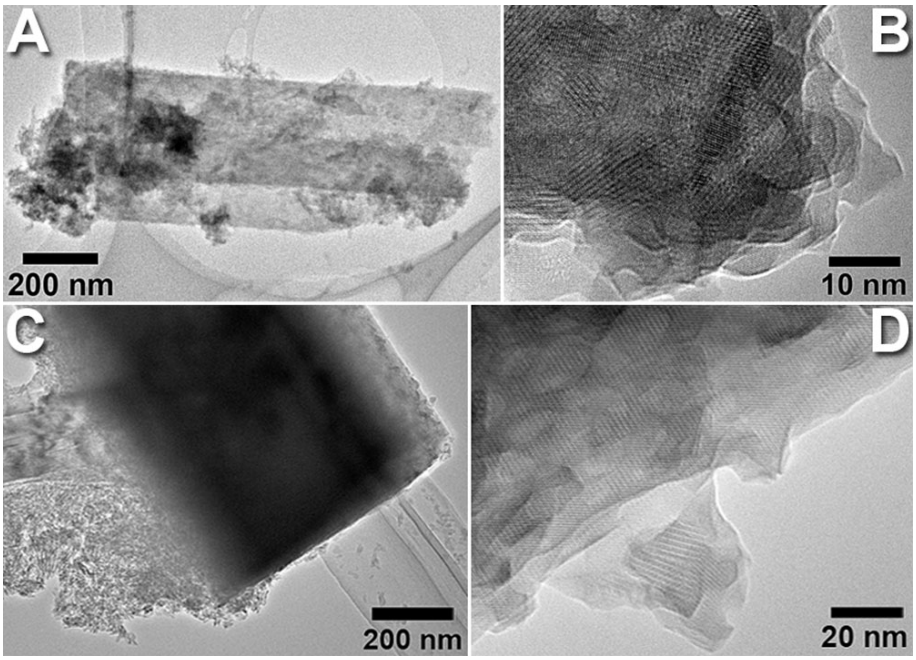

Fig. 6.6. A low-magnification (left panels) and high-resolution (right panels) TEM images of the 24 hour-derived **CPC-10%FP** (A, B) and **CPC-15%HX** (C, D) biocomposite cements illustrating close physical attachment of the cement platelet nanocrystallites to the fine-plate and hexagonal prism-like HA filler crystals.

TEM investigations of the prepared biocomposite cements subsequently confirm a close association of the cement matrix and filler. Fig. 6.6 shows the low-magnification and high resolution TEM images from the **CPC-10%FP** and **CPC-15%HX** biocomposites, reinforced by 10 and 15 wt.-% of HA crystals with fine-plate- and hexagonal prism-like particle morphologies, respectively. There is good interparticle contact between big crystals of the reinforcement phase and cement nanocrystallites (Fig. 6.6A, 6.6C), however, any defined chemical bonding or intergrowth of these two morphologies is clearly absent. The HRTEM images of the **CPC-10%FP** and **CPC-15%HX** composite samples are presented in Fig. 6.6B and 6.6D, respectively. In these figures interlocked nanoparticles with well-developed lattice fringes are seen. The crystallite sizes lie within the range of 8-15 nm, almost the same as compared with **C-D36/T48** pure CPC sample (Section 4.2.7). The nanoparticles have good crystallinity and are structurally defect free.

Thus, SEM and TEM observations lead to the conclusion that reinforced biocomposites are constituted of nanoscaled cement particles which are in close physical contact with the reinforcement crystals, overall forming a comprehensive associated microstructure inside the reinforced biocomposite cements.

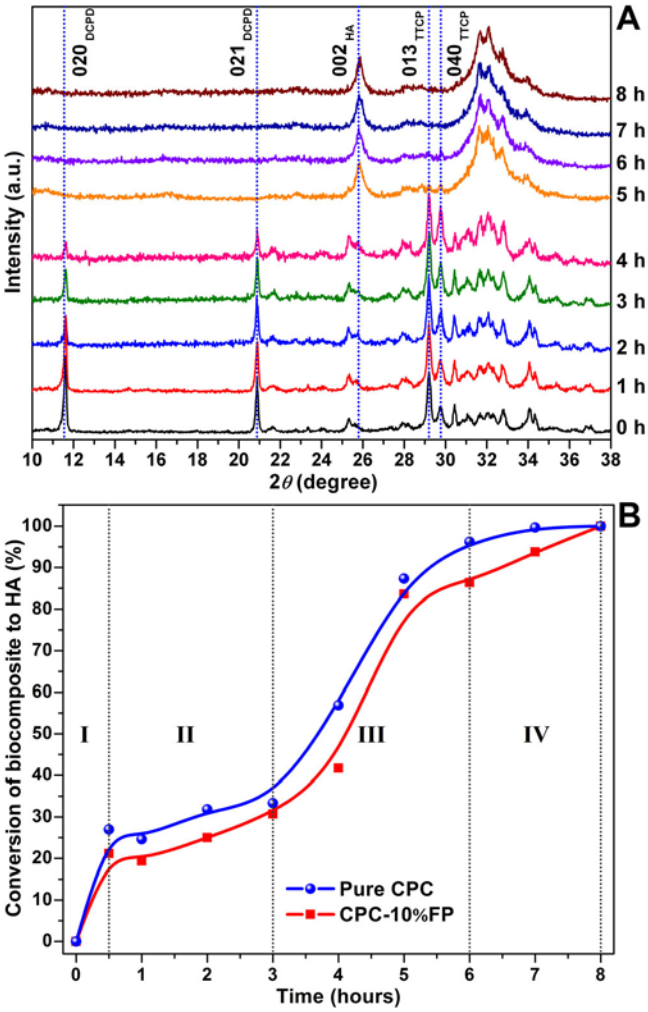

Fig. 6.7. Comparison of the XRD patterns at different times of setting reaction (A) together with estimated conversion data (solid red line in B) for the **CPC-10%FP** biocomposite cement sample. Solid blue line in (B) corresponds to the conversion data for the pure cement, drawn for comparison reasons. The dotted lines in (A) correspond to the diffraction peaks of DCPD, TTCP and HA used for the calculation of the conversion percentages of the **CPC-10%FP** biocomposite to HA phase by Eq. 3.1, presented in (B) (solid red line). Note the disappearance of DCPD and TTCP diffraction peaks already after 5 and 7 h of setting reaction, respectively.

6.2.3. Phase composition evolution during the setting reaction

In order to study the influence of the presence of the highly crystalline HA reinforcement phase on the kinetics of the biocomposite cement formation, the conversion to hydroxyapatite end product was investigated by XRD. As an example, Fig. 6.7A shows the evolution of phase composition for **CPC-10%FP** reinforced biocomposite cement during the setting reaction at the selected times of 0, 0.5, 1, 2, 3, 4, 5, 6, 7 and 8 hours.

According to XRD, this biocomposite at $t = 0$ (unreacted **D-36** and **T-48** as well as **FP** powders mixture) consists of, as expected, HA, DCPD and TTCP (JCPDS No. 72-1243, No. 9-77 and 70-1379, respectively). Further phase analysis indicates full consumption of DCPD

already at t = 5 hours, while TTCP is entirely exhausted at t = 7 hours. At this time of reaction (t = 7 hours), **CPC-10%FP** biocomposite product contains only phase-pure HA (JCPDS No. 72-1243). This HA end product is composed of Ca-deficient hydroxyapatite, originated from the dissolution-precipitation reaction between DCPD and TTCP precursors, as well as highly crystalline and nearly stoichiometric hydrothermally-derived **FP** HA. The powder XRD patterns of this reinforced biocomposite (fine-plates) at t = 7, 8 and 24 h, as well as after 1 week of incubation in water are very much similar, and no distinction in phase composition, pattern's shapes and positions/intensities of XRD peaks of the HA phase are detected. This shows that the conversion of **CPC-10%FP** sample to HA is fully complete already after 7 h of setting time. The observed conversion rate is quite high, but at the same time, is 1 h slower than those one detected for pure cement (Section 4.2.3).

The solid red line in Fig. 6.7B represents the **CPC-10%FP** to HA conversion data determined according to Eq. 3.1 (Section 3.2.1). The observed sigmoidal curve of the biocomposite conversion is similar to that of pure cement (blue line in Fig. 6.7B). This indicates that the presence of crystalline reinforced HA phase does not significantly affects the kinetics of the biocomposite cement formation, and that the formation and growth of HA nuclei remains the rate-limiting process of the setting reaction (Section 4.2.3).

6.2.4. Mechanical properties of the reinforced biocomposites

6.2.4.1 Selection of the optimal reinforcement phase

According to the compression strength study, the advanced Ca-deficient hydroxyapatite cement developed in the present work has a CS of 25 ± 3 MPa (Section 4.2.9). In order to enhance its mechanical performance as a whole, and to improve this value in particular, this CPC was reinforced with HA crystals. Firstly, five composite CPCs were generated using the same content of the filler (10 wt.-%) to select the optimal particle morphology(s) with respect to increased compression strength.

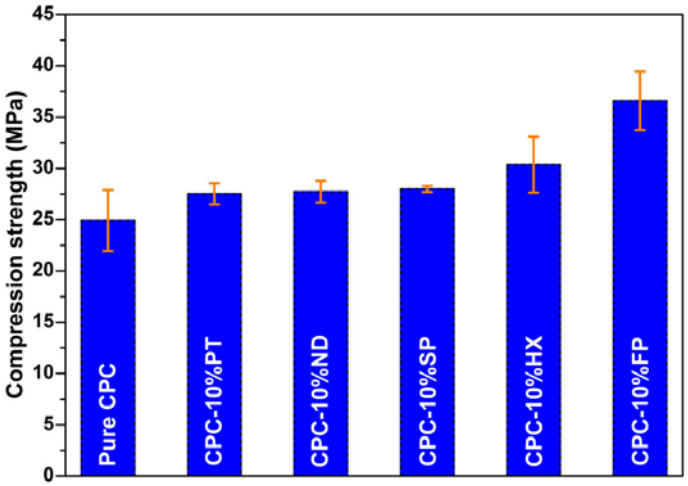

Fig. 6.8. Compressive strength comparison of advanced pure CPC and biocomposite cements reinforced by 10 wt.-% of HA particles with various morphologies.

As shown in Fig. 6.8 and enlisted in Table 6.1, an increasing of the compression strength is observed in general for all as-derive biocomposites compared to pure cement. The weaker improvement of CS (~12%) is observed *via* plates, needles as well as spherical aggregates reinforcement, while the utilization of the hexagonal prisms and fine-plates morphologies results in a marked compression strength enhancement by approximately 20 and 50%, respectively. A maximum value of 37 ± 3 MPa for **CPC-10%FP** biocomposite cement is achieved. Hence, it certainly appears that the HA crystals with fine-plate-like morphology are the most effective (*i.e.*, optimal) to stiffen resulting biocomposite materials, followed by hexagonal prism-like shape, and finally the least effective shapes are the plates, needles and spherical ones (Table 6.1, Fig. 6.8). It should be noted that, among all reinforcement phases, **FP** HA crystals exhibit smaller particle sizes, that seems to have essential influences on the CS values, in addition to the particle shape. Consequently, in the current study, the HA crystals with fine-plate- and hexagonal prism-like morphologies have been chosen to investigate the effects of filler amount on the biocomposites' mechanical properties.

6.2.4.2. Selection of the optimal volume fraction

For the aforementioned purpose, a series of the biocomposite cements reinforced with **HX** and **FP** HA crystals having filler content of 5, 10, 15, 20 or 30 wt.-% were generated. A comparison among as-prepared composite samples with different reinforcement phase content clearly shows a strong influence of the filler-addition level on the compression strength. In Fig. 6.9 the amount of the added filler *vs.* resulting compression strength is given. As can be

seen slight content of the HA crystals with hexagonal-prism- and fine-plate-like morphologies (up to 15 wt.-%) results in the increasing of the CS as compared to pure cement (Table 6.1). A further increase of the filler content leads to a strength close to that of un-reinforced CPC (~26 MPa) and to a decreased CS of ~20 MPa for the **CPC-30%HX** and **CPC-30%FP** biocomposite samples, respectively, which contain a maximum amount of the reinforcement phase. Overall, the **CPC-15%HX** and **CPC-10%FP** biocomposite samples exhibit the highest compressive strength (~33 and ~37 MPa, respectively). Thus, the compression strength experimental results reveal that the biocomposite reinforcement is not only affected by particles shape and size, but also controlled by the content of the filler particles.

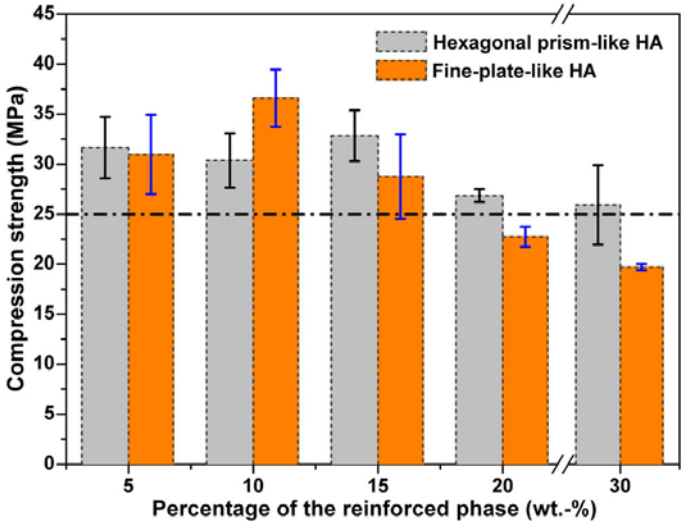

Fig. 6.9. Compression strength comparison of the biocomposite cements reinforced with 5, 10, 15, 20 and 30 wt.-% of hexagonal prism- and fine-plate-like HA particles. The black dashed line represents the CS value obtained for advanced pure CPC (25 ± 3 MPa).

6.2.4.3. Nano-indentation

The mechanical properties of the **CPC-10%FP** and **CPC-15%HX** biocomposites specimens exhibiting the best strength were further evaluated by nano-indentation, and the observed results are compared with NI data for the pure cement (Section 4.2.9). The observed elastic modulus E_s, hardness H and statistical analysis results are summarized in Table 6.2. Two representative loads *versus* displacement curves collected on these samples, along with one representative profile from pure cement are shown in Fig. 6.10. The load-displacement curves are smooth without any pop-in marks or discontinuities. This indicates that no cracking occurred during indentation. According to the displacement profiles, the peak load of 5 mN results in residual indentation of ~280 nm, which is very consistent with the NI results for pure cement (Section 4.2.9).

Table 6.2. The elastic modulus, hardness and statistical data comparison of reinforced and pure calcium phosphate bone-cements.

Sample	E_s (GPa)	H (GPa)	Significantly different [a]
CPC-10%FP	22.0 ± 2.2	0.76 ± 0.1	*cf.* **CPC-15%HX**: YES *cf.* **C-D36/T48**: YES
CPC-15%HX	22.9 ± 2.5	0.72 ± 10.1	*cf.* **CPC-10%FP**: YES *cf.* **C-D36/T48**: NO
C-D36/T48 [b]	23.1 ± 2.6	0.73 ± 0.2	*cf.* **CPC-10%FP**: YES *cf.* **CPC-15%HX**: NO

[a] – Calculated using the Mann-Whitney rank sum test. Test failed with $P < 0.050$;
[b] – Section 4.2.9 results for pure CPC.

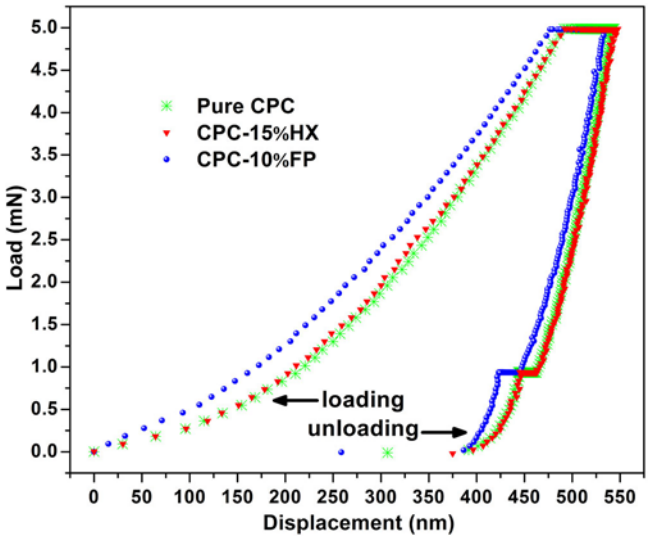

Fig. 6.10. Representative load *versus* displacement curves acquired by nano-indentation of pure cement (green) as well as **CPC-15%HX** (red) and **CPC-10%FP** (blue) biocomposite cements.

The average elastic modulus of the **CPC-10%FP** and **CPC-15%HX** biocomposites were calculated to be 22.0 ± 2.2 GPa and 22.9 ± 2.5 GPa, respectively, while the average hardness are found to be 0.76 ± 0.1 GPa and 0.72 ± 0.1 GPa, respectively. Overall, the elastic modulus and hardness of reinforced biocomposite cements are comparable to that of pure cement matrix and even the E_s and H values of the CPC-15% HX biocomposite and pure **C-D36/T48** cements are found to be a like within one standard deviation (Table 6.2).

6.3.- DISCUSSION

This thesis for a Doctor's degree focused on new composite biomaterials for bone repair and substitution. There were three research objectives: (*i*) improved hydroxyapatite calcium phosphate bone-cement aimed as a matrix for composite biomaterials; (*ii*) efficient morphology control of hydroxyapatite crystals for use in reinforcement applications via hydrothermal synthesis; and (*iii*) novel reinforced biocomposite cements applicable to a variety of bone graft designs. A combination of hydroxyapatite calcium phosphate bone-cement (matrix) and hydroxyapatite crystals (reinforcement phase) studies were employed to generate, characterize, and optimize novel biocomposites.

The key requirements for CPC matrix material are the setting within 10-30 minutes, a rapid conversion rate to hydroxyapatite end product and improved mechanical performance. It is apparent that the reactivity of the calcium phosphate bone-cement precursors is crucial for the achievement of insertion properties. Therefore, a thorough investigation by two complementary approaches: mechanochemical grinding and combinatorial methods was made to explore and evaluate advanced CPC.

Chapter IV describes the rational synthesis and systematic characterization of calcium phosphate bone-cements with dicalcium phosphate dihydrate and tetracalcium phosphate as precursors. Nine CPCs were combinatorially synthesized from reactive sub-micrometer-sized ball-milled DCPD and TTCP precursors via a dissolution-precipitation reaction using water as the liquid phase. It was established that the cement (**C-D36/T48**) prepared from the DCPD and TTCP with the average crystal sizes of ~1.13 and ~1.52 μm, respectively, is the optimal one with respect to the quickest setting time (~22 min) and the fastest conversion rate, since this precursors' crystal size combination leads to a complete transformation of DCPD and TTCP to the end product already after 6 h of setting reaction, one of the highest conversion rates among previously reported CPCs based on dicalcium and tetracalcium phosphates.

The as-prepared biomaterial consists of Ca-deficient hydroxyapatite (Ca/P ~1.49) containing HPO_4^{2-}, CO_3^{2-} anions and H_2O molecules in the crystal lattice. It is shown that the structural solidity of the cement is a result of the closely associated microstructure generated by spontaneous assembly of the precipitated platelet nanocrystals (10-15 nm) via interlocking. The CPC product is characterized by ~35 % porosity and exhibits potentially high bone-bonding ability. The compressive strength is 25 ± 3 MPa, and measured elastic modulus (~23.1 GPa) and hardness (~0.73 GPa) values match well to the reported values for trabecular

and cortical human bones, showing elastic and plastic ability to be used in medical practice as grafts.

Importantly, these properties can be improved by the reinforcement of the cement matrix by using inclusions. The enhancement depends on the inclusions' morphology. This attractive guide for optimization of the mechanical properties in the resulting reinforced biocomposite cement system motivates us to develop a practical synthetic approach to a set of hydroxyapatite filler phases with various morphologies. The use of HA as reinforcement phase is advantageous *cf.* other materials due to HA compositional similarity to the cement matrix as well as to bone and tooth mineral (bioactive reinforcement).

In particular, Chapter V describes a facile urea-assisted hydrothermal synthesis and systematic characterization of hydroxyapatite crystals with calcium nitrate tetrahydrate and diammonium hydrogen phosphate as precursors. The advantages of the proposed technique over previously reported synthetic approaches is the simple but precise control of the particle morphology of the HA crystals, which is simply achieved via an intensive, stepwise and slow thermal decomposition of urea as well as using decreased initial concentrations of starting reagents. The results demonstrate that hydroxyapatite crystals can be easily obtained on a gram scale. Whereas the plate-, hexagonal prism- and needle-like HA particles preferentially grow along the *c*-axis, the smaller and fine-plate-like HA crystals demonstrate crystal growth along the (211) and (102) directions, uncommon for hydroxyapatite. Furthermore, it was established that the hydrothermally-derived powdered products are phase-pure HA containing CO_3^{2-} anions in the crystal lattice, *i.e.* AB-type carbonated hydroxyapatite. Transmission electron microscopy and electron diffraction of selected samples reveal that the as-prepared HA crystals are single-crystalline and exhibit a nearly defect free microstructure.

The hardness and elastic modulus of the HA particles having an hexagonal prism-like particle morphology have been investigated on a nanoscale using the nano-indentation technique, and the obtained data conclusively highlight that the hardness and elastic modulus are determined by the crystal orientation and the synthesis route. In addition, NI results clearly indicate that HA crystals are markedly stiffer than the cement matrix owing to their high crystalline and composition quality.

As described in Section 2.6.1, the properties of a composite material strongly depend upon the size, shape, amount, orientation and mechanical properties of the filler, as well as upon reinforcement-matrix interface.[98] In the current investigation, the influence of filler particle morphology and content on the structure and mechanical properties of resulting composite cements was addressed. Consequently, composite biomaterials having advanced

C-D36/T48 cement as a matrix and HA crystals with plate- (**PT**), needle- (**ND**), hexagonal prism- (**HX**) or fine-plate-like (**FP**) morphologies, as well as with spherical aggregates (**SP**) appearance, as the reinforcement phase were prepared(Table 6.1).

Powder X-ray diffraction and Raman measurements showed that all 24 hour-derived reinforced biocomposite cements are phase-pure and nanocrystalline hexagonal HA crystal structure (Table 6.1, Fig. 6.3, 6.4). The morphology and nanostructure of the biocomposites were investigated using SEM and TEM, which confirmed a pronounced physical interplay between cement matrix and reinforcement phase crystals, comprehensively generating associated microstructure of the end composite products (Fig. 6.5, 6.6). Electron microscopy also demonstrated homogenous filler content throughout the biocomposite, with no evidence of chemical bonding or intergrowth with the interlocked cement nanocrystallites. Detailed powder XRD studies were also carried out to investigate the conversion rate of the reinforced biocomposite cements to HA. **CPC-10%FP** biocomposite has a very high conversion rate, comparable to that of advanced **C-D36/T48** CPC (Fig. 6.7). More specifically, this biocomposite entirely converts to the HA end product after 7 h of setting reaction, while pure cement converts within 6 h. This result suggests that the presence of the crystalline HA reinforcement phase does not leads to remarkable changes in the cement matrix setting. The observed one hour difference appears to be resulted from the less amount of water employed in the course of the reinforced biocomposite preparation.

Table 6.1 together with Fig. 6.8 and 6.9 compare the compression strength, measured by Universal Testing Machine, for all prepared biocomposites. All of the reinforced biocomposite materials exhibited enhanced CS. In particular, the composites with hexagonal prism- and fine-plate-like particle morphologies showed considerably increased compression strength (up to ~20 and 50%, repectively), while reinforcement with plates, needles and spherical aggregates resulted in moderate increases of CS by ~12% (Fig. 6.8).

It is generally accepted that stiff plate-like inclusions are the most effective in stiffening isotropic composite materials, followed by fibrous shaped morphologies, with the least effective geometry being spherical.[98, 114, 151]. However, in our case, it appears that plate-like particles are not so effective as reinforcement phases and the resulting mechanical properties of **CPC-10%PT** were comparable to those composites reinforced with needle-like and spherical-aggregate HA particles (**CPC-10%ND** and **CPC-10%SP**, respectively). In contrast, the CS value obtained for the cement reinforced with hexagonal prism-like particles is considerably higher. This indicates that, for fillers exhibiting similar particle size and structural properties, the “three-dimensional” shape of the crystals is a more determinant

factor on the final mechanical properties of reinforced biocomposites. Additionally, the strength of composites is markedly influenced by the amount of filler utilized. Upon reinforcing with 5, 10, 15, 20 and 30 wt.-% of HA crystals, the compression strength first increases, reaching a maximum of ~33 and ~37 MPa at 15 wt.-% hexagonal prisms and 10 wt.-% fine-plates. At higher values, CS of biocomposites stay close to the value found for pure, un-reinforced CPC in the case of hexagonal prism, or decreases to values lower than that of pure CPC for fine-plate inclusions (Table 6.1).

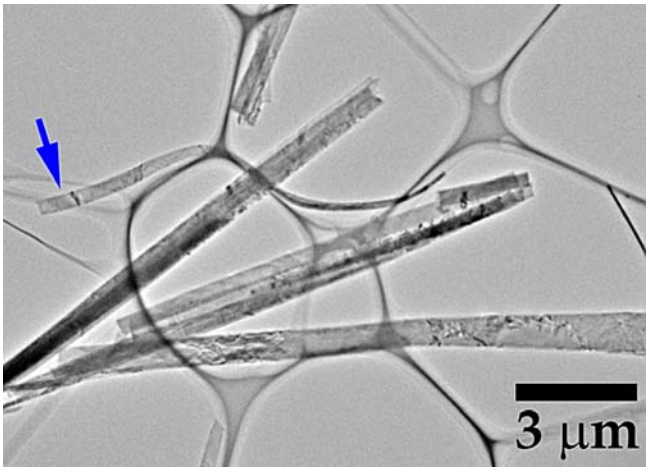

Fig. 6.11. A low-magnification TEM image of hydrothermally-derived **HX** sample, showing the appearance of the flexible belt-like HA crystals in this product.

Overall, the best strength performance through all produced CPC biomaterials was achieved by reinforcement of an advanced cement with HA fine-plate crystals (10 wt.-%). This modification leads to an enhancement of the CS to 37 MPa, thus, an increasing of ~50%. This significant breakthrough is most likely related to the synergetic effect of smaller particle sizes and complementary crystal morphologies in this hydrothermally-derived **FP** product. Specifically, in addition to rod-like and rectangular plate-like crystals (Fig. 5.11B, 5.11C), the presence of belt-like particles exhibiting limited flexibility was also detected by TEM analysis (Fig. 6.11**)**. Consequently, the energy supplied by the compression test is utilized by the **FP** crystals in elastic deformations instead of crack propagation in the matrix.

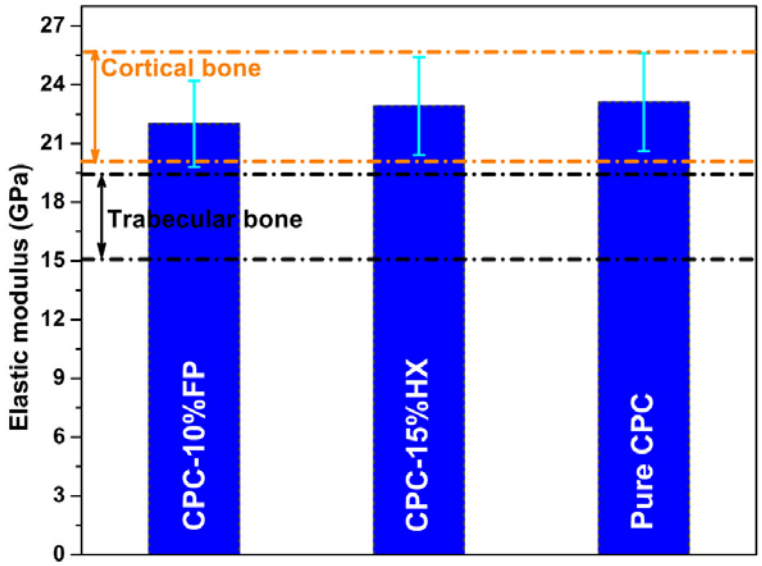

Fig. 6.12. Elastic modulus comparison of advanced pure CPC and the selected biocomposite cements. Orange and black dashed-dotted lines mark the range of E_s for cortical and trabecular bones, respectively.

The elastic moduli and hardness of the high performance biocomposites were studied by means of nano-indentation. Fig. 6.12 displays a comparison of the elastic moduli determined for **CPC-10%FP** and **CPC-15%HX** and also for the un-reinforced **C-D36/T48** together with the E_s values found for human cortical and trabecular bone. The elastic modulus and hardness of **CPC-10%FP** is significantly different than those values calculated for **CPC-15%HX** and pure CPC. Compared to human bones, the elastic modulus of both composites and pure CPC is slightly higher than observed in human trabecular bone[7] (15.0-19.4 GPa) and lies in the range of human cortical bone[198] (20.0-25.8 GPa). The hardness of **CPC-10%FP** (~0.76 GPa) is higher than observed in human trabecular bone[7] (0.52-0.62 GPa) and is also slightly higher than in human cortical bone[7] (0.62-0.74 GPa). **CPC-15%HX** and pure CPC hardnesses are higher that the calculated values for human trabecular bone,[7] but they are consistent with H seen in human cortical bone.[7] It can be concluded that the as-prepared biocomposites compare closely with human bone in terms of elasticity as well as plasticity. This is important because good biomechanical compatibility requires the elastic moduli of biocomposites and human bone to be closely matched, thus avoiding stress shielding of nearby bone from mechanical forces and the sequent bone absorption observed when implant materials with a high elastic modulus are employed as bone graft (Section 2.3.4).

Opposite to CS measurements, the elastic modulus of **CPC-10%FP** was determinate to be significantly different and lower than the calculated E_s for **CPC-15%HX** biocomposite

and pure CPC (~22.0, ~22.9 and ~23.1 GPa, respectively). Balac *et al.* showed that E_s is slightly dependent on particle shape, but very sensitive to HA particle volume fraction in reinforced polymer composites.[206] These founds suggest that the difference in E_s for **CPC-10%FP** and **CPC-15%HX** can be related with the slightly different wt.-% employed of each reinforcement phase more than with the inclusions' morphology.

The elastic modulus of the **C-D36/T48** cement reinforced with hexagons or fine-plate HA single crystals was expected to be higher than those of pure cement, at least for the biocomposite with hexagonal heterogeneities, stiffer than the CPC matrix (~64 *vs.* ~23 GPa, respectively). However, the measured E_s of **CPC-10%FP** biocomposite is ~5% lower than those of **C-D36/T48**, and E_s of **CPC-15%HX** product is not significantly different *cf.* pure CPC (Table 6.2). Although the addition of a stiffer reinforcement phase normally should results in an improvement on the biocomposite' elastic modulus,[151, 207] few works report the opposite effect. For example, Fu *et al.* observed an E_s decreasing for a 3D carbon fibre reinforced HA/epoxy composite.[208] They propose that this result is due to a weakened fibre-matrix interface consequence of the composite sample preparation.[208] Gorst *et al.* also show that E_s of a CPC is reduced through the incorporation of polyglactin fibres stiffer that un-reinforced CPC, possibly owing to the choice of fibre.[100] They suggest that during the initial take-up of load there will be elements of bedding-in as the braids align themselves. Consequently, the initial or small strain modulus of elasticity of the fibres may be less than the values calculated for pure fibres, and possibly less than the modulus of elasticity of un-reinforced CPC. Therefore, the fibres would act as flaws in the CPC leading to a decrease in the modulus of elasticity of the composite.[100]

One possibility for the observed slightly decreasing of **CPC-10%FP** biocomposite elastic modulus can be due to fibre debonding, since the performance of many fibre composite materials is very sensitive to the mechanical properties of the interface region, *i.e.*, interfacial decohesion leads to a reduction in stiffness.[209]

Also, it is possible that the fine-plate inclusions are, in fact, more compliant that the CPC matrix due to their thickness of only few nanometers. In fact, the TEM observed somehow flexibility might be an indicator of a low stiffness. If this is the case, E_s of the **CPC-10%FP** will be reduce *cf.* pure CPC. Soft inclusions are used intentionally as crack stoppers to enhance the toughness of polymers such as polystyrene with a small decrease in stiffness.[98]

Nevertheless, the measured elastic modulus of ~22.0 GPa for **CPC-10%FP** biocomposite still lays in the range of human cortical bones.[198] Additionally, debonding of the

fibre-matrix interface is one of the toughening mechanisms that contribute to the increase of fracture toughness of ceramic materials (Section 2.6.2). Therefore, it is apparent that either possibility will improve **CPC-10%FP** fracture toughness with only a very small sacrifice in the E_s, which even does not affect the isoelasticity between as-prepared biocomposite and human cortical bone.

The elastic modulus of **CPC-15%HX** is not significantly different than the calculated for pure CPC (~22.9 and ~23.1 GPa, respectively). This fact might be due to a small wt.-% of hexagonal reinforcement phase or to the random orientation of the hexagonal crystals. For example, Xu *et al.* also observed that E_s of a CPC was not changed as a result of reinforcement with only 6 vol.-% of aramid fibres, stiffer than CPC matrix.[210] The observed effect of the inclusions on the biocomposite E_s with 10 wt.-% of fine-plate crystals is due to a bigger surface area of the fine-plate crystals *cf.* hexagonal particles. A bigger surface area implies more energy absorption, which leads to a decreasing of biocomposite E_s.

Opposite to the elastic modulus trend, the hardness for **CPC-10%FP** biocomposite was calculated to be ~4% higher than the observed for **CPC-15%HX** and pure CPC (~0.76, ~0.72 and ~ 0.73 GPa, respectively). Fine-plate HA crystals exhibit a bigger surface area *cf.* hexagonal crystals. Thus, when applying a force to the biocomposite, the produced deformations are somehow stopped by the large free surfaces of fine-plate crystals, acting as barriers to the propagation of the deformation. Consequently, the hardness of this biocomposite is slightly higher than those of pure CPC.

Similar with E_s tendency, **CPC-15%HX** hardness was found to be not significantly different from the observed hardness for pure CPC. This fact can be due to a small presence of hexagonal reinforcement phase in the final biocomposite

6.4.- CONCLUDING REMARKS

The mechanical properties of advanced CPC were successfully enhanced *via* reinforcement by HA crystals with various particle morphologies. It is shown that the strength performance these novel reinforced biocomposites is determined by the size, shape and quantity of the reinforcement phase. An improvement in compression strength of ~50% was achieved using hydrothermally-derived hydroxyapatite crystals with complementary morphologies used as a reinforcement phase.

The measured mechanical properties of the optimised biocomposites were shown to be very similar to those seen in human bone. This is of great consequence to their potential application in bone repair and substitution as the biomechanical aspects of CPC biocomposites play a large role in their biocompatibility and the scope of their application.

VII

CONCLUSIONS

1. Using a combinatorial approach we rationally prepared an advanced CPC from ball-milled DCPD and TTCP powders of different crystal sizes that sets in ~22 minutes and entirely converts to the end product already after 6 hours of setting reaction.
2. This cement is a porous, nanocrystalline, and potentially bioactive Ca-deficient carbonated hydroxyapatite. The cement demonstrates essential mechanical performance, in particular, the compressive strength is ~25 MPa, and the measured elastic modulus (~20.7 GPa) and hardness (~0.63 GPa) values match well to the reported values for trabecular and cortical human bones.
3. For the reinforcement phase we successfully synthesized hydroxyapatite crystals with various controlled morphologies *via* a urea-assisted hydrothermal reaction between $Ca(NO_3)_2{\cdot}4H_2O$ and $(NH_4)_2HPO_4$ at a low temperature of 90°C.
4. Our detailed experimental studies clearly demonstrate that the as-derived products are composed of single-crystalline, structural defect-free, carbonated hydroxyapatite crystals, which exhibit, plate-like, hexagonal prism-like, needle-like or fine-plate particle morphologies depending upon the conditions used.
5. We have been able to probe the mechanical properties of hydroxyapatite single crystals by nano-indentation, and the obtained data conclusively highlight that the hardness and elastic modulus are determined by the crystal orientation and the synthesis route.
6. The mechanical properties of advanced CPC were successfully improved by reinforcement with HA crystals of various particle morphologies. It was shown that the strength performance of these novel reinforced biocomposites is determined by the size, shape and quantity of the reinforcement phase.
7. An improvement in compression strength of ~50% (~37 MPa) was achieved using hydrothermally-derived hydroxyapatite crystals with fine-plate morphology as the reinforcement phase.
8. The measured mechanical properties of the optimised biocomposites were shown to be very similar to those seen in human bone. This is of great consequence to their potential application in bone repair and substitution as the biomechanical aspects of CPC biocomposites play a large role in their biocompatibility and the scope of their application.
9. In addition to finding and developing a novel composite calcium phosphate bone-cement with enhanced mechanical properties, this research has led to improved understanding of the processing-structure-property relationships of CPC-based biomaterials used in bone repair and substitution.

VIII

REFERENCES

(1) Currey, J. D., *Bones. Structure and mechanics*. 1st ed.; Princeton University Press: Princeton, New Jersey, 2002.

(2) Rho, J.-Y.; Kuhn-Spearing, L.; Zioupos, P., Mechanical properties and the hierarchical structure of bone. *Med. Eng. Phys.* **1998**, 20(2), 92-102.

(3) In *The bone quality book. A guide to factors influencing bone strength.*, Dempster, D.; Felsenberg, D.; Van der Geest, S., Eds. Elsevier: Amsterdam, 2006.

(4) Kuhn, L. T.; Fink, D. J.; Heuer, A. H., Biomimetic strategies and materials processing. In *Biomimetic materials chemistry*, Mann, S., Ed. VCH Publishers: New York, 1996; pp 41-68.

(5) Mann, S., *Biomineralization. Principles and concepts in bioinorganic materials chemistry*. 1st ed.; Oxford University Press: Oxford, 2001; p 10, 141-155.

(6) Meyers, M. A.; Chen, P.-Y.; Lin, A. Y.-M.; Seki, Y., Biological materials: structure and mechanical properties. *Prog. Mat. Sci.* **2008**, 53(1), 1-206.

(7) Rho, J.-Y.; Roy, M. E.; Tsui, T. Y.; Pharr, G. M., Elastic properties of microstructural components of human bone tissue as measured by nanoindentation. *J. Biomed. Mater. Res., Part A* **1999**, 45(1), 48-54.

(8) Hench, L. L., Bioceramics: from concept to clinic. *J. Am. Ceram. Soc.* **1991**, 74(7), 1487-1510.

(9) Elliott, J. C., *Structure and chemistry of the apatites and other calcium ortophosphates*. 1st ed.; Elsevier: Amsterdam, 1994.

(10) Jee, W. S. S., The skeletal tissues. In *Histology: cell and tissue biology*, 5th ed.; Weiss, L., Ed. Elsevier: Amsterdam, 1983; pp 206-254.

(11) Reichenmiller, K.; Klein, C., Formation of teeth. In *Handbook of biomineralization*, Epple, M.; Baeuerlein, E., Eds. Wiley-VCH: Weinheim, 2007; pp 159-176.

(12) Dorozhkin, S. V., Calcium orthophosphates. *J. Mater. Sci.* **2007**, 42(4), 1061-1095.

(13) Schlickewei, W.; Schlickewei, C., The use of bone substitutes in the treatment of bone defects - the clinical view and history. *Macromol. Symp.* **2007**, 253(1), 10-23.

(14) Williams, D. F., Biofunctionality and biocompatibility. In *Medical and dental materials*, Williams, D. F., Ed. VCH: Weinheim, 1992; pp 1-28.

(15) Laurencin, C.; Khan, Y.; El-Amin, S. F., Bone graft substitutes. *Expert Rev. Med. Devices* **2006**, 3(1), 49-57.

(16) Carson, J. S.; Bostrom, M. P. G., Synthetic bone scaffolds and fracture repair. *Injury, Int. J. Care Injured* **2007**, 38(1 (Supp.1)), S33-S37.

(17) Habibovic, P.; de Groot, K., Osteoinductive biomaterials - properties and relevance in bone repair. *J. Tissue Eng. Regen. Med.* **2007**, 1(1), 25-32.

(18) Kenley, R. A.; Kalvin, Y.; Abrams, J.; Ron, E.; Turek, T.; Marden, L. J.; Hollinger, J. O., Biotechnology an bone graft substitutes. *Pharm. Res.* **1993**, 10(10), 1393-1401.

(19) Asselmeier, M. A.; Caspari, R. B.; Bottenfield, S., A review of allograft processing and sterilization techniques and their role in transmission of the human immunodeficiency virus. *Am. J. Sports Med.* **1993**, 21(2), 170-175.

(20) Hench, H. H.; Ethridge, E. C., Biomaterials: an interfacial approach. In *Biophysics and bioengineering series*, Noordergraaf, A., Ed. Academic Press: New York, 1982; Vol. 4, pp 62-86.

(21) Park, J. B.; Bronzino, J. D., *Biomaterials. Principles and applications*. 1st ed.; CPC Press: Boca Raton, FL, 2003; p i-vii.

(22) Williams, D. F., Definitions in biomaterials: proceedings of a consensus conference of the European Society of Biomaterials, Chester, England, March 3-5 1986. In *Progress in biomedical engineering*, Williams, D. F., Ed. Elsevier: Amsterdam, 1987; Vol. 4, p 54.

(23) Bruck, S. D., *Properties of biomaterials in the physiological environment*. 1st ed.; CRC Press: Boca Raton, FL, 1980; p 23-34.

(24) *Clinical applications of biomaterials*. NHI Consens. Statement Nov. 1-3. **1982**, 4(5), 1-19.

(25) Peaboy Museum of Archaeology and Ethnology. Harvard University (Cambridge, MA, U.S.A.); http://www.peabody.harvard.edu/.

(26) Hench, H. H., Bonding mechanism at the interface of ceramic prosthetic materials. *J. Biomed. Mater. Res.* **1971**, 2(1), 117-141.

(27) Lloyd, A. W., Interfacial bioengineering to enhance surface biocompatibility. *Med. Device Technol.* **2002**, 13(1), 18-21.

(28) Cutter, C. S.; Mehrara, B. J., Bone grafts and substitutes. *J. Long Term Eff. Med. Implants* **2006**, 16(3), 249-260.

(29) Taş, A. C., Participation of calcium phosphate bone substitutes in the bone remodeling process: influence of materials chemistry and porosity. *Key Eng. Mat.* **2004**, 264-268, 1969-1972.

(30) Nair, L. S.; Laurencin, C. T., Biodegradable polymers as biomaterials. *Prog. Polym. Sci.* **2007**, 32(8-9), 762-798.

(31) Park, J. B.; Kim, Y. K., Metallic biomaterials. In *Biomaterials. Principles and applications*, Park, J. B.; Bronzino, J. D., Eds. CRC Press: Boca Raton, FL, 2003; pp 1-20.

(32) Machado, L. G.; Savi, M. A., Medical applications of shape memory alloys. *Braz. J. Med. Biol. Res.* **2003**, 36(6), 683-691.

(33) Hanawa, T., Evaluation techniques of metallic biomaterials in vitro. *Sci. Tech. Adv. Mat.* **2002**, 3(4), 289-295.

(34) Biehl, V.; Breme, J., Metallic biomaterials. *Mat.-wiss. u. Werkstofftech.* **2001**, 32(2), 137-141.

(35) Parikh, S. N., Bone graft substitutes: past, present and future. *J. Postgrad. Med.* **2002**, 48(2), 142-148.

(36) Lee, K.-Y.; Park, M.; Kim, H.-M.; Lim, Y.-J.; Chun, H.-J.; Kim, H.; Moon, S.-H., Ceramic bioactivity: progresses, challenges and perspectives. *Biomed. Mater.* **2006**, 1(2), R31-R37.

(37) Charnley, J., Anchorage of femoral head prosthesis to the shaft of the femur. *J. Bone Joint Surg. Br.* **1960**, 42B(1), 28-30.

(38) Lee, H. B.; Khang, G.; Lee, J. H., Polymeric biomaterials. In *Biomaterials. Principles and applications*, Park, J. B.; Bronzino, J. D., Eds. CRC Press: Boca Raton, FL, 2003; pp 55-77.

(39) Cheung, H.-Y.; Lau, K.-T.; Lu, T.-P.; Hui, D., A critical review on polymer-based bio-engineered materials for scaffold development. *Compos. Part B* **2007**, 38(3), 291-300.

(40) Jagur-Grodzinski, J., Biomedical application of functional polymers. *React. Funct. Polym.* **1999**, 39(2), 99-138.

(41) Jan, C.; Grzegorz, K., The study of lifetime of polymer and composite bone joint screws under cyclical loads and *in vitro* conditions. *J. Mater. Sci. Mater. Med.* **2005**, 16(11), 1051-1060.

(42) Abu Bakar, M. S.; Cheang, P.; Khor, K. A., Mechanical properties of injection molded hydroxyapatite-polyetheretherketone biocomposites. *Compos. Sci. Technol.* **2003**, 63(3), 421-425.

(43) Lu, H. H.; El-Amin, S. F.; Scott, K. D.; Laurencin, C. T., Three-dimensional, bioactive, biodegradable, polymer-bioactive glass composite scaffolds with improved mechanical properties support collagen synthesis and mineralization of human osteoblast-like cell *in vitro*. *J. Biomed. Mater. Res., Part A* **2003**, 64A(3), 465-474.

(44) Billotte, W. G., Ceramic biomaterials. In *Biomaterials. Principles and applications*, Park, J. B.; Bronzino, J. D., Eds. CRC Press: Boca Raton, FL, 2003; pp 21-53.

(45) Feenstra, L.; de Groot, K., Medical use of calcium phosphate ceramics. In *Bioceramics of calcium phosphate*, de Groot, K., Ed. CRC Press: Boca Raton, FL, 1983; pp 131-141.

(46) Graves, G. A.; Hentrich, R. L.; Stein, H. G.; Bajpai, P. K., Resorbable ceramic implants in bioceramics. In *Engineering and medicine, part I*, Hall, C. W.; Hulbert, S. F.; Levine, S. N.; Young, F. A., Eds. Wiley-Interscience: New York, 1972; pp 91-115.

(47) Dorozhkin, S. V., Calcium orthophosphate cements for biomedical application. *J. Mater. Sci.* **2008**, 43(9), 3028-3057.

(48) Bohner, M., Calcium orthophosphates in medicine: from ceramics to calcium phosphate cements. *Injury, Int. J. Care Injured* **2000**, 31(Supp 4), D37-D47.

(49) Driessens, F. C. M.; Boltong, M. G.; de Maeyer, E. A. P.; Wenz, R.; Nies, B.; Planell, J. A., The Ca/P range of nanoapatitic calcium phosphate cements. *Biomaterials* **2002**, 23(19), 4011-4017.

(50) Gbureck, U.; Barralet, J. E.; Hofmann, M.; Thull, R., Mechanical activation of tetracalcium phosphate. *J. Am. Ceram. Soc.* **2004**, 87(2), 311-313.

(51) Vallet-Regí, M.; González-Calbet, J. M., Calcium phosphates as substitution of bone tissues. *Prog. Solid State Chem.* **2004**, 32(1-2), 1-31.

(52) Lynn, A. K.; Bonfield, W., A novel method for the simultaneous, titrant-free control of pH and calcium phosphate mass yield. *Acc. Chem. Res.* **2005**, 38(3), 202-207.

(53) In *Phase diagrams for ceramist*, Levin, E. M.; Robbins, C. R.; McMurdie, H. F., Eds. American Ceramic Society: Columbus, OH, 1964, Diag. 246; Vol. I.

(54) Brown, W. E., Octacalcium phosphate and hydroxyapatite: crystal structure of octacalcium phosphate. *Nature* **1962**, 196(4859), 1048-1050.

(55) Kurashina, K.; Kurita, H.; Hirano, M.; Kotani, A.; Klein, C. P. A. T.; de Groot, K., In vivo study of calcium phosphate cements: implantation of an α-tricalcium phosphate/dicalcium phosphate dibasic/tetracalcium phosphate monoxide cement paste. *Biomaterials* **1997**, 18(7), 539-543.

(56) Kurashina, K.; Kurita, H.; Hirano, M.; Blieck, J. M. A.; Klein, C. P. A. T.; de Groot, K., Calcium phosphate cement: *in vitro* and *in vivo* studies of the *α*-tricalcium phosphate-dicalcium phosphate dibasic-tetracalcium phosphate monoxide system. *J. Mater. Sci. Mater. Med.* **1995**, 6(6), 340-347.

(57) Driessens, F. C. M.; Planell, J. A.; Boltong, M. G.; Khairoun, I.; Ginebra, M. P., Osteotransductive bone cements. *Proc. Inst. Mech. Eng. H* **1998**, 212(6), 427-435.

(58) Gauthier, O.; Khairoun, I.; Bosco, J.; Obadia, L.; Bourges, X.; Rau, C.; Magne, D.; Bouler, J. M.; Aguado, E.; Daculsi, G.; Weiss, P., Noninvasive bone replacement with a new injectable calcium phosphate biomaterial. *J Biomed Mater Res, Part A* **2003**, 66A(1), 47-54.

(59) Brown, W. E.; Chow, L. C., A new calcium phosphate setting cement. *J. Dent. Res.* **1983**, 62, 672.

(60) Kingery, W. D., Cold setting properties. *J. Am. Ceram. Soc.* **1950**, 33(8), 242-247.

(61) Driskell, T. D.; Heller, A. L.; Koenigs, J. F. *Dental treatments*. US Patent No. 3913229, 1975

(62) Monma, H.; Kanazawa, T., The hydratation of a *α*-tricalcium phosphate. *Yogyo-Kyokai-Shi* **1976**, 84(4), 209-213.

(63) LeGeros, R. Z.; Chohayeb, A.; Shulman, A., Apatitic calcium phosphates: possible dental restorative materials. *J. Dent. Res.* **1982**, 61, 343.

(64) Constantz, B. R.; Ison, I. C.; Fulmer, M. T.; Poser, R. D.; Smith, S. T.; Van Wagoner, M.; Ross, J.; Goldstein, S. A.; Jupiter, J. B.; Rosenthal, D. I., Skeletal repair by *in situ* formation of the mineral phase of bone. *Science* **1995**, 267(5205), 1796-1799.

(65) Kveton, J. F.; Friedman, C. D.; Costantino, P. D., Indications for hydroxyapatite cement reconstruction in lateral skull base surgery. *Am. J. Otol.* **1995**, 16(4), 465-469.

(66) Ginebra, M. P.; Traykova, T.; Planell, J. A., Calcium phosphate cements: Competitive drug carriers for the musculoskeletal system? *Biomaterials* **2006**, 27(10), 2171-2177.

(67) Ginebra, M. P.; Traykova, T.; Planell, J. A., Calcium phosphate cements as bone drug delivery systems: A review. *J. Contr. Release* **2006**, 113(2), 102-110.

(68) Larsson, S.; Bauer, T. W., Use of injectable calcium phosphate cement for fracture fixation: a review. *Clin. Orthop. Relat. Res.* **2002**, 395(February), 23-32.

(69) Bohner, M.; Gbureck, U.; Barralet, J. E., Technological issues for the development of more efficient calcium phosphate bone cements: A critical assessment. *Biomaterials* **2005**, 26(33), 6423-6429.

(70) Bohner, M., Reactivity of calcium phosphate cements. *J. Mater. Chem.* **2007**, 17(38), 3980-3986.

(71) Fernández, E.; Gil, F. J.; Ginebra, M. P.; Driessens, F. C. M.; Planell, J. A.; Best, S. M., Calcium phosphate bone cements for clinical applications. Part I: Solution chemistry. *J. Mater. Sci. Mater. Med.* **1999**, 10(3), 169-176.

(72) Fernández, E.; Gil, F. J.; Ginebra, M. P.; Driessens, F. C. M.; Planell, J. A.; Best, S. M., Calcium phosphate bone cements for clinical applications. Part II: Precipitate formation during setting reactions. *J. Mater. Sci. Mater. Med.* **1999**, 10(3), 177-183.

(73) Behiri, J. C.; Bonfield, W., Fracture mechanics of bone: the effects of density, specimen thickness, and crack velocity on longitudinal fracture. *J. Biomech.* **1984**, 17(1), 25-34.

(74) Dorozhkin, S. V.; Epple, M., Biological and medical significance of calcium phosphates. *Angew. Chem. Int. Ed.* **2002**, 41(17), 2130-3146.

(75) Barralet, J. E.; Grover, L.; Gaunt, T.; Wright, A. J.; Gibson, I. R., Preparation of macroporous calcium phosphate cement tissue engineering scaffold. *Biomaterials* **2002**, 23(15), 3063-3072.

(76) Ni, G. X.; Lu, W. W.; Tang, B.; Ngan, A. H. W.; Chiu, K. Y.; Cheung, K. M. C.; Li, Z. Y.; Luk, K. D. K., Effect of weight-bearing on bone-bonding behaviour of strontium-containing hydroxyapatite bone cement. *J. Biomed. Mater. Res., Part A* **2007**, 83A(2), 570-576.

(77) Jansen, J. A.; Ooms, E.; Verdonschot, N.; Wolke, J. G. C., Injectable calcium phosphate cement for bone repair and implant fixation. *Orthop. Clin. North Am.* **2005**, 36(1), 89-95.

(78) Vereecke, G.; Lemaître, J., Calculation of the solubility diagrams in the system $Ca(OH)_2$-H_3PO_4-KOH-HNO_3-CO_2-H_2O. *J. Cryst. Growth* **1990**, 104(4), 820-832.

(79) Constantz, B. R.; Barr, B. M.; Ison, I. C.; Fulmer, M. T.; Baker, J.; McKinney, L.; Goodman, S. B.; Gunasekaren, S.; Delaney, D. C.; Ross, J.; D., P. R., Histological, chemical, and crystallographic analysis of four calcium phosphate cements in different rabbit osseous sites. *J. Biomed. Mater. Res.* **1998**, 43(4), 451-461.

(80) Driessens, F. C. M.; Boltong, M. G.; Bermúdez, O.; Planell, J. A.; Ginebra, M. P.; Fernández, E., Effective formulations for the preparation of calcium phosphate bone cements. *J. Mater. Sci. Mater. Med.* **1994**, 5(3), 164-170.

(81) Schmit, J. P.; Hollinger, J. O.; Milan, S. B., Reconstruction of bone using calcium phosphate bone cements: A critical review. *J. Oral Maxillofac. Surg.* **1999**, 57(9), 1122-1126.

(82) Burguera, E. F.; Xu, H. H. K.; Takagi, S.; Chow, L. C., High early strength calcium phosphate bone cement: effects of dicalcium phosphate dihydrate and absorbable fibres. *J. Biomed. Mater. Res., Part A* **2005**, 75A(4), 966-975.

(83) Miyamoto, Y.; Ishikawa, K.; Fukao, H.; Sawada, M.; Nagayama, M.; Kon, M.; Asaoka, K., In vivo setting behaviour of fast-setting calcium phosphate cement. *Biomaterials* **1995**, 16(11), 855-860.

(84) Brown, P. W.; Fulmer, M., Kinetics of hydroxyapatite formation at low temperature. *J. Am. Ceram. Soc.* **1991**, 74(5), 934-940.

(85) Brown, P. W.; Hocker, N.; Hoyle, S., Variations in solution chemistry during the low-temperature formation of hydroxyapatite. *J. Am. Ceram. Soc.* **1991**, 74(8), 1848-1854.

(86) Senna, M., Determination of effective surface area for the chemical reaction of fine particulate materials. *Part. Part. Syst. Charact.* **1989**, 6(1-4), 163-167.

(87) Lilley, K. J.; Gbureck, U.; Wright, A. J.; Farrar, D. F.; Barralet, J. E., Cement from nanocrystalline hydroxyapatite: effect of calcium phosphate ratio. *J. Mater. Sci. Mater. Med.* **2005**, 16(12), 1185-1190.

(88) Ishikawa, K.; Takagi, S.; Chow, L. C.; Ishikawa, Y., Properties and mechanisms of fast-setting calcium phosphate cements. *J. Mater. Sci. Mater. Med.* **1995**, 6(9), 528-533.

(89) Fleisch, H.; Russell, R. G.; Francis, M. D., Diphosphonates inhibit hydroxyapatite dissolution in vitro and bone resorption in tissue culture and in vivo. *Science* **1969**, 165(3899), 1262-1264.

(90) Tang, R.; Nancollas, G. H.; Orme, C. A., Mechanism of dissolution of sparingly soluble electrolytes. *J. Am. Chem. Soc.* **2001**, 123(23), 5437-5443.

(91) Liu, C.; Shen, W., Effect of crystal seeding on the hydration of calcium phosphate cement. *J. Mater. Sci. Mater. Med.* **1997**, 8(12), 803-807.

(92) TenHuisen, K. S.; Brown, P. W., Effects of magnesium on the formation of calcium-deficient hydroxyapatite from $CaHPO_4.2H_2O$ and $Ca_4(PO_4)_2O$. *J. Biomed. Mater. Res.* **1997**, 36(2), 306-314.

(93) Wang, X.; Ma, J.; Wang, Y.; He, B., Structural characterization of phosphorylated chitosan and their applications as effective additives of calcium phosphate cements. *Biomaterials* **2001**, (22), 2247-2255.

(94) Burguera, E. F.; Guitián, F.; Chow, L. C., A water setting tetracalcium phosphate-dicalcium phosphate dihydrate cement. *J. Biomed. Mater. Res., Part A* **2004**, 71A(2), 275-282.

(95) Chen, W. C.; Ju, C. P.; Chern Lin, J. H., Effect of heat treatment on compressive strength and setting behaviour of TTCP/DCPA-derived calcium phosphate cement. *J. Mater. Sci. Lett.* **2002**, 21(20), 1583-1585.

(96) Dorner-Reisel, A.; Müller, E.; Tomandl, G., Short fiber reinforced hydroxyapatite-based bioceramics. *Adv. Eng. Mater.* **2004**, 6(7), 572-577.

(97) Kobayashi, S.; Kawai, W.; Wakayama, S., The effect of pressure during sintering on the strength and fracture toughness of hydroxyapatite ceramics. *J. Mater. Sci. Mater. Med.* **2006**, 17(11), 1089-1093.

(98) Lakes, R. S., Composite biomaterials. In *Biomaterials. Principles and applications*, 2nd ed.; Park, J. B.; Bronzino, J. D., Eds. CRC Press: Boca Raton, FL, 2003; pp 79-93.

(99) Xu, H. H. K.; Frederick, C.; Eichmiller, F. C.; Giuseppetti, A. A., Reinforcement of a self-setting calcium phosphate cement with different fibers *J. Biomed. Mater. Res., Part A* **2000**, 52(1), 107-114.

(100) Gorst, N. J. S.; Perrie, Y.; Gbureck, U.; Hutton, A. L.; Hofmann, M. P.; Grover, L. M.; Barralet, J. E., Effects of fibre reinforcement on the mechanical properties of brushite cement. *Acta Biomater.* **2006**, 2(1), 95-102.

(101) Pott, F., Some aspects on the dosimetry of the carcinogenic potency of asbestos and other fibrous dusts. *Staub-Reinh. Luft* **1978**, 38(12), 486-490.

(102) Stanton, M. F., Relation of particle dimension to carcinogenicity in amphibole asbestoses and other fibrous minerals. *J. Nat. Cancer Inst.* **1981**, 67(5), 965-975.

(103) de With, G.; Corbijn, A. J., Metal fibre reinforced hydroxy-apatite ceramics. *J. Mater. Sci.* **1989**, 24(9), 3411-3415.

(104) Knepper, M.; Milthorpe, B. K.; Moricca, S., Interdiffusion in short-fibre reinforced hydroxyapatite ceramics. *J. Mater. Sci. Mater. Med.* **1998**, 9(10), 589-596.

(105) Dorner-Reisel, A.; Berroth, K.; Neubauer, R.; Nestler, K.; Marx, G.; Scislo, M.; Müller, E.; Ślósarczyk, A., Unreinforced and carbon fibre reinforced hydroxyapatite: resistance against microabrasion. *J. Europ. Ceram. Soc.* **2004**, 24(7), 2131-2139.

(106) Park, K.; Sundaresan, S.; Vasilos, T.; Sung, C., SiC whisker- and C fiber-reinforced calcium phosphate composites. *J. Mater. Res.* **1994**, 9(10), 2476-2479.

(107) Kumar, R.; Prakash, K. H.; Cheang, P.; Khor, K. A., Microstructure and mechanical properties of spark plasma sintered zirconia-hydroxyapatite nano-composite powders. *Acta Mater.* **2005**, 53(8), 2327-2335.

(108) Lee, B.-T.; Lee, C.-W.; Youn, M.-H.; Song, H.-Y., Relationship between microstructure and mechanical properties of fibrous HAp-(t-ZrO_2)/$Al2O_3$-(m-ZrO_2) composites. *Mater. Sci. Eng. A* **2007**, 458(1-2), 11-16.

(109) Wang, X.; Ye, J.; Xiao, F.; Chang, Y.; Wan, C.; Yang, M., Reinforcement of calcium phosphate cement by bio-mineralized carbon nanotube *J. Am. Ceram. Soc.* **2007**, 90(3), 962-964.

(110) Xu, H. H. K.; Eichmiller, F. C.; Barndt, P. R., Effects of fiber length and volume fraction on the reinforcement of calcium phosphate cement. *J. Mater. Sci. Mater. Med.* **2001**, 12(1), 57-65.

(111) Suchanek, W.; Yoshimura, M., Processing and properties of hydroxyapatite-based biomaterials for use as hard tissue replacement implants. *J. Mater. Res.* **1998**, 13(1), 94-117.

(112) Xu, H. H. K.; Simon, C. G., Self-hardening calcium phosphate cement-mesh composite: Reinforcement, macropores, and cell response. *J Biomed Mater Res, Part A* **2004**, 69A(2), 267-278.

(113) Kasuga, T.; Ota, Y.; Tsuji, K.; Abe, Y., Preparation of high-strength calcium phosphate ceramics with low modulus of elasticity containing β-$Ca(PO_3)_2$ fibers *J. Am. Ceram. Soc.* **1996**, 79(7), 1821-1824.

(114) Müller, F. A.; Gbureck, U.; Kasuga, T.; Mizutani, Y.; Barralet, J. E.; Lohbauer, U., Whisker-reinforced calcium phosphate cements. *J. Am. Ceram. Soc.* **2007**, 90(11), 3694-3697.

(115) Lemaître, J.; Munting, E.; Mirtchi, A. A., Setting, hardening and resorption of calcium phosphate hydraulic cements. *Rev. Stomatol. Chir. Maxillofac.* **1992**, 93(3), 163-165.

(116) Gisep, A.; Wieling, R.; Bohner, M.; Matter, S.; Schneider, E.; Rahn, B., Resorption patterns of calcium-phosphate cements in bone. *J. Biomed. Mater. Res., Part A* **2003**, 66A(3), 532-540.

(117) Ioku, K., Preparation and application of calcium phosphate fibers In *Calcium phosphates in biological and industrial systems*, Amjad, Z., Ed. Kluwer: Boston, Mass., 1998; pp 357-369.

(118) Arita, K.; Lucas, M. E.; Nishino, M., The effect of adding hydroxyapatite on the flexural strength of glass ionomer cement. *Dent. Mater. J.* **2003**, 22(2), 126-136.

(119) Corno, M.; Busco, C.; Civalleri, B.; Ugliengo, P., Periodic *ab initio* study of structural and vibrational features of hexagonal hydroxyapatite $Ca_{10}(PO_4)_6(OH)_2$. *Phys. Chem. Chem. Phys.* **2006**, 8(21), 2464-2472.

(120) Kay, M. I.; Young, R. A.; Posner, A. S., Crystal structure of hydroxyapatite. *Nature* **1964**, 204(4963), 1050-1053.

(121) Kawasaki, T., Hydroxyapatite as a liquid chromatographic packing. *J. Chromatogr.* **1991**, 544(1-2), 147-184.

(122) Golden, D. C.; Ming, D. W., Nutrient-substituted hydroxyapatites: synthesis and characterization. *Soil Sci. Soc. Am. J.* **1999**, 63(3), 657-664.

(123) Lange Ness, R. L.; Vlek, P. L. G., Mechanism of calcium and phosphate release from hydroxy-apatite by mycorrhizal hyphae. *Soil Sci. Soc. Am. J.* **2000**, 64(3), 949-955.

(124) Kaneda, K.; Mori, K.; Hara, T.; Mizugaki, T.; Ebitani, K., Design of hydroxyapatite-bound transition metal catalysts for environmentally-benign organic syntheses. *Catal. Surv. Asia* **2004**, 8(4), 231-239.

(125) Tang, X.-Y.; Zhu, Y.-G.; Chen, S.-B.; Tang, L.-L.; Chen, X.-P., Assessment of the effectiveness of different phosphorus fertilizers to remediate Pb-contaminated soil using in vitro test. *Environ. Int.* **2004**, 30(4), 531-537.

(126) Conca, J. L.; Wright, J., An apatite II permeable reactive barrier to remediate ground water containing Zn, Pb and Cd *Appl. Geochem.* **2006**, 21(8), 1288-1300.

(127) Russell, R. G. G.; Caswell, A. M.; Hearn, P. R.; Sharrard, R. M., Calcium in mineralized tissues and pathological calcification. *Brit. Med. Bull.* **1986**, 42(4), 435-446.

(128) Péru, L.; Daculsi, G., Synthetic calcium phosphates: models for biological crystals? *Clin. Mater.* **1994**, 15(4), 267-272.

(129) Vasiliev, A. N.; Zlotnikov, E.; Khinast, J. G.; Riman, R. E., Chemisorption of silane compounds on hydroxyapatites of various morphologies. *Scripta Mater.* **2008**, 58(12), 1039-1042.

(130) Roeder, R. K.; Sproul, M. M.; Turner, C. H., Hydroxyapatite whiskers provide improved mechanical properties in reinforced polymer composites. *J. Biomed. Mater. Res.* **2003**, 67A(3), 801-812.

(131) Daubreé, A., Expériences sur la production artificielle de l'apatite, de la topaze, et de quelques autres métaux fruoriféres. *Compt. Rend. Acad. Sci. Paris* **1851**, Vol. 32, 625.

(132) Jaffe, E. B., Abstracts of the literature on synthesis of apatites and some related phosphates. *U.S. Geol. Surv.* **1951**, Circular 135, 78 pages.

(133) Park, H. C.; Baek, D. J.; Park, Y. M.; Yoon, S. Y., Thermal stability of hydroxyapatite whiskers derived from the hydrolysis of α-TCP. *J. Mater. Sci.* **2004**, 39(7), 2531-2534.

(134) Taş, A. C., Molten salt synthesis of calcium hydroxyapatite whiskers. *J. Am. Ceram. Soc.* **2001**, 84(2), 295-300.

(135) Koutsopoulos, S., Synthesis and characterization of hydroxyapatite crystals. A review study on the analytical methods. *J. Biomed. Mater. Res.* **2002**, 62(4), 600-612.

(136) Tanahashi, M.; Kamiya, K.; Suzuki, T.; Nasu, H., Fibrous hydroxyapatite grown in the gel system: effects of pH of the solution on the growth rate and morphology. *J. Mater. Sci. Mater. Med.* **1992**, 3(1), 48-53.

(137) Wang, X.; Zhuang, J.; Peng, Q.; Li, Y., Liquid-solid-solution synthesis of biomedical hydroxyapatite nanorods. *Adv. Mater.* **2006**, 18(15), 2031-2034.

(138) Byrappa, K.; Yoshimura, M., *Handbook of hydrothermal technology. A technology for crystal growth and materials processing*. 1st ed.; Noyes Publications: New Jersey, 2001.

(139) Yoshimura, M.; Byrappa, K., Hydrothermal processing of materials: past, present and future. *J. Mater. Sci.* **2008**, 43(7), 2085-2103.

(140) Loo, S. C. J.; Siew, Y. E.; Ho, S.; Boey, F. Y. C.; Ma, J., Synthesis and hydrothermal treatment of nanostructured hydroxyapatite of controllable sizes. *J. Mater. Sci. Mater. Med.* **2008**, 19(3), 1389-1397.

(141) Nagata, F.; Toriyama, M.; Teraoka, K.; Yokogawa, Y., Influence of ethylamine on the crystal growth of hydroxyapatite crystals. *Chem. Lett.* **2001**, 30(8), 780-781.

(142) Ashok, M.; Narayana Kalkura, S.; Meenakshi Sundaram, N.; Arivuoli, D., Growth and characterization of hydroxyapatite crystals by hydrothermal method. *J. Mater. Sci. Mater. Med.* **2007**, 18(15), 895-898.

(143) Wei, M., Ribbon-like and rod-like hydroxyapatite crystals deposited on titanium surface with electrochemical method. *Mater. Lett.* **2007**, 61(19-20), 4062-4065.

(144) Zhou, Z.-H.; Zhou, P.-L.; Yang, S.-P.; Yu, X.-B.; Yang, L.-Z., Controllable synthesis of hydroxyapatite nanocrystals via a dendrimer-assisted hydrothermal process. *Mater. Res. Bull.* **2007**, 42(9), 1611-1618.

(145) Zhang, H. G.; Zhu, Q.; Wang, Y., Morphologically controlled synthesis of hydroxyapatite with partial substitution of fluorine. *Chem. Mater.* **2005**, 17(23), 5824-5830.

(146) Aizawa, M.; Porter, A. E.; Best, S. M.; Bonfield, W., Ultrastructural observation of single-crystal apatite fibres. *Biomaterials* **2005**, 26(17), 2005.

(147) Aizawa, M.; Ueno, H.; Itatani, K.; Okada, I., Syntheses of calcium-deficient apatite fibres by a homogeneous precipitation method and their characterizations. *J. Europ. Ceram. Soc.* **2006**, 26(4-5), 501-507.

(148) Zhang, H.; Wang, Y.; Yan, Y.; Li, S., Preparation of biocompatible hydroxyapatite whiskers from moderately acid solution. *Ceram. Int.* **2003**, 29(4), 413-418.

(149) Zhang, H.; Yan, Y.; Wang, Y.; Li, S., Thermal stability of hydroxyapatite whiskers prepared by homogenous precipitation. *Adv. Eng. Mater.* **2002**, 4(12), 916-919.

(150) Andrés-Vergés, M.; Fernádez-González, C.; Martínez-Gallego, M., Hydrothermal synthesis of calcium deficient hydroxyapatite with controlled size and homogeneous morphology. *J. Europ. Ceram. Soc.* **1998**, 18(9), 1245-1250.

(151) Roeder, R. K.; Sproul, M. M.; Turner, C. H., Hydroxyapatite whiskers provide improved mechanical properties in reinforced polymer composites. *J. Biomed. Mater. Res., Part A* **2003**, 67A(3), 801-812.

(152) Yoshimura, M.; Suda, H., Hydrothermal synthesis of biocompatible whiskers. *J. Mater. Sci.* **1994**, 29(13), 3399-3402.

(153) Willard, H. H.; Tang, N. K., A study of the precipitation of aluminum basic sulfate by urea. *J. Am. Chem. Soc.* **1937**, 59(7), 1190-1196.

(154) Kokubo, T.; Kushitani, H.; Sakka, S.; Kitsugi, T.; Yamamuro, T., Solutions able to reproduce in vivo surface-structure changes in bioactive glass-ceramic A-W^3. *J. Biomed. Mater. Res.* **1990**, 24(6), 721-734.

(155) Stoe & Cie GmbH 2004 (http://www.stoe.com).

(156) Fukase, Y.; Eanes, E. D.; Takagi, S.; Chow, L. C.; Brown, W. E., Setting reactions and compressive strengths of calcium phosphate cements. *J. Dent. Res.* **1990**, 69(12), 1852-1856.

(157) Gamble, J. E., *Chemical anatomy, physiology and pathology of extracellular fluid*. 1st ed.; Harvard University Press: Cambridge, MA, 1967; p 1-17.

(158) Kokubo, T.; Takadama, T., Simulated body fluid (SBF) as a standard tool to test the bioactivity of implants. In *Handbook of biomineralization. Medical and clinical aspects.*, Epple, M.; Baeuerlein, E., Eds. Wiley-VCH: Weinheim, 2007; pp 97-108.

(159) Oliver, W. C.; Pharr, G. M., An improved technique for determining hardness and elastic-modulus using load and displacement sensing indentation experiments. *J. Mater. Res.* **1992**, 7(6), 1564-1583.

(160) Turner, C. H.; Burr, D. B., Experimental techniques for bone mechanics. In *Bone mechanics handbook*, 2nd ed.; Cowin, S. C., Ed. CPC Press: Boca Raton, FL, 2001; pp 7-20.

(161) Grenoble, D. E.; Katz, J. L.; Dunn, K. L.; Gilmore, R. S.; Murty, K. L., The elastic properties of hard tissues and apatites. *J. Biomed. Mater. Res.* **1972**, 6(3), 221-223.

(162) Moreno, E. C.; Brown, W. E.; Osborn, G., Solubility of dicalcium phosphate dihydrate in aqueous systems. *Soil Sci. Soc. Am. J.* **1960**, 24(2), 94-98.

(163) Brown, W. E.; Epstein, E. F., Crystallography of tetracalcium phosphate. *J. Res. Natl. Bur. Stand.* **1965**, 69A(6), 547-551.

(164) Guo, D.; Xu, K.; Han, Y., Influence of cooling modes on purity of solid-state synthesized tetracalcium phosphate. *Mater. Sci. Eng. B* **2005**, 116(2), 175-181.

(165) Brown, W.E.; Chow, L.C. *Dental restorative cement pastes*. US Patent No. 4518430, 1985.

(166) Greish, Y. E.; Brown, P. W., Phase evolution during the formation of stoichiometric hydroxyapatite at 37.4°C. *J. Biomed. Mater. Res., Part B* **2003**, 67B(1), 632-637.

(167) Martin, I.; Brown, P., Mechanical properties of hydroxyapatite formed at physiological temperature. *J. Mater. Sci. Mater. Med.* **1995**, 6(3), 138-145.

(168) Boskey, A. L.; Posner, A. S., Conversion of amorphous calcium phosphate to microcrystalline hydroxyapatite. A pH dependent, solution-mediated, solid-solid conversion. *J. Phys. Chem.* **1973**, 77(19), 2313-2317.

(169) Winand, L., Étude physico-chimique du phosphate tricalcique hydraté et de l'hydroxylapatite. *Ann. Chim. (Paris) 13th Series* **1961**, 6, 951-967.

(170) Nakamoto, K., *Infrared and Raman spectra of inorganic and coordination compounds, Part B: applications in coordination, organometallic and bioinorganic chemistry*. 5th ed.; John Wiley & Sons Inc: New York, 1997; p 54, 148.

(171) Fowler, B. O., Infrared studies of apatites. I. Vibrational assignments for calcium, strontium, and barium hydroxyapatites utilizing isotopic substitution. *Inorg. Chem.* **1974**, 13(1), 194-207.

(172) Monma, H.; Takahashi, T., Preparation and thermal changes of carbonate-containing apatite. *Gypsum & Lime* **1987**, 210, 287-291.

(173) Steger, E.; Herzog, K., Zum schwingungsspektrum der phosphorsäure. I. Infrarot- und Raman-spektren von phosphatlösungen. *Anorg. Allg. Chem.* **1964**, 331(3-4), 169-182.

(174) Socrates, G., *Infrared and Raman characteristic group frequencies, tables and charts*. 3th ed.; John Wiley & Sons, Ltd: Chichester, England, 2001, p. 276.

(175) Sauer, G. R.; Zunic, W. B.; Durig, J. R.; Wuthier, R. E., Fourier transform Raman spectroscopy of synthetic and biological calcium phosphates. *Calcif. Tissue Int.* **1994**, 54(5), 414-420.

(176) Dorozhkina, E. I.; Dorozhkin, S. V., Mechanism of the solid-state transformation of a calcium-deficient hydroxyapatite (CDHA) into biphasic calcium phosphate (BCP) at elevated temperatures. *Chem. Mater.* **2002**, 14(10), 4267-4272.

(177) Lazić, S.; Katanić-Popović, J.; Zec, S.; Miljević, N., Properties of hydroxyapatite crystallized from high temperature alkaline solutions. *J. Cryst. Growth.* **1996**, 165(1-2), 124-128.

(178) Sing, K. S. W.; Everett, D. H.; Haul, R. A. W.; Moscou, L.; Pierotti, R. A.; Rouquerol, J.; Siemieniewska, T., Reporting physisorption data for gas/solid systems with special reference to the determination of surface area and porosity. *Pure Appl. Chem.* **1985**, 57(4), 603-619.

(179) O'Regan, B.; Grätzel, M., A low-cost, high-efficiency solar cell based on dye-sensitized colloidal TiO_2 films. *Nature* **1991**, 353(6346), 737-740.

(180) Li, X.; Bhushan, B., A review of nanoindentation continuous stiffness measurement technique and its applications. *Mater. Charact.* **2002**, 48(1), 11-36.

(181) Chow, L.C., Takagi, S. *Self-setting calcium phosphate cements and methods for preparing and using them*. US Patent No. 5525148, 1996.

(182) Xu, H. H. K.; Burguera, E. F.; Carey, L. E., Strong, macroporous, and in situ-setting calcium phosphate cement-layered structures. *Biomaterials* **2007**, 28(26), 3786-3796.

(183) Liu, C.; Shao, H.; Chen, F.; Zheng, H., Effects of the granularity of raw materials on the hydration and hardening process of calcium phosphate cement. *Biomaterials* **2003**, 24(23), 4103-4113.

(184) Otsuka, M.; Matsuda, Y.; Suwa, Y., Effect of particle size of metastable calcium phosphate on mechanical strength of a novel self-setting bioactive calcium phosphate cement. *J. Biomed. Mater. Res.* **1995**, 29(1), 25-32.

(185) Sun, L.; Chow, L. C.; Bauer, T. W.; Burguera, E. F.; Frukhtbeyn, S. A., Influence of particle size on DCPD hydrolysis and setting properties of TTCP/DCPD cement. *Key Eng. Mat.* **2005**, 284-286, 23-26.

(186) Burguera, E. F.; Guitián, F.; Chow, L. C., A rapid setting TTCP-DCPD cement. Study of the setting reaction as a function of time. *Key Eng. Mat.* **2005**, 284-286, 15-18.

(187) Perloff, A.; Posner, A. S., Preparation of pure hydroxyapatite crystals. *Science* **1956**, 124(3222), 583-584.

(188) Walsh, D.; Tanaka, J., Preparation of a bone-like apatite foam cement. *J. Mater. Sci. Mater. Med.* **2001**, 12(4), 339-343.

(189) Ison, I. C.; Fulmer, M. T.; Barr, B. M.; Constanz, B. R., In *Hydroxyapatite and Related Materials*, Brown, P. W.; Constantz, B. R., Eds. CRC Press: Boca Raton, Florida, 1994; p 215.

(190) Barralet, J. E.; Gaunt, T.; Wright, A. J.; Gibson, I. R.; Knowles, J. C., Effect of porosity reduction by compaction on compressive strength and microstructure of calcium phosphate cement. *J. Biomed. Mater. Res., Part B* **2002**, 63(1), 1-9.

(191) Hench, L. L.; Clark, A. E., Adhesion to bone. In *Biocompatibility of orthopedic implants*, Williams, D. F., Ed. CRC Press: Boca Raton, FL, 1982, Vol. II; pp 129-170.

(192) Chow, L. C.; Hirayama, S.; Takagi, S.; Parry, E., Diametral tensile strength and compressive strength of a calcium phosphate cement: effect of applied pressure. *J. Biomed. Mater. Res., Part B* **2000**, 53(5), 511-517.

(193) Komath, M.; Varma, H. K.; Sivakumar, R., On the development of an apatitic calcium phosphate bone cement. *Bull. Mater. Sci.* **2000**, 23(2), 135-140.

(194) Hoshikawa, A.; Fukui, N.; Fukuda, A.; Sawamura, T.; Hattori, M.; Nakamura, K.; Oda, H., Quantitative analysis of the resorption and osteoconduction process of a calcium phosphate cement and its mechanical effect for screwfixation. *Biomaterials* **2003**, 24(27), 4967-4975.

(195) Zhang, Z. F.; Zhang, H.; Pan, X. F.; Das, J.; Eckert, J., Effect of aspect ratio on the compressive deformation and fracture behaviour of Zr-based bulk metallic glass. *Phil. Mag. Lett.* **2005**, 85(10), 513-521.

(196) Xu, H.; Smith, D.; Simon, C., Strong and bioactive composites containing nano-silica-fused whiskers for bone repair. *Biomaterials* **2004**, 25(19), 4615-4626.

(197) Ni, G. X.; Choy, Y. S.; Lu, W. W.; Ngan, A. H. W.; Chiu, K. Y.; Li, Z. Y.; Tang, B.; Luk, K. D. K., Nano-mechanics of bone and bioactive bone cement interfaces in a load-bearing model. *Biomaterials* **2006**, 27(9), 1963-1970.

(198) Guo, X. E., Mechanical properties of cortical bone and cancellous bone tissue. In *Bone mechanics handbook*, 2nd ed.; Cowin, S. C., Ed. CPC Press: Boca Raton, FL, 2001; pp 10-9.

(199) Kolen'ko, Y. V.; Kovnir, K. A.; Neira, I. S.; Taniguchi, T.; Ishigaki, T.; Watanabe, T.; Sakamoto, N.; Yoshimura, M., A novel, controlled and high-yield solvothermal drying route to nanosized barium titanate powders. *J. Phys. Chem. C* **2007**, 111(20), 7306-7318.

(200) Nancollas, G. H.; Marshall, R. W., The kinetics of dissolution of dicalcium phosphate dihydrate crystals. *J. Dent. Res.* **1971**, 50(5), 1268-1272.

(201) Viswanath, B.; Raghavan, R.; Ramamurty, U.; Ravishankar, N., Mechanical properties and anisotropy in hydroxyapatite single crystals. *Scripta Mater.* **2007**, 57, 361-364.

(202) Kumar, R. R.; Wang, M., Modulus and hardness evaluations of sintered bioceramic powders and functionally graded bioactive composites by nano-indentation technique. *Mat. Sci. Eng. A* **2002**, 338, 230-236.

(203) Teraoka, K.; Ito, A.; Maekawa, K.; Onuma, K.; Tateishi, T.; Tsutsumi, S., Mechanical properties of hydroxyapatite and OH-carbonates hydroxyapatite single crystals. *J. Dent. Res.* **1998**, 77(7), 1560-1568.

(204) Imbeni, V.; Kruzic, J. J.; Marshall, G. W.; Marshall, S. J.; Ritchie, R. O., The dentin-enamel junction and the fracture of human teeth. *Nature Mater.* **2005**, 4(3), 229 - 232.

(205) Katz, J. L.; Ukraincik, K., On the anisotropic elastic properties of hydroxyapatite. *J. Biomech.* **1971**, 4(3), 221-227.

(206) Balac, I.; Uskokovic, P. S.; Aleksic, R.; Uskokovic, D., Predictive modeling of the mechanical properties of particulate hydroxyapatite reinforced polymer composites. *J. Biomed. Mater. Res., Part A* **2002**, 63(6), 793-799.

(207) Converse, G. L.; Yue, W.; Roeder, R. K., Processing and tensile properties of hydroxyapatite-whisker-reinforced polyetheretherketone. *Biomaterials* **2007**, 28(6), 927-935.

(208) Fu, T.; Zhao, J.-L.; Xu, K.-W., The designable elastic modulus of 3-D fabric reinforced biocomposites. *Mater. Lett.* **2007**, 61(2), 330-333.

(209) Ben Cheokh Larbi, A.; Sai, K.; Sidhom, H.; Baptiste, D., Constitutive model of micromechanical damage to predict reduction in stiffness of a fatigued SMC composite. *J. Mater. Eng. Perform.* **2006**, 15(5), 575-580.

(210) Xu, H. H. K.; Quinn, J. B.; Takagi, S.; Chow, L. C.; Eichmiller, F. C., Strong and macroporous calcium phosphate cement: effects of porosity and fiber reinforcement on mechanical properties. *J Biomed Mater Res, Part A* **2001**, 57(3), 457-466.

GLOSSARY OF COMMON TERMS

- ***a*-surface** – See *Prismatic plane*.
- **Allografts** – Bones taken from donors or cadavers and implanted into another individual of the same specie.
- **Alloplastic** – It refers to inorganic materials implanted in living tissue.
- **Anisotropy** – In anisotropic systems the values of a property change with the crystallographic direction.
- **Autografts** – Involves harvesting healthy bone from one anatomical site and implanting the graft material in a defect site of the same individual.
- **Basal plane** – The plane which is perpendicular to the *c*-axis of the hexagonal structure.
- **Bioactivity** – It refers to the property of a biomaterial to establish chemical bonds with the host tissue when is used as an implant.
- **Biodegradability** – See *bioresorbability*.
- **Biocompatibility** – It involves the acceptance of an artificial implant by the surrounding tissues and by the body as a whole.
- **Biocomposite** – Composite employed as biomaterial.
- **Biomaterial** – It is any substance (other than drugs) or combination of substances, synthetic or natural in origin, which can be used for any period of time, as a whole or as a part of a system which treats, augments, or replaces any tissue, organ or function of the body.
- **Bioresorbability** – Property of a biomaterials used as a implant to be replaced by the surrounding tissues.
- **Biphasic calcium phosphate** – It is an intimate mixture of HA and β-TCP in various HA/β-TCP ratios.
- **Bone bonding** – It refers to the ability of bone tissue to bond to the surface of a synthetic material.
- **Brittle** – A material is brittle if it is liable to fracture when subjected to a force. Opposite to toughness.
- ***c*-surface** – See *Basal plane*.
- **Cohesive time** – It is the time from which a cement no longer disintegrates when immersed in an aqueous phase.
- **Composite** – Composite materials are solids which contain two or more distinct constituent materials or phases on a scale larger than the atomic and in which properties are significantly altered in comparison with those of a homogeneous material.
- **Compressive strength** – The capacity of a material to bear axially directed pushing forces. When the limit of compressive strength is reached, materials broken.
- **Calcium phosphate (bone-)cements** – A mixture of calcium orthophosphates that react in an aqueous/physiological medium at room/body temperature to form (precipitate) DCPD or HA.
- **Creep** – It is a deformation under a constant load.

- **Ductile** – A ductile material is capable of withstanding a certain amount of force, by changing its form, before fracturing or breaking (related with plastic behaviour). In metals it refers to the fact that they can be pulled out into wires.
- **Elastic modulus** – The mathematical description of an object or substance's tendency to be deformed elastically under the action of a load. It is a measure of the stiffness of a material.
- **Fibre** – Particles with one long dimension.
- **Final setting time** – It refers to the fact that, after this time, the setting reaction has proceeded to an extent that the manipulation of the CPC will not deteriorate its mechanical properties.
- **Fracture toughness** – It is the ability of a material containing a crack to resist fracture.
- **Growth factor** – It refers to a naturally occurring protein capable of stimulating cellular differentiation and maturation. For example, bone morphogenic proteins stimulate bone cell differentiation.
- **Hardness** – It refers to various properties of matter in the solid phase that give it high resistance to permanent shape changes when a force is applied. It is related with plastic deformations. In bones, hardness reflects the degree and quality of mineralization of the bone.
- **Initial setting time** – It marks the onset of hardening after water has been added to the CPC precursors.
- **Immunogenicity** – It is the ability of a particular substance (antigen), to provoke an immune response; a collection of mechanisms within an organism that protects against disease by identifying and killing pathogens.
- **Isotropy** – Isotropic systems have identical values of a property in all crystallographic directions.
- **Osseointegration** – It is the direct structural and functional connection between living bone and the surface of an artificial implant.
- **Osteoblast** – From the Greek "bone" and "germ" or embryonic. It is a bone cell, present on the bone surface, responsible for bone formation.
- **Osteoclasts** – From the Greek words for "bone" and "broken". It is a type of bone cell, located on the bone surface, which removes bone tissue by removing its mineralized matrix. This process is known as bone resorption.
- **Osteoconductivity** – It refers to the ability of some materials to serve as a scaffold on which bone cells can attach, grow and divide. In this way, the bone healing response is "conducted" through the graft site. They promotes bone apposition on its surface or down into pores or channels functioning in part as a receptive scaffold to facilitate enhanced bone formation.
- **Osteocytes** – Mature osteoblasts. They are actively involved in the routine turnover of bone matrix through various mechanosensory mechanisms.
- **Osteogenicity** – It is the supply of bone-forming cells by the marrow of the harvested bone.

- **Osteoinductivity** – Associated to the process whereby implanted proteins and growth factors induce new bone to grow.
- **Platelet** – Particles with two long dimensions.
- **Prismatic plane** – The plane which is parallel to the *c*-axis of the hexagonal structure.
- **Shear strength** – It is the resistance to the deformation when the stress (amount of force exerted per unit area) is parallel or tangential to a face of the material.
- **Stress shielding** – If biomaterials used as implants are much stiffer than bone, they shield the nearby bone from mechanical stress. Stress shielding results in a kind of disuse atrophy: the bone resorbs. Therefore, the integrity of the bone/implant interface is compromised.
- **Tensile strength** – The resistance of a material to a force tending to tear it apart, measured as the maximum tension the material can withstand without tearing.
- **Torque** – It is a vector that measures how much a force acting on an object causes that object to rotate.
- **Toughness** – Resistance to fracture of a material when a force is applied. It is the opposite of brittleness.
- **Wear** – In materials science, wear is the erosion of material from a solid surface by the action of another solid.
- **Whiskers** – Fibrous single crystals with no dislocations usually grown at high temperatures and with great aspect ratio (length/diameter), thus, with small diameters and big lengths.
- **Xenografts** – It refers to bone tissue collected from one specie and implanted into a different one, *i.e.* ivory or bovine bone.
- **Young's modulus** – See *elastic modulus*.

ANNEXE I

TABLES

Table AI.1. Assignments and positions of the bands in Raman spectrum of the 24 hour-derived **C-D36/T48** optimal cement.

Detected modes	Wavenumber (cm^{-1})
$\nu_2(HPO_4^{2-})$	395 (sh)
$\nu_2(PO_4^{3-})$	440 (s) 457 (sh) 488 (s, shp)
$\nu_4(PO_4^{3-})$	598 (s) 624 (sh)
$\nu_1(HPO_4^{2-})$	893 (w, shp)
$\nu_1(PO_4^{3-})$	969 (vs, shp)
$\nu_3(PO_4^{3-})$	1052 (shp) 1077 (shp)
$\nu_3(HPO_4^{2-})$	1134 (w)
$\nu(OH^-)$	3576 (s, shp)

Throughout this table, a set of acronyms is used: s – strong, sh – shoulder; shp – sharp; v – very; w – weak.

Table AI.2. Summary of synthetic conditions and results from conducted hydrothermal reactions.

Applied temperature cycle	Concentration, M				pH_{final}	XRD phase composition [a]		SEM particles' morphology	
	$[Ca^{2+}]$	$[PO_4^{3-}]$	[Urea]	$[HNO_3]$		Cotton-like suspension [b]	Wall-product [c]	Cotton-like suspension [b]	Wall-product [c]
Scheme I	0.0835	0.05	0.25	0.50	8.50	HA [d]	HA	Plates	Plates and agglomerated hexagonal prisms
Scheme II	0.0835	0.05	0.25	0.50	8.48	HA	None	Fine-plates	None
				1.00	7.86	HA			
	0.1670	0.10	0.50	0.50	8.12	HA [d]	HA	Hexagonal prisms	Irregular and agglomerated hexagonal prisms
				1.00	7.89	HA [d]	HA		
	0.3340	0.20	1.00	0.50	7.12	HA + OCP [e] + DPCA	DCPA [f] + HA + OCP	—	—
				1.00	7.83	HA + OCP [e]	HA [g] + OCP	Plates	Plates and agglomerated hexagonal prisms
Scheme III	0.0835	0.05	0.25	0.50	8.25	HA	None	Fine-plates	None
				1.00	8.24	HA			
	0.1670	0.10	0.50	0.50	8.41	HA [d]	HA	Needles	Short hexagonal prisms
				1.00	8.00	HA [d]	HA		Needles and agglomerated hexagonal prisms
	0.3340	0.20	1.00	0.50	7.46	HA + OCP [e]	—	—	—
				1.00	6.99	HA + OCP [e]			
Scheme IV	0.0835	0.05	0.25	0.50	8.37	HA	None	Fine-plates	None
				1.00	8.15	HA			
	0.1670	0.10	0.50	0.50	6.96	HA + OCP [e]	—	—	—
				1.00	7.80	HA + OCP [e]			
	0.3340	0.20	1.00	0.50	7.18	HA + OCP [e]	—	—	—
				1.00	7.99	HA + OCP [e]			

[a] – References for the hydroxyapatite (HA) $Ca_{10}(PO_4)_6(OH)_2$, octacalcium phosphate (OCP) $Ca_8H_2(PO_4)_6{\cdot}5H_2O$ and dicalcium phosphate anhydrous (DCPA) $CaHPO_4$ phases – JCPDS card numbers [72-1243], [74-1301] and [70-1425] respectively. [b] – An abundant cotton-like suspension product (Fig. 6.3A). [c] – Secondary wall-product firmly attached to PTFE vessel's walls (Fig. 6.3B). [d] – There are inconsistencies in the intensity of the observed XRD reflections *cf.* the reported ones in JCPDS database, indicating the texturing of the particles. [e] – Major amount of the octacalcium phosphate phase. [f] – Major amount of the dicalcium phosphate anhydrous phase. [g] – Major amount of the hydroxyapatite phase.

Table AI.3. Comparison of synthetic conditions and results from hydrothermal reactions conducted with different urea concentrations. Reagent concentrations: $[Ca^{2+}]$ = 0.167 M, $[PO_4^{3-}]$ = 0.1 M, $[HNO_3]$ = 0.5 M. Only cotton-like suspension products (Fig. 6.3A) were analyzed.

Applied temperature cycle	Concentration of urea, M	pH_{final}	XRD phase composition [a]	SEM particles' morphology	XRD reaction solution phase composition [b]
Scheme II	0.250	7.05	HA [c,d] + OCP	Plates	NH_4NO_3
	0.375	8.32	HA [d]	Plates and needles	NH_4NO_3
	0.500	8.15	HA [d]	Hexagonal prisms	Urea + NH_4NO_3
	0.625	7.53	HA + OCP [e]	Plates and needles	Urea + NH_4NO_3
	0.750	8.02	HA + OCP [e]	Plates and needles	Urea + NH_4NO_3
	1.000	8.09	HA + OCP [e]	Plates and needles	Urea + NH_4NO_3
Scheme III	0.250	7.21	HA + OCP [e]	Plates and needles	NH_4NO_3
	0.375	8.10	HA [d]	Plates and needles	Urea + NH_4NO_3
	0.450	8.59	HA [d]	Plates and needles	Urea + NH_4NO_3
	0.500	8.25	HA [d]	Needles	Urea + NH_4NO_3
	0.550	8.32	HA [d]	Needles	Urea + NH_4NO_3
	0.750	8.77	HA [d]	Plates	Urea + NH_4NO_3
	1.000	8.29	HA + OCP [e]	Plates	Urea + NH_4NO_3

[a] – References for the hydroxyapatite (HA) $Ca_{10}(PO_4)_6(OH)_2$, octacalcium phosphate (OCP) $Ca_8H_2(PO_4)_6{\cdot}5H_2O$, ammonium nitrate NH_4NO_3 and urea H_2NCONH_2 phases – JCPDS card numbers [72-1243], [74-1301], [8-452] and [8-822] respectively. [b] – Prior to the XRD analysis, the liquid from the reaction solution was evaporated at 60°C. [c] – Major amount of the hydroxyapatite phase. [d] – There are inconsistencies in the intensity of the observed XRD reflections *cf.* the reported ones in JCPDS database, indicating the texturing of the particles. [e] – Major amount of the octacalcium phosphate phase.

Table AI.4. Assignments and positions of the bands in IR spectra from the **PT**, **HX**, **ND** and **FP** powdered samples prepared by hydrothermal method.

Detected modes	Wavenumber, cm^{-1}			
	Sample PT	**Sample HX**	**Sample ND**	**Sample FP**
$\nu_s(OH^-)$	3572 (shp)	3572 (shp)	3568 (shp)	3570 (shp)
$\nu_{asym}+\nu_{sym}(O\text{-}H)_{water}$	3294 (b)	3361 (b)	~3327 (sh)	~3359 (sh)
$\nu_{asym}(CO_2)$	2364 (shp)	2364 (shp)	2362 (shp)	2369 (vw)
	2341 (shp)	2341 (shp)	2341 (shp)	2345 (vw)
Harmonics(OH^-)	2129 (vw)	2131 (vw)	2131 (vw)	2131 (vw)
	2075 (vw)	2171 (w)	2075 (vw)	2075 (vw)
	1984 (w)	1998 (w)	1998 (w)	1992 (w)
$\nu_3(PO_4^{3-})$	1090 (sh)	1099 (sh)	1117 (sh, shp)	1109 (sh)
	1064 (sh)	1064 (sh)	—	—
	1024 (vs)	1026 (vs)	1028 (vs)	1036 (vs)
$\nu_1(PO_4^{3-})$	960 (shp)	960 (shp)	960 (shp)	960 (shp)
	604 (s, shp)	605 (s, shp)	602 (s, shp)	605 (s, shp)
	578 (shp)	578 (shp)	578 (sh)	578 (shp)
$\nu(CO_3^{2-})_{OH^-}$	1545 (shp)	1547 (shp)	1545 (shp)	1541 (sh)
	879 (sh)	879 (sh)	879 (sh)	879 (sh)
$\nu(CO_3^{2-})_{PO4^{3-}}$	1452 (vs)	1452 (vs)	1450 (vs)	1452 (vs)
	1423 (vs)	1421 (vs)	1421 (vs)	1417 (vs)
	874 (s, shp)	874 (s, shp)	874 (s, shp)	874 (s, shp)
$\nu_4(PO_4^{3-})$	603 (vs)	605 (vs)	602 (vs)	605 (vs)
	578 (shp)	578 (sh)	577 (sh)	576 (sh)
	563 (vs)	563 (vs)	561 (vs)	563 (vs)
$\nu_L(OH^-)$	636 (sh)	634 (sh)	634 (sh)	640 (sh)

Throughout this table, a set of acronyms is used: b – broad, s – strong, sh – shoulder; shp – sharp; v – very; w – weak.

Table AI.5. Assignments and positions of the bands in Raman spectra from the **PT**, **HX**, **ND** and **FP** powdered samples prepared by hydrothermal method.

Detected modes	Wavenumber, cm^{-1}			
	Sample PT	**Sample HX**	**Sample ND**	**Sample FP**
$\nu_2(PO_4^{3-})$	431 (s, shp) 449 (w, sh) 479 (sh)	431 (s, shp) 451 (w, sh) 480 (sh)	431 (s, shp) 450 (w, sh) 479 (shp)	432 (s, shp) 451 (w, sh) 481 (sh)
$\nu_4(PO_4^{3-})$	589 (s, shp) 612 (sh)	590 (s, shp) 611 (sh)	591 (s, shp) 610 (w, sh)	590 (s, shp) 611 (sh)
$\nu_1(PO_4^{3-})$	962 (vs, shp)	961 (vs, shp)	961 (vs, shp)	962 (vs, shp)
$\nu_3(PO_4^{3-})$	1047 (shp) 1071 (shp)	1047 (shp) 1071 (shp)	1046 (shp) 1072 (shp)	1046 (shp) 1071 (shp)
$\nu(OH^-)$	3572 (s, shp)	3572 (s, shp)	3573 (s, shp)	3572 (s, shp)

Throughout this table, a set of acronyms is used: s – strong, sh – shoulder; shp – sharp; v – very; w – weak.

Table AI.6. Assignments and positions of the bands in Raman spectrum of the 24 hour-derived **CPC-10%FP** and **CPC-10%HX** biocomposites.

Detected modes	Wavenumber (cm^{-1})	
	Sample CPC-10%FP	**Sample CPC-10%HX**
$\nu_2(HPO_4^{2-})$	396 (wv)	—
$\nu_2(PO_4^{3-})$	428 (s) 447 (sh) 479 (w, shp)	428 (s) 447 (sh) 479 (w, shp)
$\nu_4(PO_4^{3-})$	580 (s) 589 (s) 607 (w)	580 (s) 589 (s) 607 (w)
$\nu_1(HPO_4^{2-})$	896 (wv)	—
$\nu_1(PO_4^{3-})$	969 (vs, shp)	969 (vs, shp)
$\nu_3(PO_4^{3-})$	1027 (shp) 1048 (s) 1074 (s)	1027 (shp) 1048 (s) 1074 (s)
$\nu_3(HPO_4^{2-})$	1129 (vw)	—
$\nu(OH^-)$	3571 (shp)	3571 (shp)

Throughout this table, a set of acronyms is used: s – strong, sh – shoulder; shp – sharp; v – very; w – weak.

ANNEXE II

FIGURES

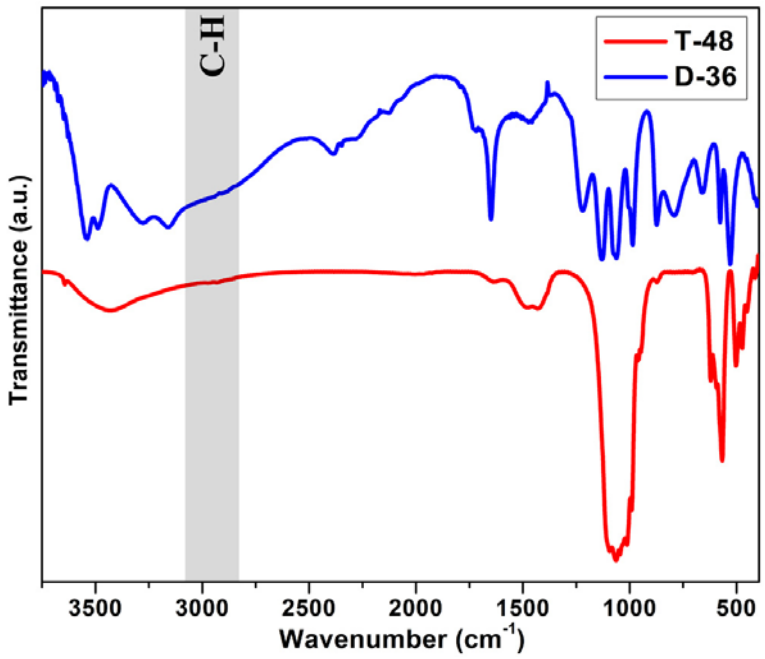

Fig. AII.1. Infrared spectroscopy data in the region 3750-395 cm^{-1}, taken from the **D-36** and **T-48** samples. Grey region represents expected characteristic C–H bands. Note the absence of the remaining organic compounds from the synthesis procedure in DCPD and TTCP ball-milled.

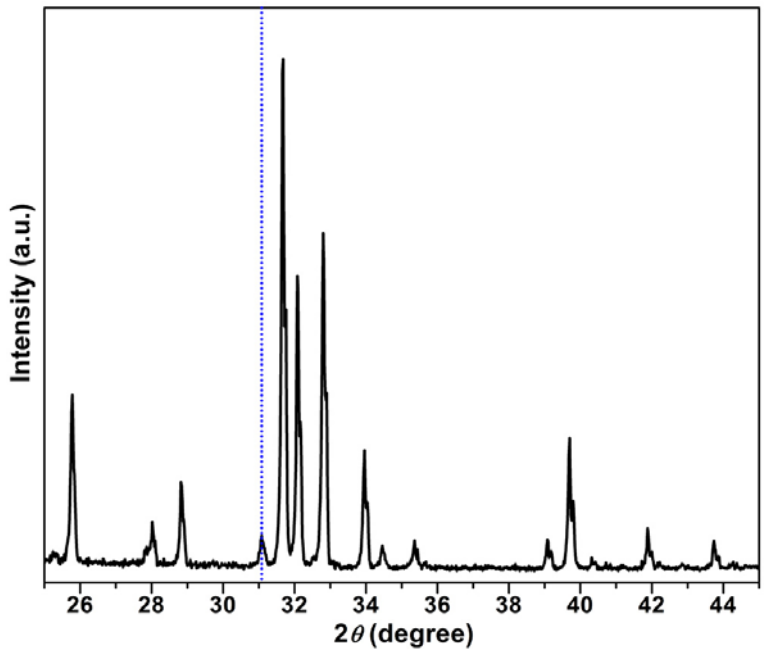

Fig. AII.2. Powder X-ray diffraction pattern from **C-D36/T48** cement after TGA/DTA measurement (25-1300°C). Note the presence of the XRD peak related to the α-TCP (dotted blue line, JCPDS No. 9-348) confirming the Ca-deficiency of this CPC.

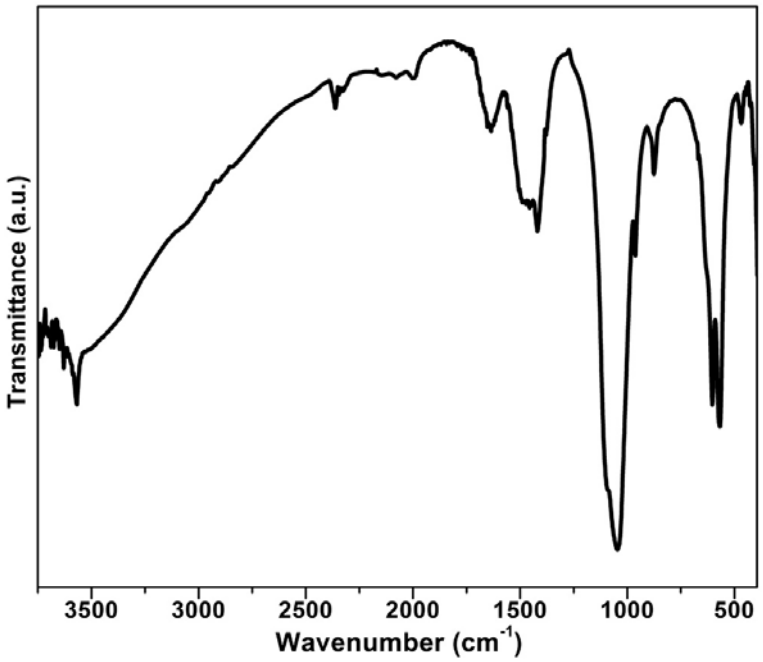

Fig. AII.3. IR spectra of the **C-D36/T48** cement after soaking in SBF for 10 days.

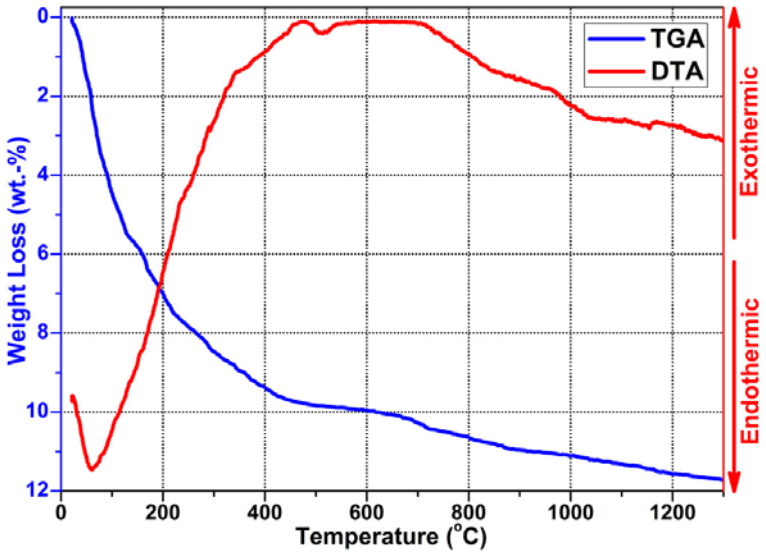

Fig. AII.4. TGA/DTA results for the **C-D36/T48** cement after soaking in SBF for 10 days.

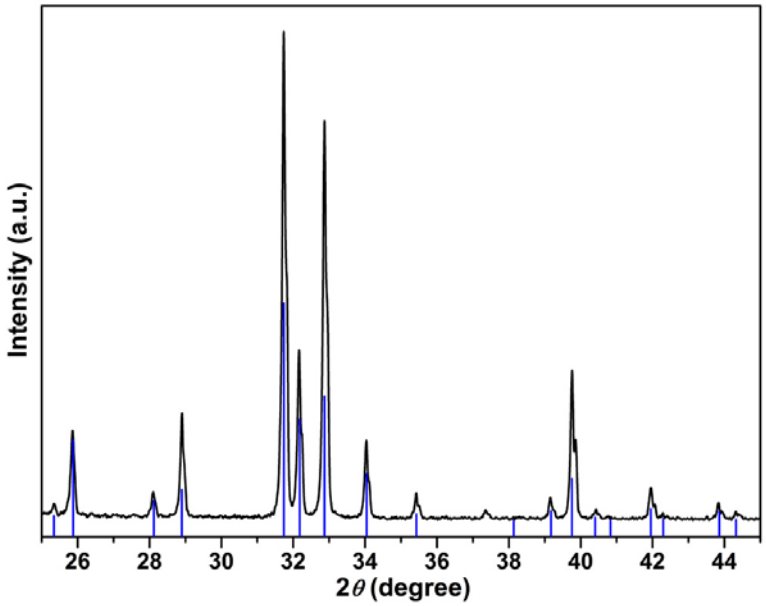

Fig. AII.5. Powder X-ray diffraction pattern from hydrothermally-derived **HX** sample after TGA/DTA measurement (25-1200°C). Tick marks below the patterns correspond to the positions of the Bragg reflections expected for the hexagonal HA (JCPDS No. 72-1243). Note the lack of the XRD peaks related to the α-TCP or β-TCP in contrast to the **C-D36/T48** cement(Fig. AII.2), confirming that the as-synthesized **HX** sample is not Ca-deficient HA.

ANNEXE III

RESEARCH PUBLICATIONS AND CONFERENCE CONTRIBUTIONS

CONFERENCES CONTRIBUTIONS

Oral presentations

- I. S. Neira, F. Guitián, T. Watanabe, M. Yoshimura, "Hydroxyapatite whiskers prepared by low-temperature hydrothermal method with homogeneous precipitation". Joint Meeting of the 8th International Symposium on Hydrothermal Reactions and 7th International Conference on Solvothermal Reactions (ISHR&ICSTR 2006), August 5-9 2006, Sendai, Japan.

Poster contributions

- I. S. Neira, F. Guitián, T. Watanabe, M. Yoshimura, "A high-yield hydrothermal route to hydroxyapatite whiskers". Joint Meeting of the 8th International Symposium on Hydrothermal Reactions and 7th International Conference on Solvothermal Reactions (ISHR&ICSTR 2006), August 5-9 2006, Sendai, Japan.

- I. S. Neira, Yu. V. Kolen'ko, H. S. Gupta, M. Yoshimura, F. Guitián, "Synthesis of a nanocrystalline calcium phosphate bone-cement exhibiting rapid conversion to hydroxyapatite". 2nd European Association for Chemical and Molecular Sciences Chemistry Congress (2ndEuCheMS), September 16-20 2008, Torino, Italy.

- I. S. Neira, Yu. V. Kolen'ko, H. S. Gupta, M. Yoshimura, F. Guitián, "Reinforcement of a develop calcium phosphate bone-cement by addition of hydroxyapatite crystals: influence of the morphology". 2nd European Association for Chemical and Molecular Sciences Chemistry Congress (2ndEuCheMS), September 16-20 2008, Torino, Italy.

- I. S. Neira, Yu. V. Kolen'ko, H. S. Gupta, M. Yoshimura, F. Guitián, "Route to an advanced calcium phosphate bone-cement and its reinforcement by hydroxyapatite crystals of various morphologies. 21st International Symposium of Ceramics in Medicine (Bioceramics 21), October 21-24 2008, Búzios, Brazil.

PUBLICATIONS

- I. S. Neira, F. Guitián, T. Taniguchi, T. Watanabe, M. Yoshimura, "Hydrothermal synthesis of hydroxyapatite whiskers with sharp faceted hexagonal morphology", *J. Mat. Sci.* **2008**, 43(7), 2171-2178.

- I. S. Neira, Yu. V. Kolen'ko, O. I. Lebedev, G. Van Tendeloo, H. S. Gupta, F. Guitián, M. Yoshimura, "Efficient morphology control of hydroxyapatite crystals *via* hydrothermal synthesis", *Cryst. Grow Des.*, accepted.

- I. S. Neira, Yu. V. Kolen'ko, O. I. Lebedev, G. Van Tendeloo, H. S. Gupta, N. Matsushita, M. Yoshimura, F. Guitián, "Nano-indentation of a nanocrystalline bioactive calcium phosphate bone-cement", *Acta Biomater.*, submitted.

- I. S. Neira, Yu. V. Kolen'ko, M. Yoshimura, F. Guitián, "Mechanical properties of a calcium phosphate bone-cement reinforced with hydroxyapatite crystals of various morphologies", *in preparation*.

J Mater Sci (2008) 43:2171–2178
DOI 10.1007/s10853-007-2032-9

Hydrothermal synthesis of hydroxyapatite whiskers with sharp faceted hexagonal morphology

Inés S. Neira · Francisco Guitián · Takaaki Taniguchi · Tomoaki Watanabe · Masahiro Yoshimura

Received: 28 October 2006 / Accepted: 20 July 2007 / Published online: 22 December 2007
© Springer Science+Business Media, LLC 2007

Abstract We report an effective method for the synthesis of hydroxyapatite whiskers with sharp faceted hexagonal shape employing a low temperature (90 °C) hydrothermal route with calcium nitrate tetrahydrate, diammonium phosphate and urea as starting materials. The key parameters of the synthesis process i.e. duration, temperature cycle of the treatment and starting pH value are carefully varied and the end products are investigated using powder X-ray diffraction (XRD), Raman-scattering, infrared spectroscopy (IR), elemental analysis, scanning electron microscopy (SEM), energy-dispersive X-ray spectroscopy (EDX), transmission electron microscopy (TEM), electron diffraction (ED), and high-resolution TEM (HRTEM) in order to find the optimal reaction conditions that lead to the desired hexagonal morphology of HA whiskers. The results demonstrate that gradual and greater increase in solution pH during the hydrothermal process favors large quantity of the single-crystalline hydroxyapatite whiskers with well defined hexagonal morphology.

Introduction

Hydroxyapatite ($Ca_{10}(PO_4)_6(OH)_2$, identified as HA from now onwards) ceramics are excellently biocompatible and osteoconductive (they enhance bone formation by acting as a scaffold on which bone cells can attach and grow) [1]. They are widely studied as an alternative to natural bone grafts because they do not present limitations in availability, potential disease transmission and/or risk of rejection which commonly occurs in natural bone materials. However the fracture toughness parameter of HA is lower than that reported for natural human bones (~1 MPa/m^2 in front of 2–12 MPa/m^2) [2], and thus, till now, its applications are limited to areas where bones are free of dynamic load i.e. for non-load bearing, for craniofacial and periodontal applications, for coatings [3, 4], or as materials for the development of scaffolds for bone tissue engineering [5, 6]. One of the most studied methods to improve the mechanical properties of HA ceramics is the addition of whiskers. Since it is well known that various fibrous bioinert materials that have been applied in HA ceramics such as SiC, C, Si_3N_4, Al_2O_3 or ZrO_2 decrease the biocompatibility and bioactivity of this ceramics [7–9], the investigation of HA with rod-like morphology have recently received much attention [10]. They have been synthesized by various methods, mainly by hydrothermal synthesis [11–13] or homogenous precipitation [14–16], and to a lesser extent, by growth in the gel system [17], molten salts synthesis [18], electrochemical deposition [19] and liquid–solid–solution synthesis [20]. Products prepared by molten salts reaction and in the gel system show important dependence on the preparation conditions. Moreover, with the molten salts method, the obtained crystals incorporates K^+ ions, and therefore, they could not be regarded as pure HA whiskers. Under hydrothermal conditions and homogeneous precipitation, crystalline HA particles can be successfully synthesized, but the particles mostly posses needle-like shape [21–25].

I. S. Neira · T. Taniguchi · T. Watanabe · M. Yoshimura (✉)
Materials and Structures Laboratory, Tokyo Institute of Technology, 4259 Nagatsuta, Midori-ku, Yokohama 226-8503, Japan
e-mail: yoshimura@msl.titech.ac.jp

I. S. Neira · F. Guitián
Instituto de Cerámica de Galicia, Universidade de Santiago de Compostela, Santiago de Compostela 15782, Spain

Although a numerous mentioned above approaches that have been already realized for the fabrication of HA with rod-like morphology (nanorods, needles, wires, fibres, etc.), some problems are still unsettled, namely, there are just few reports of preparation of HA whiskers with hexagonal morphology in literature [18, 26, 27]. Moreover, these synthetic procedures are not well developed in terms of phase purity, homogeneity of microstructural characteristics (well-defined hexagonal whisker shape, narrower particle size range, etc.), and feasibility of large-scale production, as it is reasonably expected to be in a slower, moderate-temperature hydrothermal context.

In this work, we present the hydrothermal route to HA whiskers with sharp faceted hexagonal prism morphology. This approach to HA whiskers may be useful for the detailed experimental investigation on shape-dependent mechanical properties of HA ceramics.

Experimental

Materials

$Ca(NO_3)_2 \cdot 4H_2O$ (98.5%, Wako), $(NH_4)_2HPO_4$ (99.0%, Wako), $(NH_2)_2CO$ (urea, 99.0%, Wako), HNO_3 (63%, Wako) and $C_{16}H_{33}N(CH_3)_3Br$ (Cetyltrimethylammonium bromide (CTAB), 98%, Wako) were used as received. Distilled water was also used during the hydrothermal process as well as for the preparation of the aqueous solution of nitric acid.

Hydrothermal syntheses

$Ca(NO_3)_2 \cdot 4H_2O$ (5.84 mmol), $(NH_4)_2HPO_4$ (3.50 mmol) (Ca/P molar ratio: 1.67) and urea (17.5 mmol) were mixed with 25 mL of distilled water in a polytretrafluoroethylene (PTFE) vessel (volume-40 mL). The pH was then adjusted to the 3–3.5 range by diluted 0.5 M $HNO_{3(aq)}$ using a Mettler Toledo InLab 413SG pH-meter. The vessel was capped by a PTFE cover and placed inside a stainless steel autoclave. A 1.5 mm thick, low density (0.6 g/cm^3) HYPER-SHEET gasket (GORE-TEX) with porous structure of PTEF polymer was placed between the vessel and the cover, which enables gradual release of the CO_2 forming during the urea decomposition under hydrothermal conditions. The sealed autoclave was subject to treatments of different temperature cycles (Table 1; Fig. 1) as well as several additional syntheses were performed at lower temperatures and durations. One additional synthesis was performed together with CTAB as a surfactant under critical micelle point (9.2×10^{-4} mol/L).

The product of the hydrothermal process was collected by filtration, washed four times with distilled water and once with ethanol, and then dried at 80 °C for 12 h on air. Throughout this work, a set of acronyms is used (Table 1) where the Roman characters mean the number of the sample follows.

Characterization

The products were characterized by powder X-ray diffraction (XRD) using a Rigaku RINT 2000 diffractometer with Ni-filtered CuK_α radiation (λ = 1.54178 Å), operating at 200 mA and 50 kV. Data were collected in the 2θ range of 3–70°, with a scan speed of 1°/min, and a step width of 0.02°.

The room temperature Raman scattering measurements were carried out on a Jobin Yvon T64000 spectrometer with visible Ar^+ laser light (λ = 514.532 nm) as the excitation light. The slits were adjusted so that the resolution was 1 cm^{-1}. All measurements were carried out under the microscope (the laser spot diameter was estimated to be between 1 μm and 2 μm).

The room temperature diffuse reflectance infrared (IR) Fourier-transform spectra were recorded on a Jeol JIR-7000 spectrometer with a resolution of 4 cm^{-1} and a scan time of 10. The crystalline products (~4 mg) were thoroughly grinded with (~200 mg) potassium bromide powder (KBr for IR, Wako) in an agate mortar and pestle to give a fine mixture, and subjected to IR analysis. For the background spectrum, a fine grinded KBr powder was used.

Carbon content was quantitatively determined by combustion bulk elemental analysis using a Fisons EA 1108 elemental analyzer.

The morphology and structure were studied by scanning electron microscopy (SEM) using a Hitachi S-4500 microscope operating at 15 kV, transmission electron microscopy (TEM), electron diffraction (ED) and high-resolution TEM (HRTEM) using a Hitachi H-8100 microscope operating at 200 kV. The samples for transmission electron microscopy were dispersed in ethanol and deposited on a holey carbon grid.

Energy-dispersive X-ray spectroscopy (EDX) for semi-quantitative Ca and P content determination was performed with a EDAX DX-95 spectrometer using commercial hydroxyapatite powder (HW-003, Mitsubishi Chemicals) as a standard sample (molar ratio Ca/P = 1.67).

Results

Hydrothermal synthesis

HA whiskers were prepared by a reaction between $Ca(NO_3)_2 \cdot 4H_2O$ and $(NH_4)_2HPO_4$ (Ca/P molar

Table 1 Summary of the selected hydrothermal reactions

Sample	Synthesis condition	pH_{final}	Phase composition	
			XRD	Raman
I	90 °C, 72 h	8.4	HA	HA
II	Scheme 1	8.6	HA	HA
III	Scheme 2	6.9	OCP[b] + HA + DCPA[c]	OCP[b] + HA + DCPA[c]
IV[a]	Scheme 2	7.5	OCP[b] + HA	OCP[b] + HA

[a] CTAB is used as a surfactant

[b] Major amount of the octacalcium phosphate phase ($Ca_8H_2(PO_4)_6 \cdot 5H_2O$, OCP)

[c] Minor amount of the dicalcium phosphate anhydrous phase ($CaHPO_4$, DCPA)

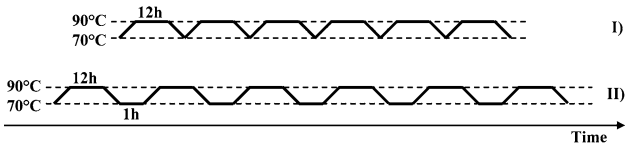

Fig. 1 Schemes of the temperature cycles applied during the experimental procedure. The temperature increasing and decreasing step was 0.5 °C/min in case of Scheme 1 and 1 h ramping at 70 °C in Scheme 2

ratio = 1.67) under hydrothermal conditions. The precursors were chosen to avoid contamination of the precipitate by incorporation of others foreign ions like K^+, Na^+, etc. Urea was utilized as a homogenous precipitation agent, since its decomposition (85–95 °C) releases $NH_{3(aq)}$ to the reaction medium which in turn gradually increase the pH.

The summary from selected hydrothermal syntheses is given in Table 1. Analysis of the obtained data reveals that important parameters for the hydrothermal synthesis of the title compound are temperature, duration, and the initial pH. The optimal values were found to be $T = 90$ °C, $t = 72$ h, and starting pH = 3.0–3.5. All our attempts to reduce the temperature and/or duration of the hydrothermal treatment as well as other starting pH range do not lead to the phase pure HA.

In order to improve the quantity of HA whiskers with well-defined hexagonal prism shape, two different temperature cycles of treatment were applied with the aim of gradually increasing the pH during the synthesis by decreasing the temperature under the urea decomposition point to interrupt it, and thus hold up the NH_3 release (Fig. 1; Table 1). It was observed that Scheme 1 (Fig. 1) results in the highest quantity of the pure HA phase whiskers with sharp faceted hexagonal shape, while all the syntheses following Scheme 2 (Fig. 1) drastically reduced the yield, although the application of a surfactant (CTAB) during the same provides possibility to obtain HA whiskers with relatively uniform size distribution (*vide infra*).

Powder X-Ray diffraction

The powder XRD pattern of the samples reveals the overall crystalline structure of the products (Fig. 2). According to the phase analysis, the patterns of the samples **I** and **II** are nearly the same and also confirm the formation of a pure phase hydroxyapatite by comparison with standard database (JCPDS No. 72-1243). However, there are some inconsistencies between the intensity of the XRD reflections corresponding to the (100), (200) and (300) diffraction peaks reported in JCPDS database and the observed ones (inset in Fig. 2); it is caused by the texturing of whisker particles samples. These results demonstrate that the as-produced HA is mainly oriented along the *c*-axis direction of the hexagonal crystal structure [18, 28].

A different result is obtained in case of samples **III** and **IV**. According to the XRD analysis (Fig. 2; Table 1) sample **III** consists of octacalcium phosphate (OCP) (JCPDS No. 74-1301), hydroxyapatite (JCPDS No. 72-1243) and dicalcium phosphate anhydrous (DCPA) (JCPDS No. 70-1425) where OCP is the main phase along with 30 wt.% of HA and a minor amount of the DCPA by-product. OCP and HA has similar structures and a rough estimation of wt.% content was made from comparison of the intensities of the main diffraction peaks after background correction, since the Rietveld profile refinement was not possible on this complex mixture. Generally powder XRD of sample **IV** is similar to that from **III** (Fig. 2), but this powder has less DCPA by-product (~10 times) and less HA (~3 times).

Raman scattering

Figure 3 shows the Raman spectra collected from the samples. The set of observed Raman bands agrees fairly well with the phase composition reported by XRD technique, which reveals that samples **I** and **II** contains pure HA only, while samples **III** and **IV** are mixtures of OCP as the most abundant phase and HA.

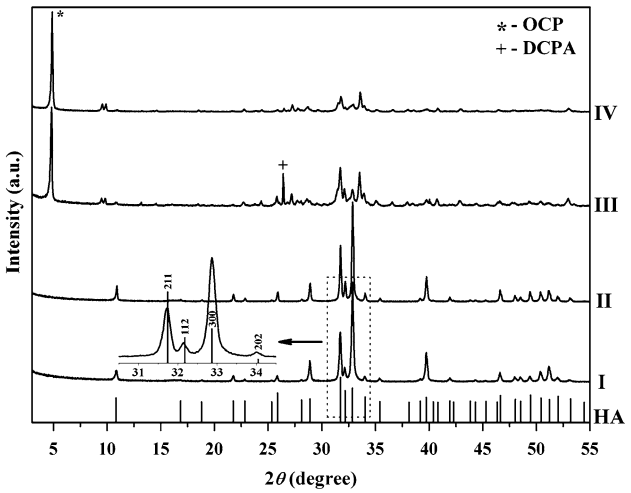

Fig. 2 Comparison of the powder diffraction patterns for the samples **I**, **II**, **III** and **IV**. An inset shows the enlarged region from 30.5° to 34.5° 2θ for the sample **I**, where most intensive peaks of HA are expected. Tick marks below the patterns correspond to the positions of the Bragg reflections expected for the HA structure. The positions of the most intense diffraction peaks for the OCP and DCPA are shown by asterisk and plus, respectively

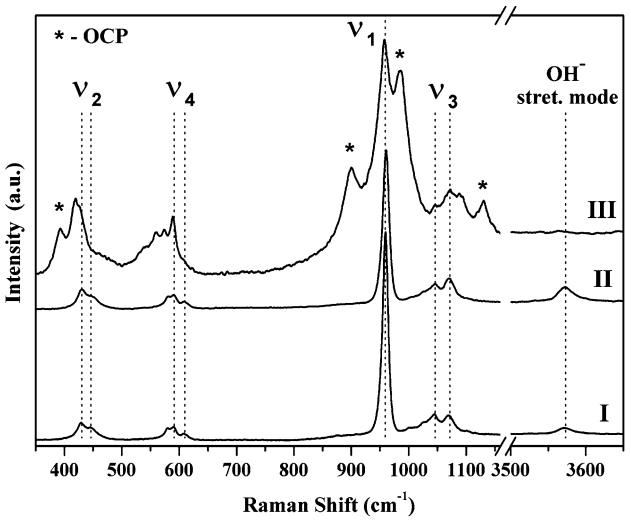

Fig. 3 Raman spectra collected from the samples **I**, **II** and **III**. Raman spectrum collected from the sample **IV** is almost identical to spectrum from sample **III**, and omitted for clarity

*Samples **I** and **II***

These Raman spectra show very strong characteristic peak at ~960 cm^{-1} due to the symmetric stretching mode $v_1(PO_4)$. Apart from this v_1 mode, two $v_2(PO_4)$ (~437 cm^{-1}), three $v_3(PO_4)$, (~1046 cm^{-1}), and four $v_4(PO_4)$ (~593 cm^{-1}) are also observed [29]. Band at 3570 cm^{-1} corresponds to stretching vibration of OH^- groups.

*Sample **III** and **IV***

Since the OCP is the phase most abundant in sample **III** according to XRD, its Raman spectrum is predominantly similar to spectra reported for this calcium phosphate [30]. OCP contains both HPO_4^{2-} and apatitic PO_4^{3-} groups in its structure. Thus, the Raman spectrum contains bands similar to those observed in samples **I** and **II** for modes v_1, v_2, v_3 and v_4, even if these bands are shifted. In addition, new peaks due to HPO_4^{2-} appear at 1130, 985, 900 and 392 cm^{-1} [30]. The disappearance of the band due to the OH^- stretching mode is explained because OCP, the principal phase in sample **III**, does not contain OH^- groups in its crystal structure. It should be emphasized that practically no differences in the intensity and band positions for the **IV** (not shown) and **III** samples were detected by Raman scattering, indicating absence of any significant change in their abundant phase composition and local structure. The observed band positions for sample **IV** are in very good agreement with published data for the OCP phase [30].

Diffuse reflectance infrared Fourier-transformed spectroscopy

The chemical and structural composition of the product was studied by IR, an useful technique to determinate the incorporation of anions, such as CO_3^{2-} and/or HPO_4^{2-}, to the crystal lattice of the as-produced powders, since XRD measurement can only clarify the average and static symmetry.

Figure 4 shows the spectra from samples **I** and **II**, which are characteristic of HA. Peaks at 3572 and 638 cm^{-1} corresponds to the stretching (v_s) and librational modes (v_L) of the hydroxyl group, respectively. Also harmonic overtones and/or combination bands appear at 2075 and 1992 cm^{-1} [29]. Bands derived from the group PO_4^{3-} appear at 1103, 1068 and 1028 cm^{-1} (attributed to the triply degenerated asymmetric stretching mode vibration—v_3); 962 cm^{-1} (symmetric stretching mode of the P–O bond—v_1); 605, 577 and 563 cm^{-1} (triply degenerated bending mode of the O–P–O bond—v_4) [29]. In addition, there are also bands that confirm the existence of carbonate ions, which indicate that the samples obtained with this hydrothermal synthesis are not stoichiometric HA, but carbonated [29]. If the CO_3^{2-} ions are occupying the OH^- sites, carbonated HA (CO_3HA) is designated as an A-type, while if they are in the PO_4^{3-} positions, CO_3HA is considered as B-type. According to the assignation of anion CO_3^{2-} [31], sample **I** and **II** can be referred as AB-type, since peaks due to type A (at 1544 and 879 cm^{-1}) and type B (at 1454, 1421 and 874 cm^{-1}) appears in the spectra.

This fact is proved well by the representative combustion bulk elemental analysis, which shows that the samples **I** and **II** contained 0.61 and 0.54 wt.% of carbon, respectively.

It should be noted that the band at 874 cm^{-1} can also be attributed to (P–OH) mode of HPO_4^{2-} group, but as can be seen in Fig. 4, the other two characteristic vibrational bands of this anion at ~980 and ~1080 cm^{-1} do not appear [32], so HA in sample **I** and **II** does not incorporate HPO_4^{2-} ions. In addition, the absence of bands at 1382 cm^{-1} indicates that NO_3^- ions coming from reactants are not included in the crystalline structure of as-produced HA [33].

Scanning electron microscopy

The morphologies of the hydrothermally produced powders, observed by SEM, are shown in Fig. 5.

Figure 5a shows a typical SEM image of the sample **I**. This sample mostly consists of the particles with plate-like morphology exhibiting a non-uniform size distribution. Also, particles with hexagonal shape have been barely observed. By contrast, SEM observations of the sample **II** (Fig. 5b) reveal a large quantity of whiskers with well-defined hexagonal morphology (one is shown in the inset to Fig. 5b) with typical widths of 0.7–3.0 μm and with lengths in the range from 3.8 μm to 9.1 μm. It should be noted that plate-like structures were almost not detected by SEM for this sample, and it can be seen that hexagonal prisms are the principal shape in sample **II**. Energy-dispersive X-ray spectroscopy (EDX) on samples **I** and **II** showed that the average molar ratios of the calcium and

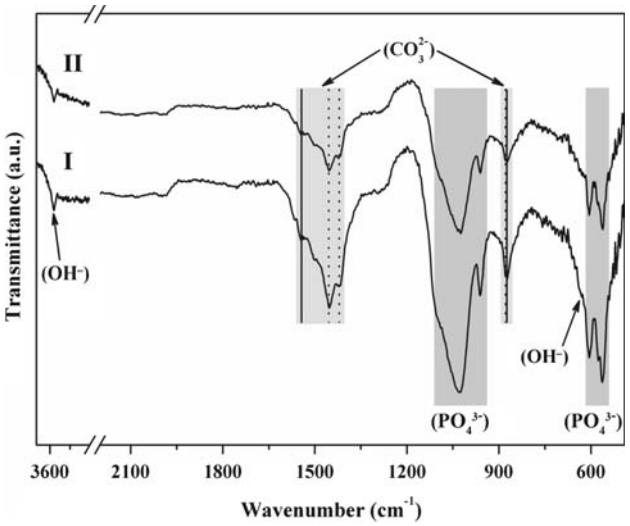

Fig. 4 IR spectra collected from the as-produced phase pure HA samples **I** and **II**. *Solid lines* are characteristic of A-type HA (partial substitution of the OH^- by CO_3^{2-}) while *dotted lines* are characteristic of B-type HA (partial substitution of the PO_4^{3-} by CO_3^{2-})

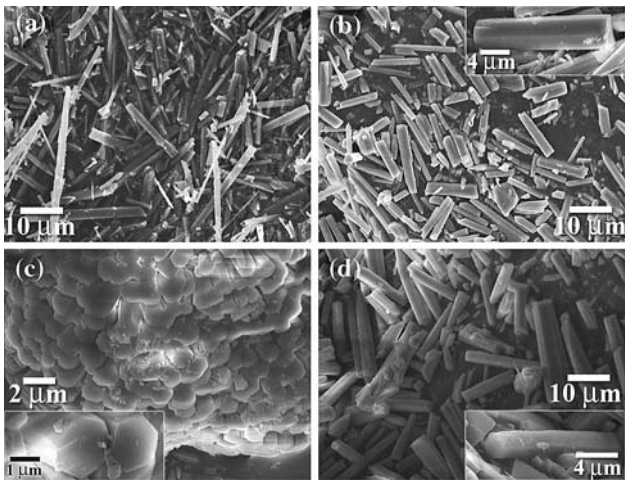

Fig. 5 SEM microphotographs are shown for hydrothermally prepared HA whiskers with the insets showing the observed well-defined hexagonal shape: (**a**) **I**, (**b**) **II**, (**c**) **III** and (**d**) **IV**

phosphorous elements (Ca/P) are ~1.76 for sample **I** and ~1.74 for sample **II**; these values are in good agreement with the stoichiometric value for HA (Ca/P = 1.67) as well as with the initial molar ratio under hydrothermal synthesis.

SEM observations of sample **III** (Fig. 5c) shows the presence of two types of well crystallized structures in the sample—mainly plate-like shapes, attributed to the OCP abundant phase [34], and big aggregates consisting of sharp faceted hexagonal crystals with quite uniform widths of about ~1.5 μm (inset in Fig. 5c). These big agglomerates of hexagons were determined to be hydroxyapatite by EDX analysis. The average molar ratio of the calcium and phosphorous elements (Ca/P) is ~1.73, which is more close to the stoichiometric value for HA (Ca/P = 1.67) than those for OCP (Ca/P = 1.33) and/or DCPA (Ca/P = 1.00). The general morphology of the sample **IV** is quite similar to that of sample **III**, with mainly plate-like structures corresponding to the OCP phase, but at the same time, the presence of non-agglomerated whiskers was also observed. The typical SEM image of a whisker region is shown in Fig. 5d. It should be emphasized, that these whiskers possess a sharp faceted hexagonal morphology (see inset to Fig. 5d) with relatively uniform size distribution with an average width of ~2.5 μm and an average length of ~14 μm, as was established from a detailed particle size analysis of 50 whiskers from several SEM micrographs. The EDX analysis of sample **IV** shows that overall Ca/P ratio in the whisker regions is ~1.72, indicating that those whiskers are HA. It should be note that the values of Ca/P ratio in hydrothermal synthesis products are higher than that of stoichiometric HA, which is believed to result from a partial substitution of the phosphate and hydroxide groups in the HA lattice by carbonate ions, in agreement with IR and elemental analyses.

Transmission electron microscopy

Transmission electron microscopy was applied to investigate the microstructure of the whiskers and the observed results are in agreement with SEM and XRD data. Figure 6a shows a typical low-magnification TEM image of as-prepared whiskers of sample **II**. The sample mostly consists of well defined and sharp faceted rod-like crystals with mean diameters of 0.7–1.0 μm, in good agreement with the SEM data. The inset in Fig. 6a is a typical electron diffraction pattern corresponding to the terminal end of HA whisker. ED reveals a high crystallinity of the whiskers, which was also confirmed by XRD. The dots of the ED pattern can be completely indexed in the HA hexagonal $P6_3/m$ space group, using the HA unit cell parameters of JCPDS No. 72-1243. It should be noted that all electron diffraction patterns along the long-axis of the whisker have the same geometry, which was subsequently confirmed to be a common feature of almost all whiskers in sample **II**, thus revealing that each HA whisker is a single crystal. The terminal end of HA whisker in Fig. 6a is shown on Fig. 6b, which reveals the presence of a local deformation in the synthesized whiskers. HRTEM analysis (Fig. 6c) of an edge area of the terminal end of HA whisker also indicates that the whisker is highly crystalline. The crystal lattice can be estimated to be about 8.2 and 3.4 Å, corresponding to the (210) and (002) planes of the hexagonal crystal structure of HA, respectively, indicating that the hydroxyapatite whisker grow along the *c*-axis, which is in good agreement with XRD data, discussed above.

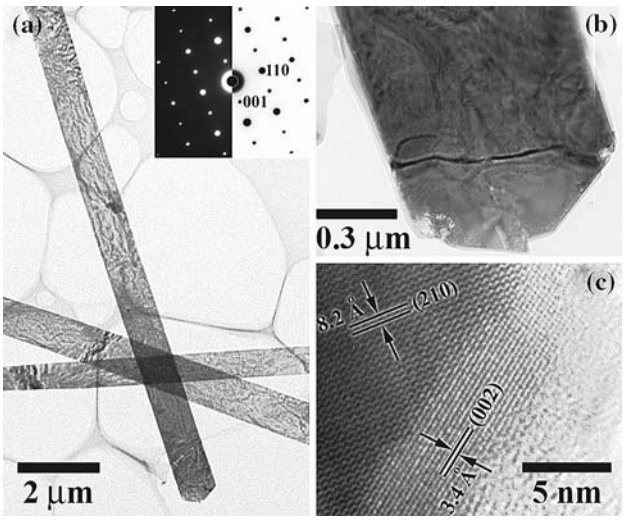

Fig. 6 (**a**) A low-magnification TEM image and corresponding ED pattern (inset) of HA whiskers of sample **II**; (**b**) TEM image of the terminal end of HA whisker in (**a**); (**c**) HRTEM image of an edge area of the lamellar terminal end of HA whisker in (**b**), with (210) and (002) lattice planes visible

Discussion

In our investigation, samples **I** and **II** are the products of the hydrothermal reaction between $Ca(NO_3) \cdot 4H_2O$ and $(NH_4)_2HPO_4$ at 90 °C for 72 h and Scheme 1 temperature cycle (Fig. 1), respectively, in presence of urea. According to XRD, powders **I** and **II** are pure HA hexagonal phases which is also confirmed by Raman spectroscopy. Moreover, powder XRD results demonstrate that the particles in as-prepared samples **I** and **II** are mainly oriented along the *c*-axis direction of the hexagonal crystal structure [28]. SEM investigation clearly indicates the presence of whisker structures with well-defined hexagonal prism morphology, especially in case of sample **II**. TEM/ED/HRTEM confirms that the whiskers in the sample **II** are single crystals, sharp faceted and oriented with their axis along *c*-axis. Existence of local deformations in hydrothermally prepared whiskers was also revealed by TEM.

It is to be noted that IR spectroscopy provides important information about the local and dynamic state of whiskers. For samples **I** and **II** it reveals that they are not stoichiometric HA owing to a partial substitution of the both PO_4^{3-} and OH^- groups by carbonate anion, indicating CO_3HA formation (type AB). Biological HA has multiple substitutions and deficiencies at all ionic sites and contains 3–5 wt.% carbonate groups [35], thus obtaining CO_3HA whiskers is the requirement rather than a problem for its application for a biodegradable bioceramics [36]. Apparently, carbonate anions come from the urea decomposition into $NH_{3(aq)}$ and $CO_{2(g)}$. Although $CO_{2(g)}$ is mostly released from the system through the porous PTEF gasket, however it's also partially dissolved into the water, and therefore, easily incorporated into HA product due its strong ability to incorporate different ions [35].

It was established that the optimal initial pH values resulting in the pure HA phase formation lay in the range of 3.0–3.5. For the sample **I** the initial pH was 3.0 while after hydrothermal reaction it becomes 8.4 due to the urea decomposition, and thus providing the proper condition for the phase pure HA formation, according to the solubility diagrams of calcium phosphates [37]. HA cannot be synthesized directly at the initial pH and the synthesis must proceed through multiple steps; first the formation of DCPA, following the formation of OCP, which should act as the precursors for the final HA whiskers formation [35].

SEM observation shows that in sample **I**, HA mainly retains the plate-like morphology of OCP [34], which is because of the similarities between its structures, and OCP act as a template for epitaxial growth of HA [38]. In order to increase the quantity of hexagonal whiskers, a gradual increase of the pH in the reaction medium (sample **II**) was

performed by varying the temperature between 70 °C and 90 °C, followed by ramping at 90 °C for 12 h in the range of urea decomposition (Fig. 1, Scheme 1). Such gradual increasing ensures a low speed of HA nucleus formation as well as slow crystallization of hexagonal whiskers of HA, thus excluding the intensive epitaxial growth from the OCP template. SEM images of sample **II** reveal that the quantity of particles with hexagonal well-defined prism morphology is highest in present study and considerably larger in comparison with sample **I**, but at the same time, the size distribution of the as-produced whiskers is non-uniform.

In light of this, one very important question appears, can we control the HA whisker size distribution in the products? In order to verify this question, the synthesis with another temperature cycle of hydrothermal treatment (Fig. 1, Scheme 2) which is similar to the mentioned above including one addition ramp step at 70 °C for 1 h was performed (Table 1, samples **III** and **IV**) with respect to more gradual increasing of the pH.

According to XRD and Raman spectroscopy, syntheses by Scheme 2 resulted in the reduction of yield of the title compound. For example, in case of sample **III** OCP is a most abundant phase, consequently, large quantity of plate-like structures, attributed to the OCP morphology [34], were detected by SEM in this powder. Taking into account that the final pH of the reaction solution for sample **III** was 6.9, it is believed that 72 h is not enough for the proper degree of urea decomposition under this cycle and therefore leads to the low yield of HA phase under Scheme 2 process (Fig. 1). According to XRD, content of HA in sample **III** is ~30 wt.%. SEM reveals that HA structures are mostly gathered in big aggregates with a radial growth consisting of hexagonal crystals with quite uniform widths of about ~1.5 μm.

To avoid such aggregation, an additional synthesis with CTAB as a surfactant was carried out (sample **IV**). In addition, the cation surfactant CTAB ionizes completely in an aqueous system, resulting in an amino cation with tetrahedral structure. Owing to the charge and structure complementarity, these positive headgroups may bond to the phosphate reactant, PO_4^{3-} ions, which are also tetrahedral in structure, and thus provide a control of the crystallization process [39]. As a result, the growth of HA with rod-like morphology is expected to be a favor at low pH [40]. SEM images show that the HA whiskers formed in this case possess relatively uniform size distribution. This results from samples **III** and **IV** suggest that the slow control of the pH increase by controlling the urea decomposition, provide the conditions for the HA crystallization to form more uniform structures. At the same time, the low value of final pH obtained for these samples and its phase composition, also show that not all the urea is decomposed, establishing the fact that pH has not increased enough to continue the hydrolysis of precursors to form HA.

The achievement of a uniform distribution and controlled growth of whiskers based on HA has great importance in improving the mechanical properties of hydroxyapatite ceramics. The mechanism of the whiskers crystallization and growth under hydrothermal conditions is therefore under investigation.

Conclusions

Hydroxyapatite whiskers were successfully produced by a simple approach, based on the reaction between $Ca(NO_3) \cdot 4H_2O$, $(NH_4)_2HPO_4$ and urea under hydrothermal conditions. Investigation of the influence of the temperature and duration of the hydrothermal treatment as well as the initial pH value on the phase composition of the product has resulted in the optimization of the synthetic conditions, leading to the large quantity synthesis. Gradual increase of the pH technique and the use of surfactant during the synthesis allowed producing single-crystalline whiskers with sharp faceted hexagonal prism morphology elongated along the *c*-axis of the apatite crystal structure.

Acknowledgements We are grateful to Dr. Yu. V. Kolen'ko and Prof. M. Aizawa for the fruitful discussion. The work is partially supported by the Spanish Ministry of Science and Technology, under the project MAT2002-03857.

References

1. Suchanek W, Yoshimura M (1998) J Mater Res 13:94
2. Barralet JE, Grover L, Gaunt T, Wright AJ, Gibson IR (2002) Biomaterials 23:3063
3. Hench LL (1991) J Am Ceram Soc 74:1487
4. Dorozhkin SV, Epple M (2002) Angew Chem Int Ed Engl 41:3130
5. Ong JL, Chan DC (2000) Crit Rev Biomed Eng 28:667
6. Bohner M (2001) Key Eng Mater 192–195:765
7. Park K, Sundaresan S, Vasilos T, Sung C (1994) J Mater Res 9:2476
8. Ruys AJ, Wei M, Milthorpe BK, Brandwood A, Sorrell CC (1993) J Aust Ceram Soc 29:51
9. De With G, Corbijn AJ (1989) J Mater Sci 24:3411. doi: 10.1007/BF01139073
10. Ioku K (1998) In: Amjad Z (ed) Calcium phosphates in biological and industrial systems. Kluwer, Boston, p 357
11. Yubao L, De Groot K, De Wijn J, Klein CPAT, Meer SVD (1994) J Mater Sci Mater Med 5:326
12. Yoshimura M, Suda H, Okamoto K, Ioku K (1994) J Mater Sci 29:3399. doi:10.1007/BF00352039
13. Suchanek W, Yashima M, Kakihana M, Yoshimura M (1997) J Am Ceram Soc 80:2805
14. Fujishiro Y, Yabuki H, Kawamura K, Sato T, Okuwaki A (1993) J Chem Tech Biotechnol 57:349
15. Zhang H, Yan Y, Wang Y, Li S (2002) Adv Eng Mater 4:916

16. Kandori K, Horigami N, Yasukawa A, Ishikawa T (1997) J Am Ceram Soc 80:1157
17. Mizutani Y, Hattori M, Okuyama M, Kasuga T, Nogami M (2005) J Eur Ceram Soc 25:3181
18. Taş AC (2001) J Am Ceram Soc 84:295
19. Lu X, Zhao Z, Leng Y (2005) J Cryst Growth 284:506
20. Wang X, Zhuang J, Peng Q, Li Y (2006) Adv Mater 18:2031
21. Liu J, Ye X, Wang H, Zhu M, Wang B, Yan H (2003) Ceram Int 29:629
22. Fujishiro Y, Yabuki H, Kawamura K, Sato T, Okuwaki A (1993) J Chem Tech Biotechnol 57:349
23. Park HC, Baek DJ, Park YM, Yoon SY, Stevens R (2004) J Mater Sci 39:2531. doi:10.1023/B:JMSC.000002021.82216.6b
24. Aizawa M, Kinoshita M, Yamada K, Itatani K, Kishioka A (1998) Inorg Mater 5:387
25. Ioku K, Yamauchi S, Fujimori H, Goto S, Yoshimura M (2002) Solid State Ionics 151:147
26. Andrés-Vergés M, Fernández-González C, Martínez-Gallego M (1998) J Eur Ceram Soc 18:1245
27. Yao J, Tjandra W, Chen YZ, Tam KC, Ma J, Soh B (2003) J Mater Chem 13:3053
28. Aizawa M, Ueno H, Itatani K, Okada I (2006) J Eur Ceram Soc 26:501
29. Koutsopoulos S (2002) J Biomed Mater Res 62:600
30. Sauer GR, Zunic WB, Durig JR, Wuthier RE (1994) Calcif Tissue Int 54:414
31. Monma H, Takahashi T (1987) Gypsum lime 210:287
32. Steger E, Herzog K (1964) Anorg All Chem 331:169
33. Nakamoto K (1997) Infrared and Raman spectra of inorganic and coordination compounds, part B: applications in coordination, organometallic and bioinorganic chemistry, 5th edn. Wiley, New York, p 87
34. Brown WE (1962) Nature 196:1048
35. Elliot JC (1994) Structure and chemistry of the apatites and other calcium ortophosphates. Elsevier, Amsterdam, p 80, 154, 260
36. Ison IC, Fulmer MT, Barr BM, Constanz BR (1994) In: Brown PW, Constanz B (eds) Hydroxyapatite and related materials. CRC Press, Boca Raton FL, p 215
37. Levin EM, Robbins CR and Mcmurdie HF (1964) Phase diagrams for ceramist, vol I. American Ceramic Society, Columbus, OH, fig. 246
38. Brown WE, Smith JP, Lehr JR, Frazier AW (1962) Nature 196:1050
39. Li Y, Li YD, Deng ZX (2001) Int J Inorg Mater 3:633
40. Wang YJ, Chen JD, Wei K, Zhang SH, Wang XD (2006) Mater Lett 60:3227